

**STUDY AND DEVELOPMENT OF EMISSION TOMOGRAPHY  
AND GAMMA IMAGING TECHNIQUES FOR NUCLEAR  
APPLICATIONS**

*By*

**TUSHAR ROY**

**PHYS01200804006**

**Bhabha Atomic Research Centre, Mumbai**

*A thesis submitted to the*

*Board of Studies in Physical Sciences*

*In partial fulfillment of requirements*

*for the Degree of*

**DOCTOR OF PHILOSOPHY**

*of*

**HOMI BHABHA NATIONAL INSTITUTE**



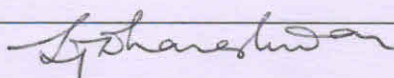
**January, 2016**

# Homi Bhabha National Institute

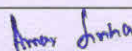
## Recommendations of the Viva Voce Committee

As members of the Viva Voce Committee, we certify that we have read the dissertation prepared by TUSHAR ROY entitled "Study and Development of Emission Tomography and Gamma Imaging Techniques for Nuclear Applications" and recommend that it may be accepted as fulfilling the thesis requirement for the award of Degree of Doctor of Philosophy.

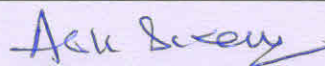
Chairman – Dr. L. J. Dhareshwar



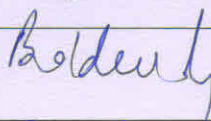
Guide / Convener – Dr. Amar Sinha



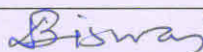
Co-guide - Dr. Alok Saxena



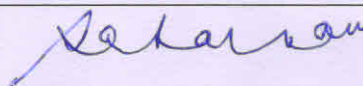
Examiner – Dr. Baldev Raj



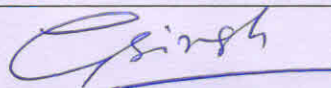
Member 1- Dr. D. C. Biswas



Member 2- Dr. A. V. R. Reddy



Technology Advisor – Dr. Gursharan Singh



Final approval and acceptance of this thesis is contingent upon the candidate's submission of the final copies of the thesis to HBNI.

I/We hereby certify that I/we have read this thesis prepared under my/our direction and recommend that it may be accepted as fulfilling the thesis requirement.

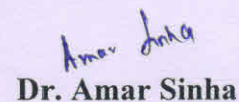
Date: 29<sup>th</sup> January, 2016



Place: MUMBAI

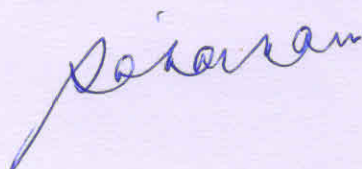
Dr. Alok Saxena

Co-guide



Dr. Amar Sinha

Guide



## **STATEMENT BY AUTHOR**

This dissertation has been submitted in partial fulfillment of requirements for an advanced degree at Homi Bhabha National Institute (HBNI) and is deposited in the Library to be made available to borrowers under rules of the HBNI.

Brief quotations from this dissertation are allowable without special permission, provided that accurate acknowledgement of source is made. Requests for permission for extended quotation from or reproduction of this manuscript in whole or in part may be granted by the Competent Authority of HBNI when in his or her judgment the proposed use of the material is in the interests of scholarship. In all other instances, however, permission must be obtained from the author.

**(Tushar Roy)**

## **DECLARATION**

I, hereby declare that the investigation presented in the thesis has been carried out by me. The work is original and has not been submitted earlier as a whole or in part for a degree / diploma at this or any other Institution / University.

**(Tushar Roy)**

## List of Publications arising from the thesis

### JOURNAL

#### a. Published

1. “A practical fan-beam design and reconstruction algorithm for Active and Passive Computed Tomography of radioactive waste barrels”,

**Tushar Roy**, M. R. More, Jilju Ratheesh and Amar Sinha, *Nuclear Instruments & Methods A*, **2015**, 794, 164-170

2. “Three-dimensional SPECT imaging with LaBr<sub>3</sub>:Ce scintillator for characterization of nuclear waste”,

**Tushar Roy**, Jilju Ratheesh and Amar Sinha, *Nuclear Instruments & Methods A*, **2013**, 735, 1-6.

3. “A Simplified Approach for Generation of Projection Data for Cone Beam Tomography”,

**Tushar Roy**, P.S.Sarkar and A.Sinha, *Pramana*, **2010**, Vol. 76, Number 4, 667-679.

#### c. Communicated

4. “Active and Passive CT for waste assay using LaBr<sub>3</sub>(Ce) detector”,

**Tushar Roy**, Yogesh Kashyap, M. R. More, Jilju Ratheesh and Amar Sinha, *Insight-BJNDT*

### CONFERENCE PROCEEDING

1. “Simulation Study of Single Photon Emission Computed Tomography for Industrial Applications”,

**Tushar Roy**, P.S.Sarkar and Amar Sinha, *AIP Conference Proceedings*, Volume 1050 (**2009**)

## CONFERENCE

1. “Active and Passive Computed Tomography for Waste Assay”,

**Tushar Roy**, Jilju Ratheesh, Mahendra More and Amar Sinha, *APCNDT-14 (2013)*

2. “Single Photon Emission Computed Tomography: An NDT tool for Waste Assay”, **Tushar Roy**, Jilju Ratheesh and Amar Sinha; *NDE-13 (2012)*

3. “Single Photon Emission Computed Tomography: A Simulation Study”,

**Tushar Roy**, P.S.Sarkar, Y.S.Kashyap and Amar Sinha; *Conference on Computed Tomography (CT-2008) (2008)*

**(Tushar Roy)**

## **ACKNOWLEDGEMENTS**

First and foremost, I would like to thank my guide, Dr. Amar Sinha, for introducing me to this enriching area of research. His expertise and valuable guidance in many areas of imaging, in general, and Emission Tomography, in particular, has been of immense help to me.

I am also grateful to Dr. Yogesh Kashyap, Dr. Mayank Shukla and Dr. P S Sarkar for their helpful discussion over the course of this work. I would also like to acknowledge the dedication and support of Ms. Jilju Ratheesh and Mr. M R More for assisting me in data acquisition.

Special thanks to my doctoral committee, Dr. L J Dhareshwar, Dr. Gursharan Singh, Dr. A V R Reddy and Dr. D C Biswas, for their encouragement and valuable suggestions.

Acknowledgements are also due to my colleagues – Tarun, Ashish, Saroj, Nirmal, Shefali and Payal – for all their friendship, help and advice.

Lastly, I would like to thank my parents for their blessings and supporting me in my academic endeavours. This acknowledgement would be incomplete without thanks to my wife, Susmita, and daughter, Trishna, who had to endure many working weekends and evenings during the course of this research work and whose encouragement has been vital.

## LIST OF ABBREVIATIONS

A&PCT	Active & Passive Computed Tomography
ART	Algebraic Reconstruction Technique
CT	Computed Tomography
ECT	Emission Computed Tomography
EM	Expectation Maximization
FDK	Feldkamp-Davis-Kress
FBP	Filtered Backprojection
FWHM	Full width at half maximum
GPU	Graphical Processor Unit
LS	Least Square
MAP	Maximum <i>a posteriori</i>
MAP-EM	Maximum <i>a posteriori</i> - Expectation Maximization
MLEM	Maximum Likelihood Expectation Maximization
OSEM	Ordered Subsets Expectation Maximization
PET	Positron Emission Tomography
PHWR	Pressurized Heavy Water Reactor
SART	Simultaneous Algebraic Reconstruction Technique
SIRT	Simultaneous Iterative Reconstruction Technique
SGS	Segmented Gamma-ray Spectrometry
SPECT	Single Photon Emission Computed Tomography
TCT	Transmission Computed Tomography

## LIST OF NOTATIONS

$\mathfrak{R}_{att}$	Attenuated Radon Transform
$\mathcal{B}$	Backprojection operator
$D_{\mu}$	Divergent Beam Transform
$\mathfrak{F}$	Fourier transform
$\mathcal{H}$	Hilbert transform
$L$	Likelihood function
$\mu$	Linear attenuation coefficient
$n_{\theta}$	Number of (angular) projections
$n_p$	Number of detector bins in each projection
$n_z$	Number of Z-slices
$A$	Probability system matrix
$g$	Projection vector
$\mathfrak{R}$	Radon transform
$f$	Source activity vector
$\otimes$	Convolution operator
$\odot$	Element-by-Element Multiplication Operator

# CONTENTS

	<b>Page No.</b>
<b>SYNOPSIS</b>	xiv
<b>LIST OF FIGURES</b>	xxiv
<b>LIST OF TABLES</b>	xxxiii
<b>CHAPTER 1 Introduction</b>	1
1.1 Brief history of SPECT Imaging	4
1.2 Imaging with radiation	7
1.3 Transmission tomography	8
1.4 Emission tomography	9
1.4.1 Positron emission Tomography (PET)	9
1.4.2 Attenuation Compensation in PET	11
1.4.3 Single Photon Emission Computed Tomography (SPECT)	13
1.4.4 Attenuation Compensation in SPECT	14
1.5 Active and Passive Computed Tomography (A&PCT)	15
1.6 Formation of planar image in SPECT	17
1.7 Development of Reconstruction Algorithms in SPECT	19
1.7.1 Analytical Reconstruction	19
1.7.2 Iterative Reconstruction	20
1.8 Detection of Gamma Rays	21
1.8.1 Scintillation detector	21
A. Sodium Iodide	
B. Lanthanum Bromide	
1.8.2 Semiconductor detector	24
A. High Purity Germanium	
1.9 Image degradation in SPECT	26
1.9.1 Attenuation	26
1.9.2 Collimator blurring	26
1.9.3 Scatter	27
1.9.4 Poisson noise	28

1.10	Applications of SPECT in nuclear technology	28
1.10.1	Waste assay	29
1.10.2	Rod-by-rod fuel properties of fuel assemblies	29
1.10.3	Verification of spent fuel integrity	30
1.11	Aims and Scope of the Thesis	31
<b>CHAPTER 2</b>	<b>SPECT Reconstruction Techniques</b>	<b>36</b>
2.1	Analytical Reconstruction Technique	39
2.1.1	The Radon transform	39
2.1.2	The Fourier Slice Theorem	40
2.1.3	Direct Fourier Method	42
2.1.4	Backprojection	42
2.1.5	Filtered Backprojection Method	45
2.1.6	Attenuated Radon transform	47
2.1.7	Novikov's Explicit Inversion Formula	48
2.1.8	The Hilbert Transform	49
2.1.9	Relation between Hilbert Transform and Fourier Transform	49
2.1.10	The $\pm\pi/2$ phase shift	50
2.1.11	Fan-Beam Reconstruction with Equally Spaced Detectors	51
2.1.12	Cone-Beam Reconstruction with Circular Scanning Geometry	53
2.1.13	Optimal Number of Projections in FBP	54
2.2	Algebraic Reconstruction Technique (ART)	55
2.2.1	Observation model	55
2.2.2	The Linear Least Square Estimation	56
2.2.3	Implementation of ART	56
2.2.4	Simultaneous Iterative Reconstruction Technique (SIRT)	58
2.2.5	Simultaneous ART (SART)	58
2.3	Statistical approach	59

2.3.1	Bayesian estimation	59
2.3.2	Maximum likelihood estimation	60
2.3.3	Ordered-Subsets Expectation Maximization (OSEM)	62
2.3.4	Maximum <i>a posteriori</i> Expectation Maximization (MAP-EM)	63
2.4	Analytical vs. Iterative	64
2.5	Algorithms used in this thesis	65
<b>CHAPTER 3</b>	<b>Modelling the Forward Projection</b>	<b>66</b>
	<b>Section I: Generation of Projection Data</b>	
3.1	Parallel beam geometry	68
3.2	Fan beam and cone beam geometry	69
3.3	Voxel Based Approach for Cone Beam Data	69
3.3.1	Transmission Tomography Data	69
3.3.2	Emission Tomography Data	71
3.4	Novel Approach for Cone Beam Projection Data	74
3.4.1	Transmission Tomography Projection Data Generation	74
3.4.2	Emission Tomography Projection Data Generation	77
3.5	Testing the projection data	78
3.5.1	Reconstruction of Transmission projection Data using FDK algorithm	79
3.5.2	Reconstruction of Emission projection Data using Novikov's inversion formula	80
3.6	Computation Time	82
3.7	Image comparison: correlation coefficient	82
3.7.1	Projection data comparison	82
3.7.2	Reconstructed image comparison	84
	<b>Section II: Generation of Probability System Matrix</b>	
3.8	The Probability System Matrix	86
3.8.1	Structure of system matrix	87
3.9	2D Reconstruction: Parallel Beam System Model	88
3.9.1	Geometrical factor	91

	3.9.2	Attenuation factor	93
	3.9.3	Other Projections	96
3.10		2D Reconstruction : Fan Beam System Model	98
3.11		Fully 3D Reconstruction	103
	3.11.1	Geometrical factor	105
	3.11.2	Attenuation factor	106
	3.11.3	Other Projections	106
<b>CHAPTER 4</b>		<b>Simulation Studies</b>	108
4.1		Phantoms	109
	4.1.1	Phantom 1: Point sources (2D)	109
	4.1.2	Phantom 2: Distributed sources with uniform attenuation (2D)	110
	4.1.3	Phantom 3: Distributed sources with non-uniform attenuation (2D)	110
	4.1.4	Phantom 4: Waste drum with distributed sources and point sources in low attenuating matrix (3D)	111
	4.1.5	Phantom 5: Waste drum with distributed sources in high attenuating matrix (3D)	113
	4.1.6	Phantom 6: PHWR Fuel Bundle	114
4.2		2D Reconstruction (Parallel Beam)	115
	4.2.1	Phantom 1: Point Sources	115
	4.2.2	Phantom 2: Distributed sources with uniform attenuation (2D)	120
	4.2.3	Phantom 3: Distributed sources with non-uniform attenuation (2D)	123
4.3		2D Reconstruction (Fan Beam)	126
	4.3.1	Phantom 1: Point sources	126
	4.3.2	Phantom 3: Distributed sources with non-uniform attenuation	128
4.4		3D Reconstruction – Line Integral Model	130
	4.4.1	Phantoms 4 and 5: Waste drum	130
	4.4.2	Phantom 6 : PHWR fuel bundle	132

4.5	3D Reconstruction – 3D Collimator Model	134
4.5.1	Phantom 1: Point sources	135
4.6	Error Estimation of Reconstructed Image	138
	a) Mean Squared Error (MSE)	
	b) Contrast (C)	
	c) Spatial deviation	
	d) Deviation in reconstructed activity	
4.7	Effect of Collimation	140
4.8	Discussion	143
<b>CHAPTER 5</b>	<b>Experimental Results</b>	144
5.1	Experimental set-up	144
5.1.1	Sample Stage	145
5.1.2	Sample (Matrix)	146
	A. Sample: Hollow SS rods	
	B. Sample: Solid Perspex disc with indexed holes	
	C. Sample: Aluminum drum	
	D. Sample: SS waste barrel	
5.1.3	Source (Passive)	148
5.1.4	Active Source	148
5.1.5	Detector	149
	A. NaI(Tl)	
	B. LaBr <sub>3</sub> (Ce)	
	C. High Purity Ge (HPGe)	
5.1.6	Collimator	152
5.1.7	Data Acquisition System	153
	<b>Section I: SPECT Reconstruction with <sup>137</sup>Cs sources</b>	
5.2	2D SPECT Reconstruction: Parallel beam geometry	156
5.2.1	Sample: Hollow SS Rods	156
5.2.2	Sample: Solid Perspex disc	159
5.3	3D SPECT Reconstruction: Parallel beam	162
5.3.1	Sample: Al Drum	163
	A. Analytical Reconstruction	
	B. 2D (Stacked) MLEM Reconstruction	

	C. Fully 3D MLEM Reconstruction	
5.3.2	SS Drum	172
	A. Analytical Reconstruction	
	B. 2D (Stacked) MLEM Reconstruction	
	C. Fully 3D MLEM Reconstruction	
5.4	3D SPECT Reconstruction: Fan beam	179
5.5	Effect of Collimation	184
5.6	Discussion	187
	<b>Section II: Active and Passive CT for Nuclear Waste Assay</b>	
5.7	Active and Passive CT	189
5.8	Experimental set-up	189
5.9	A&PCT of Plutonium with LaBr <sub>3</sub> (Ce)	189
5.9.1	Experimental Results	190
5.9.1.1	Active CT	192
5.9.1.2	Passive CT	193
5.10	A&PCT of Plutonium with HPGe	195
5.10.1	Spectral Features of Plutonium	196
A.	Energy Range: 0 – 160 keV	
B.	Energy Range: 160 – 320 keV	
C.	Energy Range: 320 – 460 keV	
D.	Energy Range: 480 – 800 keV	
5.10.2	Active CT	201
5.10.3	Passive CT	202
5.11	Discussion	204
<b>CHAPTER 6</b>	<b>Concluding Remarks</b>	205
	<b>References</b>	208

## SYNOPSIS

Tomography is the science of reconstructing an object from its projection images. It has long been applied in transmission Computed Tomography (CT) to obtain cross-sectional images (attenuation map) of objects. However, there are certain nuclear applications, such as waste assay or determination of burnup in fuel assemblies, where not only the attenuation information but also the source strength or activity of the gamma emitters inside the object is required. In this case, transmission CT does not provide source strength information but only the spatial distribution of attenuating materials. Commonly used techniques like segmented gamma scanning provide only gross source strength information without giving position information. However, there is another class of tomography, known as Emission Tomography or Single Photon Emission Computed Tomography (SPECT), which can be used for not only position but also source strength imaging of gamma (emission) sources inside an object. SPECT is a non-destructive technique that assesses the distribution of gamma emitting radionuclide within a given object. It uses the decay of radioactive isotopes to image the spatial distribution of the isotope as well as to determine their source strength or activity. The intensities of the radiation measured are directly related to the radionuclide distribution inside the object. A basic difference between transmission tomography and emission tomography, also called Active and Passive CT, is the absence of external radiation source in the case of emission tomography. In fact, the source of radiation is located inside the object itself and the aim of emission tomography (Passive CT) is to find their distribution using the radiation emitted by them. The formulation in this case is fundamentally different from transmission tomography (Active CT). In the case of SPECT, the absorption of the

gamma rays as it travels from the source to the detector has to be taken into account. In the absence of absorption, the problem simply reduces to reconstructing the source term from its measured Radon transform. In the presence of absorption, however, the exponential attenuation of the gamma rays inside the object has to be considered. The source term is then reconstructed from the so-called *exponential Radon transform* or *attenuated Radon transform*.

SPECT has been widely used in medical field for functional imaging of organs (in contrast to anatomical imaging of organs in CT or MRI). However, its application in nuclear field is still quite limited. The present thesis explores the development of SPECT as a gamma imaging technique for nuclear applications as in nuclear waste assay. Characterization of nuclear waste drums is required for its safe disposal, transportation, permanent storage as well as nuclear material accounting, especially  $^{239}\text{Pu}$ . Another application is the post irradiation of fuel which, till now, is mostly done destructively by chopping the fuel and then examining it. SPECT provides a possibility for non-destructive examination of irradiated nuclear fuel and fuel bundle. Most of the literature present deals with different aspects of clinical SPECT imaging and very little information are available for nuclear applications. Hence, there is a need to develop reconstruction methods which are specifically suited for nuclear applications. This thesis aims focuses on developing analytical and iterative reconstruction methods for nuclear applications, particularly, for waste assay application.

For demonstration of SPECT imaging for nuclear waste assay, a number of factors have to be considered. Some of these factors are as follows:

- Development of analytical and iterative reconstruction codes

- Phantom generation and projection data generation for testing the algorithms
- Developing methods for construction of 2D system matrix
- Developing methods for construction of fully 3D system matrix
- Experimental validation for different geometries

The above factors have been dealt with in the present thesis and are further elaborated in the following discussion. The present work can be broadly divided in two parts. The first part involves development of reconstruction algorithm for SPECT which are suitable for nuclear waste as well as development of theoretical phantoms to validate developed reconstruction algorithms. This includes developing analytical and iterative reconstruction codes and testing them through computer simulations for various cases. The second part of the work involves experimental studies for reconstructing radioisotope activity in a given matrix. This includes lab based experiments for 2D SPECT and finally setting up a 3D SPECT imaging facility for Active and Passive CT of waste drums.

For SPECT reconstruction, a large number of iterative and analytical techniques have been developed earlier. An explicit analytical formula for inverting the attenuated Radon transform in parallel beam geometry was first given by Novikov and later by Natterer. This was extended to fan-beam and cone-beam geometries by Huang et al. The analytical reconstruction techniques are fast and provide an exact solution of the inverse problem. However, analytical techniques are incapable of taking into account various physical parameters of the system which affect the quality of the final reconstructed image. For example, Novikov's inversion formula for SPECT reconstruction takes into account the attenuation suffered by photons inside the object but does not take into

account the role of collimator which plays an integral role in the quality of reconstructed image. To solve this problem, iterative techniques are used.

Iterative techniques generally solve a set of linear equations which relate the vector of observables to the vector of unknowns through a matrix. This matrix is known as the system probability matrix (or system model), the elements of which describe the probability that a photon from a given pixel is detected in a given detector or projection bin. The system model can take into account various physical factors involved in the detection process – collimation, scatter, distance-dependent fall in intensity, transmission through collimator, etc. All these factors can be modeled into the system probability matrix. In fact, system matrix is at the heart of any iterative reconstruction. Extensive work has been done as a part of this thesis for developing analytical methods of computing the system matrix for parallel beam geometry and taking into account the attenuation and collimator effects. The method is extended to fan beam geometry also.

The system matrix discussed above is a 2D system matrix, in the sense that the reconstructions are carried out for each slice or section of a 3D object using the 2D system matrix corresponding to that particular slice. The reconstructed slices are then stacked together to form a three dimensional volume. This method is most commonly used as it is computationally less intensive and easier to apply. However, this method does not take into account the inter-slice cross talk which results in blurring in the reconstructed volume. To take into account the contribution of slices above and below the reconstruction plane, a fully 3D system matrix has been computed. This takes into account the contribution from each voxel of the three dimensional object to each

projection bin. The method increases the computational requirement manifold. However, inter-slice blurring of reconstructed images is reduced.

Once the system matrix is constructed, the problem reduces to solving the linear system of equations. A host of iterative techniques exist to solve this linear system of equations. They can be categorized under two broad headings – algebraic and statistical. The algebraic reconstruction techniques obtain the activity distribution by calculating the least squares (LS) solution for the set of equations. The LS problem is usually an ill-posed inverse problem. Also, a straightforward solution for LS problem is computationally heavy and iterative methods are used. The algebraic reconstruction techniques, such as ART, SART and SIRT are methods for solving the LS problem using different types of iterations. In algebraic methods, an additive correction term is generally applied in each iteration. The correction term is proportional to the difference between the measured projection data and calculated projection data from the previous iteration. The iterations are repeated till the solution converges.

The statistical approach takes into account the Poisson statistics of radiation. The solution for activity distribution is obtained by Bayesian point estimation: maximum a posteriori or maximum likelihood estimation. The methods for Bayesian point estimation are solved iteratively. Maximum Likelihood-Expectation Maximization (MLEM) and its variants are the most common statistical iterative algorithms used in SPECT reconstruction. A Poisson statistical model is applied to the projection data in these studies.

The purpose of MLEM is to find the best estimate for  $f$ : “the mean number of radioactive disintegrations  $\hat{f}$  in the image that can produce the sinogram  $g$  with the

highest likelihood”. Each projection is a linear combination of Poisson distributed variables  $A_{ij}$ . Each iteration of the algorithm consists of two steps:

**E-step:** the expectation step which forms the expression of the likelihood of any reconstructed image given the measured data.

**M-step:** the maximization step which finds the image with the most likelihood to give the measured data. The maximum is found when the derivative of the log-likelihood is zero. One remarkable feature of EM algorithm is the non-negativity of the estimate: if the initial guess is positive, the estimate is positive after each iteration.

MLEM algorithm converges extremely slowly and may require nearly 100-200 iterations. To accelerate the MLEM reconstruction, an OSEM (Ordered Subsets Expectation Maximization) algorithm is used. Instead of using the whole set of projections, OSEM uses a subset of projections at each sub-iteration step.

Iterative techniques can model the physical system rather accurately. The main disadvantage of iterative techniques is being computationally intensive and mathematical complexity involved in computing the probability system matrix. Also, for large sized images, the memory involved in computation is huge. This requires the use of accelerated GPU based approach or parallel computing.

As a part of this work, an experimental facility has been set-up for three dimensional SPECT imaging. One of the highlights of the present work is the use of  $\text{LaBr}_3(\text{Ce})$  detectors for imaging.  $\text{LaBr}_3(\text{Ce})$  has an intermediate energy resolution between  $\text{NaI}(\text{Tl})$  and  $\text{HPGe}$  detectors. I have explored the use of  $\text{LaBr}_3(\text{Ce})$  detectors for SPECT imaging of low level wastes. Complex spectra have also been analyzed with  $\text{HPGe}$ . However, these detectors are costly and cannot be used in large numbers due to

geometrical constraints. There are cases where high scanning speed is required and detectors with even an intermediate energy resolution are sufficient to analyze the spectra.  $\text{LaBr}_3(\text{Ce})$  provides such an opportunity as a large number of detectors can be used. Though some simulation studies have been reported, this is the first instance of experimental SPECT imaging with  $\text{LaBr}_3(\text{Ce})$  being reported.

The thesis is organized in seven chapters to discuss different aspects of the present work. The contents of the chapters are summarized as follows. Chapter 1 comprises a general introduction to SPECT imaging. This chapter discusses the major issues of SPECT with a focus on nuclear applications in particular. Mechanism of gamma ray interaction with matter and their detection are stated. Further, the basic concept of imaging using radiation sources, in general, and transmission tomography and emission tomography (or SPECT), in particular, is discussed in detail. Different aspects of SPECT imaging, such as effect of attenuation, noise, collimation and scatter are briefly explained. An overview of the history of SPECT imaging along with a brief summary of literature survey on analytical and iterative algorithms is also provided. Some of the nuclear applications of SPECT, such as, waste assay and burnup determination of individual rods in a fuel bundle have been discussed.

Chapter 2 throws light on mathematical aspects of different reconstruction algorithms in SPECT. The reconstruction algorithms can be broadly classified into analytical and iterative reconstructions. To explain analytical reconstruction proposed by Novikov for inversion of attenuated Radon transform, a mathematical background of Radon transform and filtered backprojection has been provided. The iterative approach allows a complex model of gamma radiation interaction to be taken into account

including the effect of collimation and scatter as well as statistical variability of measured data. Different EM techniques – MLEM, OSEM and MAP-EM have been discussed.

Chapter 3 discusses modeling of the forward projection, that is, generation of the projection data. This chapter is divided into two sections. The first section describes a novel approach developed in this thesis for generation of forward projection for fan and cone beam geometries. This method does not take into account the effect of collimator, scattering or distance. The projection data generated thus corresponds to an ‘ideal’ collimator system where the detector ‘sees’ photons along a straight line path only. The second section describes the analytical method used in this thesis to obtain the probability system matrix. This is a more rigorous approach which takes into account the effect of collimator and distance (scattering has been neglected). The projection data generated using this system matrix mimics the experimental parameters more closely as compared to the ideal approach in section one. In addition to producing projections, this system matrix can be used for iterative reconstructions. Finally, a fully 3D system matrix has been computed for fully 3D reconstruction which takes into account the contribution of slices below and above the reconstruction plane to the reconstructed image.

Chapter 4 deals with the computer simulations used to test analytical and iterative reconstruction techniques developed in this thesis. Both the line integral approach (no collimator) and collimator modeled approach have been considered for constructing the simulated projections. Different 2D phantoms have been considered to elucidate the contribution of collimator modeled system matrix in reconstruction. Analytical reconstruction codes have been developed for parallel, fan and cone beam configurations. 3D phantoms for simulated waste drum have been used to test analytical fan and cone

beam reconstruction codes. For experiments, however, cone beam geometry has not been explored.

Chapter 5 presents the experimental results. The experimental SPECT imaging system consists of the following: (a) Sample Stage – to manoeuvre the sample during acquisition; (b) Collimator – to define the path of gamma rays accepted by the detector; (c) Detector – to record gamma photon events and (d) Data Acquisition System – to record, save and/or display the data for offline processing. The choice of detector depends on particular application (in terms of energy resolution and efficiency) and cost. As multiple detectors are required in SPECT imaging, NaI(Tl) is commonly preferred because of its high efficiency and low cost. However, NaI(Tl) has poor energy resolution and cannot be employed for situations where a complex energy spectrum is to be analyzed. An important aspect of this thesis is to explore the use of LaBr<sub>3</sub>(Ce) detector for SPECT imaging. Initial feasibility experiments were carried out for 2D imaging with <sup>137</sup>Cs sources. Finally a 3D SPECT imaging lab was set up for scanning of mock waste drums with <sup>137</sup>Cs sources. For reconstruction, both analytical and iterative reconstructions have been employed and results have been presented. This chapter also includes a section on the application of SPECT imaging in the context of nuclear waste assay. An active and passive computed tomography (A&PCT) has been carried out for assessing the distribution and quantification of <sup>239</sup>Pu in waste drums. During the ACT measurements, an external gamma/X-ray source is used to determine the attenuation map of the object. With this knowledge of the attenuation map, the PCT measurements are then carried out to reconstruct the gamma sources inside the object.

Chapter 6 concludes with a summary of works and discusses briefly the important outcomes of the work and future directions.

The highlights of the work done under this thesis may be summarized as follows:

- (i) Implementation of analytical and iterative reconstruction codes
- (ii) Novel method for generation of fan and cone beam data for simulated objects
- (iii) Development and implementation of fully 3D SPECT reconstruction
- (iv) Development and implementation of a practical fan-beam Active and Passive CT technique for waste assay
- (v) Developing a three dimensional SPECT imaging facility for scanning of waste drums using LaBr<sub>3</sub>(Ce) detectors
- (vi) Active and Passive CT for <sup>239</sup>Pu assay in waste drums

## LIST OF FIGURES

Figure No.	Figure Caption	Page No.
<b>CHAPTER 1</b>		
<b>Fig. 1.1</b>	Schematic configuration for transmission tomography	8
<b>Fig. 1.2</b>	Schematic configuration for positron emission tomography	10
<b>Fig. 1.3</b>	Schematic arrangement for co-incidence detection in PET	11
<b>Fig. 1.4</b>	Schematic configuration for SPECT	13
<b>Fig. 1.5</b>	Formation of image in SPECT using collimated detector	14
<b>Fig. 1.6</b>	A typical SPECT set-up. The gamma photon emitted (a) is absorbed by the collimator (b) reaches the detector (c) misses the detector completely	17
<b>Fig. 1.7</b>	Steps in SPECT image formation (a) Projection of a 2D object (b) Collection of projections for different rotations (c) Sinogram (d) Reconstructed object	18
<b>Fig. 1.8</b>	Energy band diagram for an activated inorganic scintillator	22
<b>Fig. 1.9</b>	Comparison of NaI(Tl), LaBr <sub>3</sub> (Ce) and HPGe spectra	25
<b>Fig. 1.10</b>	Waste assay at Lawrence Livermore National Laboratory using A&PCT technique (a) high resolution transmission tomograph (b) active data set (c) passive data set	29
<b>Fig. 1.11</b>	Ba-140 distribution in BWR fuel assembly	30
<b>Fig. 1.12</b>	Experimentally obtained image of the fuel model with a non-active rod in position (E,5) and an empty rod, representing the water channel, in position (D,4)	31
<b>CHAPTER 2</b>		
<b>Fig. 2.1</b>	Co-ordinate system for parallel beam projection	40
<b>Fig. 2.2</b>	Fourier Slice Theorem: It relates the Fourier transform of a projection with the Fourier transform through the object along a	41

radial line at an angle  $\theta$

<b>Fig. 2.3</b>	Projection and backprojection	43
<b>Fig. 2.4</b>	Backprojection reconstructs an image by taking each view and smearing it along the path it was originally acquired. The resulting image is a blurry version of the correct image	44
<b>Fig. 2.5</b>	Effect of number of projections on the backprojected image	44
<b>Fig. 2.6</b>	Flowcharts of analytical algorithms (a) Direct Fourier Transform (b) Filtered Backprojection	45
<b>Fig. 2.7</b>	In filtered backprojection, negative wings are introduced to eliminate blurring	45
<b>Fig. 2.8</b>	Fan-beam geometry	52
<b>Fig. 2.9</b>	Cone beam geometry	53
<b>Fig. 2.10</b>	Three possible grouping patterns of subsets in OSEM reconstruction	62

---

### CHAPTER 3

---

<b>Fig. 3.1</b>	Fan beam geometry for transmission tomography. $w_{ij}$ 's are calculated for all the pixels lying on the ray path $\mathbf{r}_\eta$	70
<b>Fig. 3.2</b>	A ray emanating from the source $S$ is subsequently attenuated on passing through a pixel $(i, j)$ lying on the path $\mathbf{r}_\eta$	71
<b>Fig. 3.3</b>	Fan beam geometry for emission tomography. The shaded pixel represents the source. $w_{ij}$ 's are calculated for all the pixels lying on the ray path $\mathbf{r}_\eta$	72
<b>Fig. 3.4</b>	A ray emanating from a source pixel $(i_s, j_s)$ is subsequently attenuated on passing through a pixel $(i, j)$ on the path $\mathbf{r}_\eta$ . The dotted line traces the ray back to the focal point $S$	73
<b>Fig. 3.5</b>	Cone beam geometry for projection data generation	75
<b>Fig. 3.6</b>	Transformation of a point $P$ to $P''$ under two subsequent rotations	77

<b>Fig. 3.7</b>	Phantom 1 (a) original object (b) sinogram (c) reconstructed object	79
<b>Fig. 3.8</b>	Phantom 2 (a) Activity (b) Attenuation map (c) sinogram (d) reconstructed activity ( <b>Note:</b> The boundary of the drum is shown only for illustration purpose)	80
<b>Fig. 3.9</b>	Plot of correlation coefficient between the projection data (for Phantom 3) computed geometrically and the projection data calculated using the algorithm) as a function of the rotation angle	83
<b>Fig. 3.10</b>	(a) Phantom 3 (b), (c) Reconstructed images using projection data calculated using the algorithm and the projection data computed geometrically respectively (d) Plot of correlation coefficient as a function of Z-slice no.	84
<b>Fig. 3.11</b>	Plot of correlation coefficient as a function of Z-slice no. for Phantom 1	85
<b>Fig. 3.12</b>	2D System Matrix for different collimation ratio (a) 5 (b) 20. The total number of elements in each case is $3.24 \times 10^5$	88
<b>Fig. 3.13</b>	Pixels contributing to the probability system matrix in the case of ideal collimator (dark grey) and non-ideal collimator (light grey)	90
<b>Fig. 3.14</b>	Area of the $j^{th}$ detector as seen by $i^{th}$ pixel	92
<b>Fig. 3.15</b>	A ray starting from a (red) pixel passes through (yellow) pixels on its way to the detector bin	94
<b>Fig. 3.16</b>	Intersection of a ray with a pixel	95
<b>Fig. 3.17</b>	Schematic arrangement for multiple detector A&PCT scan in (a) Parallel beam and (b) Fan beam configurations showing the requirement of active source(s)	99
<b>Fig. 3.18</b>	Computing the geometrical factor of system matrix	102
<b>Fig. 3.19</b>	Schematic representation of 2D (stacked) and fully 3D Reconstruction	103
<b>Fig. 3.20</b>	Area of the $j^{th}$ detector as seen by $i^{th}$ pixel for 3D case	105

---

---

**CHAPTER 4**

---

<b>Fig. 4.1</b>	Phantom 1 <b>(a)</b> Activity map <b>(b)</b> Attenuation map	110
<b>Fig. 4.2</b>	Phantom 2 <b>(a)</b> Activity map <b>(b)</b> Attenuation map	110
<b>Fig. 4.3</b>	Phantom 3 <b>(a)</b> Activity map <b>(b)</b> Attenuation map	111
<b>Fig. 4.4</b>	Phantom 4 <b>(a)</b> Activity map <b>(b)</b> Attenuation map	112
<b>Fig. 4.5</b>	Phantom 5 <b>(a)</b> Activity map <b>(b)</b> Attenuation map	114
<b>Fig. 4.6</b>	Phantom 6 <b>(a)</b> 3D Activity map <b>(b)</b> Cross-sectional view	115
<b>Fig. 4.7</b>	<b>(a)</b> Sinogram <b>(b)</b> Analytical reconstruction for line integral modeled projection	116
<b>Fig. 4.8</b>	<b>(a)</b> Sinogram <b>(b)</b> Analytical reconstruction for collimator modeled projection	116
<b>Fig. 4.9</b>	Line profile at 0° and 90° <b>(a)</b> and <b>(c)</b> Line integral model <b>(b)</b> and <b>(d)</b> Collimator model	117
<b>Fig.4.10</b>	<b>(a)</b> Sinogram for collimator modeled projection with Poisson noise <b>(b)</b> ART <b>(c)</b> SART <b>(d)</b> MLEM <b>(e)</b> OSEM reconstructions	118
<b>Fig.4.11</b>	Line profile for reconstructed image using various reconstruction techniques	119
<b>Fig.4.12</b>	<b>(a)</b> Sinogram <b>(b)</b> Analytical reconstruction for collimator modeled projection	120
<b>Fig.4.13</b>	<b>(a)</b> Sinogram for collimator modeled projection with Poisson noise <b>(b)</b> ART <b>(c)</b> SART <b>(d)</b> MLEM <b>(e)</b> OSEM reconstructions	121
<b>Fig.4.14</b>	Line profile for reconstructed image using various reconstruction techniques	121
<b>Fig. 4.15</b>	<b>(a)</b> Sinogram for collimator modeled projection with Poisson noise <b>(b)</b> ART <b>(c)</b> SART <b>(d)</b> MLEM <b>(e)</b> OSEM reconstructions	122
<b>Fig. 4.16</b>	<b>(a)</b> Sinogram <b>(b)</b> Analytical reconstruction for line integral modelled projection	123
<b>Fig. 4.17</b>	<b>(a)</b> Sinogram <b>(b)</b> Analytical reconstruction for collimator modelled projection	124
<b>Fig. 4.18</b>	<b>(a)</b> Sinogram for collimator modeled projection with Poisson	125

	noise <b>(b)</b> ART <b>(c)</b> SART <b>(d)</b> MLEM <b>(e)</b> OSEM reconstructions	
<b>Fig. 4.19</b>	<b>(a)</b> Sinogram <b>(b)</b> Analytical reconstruction for collimator modelled projection in fan beam geometry	126
<b>Fig. 4.20</b>	<b>(a)</b> Sinogram for collimator modeled projection with Poisson noise <b>(b)</b> ART <b>(c)</b> SART <b>(d)</b> MLEM <b>(e)</b> OSEM reconstructions for fan beam geometry	127
<b>Fig. 4.21</b>	<b>(a)</b> Sinogram <b>(b)</b> Analytical reconstruction for collimator modeled projection in fan beam geometry	128
<b>Fig. 4.22</b>	<b>(a)</b> Sinogram for collimator modeled projection with Poisson noise <b>(b)</b> ART <b>(c)</b> SART <b>(d)</b> MLEM <b>(e)</b> OSEM reconstructions for fan beam geometry	129
<b>Fig. 4.23</b>	CT reconstructed image <b>(a)</b> Phantom 4 <b>(b)</b> Phantom 5	130
<b>Fig. 4.24</b>	Reconstructed activity of Phantom 4 <b>(a)</b> Parallel beam <b>(b)</b> Fan beam <b>(c)</b> Cone beam	131
<b>Fig. 4.25</b>	Reconstructed activity of Phantom 5 <b>(a)</b> Parallel beam <b>(b)</b> Fan beam <b>(c)</b> Cone beam	132
<b>Fig. 4.26</b>	Parallel beam reconstruction: Reconstructed activity of PHWR fuel bundle <b>(a)</b> cross-sectional view <b>(b)</b> 3D view	133
<b>Fig. 4.27</b>	Fan beam reconstruction: Reconstructed activity of PHWR fuel bundle <b>(a)</b> cross-sectional view <b>(b)</b> 3D view	133
<b>Fig. 4.28</b>	Cone beam reconstruction: Reconstructed activity of PHWR fuel bundle <b>(a)</b> cross-sectional view <b>(b)</b> 3D view	134
<b>Fig. 4.29</b>	Phantom 1 (3D) <b>(a)</b> Slice 3 <b>(b)</b> Slice 6 <b>(c)</b> Slice 9	135
<b>Fig. 4.30</b>	Reconstructed activity using FBP for different z-slices	136
<b>Fig. 4.31</b>	Reconstructed activity using 3D (stacked) MLEM for different z-slices	137
<b>Fig. 4.32</b>	Reconstructed activity using fully 3D MLEM for different z-slices	137
<b>Fig. 4.33</b>	Reconstructed activity 3D view <b>(a)</b> FBP <b>(b)</b> 3D (stacked) MLEM <b>(c)</b> Fully 3D MLEM	138
<b>Fig. 4.34</b>	FBP reconstructed images showing the effect of collimator blurring for collimation ratio of <b>(a)</b> 1 <b>(b)</b> 2.5 <b>(c)</b> 5 <b>(d)</b> 7.5 <b>(e)</b> 10	141

(f) 15 (g) 20

<b>Fig. 4.35</b>	FBP reconstructed images showing the effect of collimator blurring for collimation ratio of (a) 1 (b) 2.5 (c) 5 (d) 7.5 (e) 10 (f) 15 (g) 20	142
------------------	--	-----

---

## CHAPTER 5

---

<b>Fig. 5.1</b>	Experimental set-up for 3D imaging	145
<b>Fig. 5.2</b>	Hollow SS rods (a) Photograph (b) Cross-section (schematic)	146
<b>Fig. 5.3</b>	Solid perspex discs with indexed holes (a) Photograph (b) Cross-section (schematic)	146
<b>Fig. 5.4</b>	Aluminum drum	147
<b>Fig. 5.5</b>	SS waste barrel	147
<b>Fig. 5.6</b>	Decay scheme of $^{137}\text{Cs}$	148
<b>Fig. 5.7</b>	Energy resolution of NaI(Tl)	149
<b>Fig. 5.8</b>	Intrinsic photopeak efficiency of 1" X 1" LaBr <sub>3</sub> (Ce) as a function of energy	150
<b>Fig. 5.9</b>	Energy resolution of LaBr <sub>3</sub> (Ce) as a function of energy	150
<b>Fig. 5.10</b>	(a) Intrinsic photopeak efficiency of HPGe as a function of energy (b) Energy resolution of HPGe as a function of energy	151
<b>Fig. 5.11</b>	Gamma spectrum recorded with NaI(Tl), LaBr <sub>3</sub> (Ce) and HPGe detectors	151
<b>Fig. 5.12</b>	Collimator with tungsten septa (a) Schematic (b) Photograph	152
<b>Fig. 5.13</b>	Collimator (10 mm X 10mm)	152
<b>Fig. 5.14</b>	Intrinsic photopeak efficiency of three NaI(Tl) detectors used in experiments	154
<b>Fig. 5.15</b>	Intrinsic photopeak efficiency of three LaBr <sub>3</sub> (Ce) detectors used in experiments	155
<b>Fig. 5.16</b>	(a) Sinogram (b) FBP reconstruction	157
<b>Fig. 5.17</b>	Reconstructed image using (a) ART (b) SART (c) MLEM (d) OSEM	157
<b>Fig. 5.18</b>	(a) Sinogram (b) FBP reconstruction	159

<b>Fig. 5.19</b>	Reconstructed image using (a) ART (b) SART (c) MLEM (d) OSEM	160
<b>Fig. 5.20</b>	TCT data for three different slices (top to bottom) at different energies (from left to right) – 244 keV, 344 keV, 444 keV, 778 keV and 867 keV; Colour bar is shown on the right (in unit of $\text{cm}^{-1}$ )	164
<b>Fig. 5.21</b>	Plot of linear attenuation coefficient as a function of energy for (a) Top row (b) Middle row (c) Bottom row of TCT data in fig. 5.19	164
<b>Fig. 5.22</b>	Sinogram of SPECT data for (a) Slice 4 (b) Slice 13 (c) Slice 18	165
<b>Fig. 5.23</b>	Analytical reconstructed slice images showing $^{137}\text{Cs}$ activity in a drum. The images show XY Slices at different Z-positions starting from bottom to top (ordered row-wise left to right)	166
<b>Fig. 5.24</b>	(a) Reconstructed 3D volume showing $^{137}\text{Cs}$ activity in the drum (b) 3D volume interpolated on a finer grid. Note that the drum outline is shown for illustration	167
<b>Fig. 5.25</b>	Intensity profile along x-axis, y-axis and z-axis respectively for Source A (a-c), Source B (d-f) and Source C (g-i)	168
<b>Fig. 5.26</b>	2D MLEM reconstructed slice images showing $^{137}\text{Cs}$ activity in a drum. The images show XY Slices at different Z-positions starting from bottom to top (ordered row-wise left to right)	169
<b>Fig. 5.27</b>	Fully 3D MLEM reconstructed slice images showing $^{137}\text{Cs}$ activity. The images show XY slices at different Z-positions starting from bottom to top (ordered row-wise left to right)	170
<b>Fig. 5.28</b>	Reconstructed activity for Al drum sample (a) FBP (b) 2D (Stacked) MLEM (c) Fully 3D MLEM	171
<b>Fig. 5.29</b>	TCT data for three different slices (top to bottom) at different energies (from left to right) – 121 keV, 244 keV, 344 keV, 444 keV, 778 keV	173
<b>Fig. 5.30</b>	Analytical reconstructed slice images showing $^{137}\text{Cs}$ activity. The images show XY Slices at different Z-positions starting from bottom to top (ordered row-wise left to right)	174
<b>Fig. 5.31</b>	3D view of $^{137}\text{Cs}$ activity	175

<b>Fig. 5.32</b>	2D MLEM reconstructed slice images showing $^{137}\text{Cs}$ activity. The images show XY Slices at different Z-positions starting from bottom to top (ordered row-wise left to right)	176
<b>Fig. 5.33</b>	Fully 3D MLEM reconstructed slice images showing $^{137}\text{Cs}$ activity. The images show XY Slices at different Z-positions starting from bottom to top (ordered row-wise left to right)	177
<b>Fig. 5.34</b>	Reconstructed activity for SS drum sample (a) FBP (b) 2D (Stacked) MLEM (c) Fully 3D	178
<b>Fig. 5.35</b>	(a) Reconstructed attenuation map (b) & (c) Analytical and 2D MLEM reconstructed of $^{137}\text{Cs}$ activity respectively	180
<b>Fig. 5.36</b>	Reconstructed (Analytical) slice images showing $^{137}\text{Cs}$ activity. The images show XY Slices at different Z-positions starting from bottom to top (ordered row-wise left to right)	181
<b>Fig. 5.37</b>	Reconstructed (2D MLEM) slice images showing $^{137}\text{Cs}$ activity. The images show XY Slices at different Z-positions starting from bottom to top (ordered row-wise left to right)	182
<b>Fig. 5.38</b>	$^{137}\text{Cs}$ activity for Slice 18, Slice 19 and Slice 20 (left to right) using analytical (a - c) and MLEM (d - f) reconstruction	184
<b>Fig. 5.39</b>	Effect of collimation ratio on analytically reconstructed image for different collimation ratio (a) 5 (b) 10 (c) 15 (d) 20	185
<b>Fig. 5.40</b>	Plot of normalized intensity as a function of pixel number for different collimation ratio (a) 5 (b) 10 (c) 15 (d) 20	186
<b>Fig. 5.41</b>	Variation of FWHM for spatial profile of intensity as function of collimation ratio	186
<b>Fig. 5.42</b>	Gamma spectrum recorded by $\text{LaBr}_3(\text{Ce})$ detector (a) $^{152}\text{Eu}$ (for Active CT) (b) 93% $^{239}\text{Pu}$ (for Passive CT). The major $^{152}\text{Eu}$ and $^{239}\text{Pu}$ peaks have been labeled	191
<b>Fig. 5.43</b>	(a) Reconstructed 3D attenuation map (b) Reconstructed Active CT slice images at different elevations	192
<b>Fig. 5.44</b>	Reconstructed 3D volume showing activity distribution of $^{239}\text{Pu}$ . The drum outline is shown for illustration	193
<b>Fig. 5.45</b>	Fully 3D MLEM reconstructed Passive CT slice images at different elevations	194

<b>Fig. 5.46</b>	Gamma spectrum of Plutonium (without Cd filter)	196
<b>Fig. 5.47</b>	Gamma spectrum of Plutonium (with Cd filter)	197
<b>Fig. 5.48</b>	Gamma spectrum of plutonium (239 - 93 %) in the energy range less than 160 keV	198
<b>Fig. 5.49</b>	Gamma spectrum of plutonium (239 - 93 %) in the energy range 160 – 320 keV	199
<b>Fig. 5.50</b>	Gamma spectrum of plutonium (239 - 93 %) in the energy range 320 – 460 keV	200
<b>Fig. 5.51</b>	Gamma spectrum of plutonium (239 - 93 %) in the energy range 460 – 800 keV	201
<b>Fig. 5.52</b>	3D view (a) Attenuation map (b) <sup>239</sup> Pu activity distribution	202
<b>Fig. 5.53</b>	3D (perspective) view with superimposed active and passive data set	203

# LIST OF TABLES

Table No.	Table Caption	Page No.
<b>CHAPTER 1</b>		
<b>Table 1.1</b>	Comparison between the characteristics of LaBr <sub>3</sub> (Ce) and NaI(Tl) scintillators of comparative size	24
<b>CHAPTER 3</b>		
<b>Table 3.1</b>	Activity table for drum D-2 ( <b>Note:</b> Central plane is the z = 0 plane)	81
<b>CHAPTER 4</b>		
<b>Table 4.1</b>	Activity table for Phantom D-1 ( <b>Note:</b> Central plane is the z = 0 plane)	112
<b>Table 4.2</b>	Activity table for Phantom D-2 ( <b>Note:</b> Central plane is the z = 0 plane)	112
<b>Table 4.3</b>	Details of PHWR fuel bundle	114
<b>Table 4.4</b>	Image assessment parameters for different reconstructed images	138
<b>CHAPTER 5</b>		
<b>Table 5.1</b>	Details of passive <sup>137</sup> Cs used	148
<b>Table 5.2</b>	Comparison of reconstructed and true source activity and spatial location	158
<b>Table 5.3</b>	Comparison of reconstructed and true source activity and spatial location	161
<b>Table 5.4</b>	Comparison of reconstructed and true source activity	172
<b>Table 5.5</b>	Comparison of reconstructed and true source activity and location	179
<b>Table 5.6</b>	Comparison of reconstructed and true source activity	183
<b>Table 5.7</b>	Main gamma rays in plutonium spectrum	190
<b>Table 5.8</b>	Reconstructed <sup>239</sup> Pu mass	195
<b>Table 5.9</b>	Reconstructed <sup>239</sup> Pu mass	203

# Introduction

Single Photon Emission Computed Tomography (SPECT) is an imaging technique to localize and quantify radionuclide activity inside an object. It uses the photons which are emitted from the radionuclide to produce an image which corresponds to the spatial distribution of the radionuclide. SPECT has been widely used for medical imaging where it is recognized as one of the best diagnostic techniques for functional imaging of organs. This technique also has great potential to be used in the nuclear industry for characterization of nuclear waste for disposal decisions, non-destructive burnup determination of fuel pins or fuel assemblies, verification of spent fuel integrity, etc. In general, it can be used for any application where position sensitive imaging of radionuclide in a matrix is required.

Characterization of nuclear waste drums, for example, is required for disposition decisions, safe transportation, permanent storage as well as nuclear material accounting, especially  $^{239}\text{Pu}$ . Manual inspection of opened drums for an assay is a risky (exposure to radiation), time-consuming, and expensive proposition because of huge cost involved for checking each opened drum and the safety precautions involved in handling active waste. Traditionally, the drums are inspected by conventional transmission radiography or tomography <sup>[1-3]</sup>. However, these techniques do not yield information about the radioisotopes inside the drum, but just on the material density. Gamma spectroscopy or segmented gamma scanning techniques <sup>[4, 5]</sup> can be used for gross activity measurement.

However, to improve accuracy and provide information about the spatial distribution of the radioisotopes, SPECT imaging is best suited.

For waste drum application, Lawrence Livermore National Laboratory had used HPGe detectors for scanning high level waste drums [2, 6-7]. However, over a period of time, the regulatory requirements have become more stringent and they now mandate characterization of not only high level waste but also a variety of nuclear wastes from low level waste drums to waste packets in small sizes. HPGe detector, besides being costly, is also bulky and need special cooling arrangements. Also for multi-detector applications which can be used for fast scanning of drums for a fast qualitative examination of thousands of such radioactive waste drums, the option of using multiple HPGe becomes very costly. Due to this, for several applications there is a need for alternate compact systems which are less cumbersome and at the same time can give reasonable SPECT images. Hence, there is a need to explore SPECT with newer detectors, which are compact and have medium energy resolution, such as LaBr<sub>3</sub>(Ce), faster reconstruction algorithms and advanced computational techniques. This thesis addresses these issues and explores the use of LaBr<sub>3</sub>(Ce) detector for SPECT imaging, which to our knowledge has not been reported earlier in published literature, though as a detector LaBr<sub>3</sub>(Ce) has been used for other spectroscopic applications. The use of LaBr<sub>3</sub>(Ce) for <sup>239</sup>Pu imaging is one of the distinguishing features of the work reported in this thesis.

Inspite of the potential applications, SPECT has found very limited use in the nuclear industry. One of the main reasons is that medical and industrial SPECT imaging is quite different in implementation. In medical SPECT, the attenuation of gamma rays

inside the organs and that in the surrounding tissues is of the same order. Also, the attenuation of the body tissues is practically known beforehand. This makes it easier and faster to reconstruct the source distribution. However, in the industrial case, most of the factors affecting attenuation are unknown and it can vary over a wide range. Also, the range of gamma energies used in both the applications is quite different. In medical SPECT, mostly  $^{99m}\text{Tc}$ ,  $^{67}\text{Ga}$  or  $^{123}\text{I}$  are used which have emission energy of less than 140 keV [8]. For nuclear SPECT, the gamma energy covers almost the whole range from 400 keV – 1500 keV depending on the different isotopes under study (eg.  $^{239}\text{Pu}$ ,  $^{137}\text{Cs}$ ,  $^{60}\text{Co}$ ,  $^{154}\text{Eu}$ , etc.). Again, the emitted gamma spectrum is complex and with multiple peaks, often closely spaced. This puts a restriction on the use of detectors with low energy resolution, such as NaI(Tl), which are commonly employed in gamma camera (or Anger camera) [9-11]. Additionally, high or medium-high energy resolution area detectors are also not available. As such, a number of individual detectors are used and the object is scanned. This increases the overall scanning time of the object, thus reducing the throughput.

Also, most of the available literature deals with different aspects of clinical SPECT imaging and very less information are available for nuclear applications. Hence, there is a need to develop reconstruction methods which are specifically suited for nuclear applications.

The goal of the present thesis is to focus on developing both analytical and iterative reconstruction methods for SPECT imaging, such as fully 3D reconstruction and fan beam reconstruction. This thesis aims to develop emission tomography as a gamma imaging technique for nuclear application such as waste assay. In particular, extensive

study of imaging of  $^{239}\text{Pu}$  using  $\text{LaBr}_3(\text{Ce})$  and its comparison with HPGe forms the highlight of this thesis. This work includes various steps starting from phantom generation to test algorithms, using new reconstruction techniques, setting up of experiments to verify them, conducting experiments with  $^{137}\text{Cs}$  and finally imaging of  $^{239}\text{Pu}$ .

This chapter is organized as follows. Section 1.1 explores the history of SPECT imaging. Section 1.2 reflects light upon the basics of imaging with radiation sources in general, and transmission tomography and emission tomography, in particular. Sections 1.3 to 1.6 describe different modalities of emission tomography, planar image formation and attenuation compensation. Section 1.7 discusses the development of different algorithms in SPECT. Section 1.8 describes interaction of gamma rays in matter and their detection using inorganic scintillators and semiconductor detectors. Section 1.9 briefly discusses the factors that degrade or affect SPECT images. Section 1.10 discusses the different nuclear applications of SPECT imaging currently being explored. The chapter concludes with a discussion of the aims and scope of the thesis.

## **1.1 Brief history of SPECT Imaging**

Although X-rays and gamma rays were discovered by 1900, the problem of generating images from measurements of the radiation around the body of a patient was considered much later. The introduction of the scintillation camera by Anger and Rosenthal in 1959 [12, 13] and its ultimate evolution into the imaging system of choice for routine nuclear medicine imaging applications resulted in a great deal of effort being expended toward the extension of the scintillation camera as a tomographic imaging device. Tomography

was first carried out in 1964 by David Kuhl, a nuclear medicine specialist in Philadelphia, and Roy Edwards by an analogue technique. In the early 1960s, Kuhl and Edwards established fundamentals for SPECT using multi-detector scanning systems to acquire cross-sectional images of radionuclide distributions <sup>[14-16]</sup>. They were the first investigators to describe true transaxial approach for emission tomography. During the period of 1963 through 1976, Kuhl and his colleagues developed a series of transaxial tomographs <sup>[17-20]</sup>. Kuhl's Mark II device consisted of two scintillation detectors and used a translate-rotate motion of the detectors. Kuhl's final tomograph was the Mark IV <sup>[20]</sup>. Each detector array had a linear array of eight discrete scintillation detectors. Kuhl even investigated the use of transmission computed tomography (CT) in 1966 <sup>[21]</sup>. John Mallard and his team in Aberdeen built the first digital CT for radio-isotope distributions from 1967 to 1969. It was known as the Aberdeen Section Scanner. This was some five years before the technique was applied to X-rays by Hounsfield, which revolutionized X-ray diagnosis, and for which he received the Nobel Prize together with Cormack in 1979. Also, during this period, Patten, Brill and their colleagues developed a novel scanner. In the 1970s, Muehllehner <sup>[22]</sup> Keyes and colleagues <sup>[23]</sup> and Jaszczak and colleagues <sup>[24]</sup> adapted the technology to a rotating scintillation camera. The result of these efforts along with the integration of computer systems was the development of the modern day SPECT system as a scintillation camera/computer system with one, two, or three heads and tomographic imaging capability. The scintillation camera collects tomographic data by rotating around the region of interest and acquiring multiple planar projection images during its rotation. It is imperative that the region of interest is included in every

projection image. If this is not the case, the resulting truncation of the images will produce artifacts in the final reconstructed images.

The camera may move in a continuous motion during acquisition but typically remains stationary during the acquisition of each projection image before advancing to the next position in a “step and shoot” mode of operation. A complete 360° rotation of a scintillation camera with a rectangular field of view will completely sample a cylindrical region of interest. Originally, camera systems were only capable of circular orbits; however, modern day systems have elliptical orbit capability. This is accomplished by equipping the collimators with sensors that detect the presence of the patient and maintain the camera head(s) in close proximity to the patient as the orbit is completed. Since the spatial resolution of collimators used with the scintillation camera degrades with distance from the collimator face, the optimum resolution is obtained in each projection image when the camera is as close to the patient as possible.

The first commercial applications of SPECT imaging were similar to the Mark IV but utilized 32 photon detectors<sup>[20]</sup>. Even though this camera had more detectors, images were frequently distorted and not very useful in assisting clinicians in diagnosing a patient's medical problem. Subsequently, SPECT imaging technology was slow to gain universal acceptance within the medical community. It was not until advancements in nuclear imaging technology in the 1980's and 1990's that SPECT began to show promise as a diagnostic tool in the clinical environment.

Today, SPECT imaging is recognized as one of the best imaging modalities to evaluate brain function and is frequently used in the diagnosis of Traumatic Brain Injury, Alzheimer's Disease and other Dementias, Stroke, Toxic Encephalopathy and is being

increasingly used as a diagnostic tool for Bipolar Disorder, Depression, Anxiety Disorders, Obsessive Compulsive Disorder and other psychiatric conditions [25].

During its formative years, SPECT was predominantly used as a medical imaging technique. However, in the last decade or so, SPECT imaging has been extended to nuclear applications such as in waste assay, burnup distribution in fuel assemblies, verification of integrity of spent fuel assemblies, etc.

## **1.2 Imaging with Radiation**

When radiation passes through an object, it interacts with matter and suffers loss in intensity. The beam is said to undergo attenuation in the medium. The loss in intensity is given by the well-known Lambert-Beer's law:

$$I = I_0 e^{-\mu x} \quad (1.1)$$

where  $I_0$  is the incident intensity,  $I$  is the transmitted intensity,  $\mu$  is the linear attenuation coefficient of the medium and  $x$  is the thickness of the medium. Here it is implicitly assumed that  $\mu$  is constant. For non-uniform  $\mu$ , Eq. 1.1 may be expressed as

$$I = I_0 e^{-\int \mu dx} \quad (1.2)$$

where the integral is over the path traversed by the radiation.

The Lambert-Beer's law forms the basis of imaging with radiation from an external source. When the incident radiation after transmission through an object is captured on a detector/screen, it forms a two-dimensional image of the three-dimensional object. This is known as the *projection* of the object, or in more general term, a *radiograph*.

### 1.3 Transmission Tomography

Tomography is derived from the Greek word ‘*tomos*’ (which means slice or section) and ‘*graphia*’ (which means draw). The word tomography means ‘reconstruction from slices’. It is applied in Computed Tomography (CT) [26, 27] to obtain cross-sectional images of objects. Fundamentally, tomographic imaging deals with reconstructing an image from its projections. The relationship between the unknown distribution (or object) and the physical quantity which can be measured (the projections) is referred to as the forward problem. The mathematical basis for tomographic imaging was laid down by Johann Radon already in 1917 [28]. This reconstruction problem belongs to the class of inverse problem, which are characterized by the fact that the information of interest is not directly available for measurements. The imaging device (the camera) provides measurements of a transformation of this information (Fig.1.1). In practice, these measurements are both imperfect (sampling) and inexact (noise).

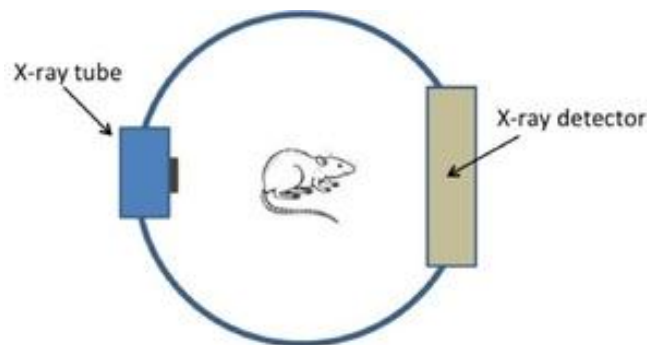


*Fig. 1.1 Schematic configuration for transmission tomography*

The projections are reconstructed on a three-dimensional grid which is discretized into unit cells known as ‘*voxels*’ (short for volume cells). The reconstructed volume represents the attenuation map of the object

## **1.4 Emission Tomography**

Emission Computed Tomography (ECT) <sup>[29]</sup> is a non-destructive technique for imaging of radionuclide distribution inside an object. It uses the decay of radioactive isotopes to image the spatial distribution of the isotope as well as to determine their source strength or activity. In medical imaging, radiotracers are administered to the patient in the form of radiopharmaceuticals either by injection or by inhalation.

A fundamental difference between transmission tomography and emission tomography is the absence of external radiation source in the case of emission tomography. In fact, the source of radiation is located inside the object itself and the aim of ECT is to find their distribution using the radiation emitted by them.

ECT can be divided into two types: Single Photon Emission Computed Tomography (SPECT) and Positron Emission Tomography (PET). The word *single* in SPECT refers to the analyzed product of the radioactive decay, a single photon, while in PET the decay produces a single positron, which is analyzed through its further interaction. After traveling a short distance the positron comes to rest and combines with an electron. The annihilation of the emitted positron results in two oppositely traveling gamma-ray photons. An ‘event’ in SPECT corresponds to the detection of a single photon whereas in PET an ‘event’ corresponds to the detection of two photons (coincidence detection).

### **1.4.1 Positron Emission Tomography (PET)**

Positron Emission Tomography <sup>[30, 31]</sup> is used for determining the concentration and location of a positron emitting compound in a desired cross-section. When an emitted

positron is brought to rest, it interacts with an electron and, as a result, their masses are annihilated, creating two photons of 511 keV each. These two photons are called annihilation gamma-ray photons and are emitted at very nearly 180° from one another (Fig. 1.2).

The fact that the annihilation of a positron leads to two gamma-ray photons traveling in opposite directions forms the basis of a unique way of detecting positrons.

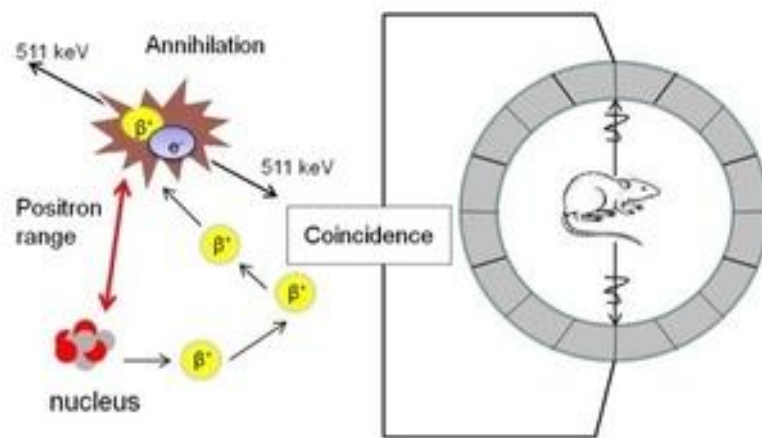


*Fig. 1.2 Schematic configuration for positron emission tomography*

Coincident detection by two physically separated detectors of two gamma-ray photons locates a positron emitting nucleus on a line joining the two detectors. The phrase “coincident detection” in the present context refers to the “coincidence resolving time” of circuits that check for whether the two photons have arrived simultaneously and is usually on the order of 10 to 25 ns - a sufficiently long interval of time to make path difference considerations unimportant. This means that if the two annihilation photons arrive at the two detectors within this time interval, they are considered to be in coincidence.

### 1.4.2 Attenuation Compensation in PET

Two major advantages of positron tomography over single photon emission tomography are: 1) inherent electronic collimation 2) easier attenuation compensation. Let us say that the detectors D1 and D2 in Fig. 1.3 are being used to measure one ray in a projection and let us also assume that there is a source of positron emitters located at the point S. Suppose for a particular positron annihilation, the two annihilation gamma-ray photons labeled  $\gamma_1$  and  $\gamma_2$  (Fig.1.3) are released toward D<sub>1</sub> and D<sub>2</sub>, respectively. The probability of  $\gamma_1$  reaching detector D<sub>2</sub>, is given by

$$\exp\left[-\int_L^{L_1} (\mu(x)dx)\right] \quad (1.3)$$

where  $\mu(x)$  is the attenuation coefficient of the object at 511 keV.

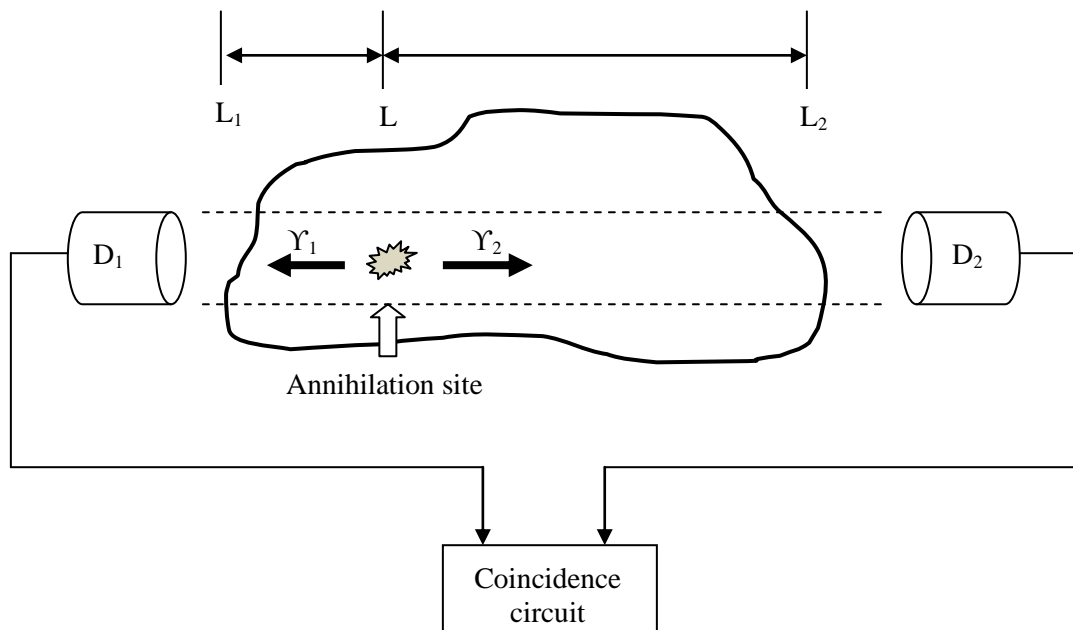


*Fig. 1.3 Schematic arrangement for co-incidence detection in PET*

Similarly, the probability of  $\gamma_1$  reaching detector  $D_2$ , is given by

$$\exp\left[-\int_L^{L_2} (\mu(x)dx)\right] \quad (1.4)$$

The probability of annihilation event as recorded by the detectors is given by the product of the two probabilities:

$$\begin{aligned} & \exp\left[-\int_L^{L_1} (\mu(x)dx)\right] \cdot \exp\left[-\int_L^{L_2} (\mu(x)dx)\right] \\ &= \exp\left[-\int_{L_1}^{L_2} (\mu(x)dx)\right] \end{aligned} \quad (1.5)$$

This is a significant advantage of PET because the attenuation factor does not depend on the position of the positron annihilation and is the same on the line joining the two detectors. Secondly, the attenuation factor is exactly the attenuation that a beam of monoenergetic photons at 511 keV would undergo in propagating from through the object over the length  $L_1L_2$ . Therefore, one can readily compensate for attenuation by first doing a transmission study (projection data can be directly used without doing reconstruction) to record total transmission loss for each ray in each projection. Then, in the positron emission study, the data for each ray can simply be attenuation compensated when corrected (by division) by this transmission loss factor. This method of attenuation compensation has been used in <sup>[32]</sup> positron emission scanners. There are other approaches to attenuation compensation in PET <sup>[33]</sup>.

Electronic collimation is inherent in PET. Consider that the annihilation event in Fig.1.3 occurs at any position other than the line joining  $D_1$  and  $D_2$ . Suppose that detector  $D_1$  detects one of the  $\gamma$  rays emitted in this event. Since the two  $\gamma$  rays are emitted at  $180^\circ$  to each other, it is evident that the other  $\gamma$  ray will not be detected by  $D_2$  and hence this event will not be registered as a coincidence event for the detector pair  $D_1$ - $D_2$ .

### 1.4.3 Single Photon Emission Computed Tomography (SPECT)

Single Photon Emission Computed Tomography (SPECT) <sup>[34]</sup> is a nuclear imaging technique for the characterization of the activity level and distribution of gamma emitting radioisotopes inside an object. SPECT involves the position-sensitive measurement of gamma rays emitted by a radionuclide (Fig.1.4). The intensities of the radiation measured are directly related to the radionuclide distribution inside the object. The data are collected with a collimated detector to segment the acquisition horizontally, vertically and angularly by translating, elevating and rotating the object over 360 degrees (Fig.1.5). The data is then reconstructed using analytical or iterative techniques to obtain information about each voxel of the inspected volume.

. In the case of tomographic imaging, the planar images are acquired at several angles to determine the three dimensional activity distributions. However, traditionally SPECT is not considered as a fully 3D imaging problem. Instead, two dimensional slices of activity distribution are reconstructed.

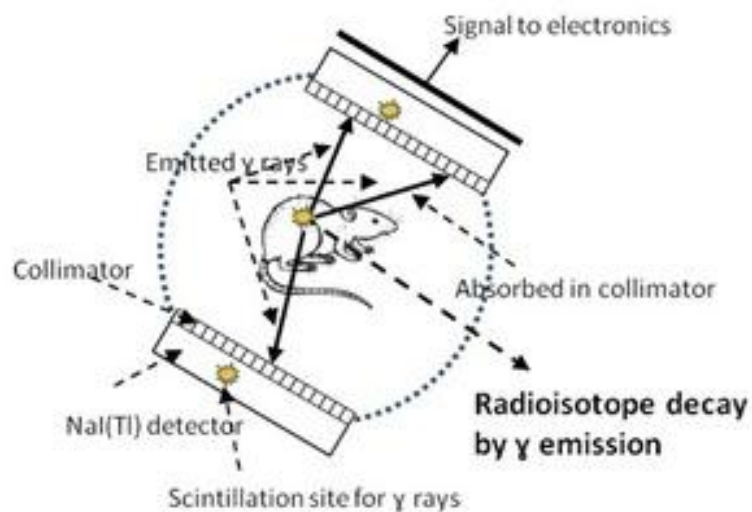


*Fig. 1.4 Schematic configuration for SPECT*

In the field of medical imaging, SPECT is considered to be one of the leading molecular imaging technologies that allow visualizing 3-dimensional (3D) functional information rather than anatomical information in the body. With a small amount of radiopharmaceuticals, SPECT can produce high contrast images of small organs/tissues/molecules and quantify the kinetic processes when these drugs interact with molecules in the body.

#### 1.4.4 Attenuation Compensation in SPECT

One of the major difficulties with tomographic imaging of a gamma-ray emitting source is caused by the attenuation that photons suffer during their travel from the emitting nuclei to the detector. The extent of this attenuation depends upon both the photon energy and the nature of the absorber. Consider two gamma sources of equal strength at points A and B in Fig. 1.5. Because of attenuation the detector will find the source at A stronger than the one at B.

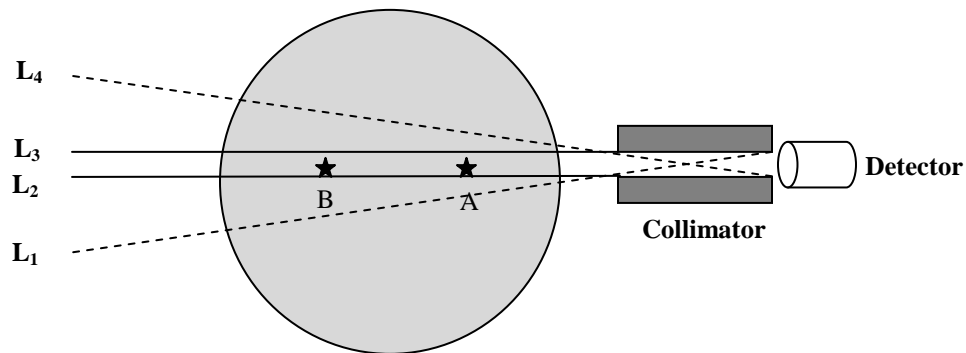


*Fig. 1.5 Formation of image in SPECT using collimated detector*

Let us consider the simplest case of uniform attenuation  $\mu$  inside the object. In this case, the attenuation suffered by photons emitted from a source, say A, will be the negative exponential of  $\mu$  times the path length from A to the edge of the object (along a

line in the direction of the detector), assuming no losses in air. However, our task is not that simple. In practice, the location of source A is unknown. Also, the attenuation coefficient would generally be non-uniform. One of the solutions to the problem is to approximate an image to be reconstructed by a grid and an assumption is made that the concentration of the nuclide and the attenuation is constant within each grid block. For a particular ray, the total attenuation length is obtained by calculating the length of the ray in a particular grid block and multiplying with the attenuation coefficient in that grid block and further summing over all the grid blocks on the ray path. The corresponding projection data can then be expressed as a set of simultaneous equations which can be solved to find the unknowns (source activity in each grid block). However, the efficiency of the reconstruction depends on the accuracy of the assumed values of the attenuation coefficients for all grid blocks.

### **1.5 Active and Passive Computed Tomography (A&PCT)**

Since the attenuation compensation is an integral part of SPECT reconstruction, the attenuation map should preferably be accurately known beforehand. For this reason, SPECT is often combined with transmission CT. This is known as Active and Passive CT.

The A&PCT method consists of two steps to perform an assay: active CT and passive CT. In active CT, attenuation map of the object is obtained. This is similar to conventional X-ray CT but it uses an external gamma source (instead of X-ray) and the spectrum is recorded using a single channel analyzer (SCA) / multi channel analyzer (MCA). It should be noted that an SCA records the number of events within a selected energy window while an MCA can record a complete energy spectrum. It differs from

conventional CT scanners in that it discriminates between photons of different energies. The gamma source used for active CT has, generally, multiple emission energies. The reconstruction results are a discrete quantitative measurement of the linear attenuation coefficient at each energy measured, i.e., there has been no integration over the energy spectrum. Thus active CT images have pixels that represent the absolute measurement of attenuation at specific energies. For a waste drum, the attenuation due to its contents is accurately measured in three dimensions and displayed as a sequence of two dimensional images at different z-planes (or elevations) of the drum. Note that active CT does not identify any isotope or measure the source strength or activity within a waste drum. Energy specific attenuation maps are then used to determine the attenuation map of the object corresponding to the emission energy of the radioisotope (inside the object) to be imaged by interpolating the above data.

Passive CT is used to measure and determine the location, identity, and strength of radioisotope sources within an object. The ray sum for passive CT (or SPECT) is the counts measured in disintegrations per unit volume per unit time of the passive source within the object. Therefore, a single-photon-emitted ray sum is the integrated radioisotope activity, modified by one or multiple of exponential attenuations, along the path from a source position within the object to the detector. The function that is imaged for passive CT is the measured gamma-ray activity at one or more energies of all detectable radioisotopes within the object. The spectrometry detection equipment collects the entire energy spectrum for each integration point and the radioisotopes are identified by their characteristic peaks within the energy spectrum.

## 1.6 Formation of planar image in SPECT

As discussed in Section 1.3, a planar image is formed by recording the transmitted intensity on a detector. The simplest model of imaging could be conceived by tracing (linear) ray path from the source to the detector and estimating the attenuation suffered over the path length (neglecting scattering). This scheme is quite straightforward in the case of transmission tomography where the source position is known. However, in the case of SPECT, the source locations are unknown and it is not possible to trace ray paths.

To solve this problem, a collimator is used which is an integral part of any SPECT imaging device. The collimator helps define the path of rays accepted by the detector. Photons that pass through the collimator are detected by the detector (Fig.1.6). Therefore collimator is a kind of lens for the detector. Depending upon their application and size of object to be imaged, various types of collimators are used – parallel, pin-hole, converging, diverging, etc. However, the parallel hole collimator still remains the simplest and most widely used.

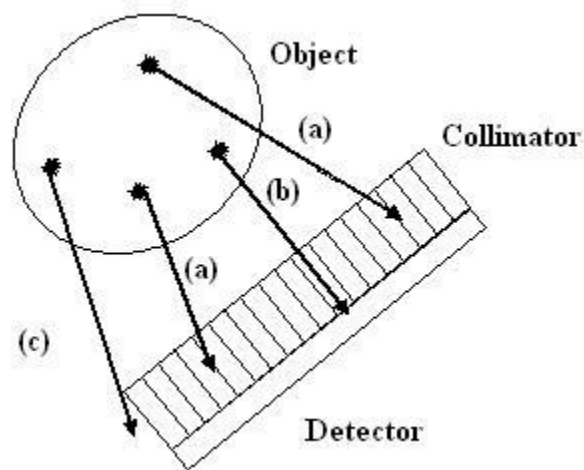


**Fig. 1.6** A typical SPECT set-up. The gamma photon emitted (a) is absorbed by the collimator (b) reaches the detector (c) misses the detector completely.

The planar image formed is a discrete map of 'pixels' (short for picture cells) each pixel having a value that is equal to the number of the photon interactions in the crystal in location of pixel. For ideal collimation, one row of pixels in planar image is contributed only by the activity in one object slice at height of the row of pixels. Thus, approximately, one row of the planar image is a projection of activity in a slice at same height, and the whole planar image is a projection of the three dimensional activity distribution.

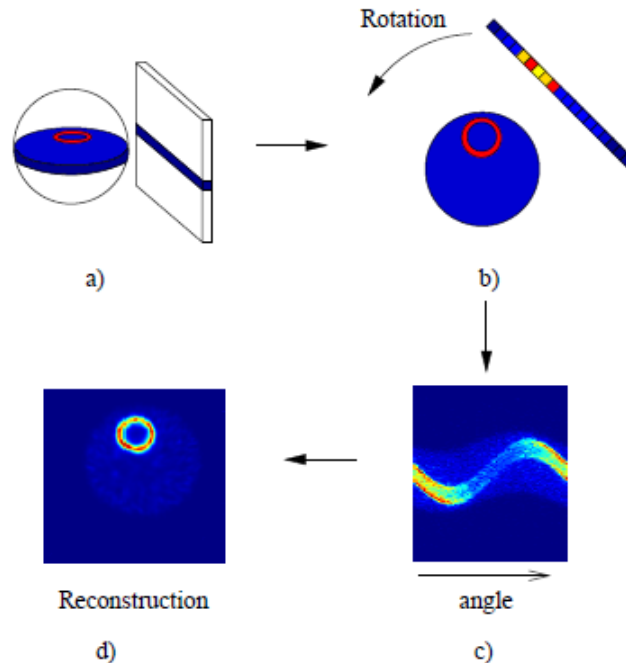


**Fig. 1.7** Steps in SPECT image formation (a) Projection of a 2D object (b) Collection of projections for different rotations (c) Sinogram (d) Reconstructed object <sup>[35]</sup>

Fig.1.7 shows the basic steps involved in the formation of a planar image in SPECT. Consider a slice of an object to be imaged. This 2D slice forms an image (projection) on the detector which corresponds to one row in the planar image. The object is then rotated at different steps over 360° and corresponding projection data are

---

recorded. When the projections for all the angles are stacked together, it forms a complete data set required for reconstruction and is known as the ‘*sinogram*’. The sinogram is then used to obtain the final reconstructed image.

## 1.7 Development of Reconstruction Algorithms in SPECT

The projection data or sinogram is used to reconstruct the activity function. SPECT reconstruction algorithms can be broadly classified as analytical and iterative. The mathematical formulation of these algorithms will be discussed in Chapter 2. Here, we briefly reflect upon the history of development of the reconstruction algorithms.

### 1.7.1 Analytical Reconstruction

First analytic methods for the attenuation correction in SPECT were proposed by Bellini *et al* <sup>[36]</sup> and Tretiak and Metz <sup>[37]</sup>; both algorithms assumed that the attenuation coefficient was constant inside a patient’s body and that the cross section of the body was convex. Two more analytic methods were introduced almost a decade later by Hawkins *et al* <sup>[38]</sup> and Inouye *et al* <sup>[39]</sup> (an algorithm similar to <sup>[38]</sup> was independently developed by Shneiberg *et al* <sup>[40, 41]</sup>). A scheme generalizing all of the above-mentioned approaches has been proposed by Metz *et al* <sup>[42]</sup>; a general analytic approach leading to a variety of reconstruction formulae was given by Kuchment *et al* <sup>[43]</sup>. Certain extensions to the underlying assumptions of constant attenuation and convex body were treated by Kuchment *et al* <sup>[43, 44]</sup>; in the former work, an inversion formula was derived for the case when attenuation depends on an observation angle (but is constant for a fixed angle). All of these analytic methods, however, are not applicable for the SPECT of regions with strongly non-uniform attenuation. Creation of the analytic SPECT reconstruction

algorithm, operative in the case of arbitrary realistic attenuation coefficient, has become possible only recently, due to the approach developed by Arbutov *et al* <sup>[45]</sup>, and due to the discovery of an explicit inversion formula for the attenuated Radon transform by Novikov <sup>[46]</sup>. A simpler derivation of a similar formula was given later by Natterer <sup>[47]</sup>.

### **1.7.2 Iterative Reconstruction**

Filtered backprojection amplifies statistical noise, which adversely affects image quality. To address this problem, Shepp and Vardi <sup>[48]</sup> introduced an iterative reconstruction technique in 1982 based on the theory of expectation maximization (EM), which has a proven theoretical convergence to an estimate of the actual image distribution that has a maximum likelihood of having projections most similar to the acquired projections. The initial implementation of these algorithms was very time consuming, with several iterations being required to reach a solution, and extensive computer power was required. Since that time, much effort has been expended in improving and testing algorithms based on this concept. Significant improvements in speed and signal-to-noise and reconstruction accuracy have resulted from these efforts. In 1994, Hudson and Larkin <sup>[49]</sup> developed the technique of ordered sets EM (OSEM) for image reconstruction from 2D projection data. This algorithm was based on the concept of dividing the projection data into small subsets and performing the EM algorithm on each subset. The solution of each subset was used as the starting point for the next subset, with subsequent subsets being selected to provide the maximum information (e.g., chose the second subset of data to be orthogonal to the first subset). The advantage of this technique is that, at the end of the first pass, the entire data set has been processed one time, but  $n$  successive approximations to the final solution have been made where  $n$  is the number of subsets.

Thus, OSEM is  $n$  times faster than the original EM algorithm. Typically, only two to three passes through the data set (iterations) are required for the reconstructed image to converge to a final value that is essentially unchanged by further iterations. Correction for scatter and attenuation effects can be performed on the acquired projection data during the reconstruction process. The advantage of this technique is that the star effect inherent in filtered backprojection is virtually eliminated since the acquired data are distributed within the object contour. Because of this result, signal-to-noise is generally improved. Filtering of the data can also be performed to further enhance the reconstructed images.

## **1.8 Detection of Gamma Rays**

The most common method of detection of gamma rays is by the scintillation produced in certain materials. The scintillation process remains one of the oldest techniques for radiation detection. Another class of gamma ray detectors is the solid state detector or semiconductor detector. This section will briefly discuss these two types of gamma detectors with specific emphasis on the detectors used for experiments in the present thesis: sodium iodide, lanthanum bromide and high purity germanium detectors.

### **1.8.1 Scintillation Detector**

The ideal scintillation material should possess the following properties <sup>[50]</sup>:

- It should convert the kinetic energy of charged particles into detectable light with high scintillation efficiency.
- This conversion should be linear-the light yield should be proportional to deposited energy over as wide a range as possible.

- The medium should be transparent to the wavelength of its own emission for good light collection.
- The decay time of the induced luminescence should be short so that fast signal pulses can be generated.
- The material should be of good optical quality and subject to manufacture in sizes large enough to be of interest as a practical detector.
- Its index of refraction should be near that of glass (~1.5) to permit efficient coupling of the scintillation light to a photomultiplier tube or other light sensor.

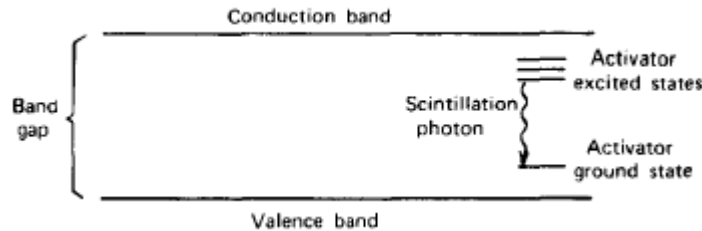


*Fig. 1.8 Energy band diagram for an activated inorganic scintillator* <sup>[50]</sup>

The most widely applied scintillators include the inorganic alkali halide crystals, of which sodium iodide <sup>[51]</sup> is the most popular. The inorganic scintillators tend to have the best light output and linearity, but with several exceptions are relatively slow in their response time. The high Z-value of the constituents and high density of inorganic crystals favor their choice for gamma-ray spectroscopy. The scintillation mechanism in inorganic materials depends on the energy states determined by the crystal lattice of the material as shown in Fig. 1.8.

## **A. Sodium Iodide**

The most notable property of thallium activated sodium iodide (NaI(Tl)) is its excellent light yield and high intrinsic efficiency. It has come to be accepted as the standard

scintillation material for routine gamma-ray spectroscopy and can be machined into a wide assortment of sizes and shapes. However, the crystal is somewhat fragile and can easily be damaged by mechanical or thermal shock.

The dominant decay time of the scintillation pulse is 230 ns. In addition to this prompt yield, phosphorescence with characteristic 0.15 s<sup>[52]</sup> decay time has also been measured which contributes about 9% to the overall light yield. At high counting rates, the phosphorescence will tend to build up due to the multiple overlap from many preceding pulses. This afterglow is often an undesirable characteristic of sodium iodide used in high count rate applications.

NaI(Tl) is hygroscopic and deteriorates due to water absorption if exposed to the atmosphere for any length of time. Crystals must therefore be hermetically sealed for normal use. However, NaI(Tl) is still the mostly used material in SPECT systems due to its high intrinsic efficiency, fast light decay time and relatively low cost.

## **B. Lanthanum Bromide**

The properties that make cerium activated lanthanum bromide (LaBr<sub>3</sub>(Ce)) scintillation detector<sup>[52-56]</sup> attractive for different applications based on gamma-ray spectrometry are:

- good energy resolution
- very fast light output decay, enabling high count rate applications
- high temperature stability
- high gamma detection efficiency
- operation at room temperature
- promising technology for manufacturing crystal at larger sizes

**TABLE 1.1** Comparison between the characteristics of  $\text{LaBr}_3(\text{Ce})$  and  $\text{NaI}(\text{Tl})$  scintillators of comparative size <sup>[53]</sup>

Parameter	$\text{LaBr}_3(\text{Ce})$	$\text{NaI}(\text{Tl})$
Crystal density (g/cc)	5.29	3.67
Thickness for 50% attenuation of 662 keV $\gamma$ (cm)	1.8	2.5
Light yield (photons/MeV)	63000	39000
1/e decay time (ns)	26	250
Energy Resolution (at 662 keV)	3-4%	6-7%

These properties compared to those of the  $\text{NaI}(\text{Tl})$  scintillator detector (see Table 1.1) make it a good choice as a gamma detector for medium energy resolution, high count rate or fast timing applications. Although the energy resolution of  $\text{LaBr}_3(\text{Ce})$  is still poor as compared to a HPGc detector, its relatively lower cost serves as an intermediate choice between  $\text{NaI}(\text{Tl})$  and HPGc, especially when a large number of detectors are to be used with a decent energy resolution. Furthermore, it does not require cooling, like HPGc does.

### 1.8.2 Semiconductor Detector

One of the major limitations of scintillation counters is their relatively poor energy resolution. The energy required to produce one information carrier (a photoelectron) is of the order of 100 eV or more, and the number of carriers created in a typical radiation interaction is usually no more than a few thousand.

The only way to reduce the statistical limit on energy resolution is to increase the number of information carriers per pulse. The use of semiconductor materials as radiation detectors <sup>[57, 58]</sup> can result in a much larger number of carriers for a given incident radiation event than is possible with any other common detector type.

### A. High Purity Germanium

The dominant characteristic of germanium detectors is their excellent energy resolution when applied to gamma-ray spectroscopy. In Fig. 1.9, comparative pulse height spectra are shown for NaI(Tl) scintillator, LaBr<sub>3</sub>(Ce) scintillator and germanium detector for identical incident gamma ray spectra. The great superiority of the germanium system in energy resolution allows the separation of many closely spaced gamma-ray energies, which remain unresolved in the NaI(Tl) spectrum. Consequently, virtually all gamma-ray spectroscopy that involves complex energy spectra is carried out with germanium detectors.

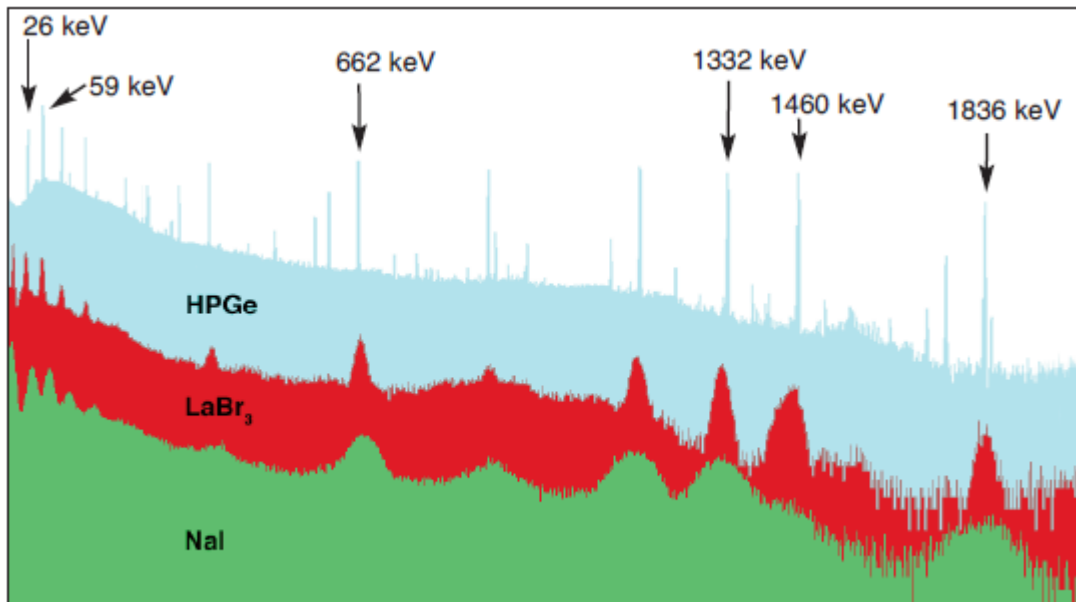


*Fig. 1.9 Comparison of NaI(Tl), LaBr<sub>3</sub>(Ce) and HPGe spectra <sup>[20]</sup>*

## 1.9 Image degradation in SPECT

Three major factors that degrade SPECT images are attenuation, collimator blurring and scatter. Image reconstruction without compensation for these degradations results in reduced contrast and reduced quantitative accuracy. Compensations for these degradations have markedly improved the image quality and quantitative accuracy in SPECT imaging. We will briefly discuss these three factors;

### 1.9.1 Attenuation

One of the primary factors affecting image quality in SPECT is photon attenuation. Photons are attenuated in the object due to photoelectric absorption and Compton scatter. Since the intensity measured by the detector depends upon the total attenuation suffered by the photon inside the object, an accurate estimation of the attenuation coefficient is vital before SPECT reconstruction can be done. In the computation of SPECT the attenuation coefficient is traditionally either assumed to have a constant value<sup>[59]</sup> or the map of coefficients is obtained beforehand using X-ray imaging (CT)<sup>[60-62]</sup>. A new approach to SPECT is to reconstruct both the activity and the attenuation distribution simultaneously from SPECT data alone<sup>[63, 64]</sup>. This leads to a nonlinear inverse problem which is more ill-conditioned than a basic SPECT problem.

### 1.9.2 Collimator blurring

The formation of planar image, as discussed in the previous section, is true for ideal collimation. Referring to Fig.1.5 in Section 1.5.4, if the collimator in front of the detector had infinite collimation, it would accept gamma-ray photons only from the region  $L_2L_3$

which is parallel to the collimator. In practice, however, 'ideal' collimation is never achieved. Each collimator has a finite angle of acceptance. Any photons within this angle of acceptance will reach the detector and register as a signal. For a finite collimation, the detector in Fig.1.5 accepts photons from the region  $L_1L_4$ . Thus, the detector not only accepts photons from object voxels in the line-of-sight but also accepts photons from other voxels in the same plane - resulting in within-slice blurring - and photons from voxels in the planes below and above the reference plane, resulting in inter-slice blurring.

The extent of blurring is decided by the  $L/d$  ratio of the collimator.  $L$  is the length of the collimator and  $d$  is the size of the collimator hole. Greater the  $L/d$ , lesser is the blurring.

### **1.9.3 Scatter**

Compton scattering results in a change in direction with loss of photon energy – the magnitude of loss being determined by the angle of scatter. Thus, Compton scattered photons enter the detector with minimal or no information on their origins due to their change in direction within the object. Pulse height analysis is used to prevent the counting of photons that have scattered through large angles (greater loss of energy) to an extent that depends on the energy range of acceptance of the detection system<sup>[65-67]</sup>.

Traditional filtered back projection techniques for SPECT reconstruction include attenuation compensation but do not model collimator blurring or scatter compensation. For nuclear applications, such as waste assay, mostly iterative reconstruction algorithms are employed as the collimator blurring and other degrading factors can be accurately

modeled and their contributions can be incorporated in the system probability matrix. This will be discussed in detail in Chapter 3.

### 1.9.4 Poisson noise

The decay of radioactive isotopes is a statistical process. If  $\bar{n}$  is the mean number of decays (in given time) of the isotope, the actual number of emissions is a random variable  $x$  with probability  $p(x)$ . The probability function of  $x$  can be approximated by Poisson distribution, that is

$$p(x) = \frac{e^{-\bar{n}} \bar{n}^x}{x!} \quad (1.6)$$

The parameter  $\bar{n}$  is both the mean and the variance of the distribution. The traditional methods for SPECT imply that the activity of emitting isotope is a deterministic variable. Newer iterative methods take into account the statistical nature of radioactive decay<sup>[48-49]</sup>.

There is also some additive noise involved in nuclear imaging. This is due to the background activity. The additive noise can be considered as measurement error of the imaging system.

## 1.10 Applications of SPECT in nuclear technology

Although major application of SPECT still remains in the field of medical imaging, some work has been done to extend this technique to nuclear applications. Some of these applications will be briefly discussed here:

### 1.10.1 Waste assay

SPECT can be used for transuranic waste assay <sup>[68 - 71]</sup> to identify, locate and accurately measure radioisotopic concentration (like <sup>239</sup>Pu) of contents of the waste barrel. This can be used for separation and disposal of wastes with long-lived isotopes.

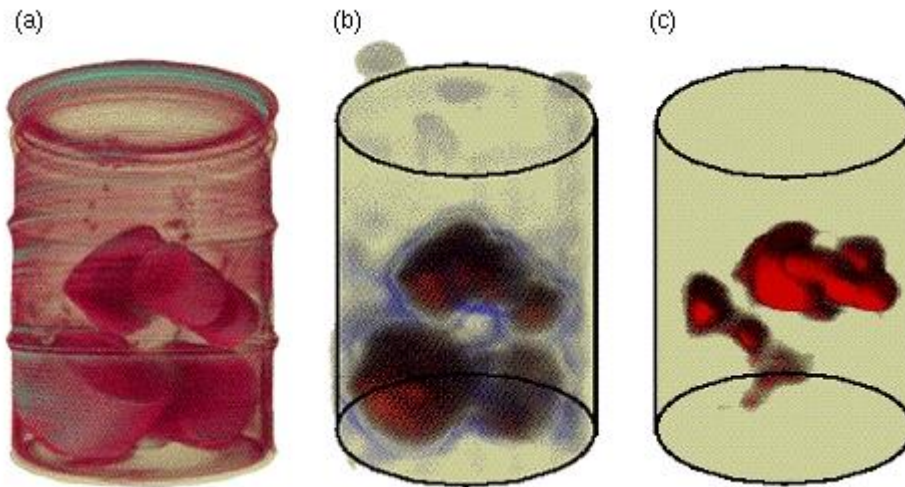


**Fig. 1.10** Waste assay at Lawrence Livermore National Laboratory <sup>[68]</sup> using A&PCT technique (a) high resolution transmission tomograph (b) active data set (c) passive data set

### 1.10.2 Rod-by-rod fuel properties of fuel assemblies

Various fuel properties, such as e.g. the burnup distribution, in fuel assemblies <sup>[72]</sup> can be found out by measuring the distribution of certain fission nuclides produced in the fission chain, such as, <sup>140</sup>Ba, <sup>134</sup>Cs, <sup>137</sup>Cs, <sup>154</sup>Eu, etc. SPECT is used to measure the activity of distribution of the fission products which is then used to calculate the fuel properties. For the case of burnup, Cs-137 is measured, and for the case of power distribution, Ba-140 is measured. There are also other fuel characteristics that may be assessed, such as fission gas release <sup>[73, 74]</sup>. This method is advantageous over the conventional techniques as this

method is non-destructive – the fuel pins need not be cut – and the whole assembly be scanned at the same time instead of examining single pins.



*Fig. 1.11 Ba-140 distribution in BWR fuel assembly <sup>[72]</sup>*

### **1.10.3 Verification of spent fuel integrity**

International safeguards have addressed the need for verifying the integrity of nuclear fuel assemblies. A possible approach for such verification is the use of SPECT to experimentally determine the internal distribution of radioactive nuclides in nuclear fuel assemblies. The utilisation of the SPECT technique for safeguards purposes has been reported by Jacobsson et al <sup>[75-77]</sup>. Removal of individual rods or groups of rods has been investigated, as well as replacement of rods with fresh fuel or fuel-like material. The investigations have indicated that the technique is applicable for partial-defect verification down to the single-rod level in both BWR and PWR fuel.

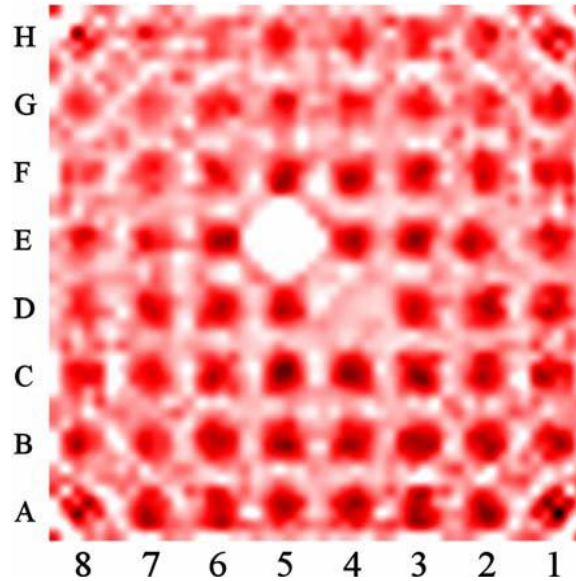


*Fig. 1.12 Experimentally obtained image of the fuel model with a non-active rod in position (E,5) and an empty rod, representing the water channel, in position (D,4)<sup>[75]</sup>*

## 1.11 Aims and Scope of the Thesis

The thesis deals with SPECT imaging and its application in nuclear field. Since a majority of work carried out in this field is in the area of medical imaging, it is imperative that a detailed study should be carried out for nuclear application of SPECT. The aim of this thesis work is to develop simulation techniques and their experimental verification for use in waste assay.

The present work can be broadly divided in two parts. The first part involves simulation studies to test the developed reconstruction codes. This includes developing analytical and iterative reconstruction codes and testing them through computer simulations for various cases. Some of the highlights include developing and implementing 2D system matrix for fan beam geometry and fully 3D system matrix for parallel beam geometry. The second part of the work involves experimental studies for reconstructing radioisotope activity in a given matrix. This includes lab based

experiments for 2D SPECT and finally setting up a 3D SPECT imaging facility for Active and Passive CT of waste drums.

The problem of the thesis work is defined and elucidated in subsequent chapters as follows.

Chapter 2 throws light on mathematical aspects of different reconstruction algorithms in SPECT. The reconstruction algorithms can be broadly classified into analytical and iterative reconstructions. To explain the analytical reconstruction proposed by Novikov for inversion of attenuated Radon transform, a mathematical background of Radon transform and filtered backprojection has been provided. The iterative approach allows a complex model of gamma radiation interaction to be taken into account including the effect of collimation and scatter as well as statistical variability of measured data. The iterative approach can be further classified into two sub-classes: algebraic and statistical. In the algebraic reconstruction technique, the formation of projections is modeled by a set of linear equations. The construction of the activity distribution is then obtained by calculating the least squares solution for the set of equations. The algebraic reconstruction techniques, such as ART, SART and SIRT have been discussed. The statistical reconstruction technique takes into account the Poisson statistics of radiation. The solution for activity distribution is obtained by Bayesian point estimation: maximum a-posteriori or maximum likelihood estimation. The methods for Bayesian point estimation are then solved iteratively. Different EM techniques – MLEM, OSEM and MAP-EM – have been discussed.

Chapter 3 discusses the modeling of the forward projection, that is, generation of the projection data. This chapter is divided into two sections. The first section describes a

novel approach developed in this thesis for generation of forward projection for fan and cone beam geometries. This method does not take into account the effect of collimator, scattering or distance. The projection data generated thus corresponds to an ‘ideal’ collimator system where the detector ‘sees’ photons along a straight line path only. This is quite useful for testing analytical reconstruction algorithms in fan and cone beam geometries. The second section describes the analytical method used in this thesis to obtain the probability system matrix. This is a more rigorous approach which takes into account the effect of collimator and distance (scattering has been neglected). The projection data generated using this system matrix mimics the experimental parameters more closely as compared to the ideal approach in section one. This system matrix is used for iterative reconstructions. Finally, a fully 3D system matrix has been computed for fully 3D reconstruction which takes into account the contribution of slices below and above the reconstruction plane to the reconstructed image.

Chapter 4 deals with the computer simulations used to test the analytical and iterative reconstructed codes developed in this thesis. Both the line integral approach (no collimator) and collimator modeled approach have been considered for constructing the simulated projections. Different 2D phantoms have been considered to elucidate the contribution of collimator modeled system matrix in reconstruction. Analytical reconstruction codes have been developed for parallel, fan and cone beam configurations. 3D phantoms for simulated waste drum have been used to test the analytical fan and cone beam reconstruction codes. For experiments, however, cone beam geometry has not been explored.

Chapter 5 presents the experimental results. The experimental SPECT imaging system consists of the following: (a) Sample Stage – to manoeuvre the sample during acquisition; (b) Collimator – to define the path of gamma rays accepted by the detector; (c) Detector – to record gamma photon events and (d) Data Acquisition System – to record, save and/or display the data for offline processing. The choice of detector depends on particular application (in terms of energy resolution and efficiency) and cost. As multiple detectors are required in SPECT imaging, NaI(Tl) is commonly preferred because of its high efficiency and low cost. However, NaI(Tl) has poor energy resolution and cannot be employed for situations where a complex energy spectrum is to be analyzed. An important aspect of this thesis is to explore the use of LaBr<sub>3</sub>(Ce) detector for SPECT imaging. LaBr<sub>3</sub>(Ce) has a better energy resolution as compared to NaI(Tl). This is the first instance of SPECT imaging with LaBr<sub>3</sub>(Ce) being reported. Initial feasibility experiments were carried out for 2D imaging with <sup>137</sup>Cs sources. Finally a 3D SPECT imaging lab was set up for scanning of mock waste drums with <sup>137</sup>Cs sources. For reconstruction, both analytical and iterative reconstructions have been employed and results have been presented. Chapter 5 (Section II) describes the application of SPECT imaging in the context of nuclear waste assay. An active and passive computed tomography (A&PCT) has been carried out for assessing the distribution and quantification of <sup>239</sup>Pu in waste drums. During the ACT measurements, an external gamma/X-ray source is used to determine the attenuation map of the object. With this knowledge of the attenuation map, the PCT measurements are then carried out to reconstruct the gamma sources inside the object.

Chapter 6 concludes with a summary of works and plans for future work.

The salient features of the work under the thesis are summarized as follows:

- (i) Implementation of analytical and iterative reconstruction techniques
- (ii) Novel method for generation of fan and cone beam data for simulated objects
- (iii) Development and implementation of fully 3D SPECT reconstruction
- (iv) Development and implementation of a practical fan-beam Active and Passive CT technique for waste assay
- (v) Developing a three dimensional SPECT imaging facility for scanning of waste drums using LaBr<sub>3</sub>(Ce) detectors
- (vi) Active and Passive CT for <sup>239</sup>Pu assay in waste drums

# SPECT Reconstruction Techniques

Mathematically, reconstruction is an inverse problem: the aim is to find vector of unknowns from the measured observables by solving a system of linear equations. Though both transmission and emission tomography are formulated as inverse problems, the system matrix relating the unknowns and observables is fundamentally different in both cases. This can be explained mathematically as follows.

In conventional tomography (transmission tomography), the object is discretized into square grids. A unit cell of this grid is called ‘pixel’ (short for ‘picture cell’) for 2D grid or ‘voxel’ (short for ‘volume cell’) for 3D grid. The system of equations may be expressed as:

$$g_i = \sum_{j=1}^N \mu_j x_j \quad (2.1)$$

where  $g_i = \ln \left( \frac{I_0}{I_i} \right)$ ,  $I_0$  is the intensity of incident radiation,  $I_i$  is the transmitted intensity and  $g_i$  is the counts recorded by the  $i^{th}$  detector bin.  $\mu_j$  and  $x_j$  are, respectively, the linear attenuation coefficient and path length traversed by the radiation in the  $j^{th}$  pixel / voxel. This can be expressed in matrix notation as

$$\begin{pmatrix} g_1 \\ g_2 \\ \cdot \\ \cdot \\ g_M \end{pmatrix} = \begin{pmatrix} x_{11} & x_{12} & \cdot & \cdot & x_{1N} \\ x_{21} & \cdot & \cdot & \cdot & \cdot \\ \cdot & \cdot & \cdot & \cdot & \cdot \\ \cdot & \cdot & \cdot & \cdot & \cdot \\ x_{M1} & \cdot & \cdot & \cdot & x_{MN} \end{pmatrix} \begin{pmatrix} \mu_1 \\ \mu_2 \\ \cdot \\ \cdot \\ \mu_N \end{pmatrix} \quad (2.2)$$

$\mu = (\mu_1, \mu_2, \dots, \mu_N)^T$  is the vector of unknown attenuation coefficients. The system matrix elements are basically path lengths and it is quite straightforward to calculate them.

In case of SPECT imaging the system of equations can again be described by the following equation:

$$g_i = \sum_{j=1}^N f_j \exp \left( -\sum_k \mu_k x_{k,ij} \right) \quad (2.3)$$

In matrix notation, this may be written as

$$g = Af \quad (2.4)$$

or,

$$\begin{pmatrix} g_1 \\ g_2 \\ \cdot \\ \cdot \\ g_M \end{pmatrix} = \begin{pmatrix} a_{11} & a_{12} & \cdot & \cdot & a_{1N} \\ a_{21} & \cdot & \cdot & \cdot & \cdot \\ \cdot & \cdot & \cdot & \cdot & \cdot \\ \cdot & \cdot & \cdot & \cdot & \cdot \\ a_{M1} & \cdot & \cdot & \cdot & a_{MN} \end{pmatrix} \begin{pmatrix} f_1 \\ f_2 \\ \cdot \\ \cdot \\ f_N \end{pmatrix} \quad (2.5)$$

where  $g = (g_1, g_2, \dots, g_M)^T$  is the observable (measured) data, i.e. projections,  $f = (f_1, f_2, \dots, f_N)^T$  is unknown spatial density distribution of nuclear disintegration events resulting in gamma emission (also called emission map) in the object, and  $A$  is a  $M \times N$  system matrix whose elements are given by (simple approximation, neglecting the solid angle and considering only attenuation)

$$a_{ij} = \exp \left( -\sum_k \mu_k x_{k,ij} \right) \quad (2.6)$$

It is evident from Eq. 2.3 that now there is an additional unknown  $\mu$  which needs to be known before  $f$  can be evaluated. Also the system matrix depends critically on  $\mu$  and is more complex to model than the previous case. Once  $\mu$  is known and system matrix is generated, we have an inverse problem on hand and most theories of inverse problem can be applied.

Reconstruction algorithms generally employed for solving SPECT problem can be divided into two classes:

- Analytical Reconstruction Technique
- Iterative Reconstruction Technique

The analytical approach assumes noiseless data, an ideal collimator, no attenuation and no scatter of gamma radiation. These assumptions can make the reconstruction result an inaccurate representation of the true activity distribution. Therefore, additional data filtering and post-processing are necessary. The most commonly used method is the Filtered Back Projection (FBP) algorithm<sup>[78]</sup> based on the inverse Radon transform. In this approach, the projections are filtered in the frequency domain and the filtered projections are backprojected in the spatial domain. The FBP method introduces streak artifacts when large differences in activity are imaged.

The iterative approach<sup>[79]</sup> allows a complex model of gamma radiation interaction to be taken into account including the effect of collimation and scatter as well as statistical variability of measured data. These are recommended for quantitative image analysis<sup>[78]</sup> which is crucial, for example, in waste assay. The iterative approach can be further classified into two sub-classes: algebraic and statistical.

In the algebraic reconstruction technique, the formation of projections is modeled by a set of linear equations. The construction of the activity distribution is then obtained by calculating the least squares solution for the set of equations. The LS problem is usually an ill-posed inverse problem and some regularization is needed. Also, a straightforward solution for LS problem is computationally heavy and iterative methods are used. The algebraic reconstruction techniques, such as ART,

SART and SIRT are methods for solving the LS problem using different types of iterations.

The statistical reconstruction technique takes into account the Poisson statistics of radiation. The solution for activity distribution is obtained by Bayesian point estimation: maximum a-posteriori or maximum likelihood estimation. The methods for Bayesian point estimation are then solved iteratively.

This chapter reviews different algorithms in SPECT available in the literature, highlighting their specific advantages and/or shortcomings.

## 2.1 Analytical Reconstruction Technique

Before discussing the analytical reconstruction technique for SPECT, we will discuss the basics of filtered backprojection technique in the context of transmission tomography.

### 2.1.1 The Radon transform

The Radon transform <sup>[28]</sup> was defined by Johann Radon in 1917. Let  $\mathbb{R}^2$  denote the 2D Euclidean space (Fig.2.1) with a point representation  $\bar{x} = (x, y)$  in Cartesian coordinate.

In the rotated co-ordinate system  $(s, t)$  with axes parallel to vectors  $\hat{\theta}(\theta)$  and  $\hat{\theta}^\perp(\theta)$ , we have

$$\begin{pmatrix} s \\ t \end{pmatrix} = \begin{pmatrix} \cos \theta & \sin \theta \\ -\sin \theta & \cos \theta \end{pmatrix} \begin{pmatrix} x \\ y \end{pmatrix} \quad (2.7)$$

and

$$\begin{pmatrix} x \\ y \end{pmatrix} = \begin{pmatrix} \cos \theta & -\sin \theta \\ \sin \theta & \cos \theta \end{pmatrix} \begin{pmatrix} s \\ t \end{pmatrix} \quad (2.8)$$

A function  $f(x, y)$  in  $\mathbb{R}^2$  is denoted by  $f(s, t) = f(x \cos \theta + y \sin \theta, -x \sin \theta + y \cos \theta)$  in the rotated co-ordinate system  $(s, t)$ , that is the rotation of  $(x, y)$  by an angle  $\theta$  in the counter-clockwise direction.

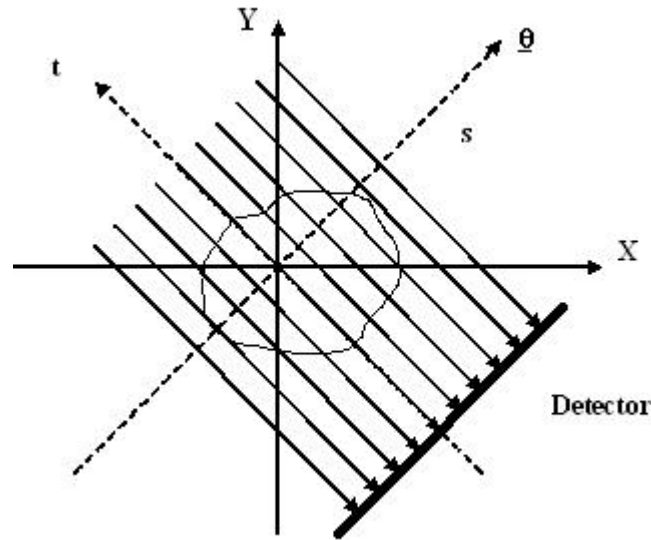


**Fig. 2.1** Co-ordinate system for parallel beam projection

The integrals of a 2D function  $f(s, t)$  along all possible lines is the two-dimensional Radon Transform  $\mathfrak{R}$  of  $f(s, t)$

$$g(s, \theta) = [\mathfrak{R}f](s, \theta) = \int_{-\infty}^{\infty} f(s, t) dt \tag{2.9}$$

### 2.1.2 The Fourier Slice Theorem

An important property of the Radon transform is its close correspondence with the Fourier transform.

The Fourier Slice Theorem (also called Central Slice Theorem) states: “The one-dimensional Fourier transform of a projection of a function  $f(x, y)$ , i.e. the Fourier transform of data along a line through the origin in the Radon space

of  $f(x, y)$ , is same as the data along the same line through the two-dimensional Fourier transform  $\mathcal{F}(u, v)$  of  $f(x, y)$ .

The Fourier transform  $\mathcal{F}$  of  $g(s, \theta)$  is given by

$$G(R, \theta) = [\mathcal{F} \mathcal{R}f](R\hat{\theta}) = \int_{-\infty}^{\infty} g(s, \theta) e^{-i2\pi R s} ds \quad (2.10)$$

Using Eq.2.9, this becomes

$$G(R, \theta) = \int_{-\infty}^{\infty} \left\{ \int_{-\infty}^{\infty} \int_{-\infty}^{\infty} f(x, y) \delta(x \cos \theta + y \sin \theta - s) dx dy \right\} e^{-i2\pi R s} ds \quad (2.11)$$

Changing the order of integration, we get

$$G(R, \theta) = \int_{-\infty}^{\infty} \int_{-\infty}^{\infty} f(x, y) \left\{ \int_{-\infty}^{\infty} \delta(x \cos \theta + y \sin \theta - s) e^{-i2\pi R s} ds \right\} dx dy \quad (2.12)$$

The inner integral in Eq. 2.11 contributes under the condition stated in Eq. 2.7. Thus we have

$$G(R, \theta) = \int_{-\infty}^{\infty} \int_{-\infty}^{\infty} f(x, y) e^{-i2\pi(x \cos \theta + y \sin \theta)R} dx dy \quad (2.13)$$

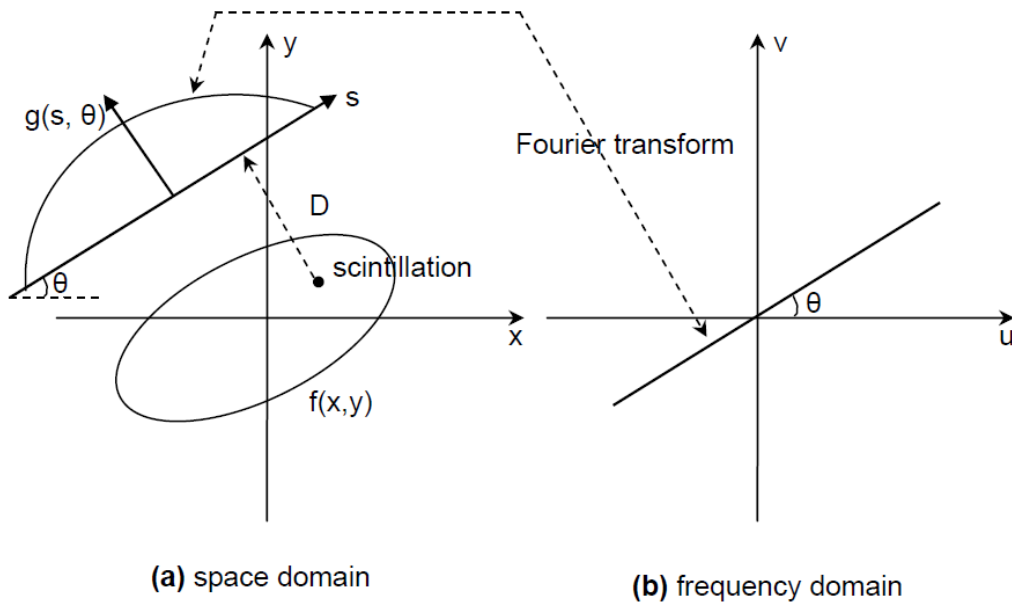


**Fig. 2.2** *Fourier Slice Theorem: It relates the Fourier transform of a projection with the Fourier transform through the object along a radial line at an angle  $\theta$*  <sup>[80]</sup>

Substituting

$$\begin{aligned} u &= R \cos \theta \\ v &= R \sin \theta \end{aligned}$$

Eq. 2.12 becomes

$$G(R, \theta) = \int_{-\infty}^{\infty} \int_{-\infty}^{\infty} f(x, y) e^{-i2\pi(xu+yv)} dx dy = \mathcal{F}(u, v) \quad (2.13)$$

Thus it is proved that the 1D Fourier Transform  $G(R, \theta)$  of projection data  $g(s, \theta)$  is indeed equal to the two-dimensional Fourier transform  $F(u, v)$  of  $f(x, y)$ . This is the Fourier Slice Theorem. Fig.2.2 shows a schematic representation of Fourier Slice Theorem.

We can rewrite Eq.2.13 as

$$G(R, \theta) = \mathcal{F}(R \cos \theta, R \sin \theta) \quad (2.14)$$

### 2.1.3 Direct Fourier Method

Once  $F(u, v)$  is obtained from the Fourier Transform  $G(R, \theta)$  of the projection data  $g(s, \theta)$  using Fourier Slice Theorem, the function  $f(x, y)$  may be calculated using the Inverse Fourier Transform on  $F(u, v)$ . This is the Direct Fourier reconstruction.

However, there is a catch. The standard Inverse Fourier Transform requires data on a rectangular grid whereas Fourier slice Theorem gives data on a polar grid. For a practical implementation, a complicated frequency space interpolation is required <sup>[80]</sup>.

### 2.1.4 Backprojection

Let us suppose that the projection data is  $[\mathcal{R}f](R\hat{\theta})$ . The backprojection operator  $\mathcal{B}$  may be defined as

$$[\mathcal{B}f](x, y) = \int_{-\pi/2}^{\pi/2} [\mathfrak{R}f](R\hat{\theta})d\theta \quad (2.15)$$

Fig.2.3 shows a schematic representation of projection and backprojection. An image of a slice through the distribution can be generated by sequentially projecting the data in each count profile collected from the selected slice back along the rays from which the data were collected and adding the data to previously projected rays (Fig.2.4 and Fig.2.5). The mathematical term for this process is the linear superposition of backprojections.

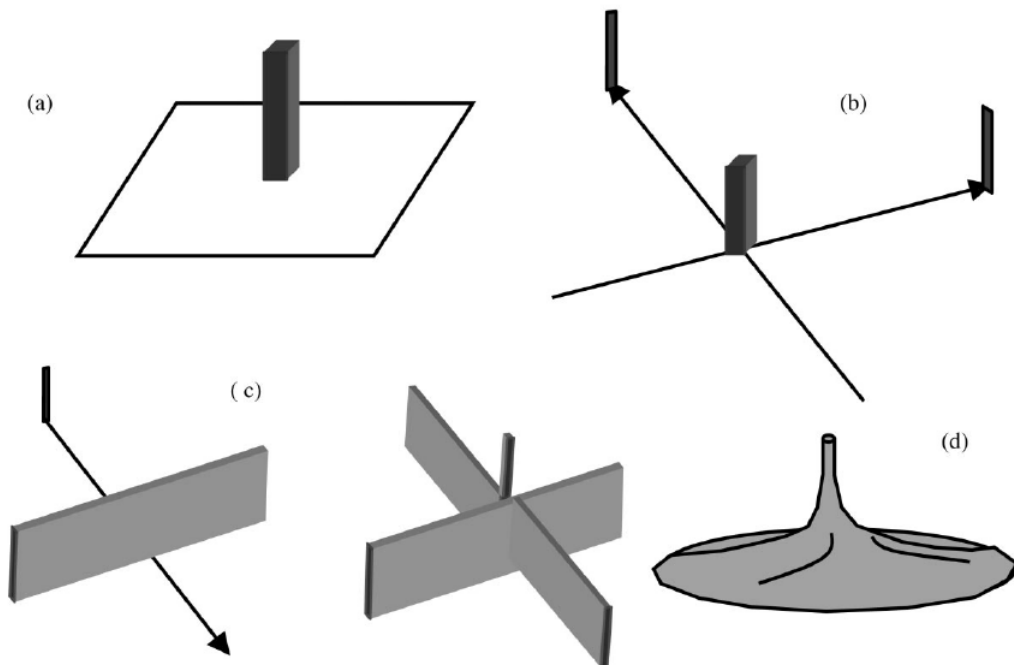


*Fig. 2.3 Projection and backprojection*<sup>[81]</sup>

Since there is no a priori knowledge of the origin of photons along each ray, the value of each pixel in the count profile is placed in each data cell of the reconstructed image along the ray. It should be noted that uniform projections are used in Fig.2.5 to illustrate the backprojection principle. In fact, the rays at the periphery of the sphere are of less intensity than at the middle. The classic “star effect” blur pattern inherent in backprojection images is also evident in these images with each ray of the star

corresponding to one projection view. The importance of collecting the appropriate number of projections is evident from this diagram. Increasing the number of projections enhances the image contrast and reduces the potential for artifacts from the “star effect.”

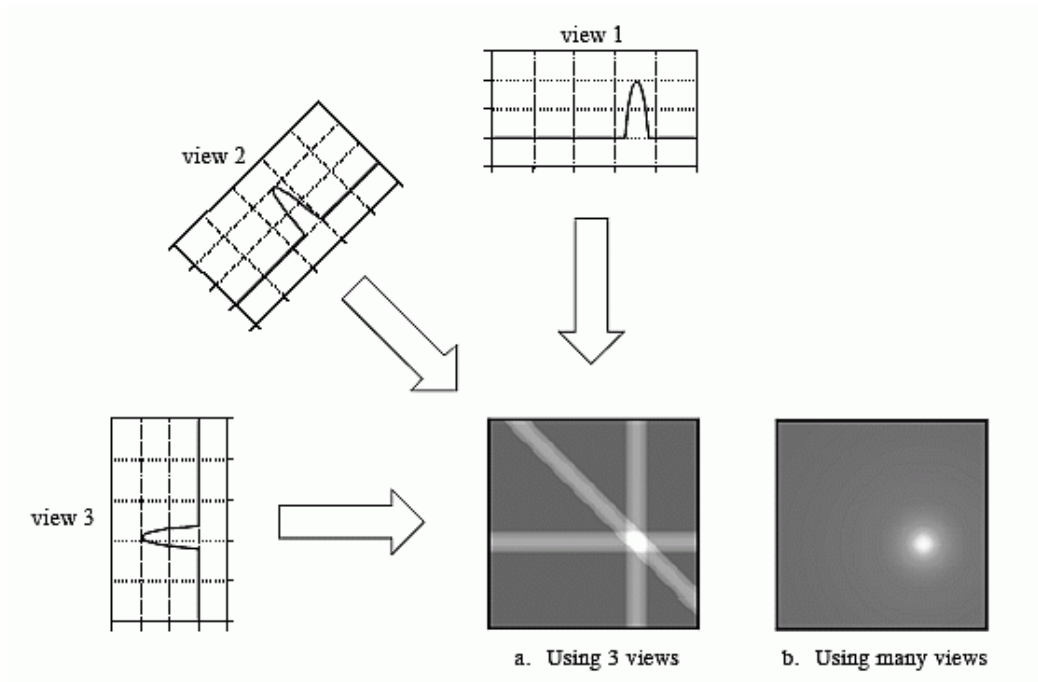


**Fig. 2.4** Backprojection reconstructs an image by taking each view and smearing it along the path it was originally acquired. The resulting image is a blurry version of the correct image<sup>[24]</sup>

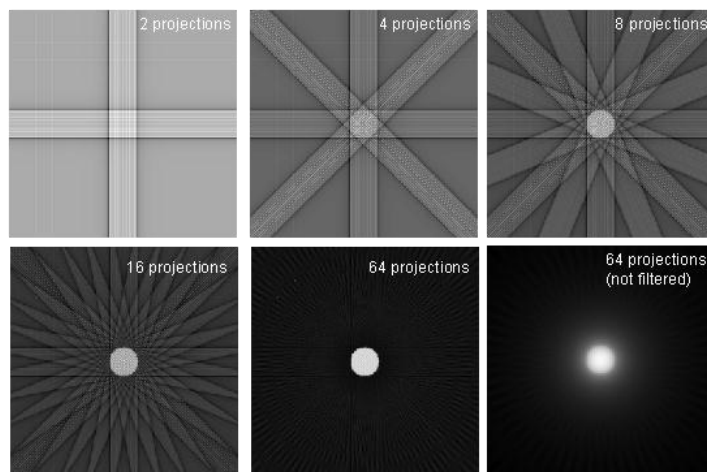


**Fig. 2.5** Effect of number of projections on the backprojected image<sup>[82]</sup>

Qualitatively, the backprojection step is akin to “smearing out” the line integral data (projection data) along the same lines in the reconstructed object that produced the line integrals in the original object.

### 2.1.5 Filtered Backprojection Method

If the reconstruction process consists of backprojection only, the net effect is a low-pass filtering which is manifested easily when we have a point object. To compensate for this low-pass filtering, it is essential to filter the projection data with a high-pass filter before the backprojection step (Fig.2.6). This forms the basis of filtered backprojection (FBP) scheme. FBP is the most widely used technique for 2D tomography reconstruction.

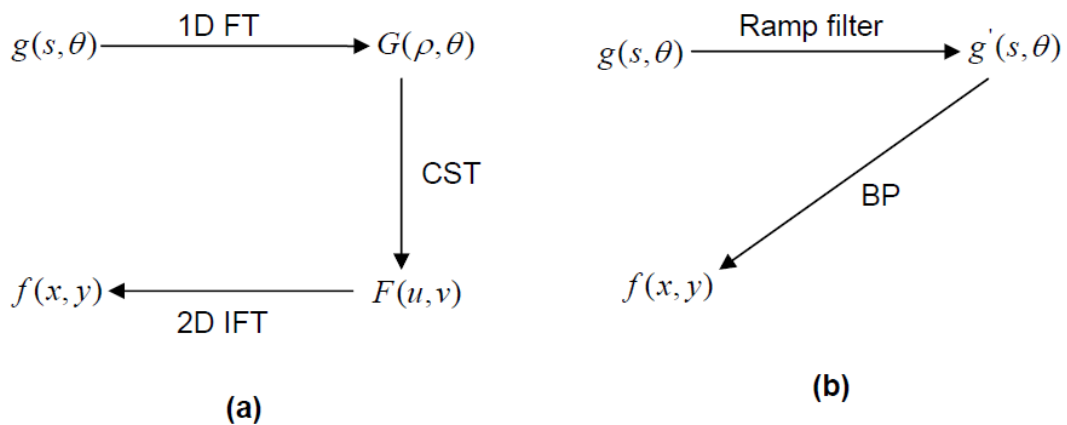


**Fig. 2.6** Flowcharts of analytical algorithms (a) Direct Fourier Transform (b) Filtered Backprojection

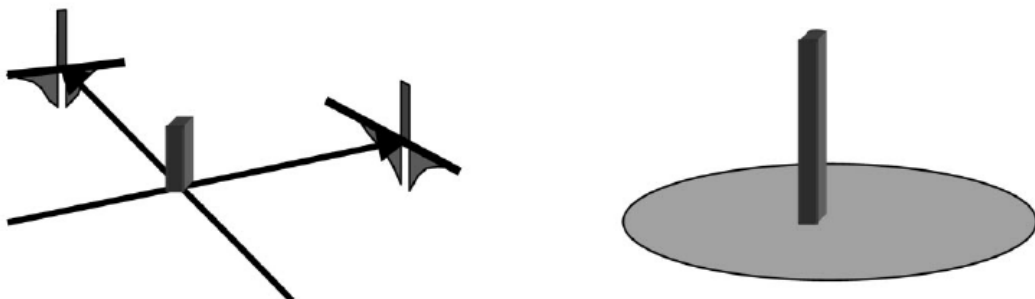


**Fig. 2.7** In filtered backprojection, negative wings are introduced to eliminate blurring<sup>[81]</sup>

Mathematically, the high-pass filter is nothing but a ramp filter in the Fourier domain. The filtered backprojection algorithm may be derived as follows. Using inverse Fourier transform on Eq. 2.15, the object function  $f(x, y)$  can be expressed as

$$f(x, y) = \int_{-\infty}^{\infty} \int_{-\infty}^{\infty} \mathfrak{F}(u, v) e^{i2\pi(ux+vy)} dudv \quad (2.16)$$

By substituting

$$\begin{aligned} u &= R \cos \theta \\ v &= R \sin \theta \end{aligned} \quad (2.17)$$

Eq. 2.16 becomes

$$f(x, y) = \int_0^{2\pi} \int_0^{\infty} \mathfrak{F}_{\theta}(R, \theta) e^{i2\pi R(x \cos \theta + y \sin \theta)} R dR d\theta \quad (2.18)$$

where  $\mathfrak{F}_{\theta}(\cdot)$  is the Fourier function in polar co-ordinates. We can re-write Eq. 2.18 as

$$\begin{aligned} f(x, y) &= \int_0^{\pi} \int_0^{\infty} \mathfrak{F}_{\theta}(R, \theta) e^{i2\pi R(x \cos \theta + y \sin \theta)} R dR d\theta \\ &\quad + \int_0^{\pi} \int_0^{\infty} \mathfrak{F}_{\theta}(R, \theta + \pi) e^{i2\pi R(x \cos(\theta + \pi) + y \sin(\theta + \pi))} R dR d\theta \end{aligned} \quad (2.19)$$

Using the fact that Fourier function  $\mathfrak{F}_{\theta}(\cdot)$  is periodic with period  $2\pi$

$$\mathfrak{F}_{\theta}(R, \theta + \pi) = \mathfrak{F}_{\theta}(-R, \theta) \quad (2.20)$$

Using the interval  $0 \leq \theta < \pi$  for  $-\infty < R < \infty$ , Eq. 2.19 may be written as

$$f(x, y) = \int_0^{\pi} \left[ \int_{-\infty}^{\infty} \mathfrak{F}_{\theta}(R, \theta) |R| e^{i2\pi R(x \cos \theta + y \sin \theta)} dR \right] d\theta \quad (2.21)$$

Using the Fourier slice theorem, the 2D Fourier transform  $\mathfrak{F}_{\theta}(R, \theta)$  is equal to the 1D

Fourier transform  $[\mathfrak{F} \mathfrak{R}f](R\hat{\theta})$  of the projection  $[\mathfrak{R}f](R\hat{\theta})$  at angle  $\theta$ , we get

$$f(x, y) = \int_0^{\pi} \left[ \int_{-\infty}^{\infty} [\mathfrak{F} \mathfrak{R}f](R\hat{\theta}) |R| e^{i2\pi R(x \cos \theta + y \sin \theta)} dR \right] d\theta$$

$$= \int_0^{\pi} \left[ \int_{-\infty}^{\infty} \left[ \int_{-\infty}^{\infty} [\mathfrak{R}f](p\hat{\theta}) e^{-i2\pi R p} dp \right] |R| e^{i2\pi R(x\cos\theta + y\sin\theta)} dR \right] d\theta \quad (2.22)$$

Eq. 2.22 describes the complete filtered backprojection scheme. The projection data

$[\mathfrak{R}f](p\hat{\xi})$  are Fourier transformed  $\left( \int_{-\infty}^{\infty} [\mathfrak{R}f](p\hat{\theta}) e^{-i2\pi R p} dp \right)$ , filtered with a ramp filter

$|R|$ , inversely Fourier transformed  $\left( \int_{-\infty}^{\infty} [\dots] e^{i2\pi R(x\cos\theta + y\sin\theta)} dR \right)$  and finally

backprojected  $\left( \int_0^{\pi} [\dots] d\theta \right)$

### 2.1.6 Attenuated Radon transform

In case of SPECT, the photons emitted by the radioisotope suffer attenuation inside the object. If attenuation is incorporated in the Radon transform, the projection takes the form

$$[\mathfrak{R}_{att} f](s, \theta) = \int_{-\infty}^{\infty} f(s\underline{\theta} + t\underline{\theta}^{\perp}) e^{-\int_0^t \mu(s\underline{\theta} + \tau\underline{\theta}^{\perp}) d\tau} dt \quad (2.23)$$

where  $\mu(\cdot)$  is the linear attenuation coefficient and  $f(\cdot)$  is the radioisotope activity/concentration.  $\mathfrak{R}_{att}(\cdot)$  is called the exponential Radon transform or the attenuated Radon transform. It can be noted that for  $\mu=0$ , the attenuated Radon transform reduces to the Radon transform.

The aim of SPECT reconstruction is to deduce the source activity distribution  $f$  from the measured projection data  $\mathfrak{R}_{att}(\cdot)$ . However, it may be noted that Eq. 2.19 has another unknown quantity -  $\mu$ . The distribution of  $\mu$  may be obtained from prior transmission tomography measurements or from assumptions of the geometry and the attenuation in the object.

Roman Novikov <sup>[48]</sup> presented an explicit analytical solution for the attenuated Radon transform (Eq. 2.23), which is presented below.

### 2.1.7 Novikov's Explicit Inversion Formula

Consider a vector  $\bar{x} = (x, y)$  in a two-dimensional Euclidean space. Let  $f(\bar{x})$  denote the distribution of radioisotope activity and  $\mu(\bar{x})$  denote the attenuation map of the surrounding object.  $\mu(\bar{x})$  may be non-uniform. The attenuated 2D Radon transform for parallel beam geometry is given by <sup>[48, 81]</sup>

$$[\mathfrak{R}_{att}f](s, \theta) = \int_{-\infty}^{\infty} f(s\bar{\theta} + t\bar{\theta}^{\perp}) e^{-D_{\mu}(s\bar{\theta} + t\bar{\theta}^{\perp}, -\bar{\theta}^{\perp})} dt \quad (2.24)$$

Where  $\bar{\theta} = \begin{pmatrix} \cos \theta \\ \sin \theta \end{pmatrix}$ ,  $\bar{\theta}^{\perp} = \begin{pmatrix} -\sin \theta \\ \cos \theta \end{pmatrix}$  and  $D_{\mu}(\bar{x}, \bar{\varphi})$  is the divergent beam transform of

$\mu(\bar{x})$  in the direction of  $\bar{\varphi} = \begin{pmatrix} \cos \varphi \\ \sin \varphi \end{pmatrix}$  defined as

$$D_{\mu}(\bar{x}, \bar{\varphi}) = \int_0^{\infty} \mu(\bar{x} + p\bar{\varphi}) dp \quad (2.25)$$

Assuming  $\mu(\bar{x})$  is known, Novikov gave an explicit inversion formula to reconstruct  $f(\bar{x})$  from the parallel projection data  $g(s, \theta) = [\mathfrak{R}_{att}f](s, \theta)$ :

$$f(\bar{x}) = \frac{1}{4\pi} \text{Re} \left\{ \nabla \cdot \int_0^{2\pi} \bar{\theta} \left\{ e^{-h(s, \theta) + D_{\mu}(\bar{x}, -\bar{\theta}^{\perp})} \mathcal{H} e^{h(s, \theta)} g(s, \theta) \right\} \Big|_{s=\bar{x} \cdot \bar{\theta}} d\theta \right\} \quad (2.26)$$

where  $h(s, \theta) = \frac{1}{2}(I + i\mathcal{H})[\mathfrak{R}\mu](s, \theta)$  and  $[\mathcal{H}\varphi](s, \theta) = \frac{1}{\pi} p.v. \int_{-\infty}^{\infty} \frac{\varphi(s', \theta)}{s - s'} ds'$

with  $i^2 = -1$ .  $I$  is the identity operator.  $\mathcal{H}$  is the Hilbert transform with respect to the second parameter and  $p.v.$  denotes Cauchy principal value of the integral.  $\nabla$  is the divergence operator defined as

$$\nabla \equiv \left( \frac{\partial}{\partial x}, \frac{\partial}{\partial y} \right)$$

### 2.1.8 The Hilbert Transform

A real function  $f(t)$  and its Hilbert transform  $\mathcal{H}[f(t)]$  are related to each other in such a way that they together create a strong analytic signal. The strong analytic signal can be written with amplitude and phase where the derivative of the phase can be identified as the instantaneous frequency. The Fourier transform of the strong analytic signal gives us a one-sided spectrum in the frequency domain.

The Hilbert transform  $\mathcal{H}[f(t)]$  of a signal  $f(t)$  is defined as

$$\mathcal{H}[f(t)] = f(t) \otimes \frac{1}{\pi t} = \frac{1}{\pi} \int_{-\infty}^{\infty} \frac{f(\tau)}{t-\tau} d\tau = \frac{1}{\pi} \int_{-\infty}^{\infty} \frac{f(t-\tau)}{\tau} d\tau \quad (2.27)$$

The Hilbert transform in the time domain is a convolution of the signal with the signal  $1/\pi t$ . The Hilbert transform in Eq.2.27 is defined in terms of Cauchy principal value of the integral. The Cauchy principal value is obtained by considering a finite range of integration that is symmetric about the point of singularity, but which excludes a symmetric subinterval, taking the limit of the integral as the length of the interval approaches  $\infty$  while, simultaneously, the length of the excluded interval approaches zero.

$$H[f(t)] = \frac{1}{\pi} \lim_{\varepsilon \rightarrow 0^+} \left( \int_{t-1/\varepsilon}^{t-\varepsilon} \frac{f(\tau)}{t-\tau} d\tau + \int_{t+\varepsilon}^{t+1/\varepsilon} \frac{f(\tau)}{t-\tau} d\tau \right) \quad (2.28)$$

### 2.1.9 Relation between Hilbert Transform and Fourier Transform

The signal  $1/\pi t$  has Fourier transform

$$-i \operatorname{sgn}(\omega) = \begin{cases} -i & \text{if } \omega > 0 \\ 0 & \text{if } \omega = 0 \\ i & \text{if } \omega < 0 \end{cases} \quad (2.29)$$

Consider  $g(t) = f(t) \otimes \frac{1}{\pi t}$

where  $\otimes$  is the convolution operator. The Fourier transform of  $g(t)$  is

$$G(\omega) = F(\omega)(-i \operatorname{sgn}(\omega)) \quad (2.30)$$

Thus, Hilbert Transform is interpreted in the Fourier space as introducing a  $\pm\pi/2$  phase shift.

### 2.1.10 The $\pm\pi/2$ phase shift

The  $\pm\pi/2$  phase shift is interpreted in the frequency domain as a multiplication with the imaginary value  $\pm i$ . Thus

$$\mathcal{H}(\omega) = \begin{cases} -i = e^{-i\pi/2} & \text{for } \omega > 0 \\ i = e^{i\pi/2} & \text{for } \omega < 0 \end{cases} \quad (2.31)$$

However,  $\mathcal{H}(\omega)$  is not a property of Fourier transform but the problem can be solved by expressing  $\mathcal{H}(\omega)$  as a limit of a bounded function  $G(\omega)$ , that is

$$G(\omega) = \begin{cases} -ie^{-\sigma\omega} & \text{for } \omega > 0 \\ ie^{\sigma\omega} & \text{for } \omega < 0 \end{cases} \quad (2.32)$$

where  $\lim_{\sigma \rightarrow 0} G(\omega) = \mathcal{H}(\omega)$

It is now possible to use the inverse Fourier transform on  $G(\omega)$ , thus

$$g(t) = \mathcal{F}^{-1}G(\omega)$$

$$\begin{aligned}
 &= \frac{1}{2\pi} \int_{-\infty}^0 i e^{\sigma\omega} e^{i\omega t} d\omega + \frac{1}{2\pi} \int_0^{\infty} -i e^{-\sigma\omega} e^{i\omega t} d\omega \\
 &= \frac{i}{2\pi} \int_0^{\infty} (e^{-(\sigma+it)\omega} - e^{-(\sigma-it)\omega}) d\omega \\
 &= \frac{i}{2\pi} \left[ -\frac{1}{\sigma+it} e^{-(\sigma+it)\omega} + \frac{1}{\sigma-it} e^{-(\sigma-it)\omega} \right]_0^{\infty} \\
 &= \frac{t}{\pi(\sigma^2 + t^2)}
 \end{aligned} \tag{2.33}$$

Now  $g(t) \rightarrow h(t)$  when  $\sigma \rightarrow 0$  and the inverse Fourier transform of the impulse response of  $\mathcal{H}(\omega)$  is

$$h(t) = \lim_{\sigma \rightarrow 0} g(t) = \lim_{\sigma \rightarrow 0} \frac{t}{\pi(\sigma^2 + t^2)} = \frac{1}{\pi t}$$

A convolution between  $f(t)$  and the impulse response  $h(t)$  gives us

$$\mathcal{H}[f(t)] = \frac{1}{\pi} \int_{-\infty}^{\infty} \frac{f(\tau)}{t - \tau} d\tau \tag{2.34}$$

which is the Hilbert transform.

### 2.1.11 Fan-Beam Reconstruction with Equally Spaced Detectors

You *et al* <sup>[82, 83]</sup> presented a modified algorithm for extending Novikov's Inversion Formula to fan beam and cone beam reconstructions.

Let  $S$  be the fan-beam focal point located on a circle of radius  $D$ . The projection data  $\tilde{g}(\beta, u)$  measured at a position  $u$  on the detector at a view angle  $\beta$  (Fig.2.8) is given by <sup>[82]</sup>:

$$\tilde{g}(\beta, u) = (\tilde{D}_{\mu} f)(\beta, u) = \int_0^{\infty} f(x_{\underline{s}} + t\underline{\alpha}) e^{-(D\mu)(x_{\underline{s}} + t\underline{\alpha}, \underline{\alpha})} dt \tag{2.35}$$

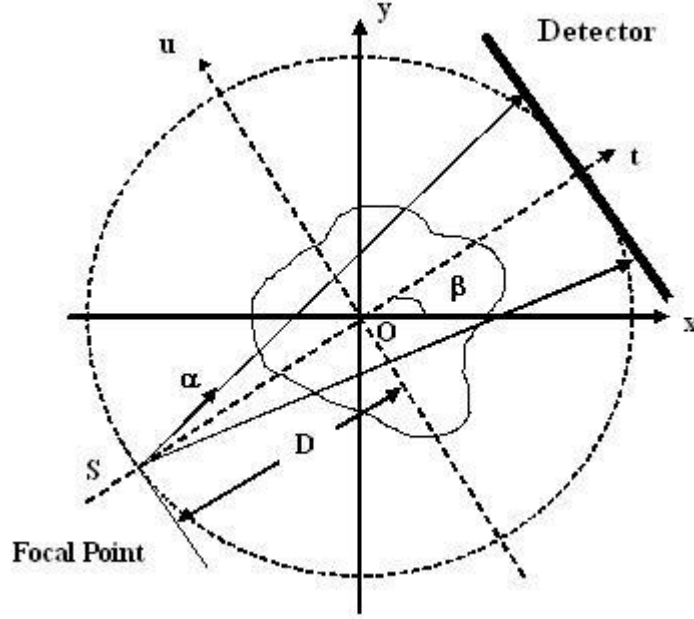


Fig. 2.8 Fan-beam geometry

The inversion formula for the fan-beam geometry is given as <sup>[82]</sup>:

$$f(\underline{x}) = \frac{1}{4\pi} \operatorname{Re} \left\{ \nabla \cdot \int_0^{2\pi} \frac{D^2}{U} \left\{ \tilde{\beta} e^{-\tilde{h}(\beta, u) + (D\mu)(x, -\tilde{\beta}^\perp)} \tilde{H} \frac{e^{\tilde{h}(\beta, u)} \tilde{g}(\beta, u)}{D^2 + u^2} \right\} \Big|_{u=u'} d\beta \right\} \quad (2.36)$$

where  $U = \frac{D + x \sin \beta - y \cos \beta}{D}$

$$\tilde{\beta} = \begin{pmatrix} \cos \left( \beta + \tan^{-1} \frac{u}{D} \right) \\ \sin \left( \beta + \tan^{-1} \frac{u}{D} \right) \end{pmatrix},$$

$$\tilde{h}(\beta, u) = \frac{1}{2} (I + i\tilde{H})(\tilde{D}\mu)(\beta, u) = \frac{1}{2} (I + i\tilde{H}) \int_0^\infty \mu(x_s + t\alpha) dt, \quad (2.37)$$

$\tilde{H}$  is the Hilbert transform defined in the fan-beam geometry <sup>[68]</sup>

$$u' = \frac{D(x \cos \beta + y \sin \beta)}{D + x \sin \beta - y \cos \beta}.$$

### 2.1.12 Cone-Beam Reconstruction with Circular Scanning Geometry

Let  $S$  be the cone-beam focal point located on a circle of radius  $D$  centred at  $O$  and in the central plane  $z = 0$ . The co-ordinate system  $(u, \xi)$  is centred at  $O$  on the detector plane such that the  $u$ -axis is parallel to the tangent of the trajectory and the  $\xi$ -axis is parallel to the  $z$ -axis (Fig.4). The projection data measured at a position  $(u, \xi)$  on the detector plane at a view angle  $\beta$  is denoted by  $\tilde{g}(\beta, u, \xi)$ .

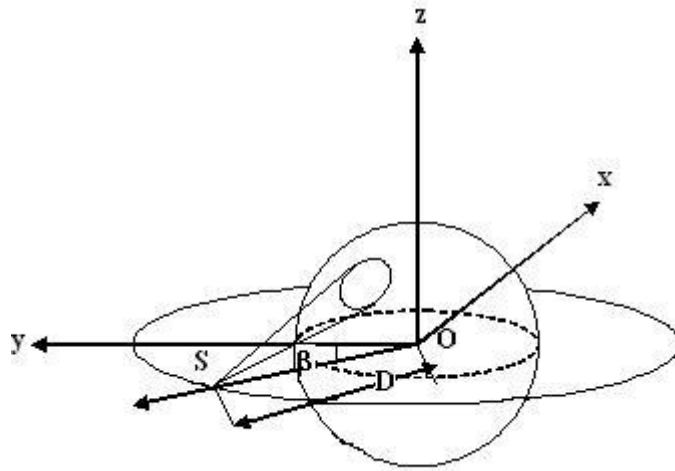


Fig. 2.9 Cone beam geometry

The inversion formula for the cone-beam geometry is given as <sup>[82]</sup>:

$$f(\underline{x}) = \frac{1}{4\pi} \operatorname{Re} \left\{ \nabla \cdot \int_0^{2\pi} \frac{D^2 \sqrt{D^2 + \xi^2}}{D-t} \left\{ \tilde{\beta} e^{-\tilde{h}(\beta, u, \xi) + (D\mu)(x, -\beta^\perp)} \tilde{H} \frac{e^{\tilde{h}(\beta, u, \xi)} \tilde{g}(\beta, u, \xi)}{D^2 + u^2 + \xi^2} \right\} \Big|_{u=u''} d\beta \right\} \quad (2.38)$$

$$\tilde{h}(\beta, u, \xi) = \frac{1}{2} (I + i\tilde{H}) (\tilde{D}\mu)(\beta, u, \xi), \quad (2.39)$$

$$u'' = \frac{Ds}{D-t}$$

$\tilde{H}$  is the Hilbert transform defined in the cone-beam geometry.

### 2.1.13 Optimal Number of Projections in FBP

What is the optimal number of projections required in FBP reconstruction? This question was answered by Guan and Gordon <sup>[84]</sup> for the 2D parallel beam case and it has been extended to 3D case by Mueller in <sup>[85]</sup>. The (approximately) optimal relation between the values  $n_\theta$  (angular projections) and  $n_l$  (discretization size of each projection) in the case of 2D transmission tomography is  $n_\theta / n_l \approx \pi / 2$  <sup>[30]</sup>. We shall find the relation in the context of SPECT.

The sampling interval in Fourier space is at least  $\Delta\omega = \omega_{Nyquist} / n_l$  and the maximum frequency is given by  $\omega_{max} = \omega_{Nyquist} / 2$  where  $\omega_{Nyquist}$  is the Nyquist frequency. Due to polar sampling in frequency space, the density of samples decreases as we go outward in the polar grid. To ensure a sampling rate of at least  $\Delta\omega$  everywhere in the polar grid, even at the boundary, the angular spacing between the projections (i.e., the Fourier slices) in frequency space needs to be:

$$\Delta\varphi = \frac{\Delta\omega}{\omega_{max}} = \frac{2}{n_l} \quad (2.40)$$

The sample space in the case of SPECT is  $[0, 2\pi]$  (even for parallel beam) in contrast to  $[0, \pi]$  sample space in the case of transmission tomography. The optimal number of projections is then:

$$n_\theta = \frac{2\pi}{\Delta\varphi} = \frac{2\pi n_l}{2} = \pi n_l \quad (2.41)$$

$$\frac{n_\theta}{n_l} \approx \pi$$

Thus, for FBP reconstruction, the angular projections should be at least three times the (linear) size of each projection.

## 2.2 Algebraic Reconstruction Techniques

In an algebraic approach to SPECT problem, it is assumed that the reconstructed object consists of a matrix of unknowns and the projection data are modeled by a set of linear equations. The solution of the reconstruction problem is then obtained by the Least Square solution for the set of equations.

### 2.2.1 Observation model

Let us consider the vector of activities in the pixels  $f = (f_1, f_2, \dots, f_N)^T \in \mathbb{R}^{N \times 1}$ . The projection data  $g = (g_1, g_2, \dots, g_M)^T \in \mathbb{R}^{M \times 1}$  can be expressed as a set of linear equations.

$$\begin{aligned}
 g_1 &= a_{11}f_1 + a_{12}f_2 + \dots + a_{1N}f_N \\
 g_2 &= a_{21}f_1 + a_{22}f_2 + \dots + a_{2N}f_N \\
 &\vdots \\
 g_M &= a_{M1}f_1 + a_{M2}f_2 + \dots + a_{MN}f_N
 \end{aligned} \tag{2.42}$$

In matrix notation, Eq.2.42 can be written as

$$\begin{pmatrix} g_1 \\ g_2 \\ \cdot \\ \cdot \\ g_M \end{pmatrix} = \begin{pmatrix} a_{11} & a_{12} & \cdot & \cdot & a_{1N} \\ a_{21} & a_{22} & \cdot & \cdot & a_{2N} \\ \cdot & \cdot & \cdot & \cdot & \cdot \\ \cdot & \cdot & \cdot & \cdot & \cdot \\ a_{M1} & a_{M2} & \cdot & \cdot & a_{MN} \end{pmatrix} \begin{pmatrix} f_1 \\ f_2 \\ \cdot \\ \cdot \\ f_N \end{pmatrix} \tag{2.43}$$

or 
$$g = Af \tag{2.44}$$

$N = n_p^2$  is the total number of pixels and  $M = n_p \cdot n_\phi$  is the number of recorded data points,  $n_p$  is the number of pixels in one row of the planar image and  $n_\phi$  is the number of acquisition angles. The matrix  $A \in \mathbb{R}^{M \times N}$  is called the observation matrix or the

probability system matrix. The matrix element  $a_{ij}$  is the probability that a  $\gamma$  photon emitted from  $i^{\text{th}}$  pixel is detected by the  $j^{\text{th}}$  projection bin.

If the matrix  $A$  is modeled correctly it includes all the physical features of the detecting system. The modeling of the probability system matrix is discussed in Chapter 3. Forming projection bins as a linear combination of activities is clearly a discrete version of integrating activities over some volume as presented in Eq.2.24. When using equation (2.43) as an observation model, it is assumed that the number of emissions in each pixel is a deterministic variable.

### 2.2.2 The Linear Least Square Estimation

Eq.2.44 can be solved using linear least square (LS) estimation. Our aim is to solve the estimate  $\hat{f}_{LS}$  satisfying the condition

$$\hat{f}_{LS} = \arg \min \|g - Af\| \quad (2.45)$$

Knowing the projection data  $g$  and constructing the probability system matrix  $A$ , our task is to solve the LS problem denoted by Eq.2.44. It may happen that the observation model Eq.2.44 is under-deterministic. In such a case the LS problem has no unique solution and some of the solutions must be chosen. Usually the minimum norm solution is used. Furthermore, the inverse problem of SPECT is usually ill-posed and some regularization may be needed in solving the LS problem. In addition, the matrix  $A$  is usually very large and the LS solution must be computed iteratively.

### 2.2.3 Implementation of ART

For the computer implementation of this method, initial guess of the solution is made. This guess, denoted by  $f_1^{(0)}, f_2^{(0)}, f_3^{(0)}, \dots, f_N^{(0)}$ , may be assigned a value of zero or, as

in the case of this thesis, an average value of the projection sum to all the initial  $f_i$ 's.

The reconstruction process may be expressed mathematically as follows <sup>[87]</sup>:

$$f_j^{(k)} = f_j^{(k-1)} + \frac{g_i - \sum_{j=1}^N f_j^{(k-1)} a_{ij}}{\sum_{j=1}^N a_{ij}^2} a_{ij} \quad (2.46)$$

In Eq.2.46,  $g_i$  is the measured ray-sum along the  $i^{th}$  ray. The term  $\sum_{j=1}^N f_j^{(k-1)} a_{ij}$  may

be considered to be the computed ray-sum for the same ray based on the  $(k-1)^{th}$  iteration. The correction  $\Delta g_i$  to the  $j^{th}$  cell is obtained by first calculating the

difference between the measured ray-sum and the computed ray-sum, normalizing

this difference by  $\sum_{j=1}^N a_{ij}^2$  and then assigning this value to all the image cells in the

$i^{th}$  ray, each assignment being weighted by the corresponding  $a_{ij}$ .

There are different variants of ART. These algorithms differ in the manner in which corrections are applied and are presented here in brief.

The ART algorithm originally proposed for CT applications by Gordon et al <sup>[86]</sup> is considered. In this method corrections are applied to all the cells through which the  $i^{th}$  ray passes, before calculating the correction for the next ray. The approximate projection data for  $i^{th}$  ray is computed as <sup>[87]</sup>

$$\hat{g}_i = \sum_{j=1}^N a_{ij} f_j \quad \text{for all } i = 1, 2, \dots, M \quad (2.47)$$

$$\hat{f}_j^{(k)} = \hat{f}_j^{(k-1)} + \lambda \frac{g_i - \sum_{j=1}^N a_{ij} \hat{f}_j^{(k-1)}}{\sum_{j=1}^N a_{ij}^2} a_{ij} \quad (2.48)$$

where  $\lambda$  is a relaxation parameter which takes value between 0 and 1.

### 2.2.4 Simultaneous Iterative Reconstruction Technique (SIRT)

Gilbert <sup>[88]</sup> developed a form of ART, called the simultaneous iterative reconstruction technique (SIRT). In SIRT, the elements of the unknown function  $f$  are modified after all the correction values corresponding to individual rays have been calculated. The algorithm is similar to additive ART but the pixel values are changed only at the end of each iteration, the change for each iteration being the average value for all the computed changes for the pixel.

$$\hat{f}_j^{(k)} = \hat{f}_j^{(k-1)} + \lambda \frac{\sum_i \left( \frac{g_i - \sum_{j'=1}^N a_{ij'} \hat{f}_{j'}^{(k-1)}}{\sum_{j'=1}^N a_{ij'}} \right) a_{ij}}{\sum_{j'=1}^N a_{ij'}} \quad (2.49)$$

Here  $\lambda$  is the relaxation factor.

### 2.2.5 Simultaneous ART (SART)

This method has been invented by Anderson and Kak <sup>[28, 87]</sup>. It connects advantages of ART and SIRT algorithms. It was found to be very efficient, accurate and superior in implementation <sup>[28, 85, 87]</sup>. The method of applying a correction is similar to ART but the structure is similar to SIRT. The correction terms in SART are simultaneously applied for all the rays in one projection. It is mathematically expressed as:

$$\hat{f}_j^{(k)} = \hat{f}_j^{(k-1)} + \lambda \frac{\sum_{i_\theta} \left( \frac{g_{i_\theta} - \sum_{j'=1}^N a_{i_\theta j'} \hat{f}_{j'}^{(k-1)}}{\sum_{j'=1}^N a_{i_\theta j'}} \right) a_{i_\theta j}}{\sum_{j'=1}^N a_{i_\theta j'}} \quad (2.50)$$

Here  $\lambda$  is the relaxation factor.

SART has many advantages, due to its image-based approach:

- It proves to be better method for cone beam reconstruction,
- It lends itself very well for a graphics hardware-accelerated approach.

However SART is slightly slower than ART in software, due to the pixel (for 2D) or voxel (for 3D) based pooling of correctional updates.

## 2.3 Statistical approach

In emission tomography, a well-known fact “the measurements are described by Poisson statistics”<sup>[89, 90]</sup> may be used to calculate  $f$  especially in statistical reconstruction approaches. There are certain basic assumptions underlying this fact:

**Assumption 1:** The spatial locations of individual radionuclei are independent random variables which are all identically distributed according to a common probability density function

**Assumptions 2:** The radionuclide decay process is a Poisson process<sup>[89]</sup>.

**Assumption 3:** Each decay or each emitted gamma photon can only be recorded at most by one detector bin, and the location of this bin is only dependent on the recorded photon, and is independent of all other photons<sup>[90]</sup>.

Therefore, a Poisson statistical model can be applied to SPECT reconstruction.

### 2.3.1 Bayesian estimation

Let us assume that the parameter vector  $f$  and measurements  $g$  are random vectors and the joint probability density function of  $f$  and  $g$  is  $p(f, g)$ . In the Bayesian estimation the aim is to find the parameter vector  $f$ , which maximizes the probability  $p(f | g)$  when the observations  $g$  are known (measured).

Baye's theorem connects the prior and posterior density functions of  $f$  and  $g$

$$p(f | g)p(g) = p(g | f)p(f) \quad (2.51)$$

Thus the posterior density function of  $f$  is

$$\begin{aligned} p(f | g) &= \frac{p(g | f)p(f)}{p(g)} \quad (2.52) \\ &\propto p(g | f)p(f) \end{aligned}$$

The function  $p(g | f)$  is called the likelihood of data. It is the density of data  $g$  for given parameter  $f$ , and it contains the physical model that connects the measurements  $g$  to the parameters  $f$ . The function  $p(f)$  is the density function of  $f$ . In the Bayesian estimation the prior assumptions of parameters  $f$  are included in  $p(f)$ . The following sections discuss some of the techniques used to solve the posterior density.

### 2.3.2 Maximum likelihood estimation

Maximum Likelihood-Expectation Maximization (MLEM) and its variants are the most common iterative algorithms used in SPECT reconstruction. It was proposed independently by Shepp and Vardi <sup>[50]</sup> and Lange and Carson <sup>[91]</sup>. A Poisson statistical model is applied to the projection data.

The purpose of MLEM is to find the best estimate for  $f$  : “the mean number of radioactive disintegrations  $\hat{f}$  in the image that can produce the sinogram  $g$  with the highest likelihood” <sup>[92]</sup>. ). Each projection  $g_i$  is a linear combination of Poisson distributed variables with mean values  $\hat{f}_j$ . Each iteration of the algorithm consists of two steps <sup>[92]</sup>:

**1. E-step:** the expectation step which forms the expression of the likelihood of any reconstructed image given the measured data

$$\begin{aligned}
 L(\hat{f}) &= P(g | \hat{f}) \\
 &= P(g_1)P(g_1)\dots\dots P(g_M) \\
 &= \prod_{i=1}^M P(g_i) \\
 &= \prod_{i=1}^M \frac{e^{-\bar{g}_i} \bar{g}_i^{g_i}}{g_i!} \tag{2.53}
 \end{aligned}$$

where  $P(g_i)$  is the probability (Poisson) of detecting  $g_i$  photons in detector bin  $i$  under the assumption that the expectation value is  $\bar{g}_i$ . The log-likelihood is given by

$$\begin{aligned}
 l(\hat{f}) &= \ln L(\hat{f}) \\
 &= \sum_{i=1}^M (-\bar{g}_i + g_i \ln(\bar{g}_i) - \ln(g_i!)) \\
 &= \sum_{i=1}^M \left( -\sum_{j=1}^N a_{ij} \hat{f}_j + g_i \ln \left( \sum_{j=1}^N a_{ij} \hat{f}_j \right) - \ln(g_i!) \right) \tag{2.54}
 \end{aligned}$$

**2. M-step:** the maximization step which finds the image with the most likelihood to give the measured data. The maximum is found when the derivative of the log-likelihood is zero:

$$\frac{\partial l(\hat{f})}{\partial \hat{f}_j} = -\sum_{i=1}^M a_{ij} + \sum_{i=1}^M \frac{g_i}{\sum_{j=1}^N a_{ij} \hat{f}_j} a_{ij} = 0 \tag{2.55}$$

The above equation can be re-written as <sup>[91, 92]</sup>

$$\hat{f}_j^{k+1} = \frac{\hat{f}_j^k}{\sum_{i=1}^M a_{ij}} \sum_{i=1}^M \frac{g_i}{\sum_{j'=1}^N a_{ij'} \hat{f}_{j'}^k} a_{ij} \tag{2.56}$$

which is the EM algorithm.

One remarkable feature of EM algorithm is the non-negativity of the estimate: if the initial guess  $\hat{f}^0$  is positive, the estimate is positive after each iteration. Thus, the EM algorithm regularizes the problem with implicit non-negativity constraint.

### 2.3.3 Ordered-Subsets Expectation Maximization (OSEM)

MLEM algorithm converges extremely slowly and may require nearly 100-200 iterations. To accelerate the MLEM reconstruction, Hudson and Larkin <sup>[93]</sup> proposed an OSEM algorithm. Instead of using the whole set of projections, OSEM uses a subset of projections at each sub-iteration step:

$$\hat{f}_j^{k+1} = \frac{\hat{f}_j^k}{\sum_{i \in S_i} a_{ij}} \sum_{i \in S_i} \frac{g_i}{\sum_{j'=1}^N a_{ij'} \hat{f}_{j'}^k} a_{ij} \quad (2.57)$$

where  $S_i = \{S_1, S_2, \dots, S_t\}$  with  $i = 1, 2, \dots, t$  with  $t$  being the number of subsets.

There are different patterns for choosing the subset: uniform, consecutive, orthogonal, etc. It is proven <sup>[94]</sup> that each subset containing equally distributed projections, i.e. a uniform pattern can produce the best reconstructed images close to MLEM reconstruction, compared to other patterns.

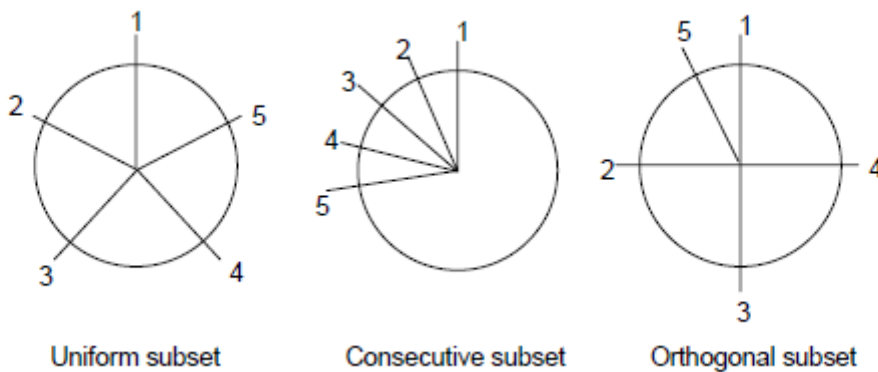


Fig. 2.10 Three possible grouping patterns of subsets in OSEM reconstruction

OSEM accelerates reconstruction by approximately a factor of  $t$  as compared to standard MLEM. Unfortunately, OSEM algorithms generally oscillate rather than converge to a ML solution. However, the convergent of OSEM in emission imaging may not be a practical problem <sup>[95]</sup> since a moderate number of iterations usually does not approach to the limit cycle yet and always gives convergent solutions.

### **2.3.4 Maximum *a posteriori* Expectation Maximization (MAP-EM)**

The reconstructed images obtained using MLEM or OSEM algorithm tend to become noisy as the number of iterations increases <sup>[92]</sup>. From the likelihood point of view, noisy reconstructed images yield a larger likelihood and produce projections, which are very close to the measured noisy projections. In order to obtain high-quality images with less noise, a maximum *a posteriori* (MAP) algorithm is used which is shown to have significant advantages over MLEM <sup>[96, 97]</sup>.

MAP estimation can be used in SPECT if some prior information of the activity distribution is known. The prior, based on an assumption of what the true image is, is introduced in the EM algorithm using Bayes' theorem. The *a posteriori* probability distribution of the image is defined as <sup>[92, 96]</sup>:

$$P(\hat{f} | g) = \frac{P(g | \hat{f})P(\hat{f})}{P(g)} \quad (2.58)$$

where  $P(g | \hat{f})$  is the likelihood function,  $P(\hat{f})$  is the prior function from the prior knowledge and  $P(g)$  is the *a priori* probability distribution of the measurements. In [98-101] anatomical information is used in prior density. The anatomical information is obtained from CT images. In that case the prior density  $P(\hat{f})$  is chosen so that the activity distribution is forced to be smooth inside the anatomical regions but gaps are accepted in the boundaries of these regions. Another common choice of the prior

density is the smoothness prior [28, 92, 102, 103]. One of the smoothing prior is the Gibbs prior [98]:

$$P(\hat{f}) = ke^{-\beta V(\hat{f})} \quad (2.59)$$

where  $V(\hat{f})$  is the so-called energy function, which is at minimum when  $\hat{f}$  is smooth, and  $\beta$  is the parameter to adjust the smoothing extent.

Using the prior in Eq.2.59, the log-likelihood is expressed as

$$\begin{aligned} l(\hat{f}) &= \ln P(\hat{f} | g) \\ &= \ln P(g | \hat{f}) + \ln P(\hat{f}) - \ln P(g) \\ &= \sum_{i=1}^M \left( -\sum_{j=1}^N a_{ij} \hat{f}_j + g_i \ln \left( \sum_{j=1}^N a_{ij} \hat{f}_j \right) - \ln(g_i!) \right) - \beta V(\hat{f}) + constant \end{aligned} \quad (2.60)$$

$$\frac{\partial l(\hat{f})}{\partial \hat{f}_j} = -\sum_{i=1}^M a_{ij} + \sum_{i=1}^M \frac{g_i}{\sum_{j=1}^N a_{ij} \hat{f}_j} a_{ij} - \beta \frac{\partial}{\partial \hat{f}_j} V(\hat{f}_j) = 0 \quad (2.61)$$

The final formula may be written as

$$\hat{f}_j^{k+1} = \frac{\hat{f}_j^k}{\sum_{i=1}^M a_{ij} + \beta \frac{\partial}{\partial \hat{f}_j} V(\hat{f}_j^k)} \sum_{i=1}^M \frac{g_i}{\sum_{j=1}^N a_{ij} \hat{f}_j^k} a_{ij} \quad (2.62)$$

This is the MAP-EM algorithm. Clearly the prior density  $P(\hat{f})$  plays the same role in MAP estimation as the side constraint in Tikhonov regularized LS estimation. The use of prior density regularizes the reconstruction problem.

## 2.4 Analytical vs. Iterative

The main advantages of analytical techniques are their fast execution and less computation. However, their mathematical formulation cannot take into account many of the physical features involved in image formation - such as collimator blurring,

distance dependent blurring, scatter, transmission through the collimator - which result in blurring or other artifacts in the image.

On the other hand, iterative techniques can model the physical system rather accurately and all such features can be accounted for. The main disadvantage of iterative techniques is being computationally intensive and mathematical complexity involved in computing the probability system matrix. Also, for large sized images, the memory involved in computation is huge. This requires the use of accelerated GPU based approach or parallel computing.

## **2.5 Algorithms used in this thesis**

As a part of this thesis, a number of algorithms have been explored. For analytical reconstruction, Novikov's Inversion formula for parallel beam geometry (Section 2.1.7; Eq. 2.26) has been implemented. For few of the studies, the modified approach of You et al for fan beam (Section 2.1.11; Eq. 2.36) and cone beam projections (Section 2.1.12; Eq. 2.38) has been used. For algebraic reconstruction, simple ART (Section 2.2.3; Eq. 2.46) and SART (Section 2.2.5; Eq. 2.50) have been used. For statistical reconstruction, MLEM (Section 2.3.2; Eq. 2.58) and OSEM (Section 2.3.3; Eq. 2.59) have been used. Custom-made codes have been developed for implementation of these algorithms.

# **Modelling the Forward Projection**

To solve the inverse problem of SPECT, the system matrix has to be modelled first. Once the system matrix is constructed, that is, the forward projection is modeled, the inverse problem can be solved using methods discussed in Chapter 2.

The modelling of the probability system matrix is one of the most critical steps in iterative reconstructions. The system matrix elements are generated such that it will produce the desired projection data. Although a lot of literature is available on hosts of reconstruction algorithms for solving the inverse problem, very few papers are available that describe the construction of the probability matrix.

This chapter concentrates on modelling the forward projection. The chapter is divided into two sections. The first section describes a novel approach for generation of forward projection for fan and cone beam geometries. This method does not take into account the effect of collimator, scattering or distance. The projection data generated thus corresponds to an ‘ideal’ collimator system where the detector ‘sees’ photons along a straight line path only. This is useful in giving an intuitive feel for testing analytical reconstruction algorithms in fan and cone beam geometries to check whether implementation seems correct or not before applying it to relevant case.

The second section describes the analytical method used in this thesis to obtain the probability system matrix. This is a more rigorous approach which takes into account the effect of collimator and distance (scattering has been neglected). The projection data

generated using this system matrix mimics the experimental parameters more closely as compared to the ideal approach in section one. This system matrix is also used for iterative reconstructions.

The system matrix has been generated for various experimental geometries / configuration. This includes 2D system matrix for parallel beam geometry and fan geometry which are used for 2D or 3D (stacked) reconstruction. Finally, a fully 3D system matrix has been evaluated which takes into account 3D nature of the collimator and closely resembles realistic experimental situation. However, it is quite challenging as the procedure is computationally intensive and results in a huge system matrix (typically, of the order of 10000 X 10000) which needs to be stored, retrieved and inverted.

## **Section I: Generation of Projection Data**

To test a developed reconstruction algorithm for parallel beam, fan beam or cone beam geometry, be it transmission or emission tomography, one needs projection data (*forward projection*). Generally mathematical phantoms are generated in three dimensions and the projection for all rotation angles is calculated. For non-symmetric objects, the process is cumbersome and computation intensive. This chapter describes a simple methodology for generation of projection data for fan beam and cone beam geometry for both transmission and emission tomography by knowing the object's attenuation and/or source spatial distribution details as input. The object detail such as internal geometrical distribution is nowhere involved in the projection data calculation. This simple approach makes use of the pixilated object matrix values in terms of the matrix indices and spatial geometrical coordinates. The projection data of some typical phantoms (generated using this

approach) are used in reconstructions using standard Feldkamp-Davis-Kress (FDK) algorithm<sup>[104]</sup> and Novikov's inversion formula.

3D cone beam tomography is an important tool for non-destructive examinations to look into the density and/or activity distribution inside an object. To perform this type of work one needs to acquire 2D projection data in cone beam geometry and after that reconstruct it with proper algorithm. In this respect, the reconstruction software, being the critical part, must be tested before reconstructing actual experimental data to check its validity and determine its resolvable ability. For this very reason, projection data are obtained by performing simulated experiments using various computational techniques such as geometrical algorithms, Monte Carlo method, etc. In all these cases, the object internal distribution and/or shape are taken into account. For a particular angle, the projection data are calculated by finding the ray integrals along the ray path. For the next rotation angle, the projection data are calculated by first rotating the object matrix to get the new object details for that angle and subsequently computing the ray integral.

### **3.1 Parallel beam geometry**

The projection data generation for parallel beam geometry is quite straightforward. The projections are basically line integrals parallel to each other and perpendicular to the face of the detectors. For zero angle (first observation), the contribution of the pixel to the line integral is simply 1 if the pixel lies on the path or 0 if the pixel does not lie on the path of the ray. For other angles, the object matrix is rotated, the new object matrix is obtained (using bilinear interpolation) and the above process may be repeated.

## **3.2 Fan beam and cone beam geometry**

For fan beam and cone beam geometry, the contribution of a voxel to the ray can take any value in the range  $[0, 1]$  depending upon the length traversed by the ray inside the voxel. Accordingly, our task is to compute the contribution of each voxel to each ray for generating the projection data. Let us see how to achieve this objective.

## **3.3. Voxel Based Approach for Cone Beam Data**

For symmetric objects, like sphere within a sphere or coaxial cylinders, the projection data calculation is quite simple as it exploits the symmetry of the object and/or takes into account the well-defined geometry of the object. However, for objects which do not have any symmetry, the conventional methodology to calculate the projection data of a phantom for cone beam geometry in cases of transmission and emission mode is to calculate the effective contribution which a voxel has on a ray passing from the source through a particular image pixel. This method is tedious and very involved. Before presenting our approach, we have discussed below the conventional method to show the computation and complexity involved.

### **3.3.1 Transmission Tomography Data**

To start on a simple note, let us consider fan-beam geometry. The source is located at  $S(x_c, y_c)$  and the object centred at  $O(0,0)$ . Let  $A$  be an  $n_x \times n_y$  object matrix. For transmission case, we have

$$A(i, j) = \mu_{ij} \quad \text{for } i = 1, 2, \dots, n_x \text{ and } j = 1, 2, \dots, n_y \quad (3.2)$$

where  $\mu_{ij}$  denotes the attenuation value at the pixel  $(i, j)$ .

For a homogeneous object,

$$\mu_{ij} = \mu_0 = \text{constant} \quad \forall i, j \quad (3.3)$$

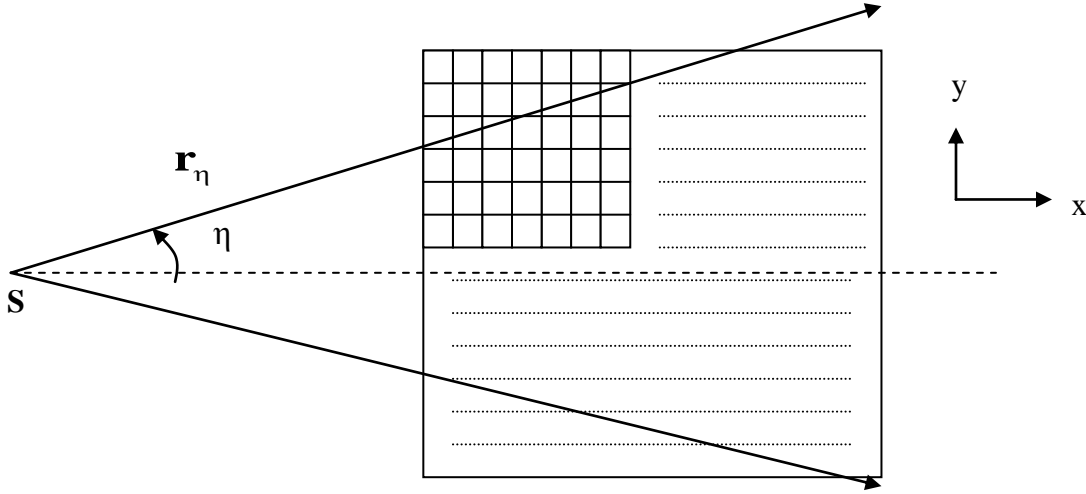


**Fig. 3.1** Fan beam geometry for transmission tomography.  $w_{ij}$ 's are calculated for all the pixels lying on the ray path  $\mathbf{r}_\eta$ .

Let pixel width along X-ray direction (i.e. x-axis) be  $\Delta$ . The ray passing through the object at a fan-angle  $\eta$  is represented by  $\mathbf{r}_\eta$ . This ray passing through the pixel  $(i, j)$  encompasses a fraction  $w_{ij}$  of the pixel length  $\Delta$  (see Fig.3.1 & Fig.3.2). Hence the effective ray path in the pixel is  $w_{ij}\Delta$ .

The ray integral  $g_\eta$  is then calculated by summing the product of  $\mu_{ij}$  and the effective path length  $w_{ij}\Delta$  over all the pixels  $(i, j)$  lying on the ray path.

$$g_\eta = \Delta \sum_{\substack{(i,j) \\ \text{on } \mathbf{r}_\eta}} \mu_{ij} w_{ij} \quad (3.4)$$

For the cone beam geometry, the procedure is similar except that in addition to the fan angle  $\eta$ , the cone angle  $\varphi$  should also be accounted for. Following the same line

of argument as above, the effective ray path in the voxel  $(i, j, k)$  (in this case, voxel is to be considered instead of pixel as was the case in 2D) becomes  $w_{ijk} \Delta$ .

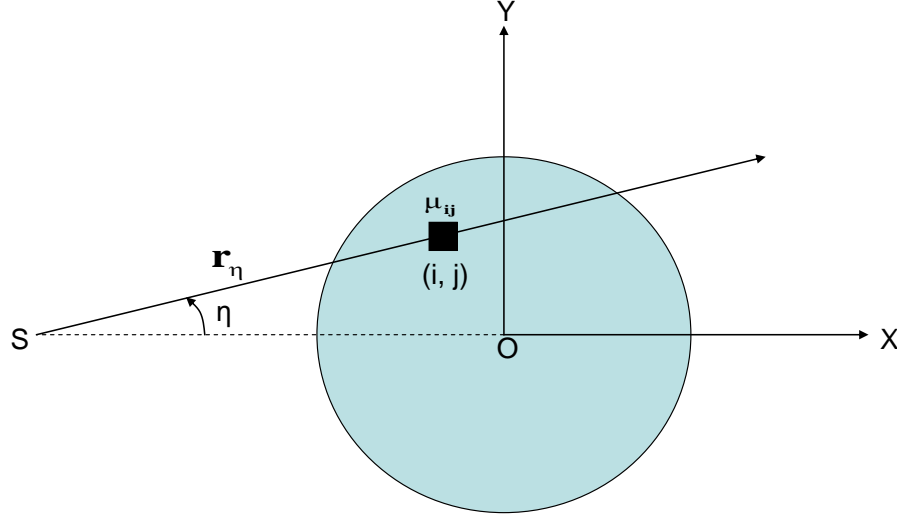


**Fig. 3.2** A ray emanating from the source  $S$  is subsequently attenuated on passing through a pixel  $(i, j)$  lying on the path  $\mathbf{r}_\eta$ .

The ray integral  $g_{\varphi, \eta}$  is now calculated by summing the product of  $\mu_{ijk}$  and the effective path length  $w_{ijk} \Delta$  over all the voxels  $(i, j, k)$  lying on the ray path.

$$g_{\varphi, \eta} = \Delta \sum_{\substack{(i, j, k) \\ \text{on } \mathbf{r}_{\varphi, \eta}}} \mu_{ijk} w_{ijk} \quad (3.5)$$

### 3.3.2 Emission Tomography Data

The projection data generation in the case of emission tomography is much more complex in the sense that the gamma ray emitted from a source point inside the object is attenuated over a part of the object, i.e. starting from the source point somewhere inside the object up to its periphery.

Consider the fan beam data collection geometry. Let  $S(x_c, y_c)$  be the focal point of the fan beam. The object is centred at  $O(0,0)$ . Let  $A$  and  $F$  be  $n_x \times n_y$  object attenuation and source matrices respectively.

$$F(i, j) = f_{ij} \quad \text{for } i=1,2,\dots,n_x \text{ and } j=1,2,\dots,n_y \quad (3.6)$$

and  $A$  is same as defined in 3.2. A photon, emitted from the pixel  $(i_s, j_s)$ , passing through a point  $(i, j)$  on the path  $\mathbf{r}_\eta$  encompasses a fraction  $w_{ij}$  of the pixel length  $\Delta$  (see Fig.3.3 & Fig.3.4).

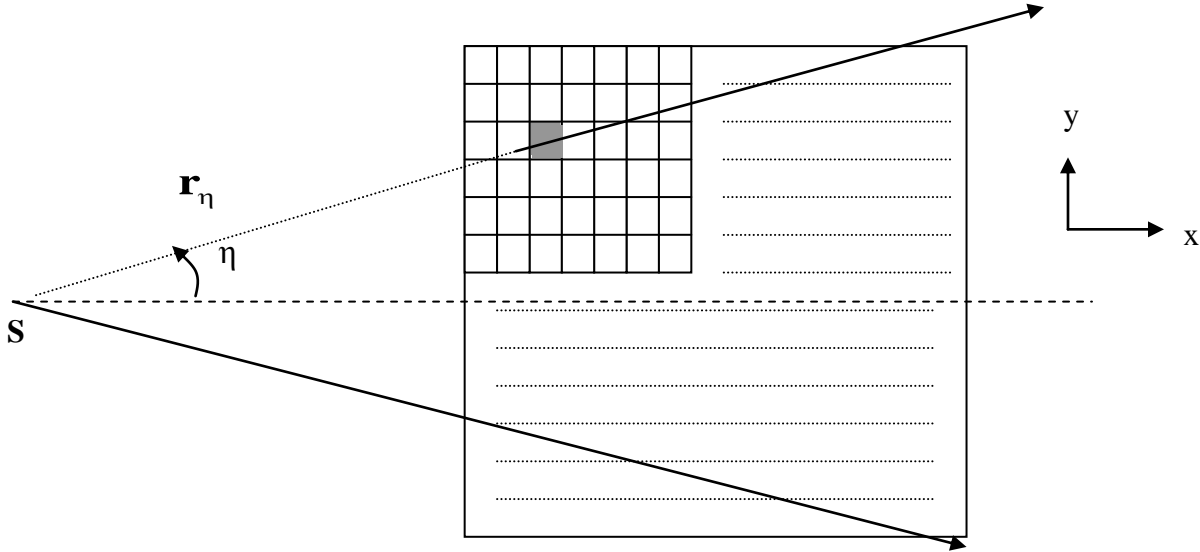


**Fig. 3.3** Fan beam geometry for emission tomography. The shaded pixel represents the source.  $w_{ij}$ 's are calculated for all the pixels lying on the ray path  $\mathbf{r}_\eta$ .

The projection data  $g_\eta$  for this path is the sum of the contributions of all such source points lying on this path. Eq. 3.4 is modified to incorporate the source term as

$$g_\eta = \sum_{\substack{(i_s, j_s) \\ \text{on } \mathbf{r}_\eta}} f_{i_s, j_s} \exp(-\Delta \sum_{\substack{(i, j)=(i_s, j_s) \\ \text{on } \mathbf{r}_\eta}}^{(i, j)=(n_x, n_y)} \mu_{ij} w_{ij}) \quad (3.7)$$

where  $f_{i_s, j_s}$  is the source term at  $(i_s, j_s)$ .

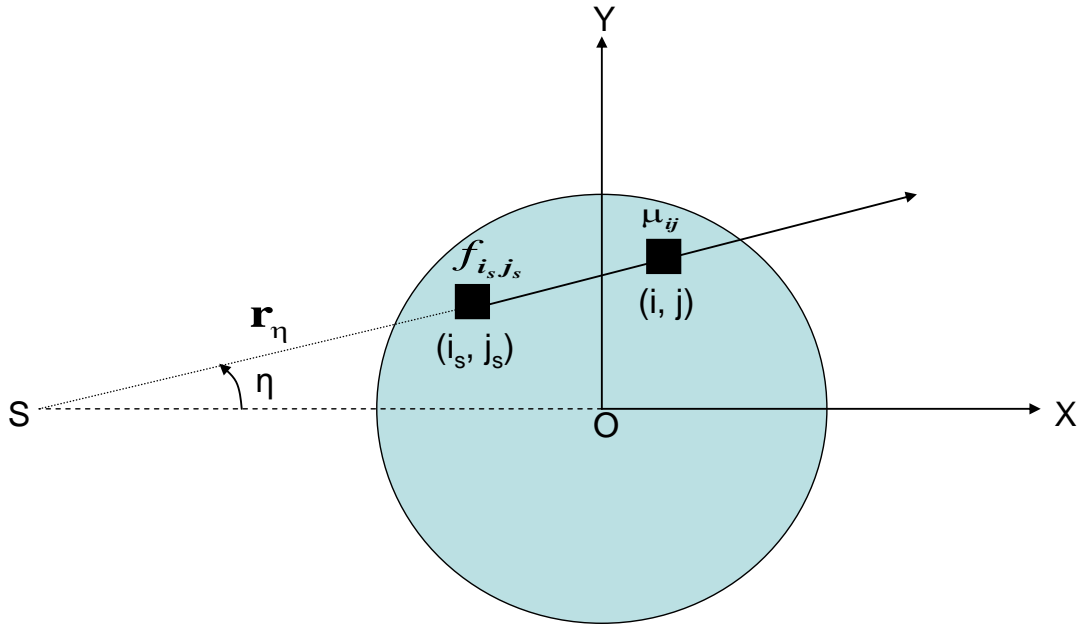


**Fig. 3.4** A ray emanating from a source pixel  $(i_s, j_s)$  is subsequently attenuated on passing through a pixel  $(i, j)$  on the path  $\mathbf{r}_\eta$ . The dotted line traces the ray back to the focal point  $S$

For cone beam data collection geometry, arguing on similar lines, the projection data

$\mathcal{G}_{\varphi, \eta}$  at cone angle  $\varphi$  and fan angle  $\eta$  is obtained by modifying Eq. 3.5 as follows:

$$g_{\varphi, \eta} = \sum_{\substack{(i_s, j_s, k_s) \\ \text{on } \mathbf{r}_{\varphi, \eta}}} f_{i_s, j_s, k_s} \exp\left(-\Delta \sum_{\substack{(i, j, k) = (n_x, n_y, n_z) \\ (i, j, k) = (i_s, j_s, k_s) \\ \text{on } \mathbf{r}_{\varphi, \eta}}} \mu_{ijk} w_{ijk}\right) \quad (3.8)$$

where  $f_{i_s, j_s, k_s}$  is the source term at  $(i_s, j_s, k_s)$

In this method, the crux of the problem is finding  $w_{ij}$  or  $w_{ijk}$  (as the case may be) which is tedious, time consuming and also computation intensive. In this technique, the object matrix is re-evaluated for each projection angle separately.

### 3.4. Novel Approach for Cone Beam Projection Data

In our novel approach, the fraction  $w_{ijk}$  of the pixel contribution to the ray path is not calculated. The method relies on finding the co-ordinates of the pixels lying on the ray path and subsequently rebinning the data to find the path integral.

#### 3.4.1 Transmission Tomography Projection Data Generation

Let  $A$  be an  $n_x \times n_y \times n_z$  object (attenuation) matrix whose elements are the attenuation values  $\mu_{ijk}$ .

$$A(i, j, k) = \mu_{ijk} \quad \text{for } i = 1, 2, \dots, n_x; j = 1, 2, \dots, n_y; k = 1, 2, \dots, n_z \quad (3.9)$$

The origin  $O(0,0,0)$  is taken to be at the centre of the object. The source is at the focal point  $S(x_c, y_c, z_c) \equiv S(-D, 0, 0)$  (see Fig.3.5) where  $D$  is the distance of the source from the centre of the object. Each voxel of size  $\Delta$  is represented by its index  $(i, j, k)$ , co-ordinates  $(x, y, z)$  and its  $\mu$ -value  $\mu_{ijk}$ . We break the cone beam into  $N_\varphi$  fans with cone angles  $\varphi$  (measured from the central plane  $z = 0$ ) varying from  $-\varphi_{\max}$  to  $+\varphi_{\max}$  and for each cone angle  $\varphi$  we break the fan into  $N_\eta$  rays with fan angles  $\eta$  varying from  $-\eta_{\max}$  to  $+\eta_{\max}$ . Considering object dimension of  $(-x_{\max} : x_{\max}, -y_{\max} : y_{\max}, -z_{\max} : z_{\max})$

$$\varphi = \tan^{-1}\left(\frac{z}{D}\right); \quad \varphi_{\max} = \tan^{-1}\left(\frac{z_{\max}}{D}\right) \quad (3.10)$$

$$\eta = \tan^{-1}\left(\frac{y}{D}\right); \quad \eta_{\max} = \tan^{-1}\left(\frac{y_{\max}}{D}\right) \quad (3.11)$$

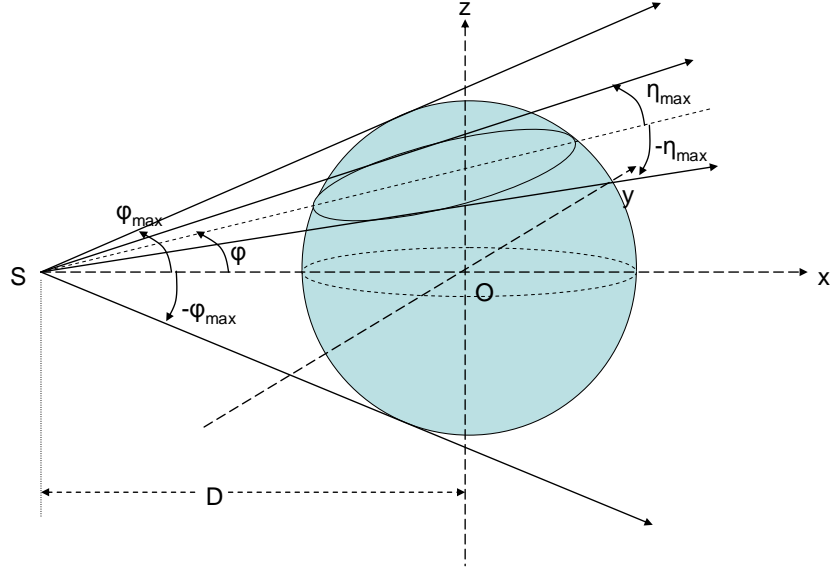


**Fig. 3.5** Cone beam geometry for projection data generation

The ray passing through the object at cone angle  $\varphi$  and fan angle  $\eta$  is represented by  $\mathbf{r}_{\varphi,\eta}$ .

The projection data for the central ray  $\mathbf{r}_{0,0}$  is given by

$$g_{0,0} = \sum_{i=1}^{n_x} \mu_{ijk} \Delta = \Delta \sum_{i=1}^{n_x} \mu_{ijk} \quad (3.12)$$

For simplicity, let us start by calculating the projection data for the central vertical plane  $y = 0$ . For this plane, fan angle  $\eta = 0$ . Consider the central ray  $\mathbf{r}_{0,0}$ . The points lying on this ray path have co-ordinates given by  $(x, 0, 0)$ . To find out the co-ordinates of the points on the path of the ray  $\mathbf{r}_{\varphi,0}$ , we rotate the frame of reference through angle  $\varphi$  about  $y$ -axis, the centre of rotation being  $S(x_c, y_c, z_c)$ . A point  $(x, y, z)$  in the original frame of reference transforms to the point  $(x', y', z')$  in the new frame of reference, where

$$\begin{aligned} x' &= (x - x_c) \cos \varphi + (z - z_c) \sin \varphi \\ y' &= y - y_c \\ z' &= -(x - x_c) \sin \varphi + (z - z_c) \cos \varphi \end{aligned} \quad (3.13)$$

Two successive points lying on the path  $\mathbf{r}_{0,0}$  separated by distance  $\Delta$  are now separated by distance  $\Delta \cos \varphi$  on the new path  $\mathbf{r}_{\varphi,0}$

Now, for the points on the ray path  $\mathbf{r}_{\varphi,\eta}$ , we rotate the frame of reference through angle  $\eta$  about z-axis, the centre of rotation being  $S(x_c, y_c, z_c)$ . A point  $(x', y', z')$  in the new frame of reference upon rotation through  $\eta$  about z-axis transforms to the point  $(x'', y'', z'')$ , where

$$\begin{aligned} x'' &= x_c + (x' \cos \eta + y' \sin \eta) \\ y'' &= y_c + (-x' \sin \eta + y' \cos \eta) \\ z'' &= z_c + z' \end{aligned} \quad (3.14)$$

Two successive points lying on the path  $\mathbf{r}_{\varphi,0}$  separated by distance  $\Delta \cos \varphi$  are now separated by distance  $\Delta \cos \varphi \cos \eta$  on the new path  $\mathbf{r}_{\varphi,\eta}$ .

In the original frame of reference, each voxel  $\Delta x \Delta y \Delta z$  located at  $(x, y, z)$  corresponds to an index  $(i, j, k)$ . Now, in the rotated frame the point  $(x'', y'', z'')$  corresponds to some index  $(i'', j'', k'')$  in the original frame of reference (see Fig.3.6). The indices  $i'', j'', k''$  may no longer be integers so they are rounded off to the nearest integer under the restriction

$$1 \leq i'' \leq n_x; 1 \leq j'' \leq n_y; 1 \leq k'' \leq n_z \quad (3.15)$$

The index  $(i'', j'', k'')$  will give us the  $\mu$ -value at that point which is  $\mu_{i'' j'' k''}$ . The projection data  $g_{\varphi,\eta}$  for the ray  $\mathbf{r}_{\varphi,\eta}$  will be the ray integral over all such voxels  $(i'', j'', k'')$  on this path.

$$g_{\varphi,\eta} = \Delta \cos \varphi \cos \eta \sum_{\substack{(i'', j'', k'') \\ \text{on } \mathbf{r}_{\varphi,\eta}}} \mu_{i'' j'' k''} \quad (3.16)$$

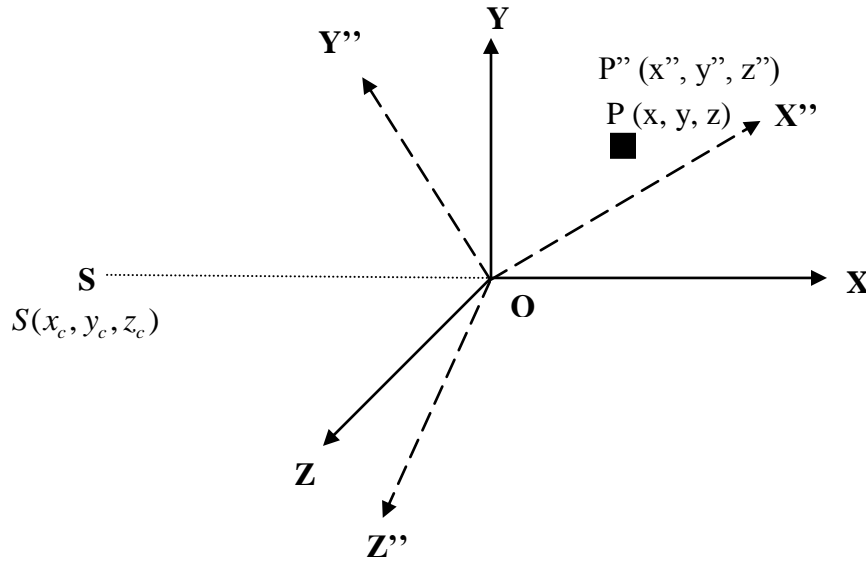


Fig. 3.6 Transformation of a point  $P$  to  $P''$  under two subsequent rotations

For the projection data set at different rotation angles  $\theta$ , where  $0 \leq \theta \leq 2\pi$ , the attenuation matrix  $A$  is first rotated through angle  $\theta$  and the new attenuation matrix obtained using bilinear interpolation. Then the above steps are performed on this rotated matrix to obtain the projection data set at angle  $\theta$ .

### 3.4.2 Emission Tomography Projection Data Generation

Let  $A$  and  $F$  be  $n_x \times n_y \times n_z$  object (attenuation) and source matrices where

$$F(i, j, k) = f_{ijk} \quad \text{for } i = 1, 2, \dots, n_x; j = 1, 2, \dots, n_y; k = 1, 2, \dots, n_z \quad (3.17)$$

and  $A$  is as defined in section 3.1. Each voxel at  $(x, y, z)$  linked to matrix index  $(i, j, k)$  has a corresponding  $\mu$ -value  $\mu_{ijk}$  and a source count  $f_{ijk}$ .

The ray path through the object at cone angle  $\varphi$  and fan angle  $\eta$  is represented by  $\mathbf{r}_{\varphi, \eta}$ . The projection data for the central ray  $\mathbf{r}_{0,0}$  is given by

$$g_{0,0} = \sum_{i_s=1}^{n_x} f_{i_s, j_s, k_s} \exp(-\Delta \sum_{i=1}^{n_x} \mu_{ijk}) \quad (3.18)$$

where  $f_{i_s, j_s, k_s}$  's are the gamma emitting source points lying on the path  $\mathbf{r}_{0,0}$ . It may be noted here that the attenuation is only summed from the emitting pixel (voxel) to the detector.

Using similar arguments as in Section 3.1, point  $(x, y, z)$  transforms to  $(x'', y'', z'')$  after rotations through angle  $\phi$  about y-axis and angle  $\eta$  about z-axis (see Eq.3.13 & Eq.3.14). Once the new index  $(i'', j'', k'')$  is known, we obtain the attenuation value  $\mu_{i'' j'' k''}$  and the source value  $f_{i'' j'' k''}$  at that point. The projection data  $g_{\phi, \eta}$  for the path  $\mathbf{r}_{\phi, \eta}$  is then given by

$$g_{\phi, \eta} = \sum_{\substack{(i'', j'', k'') \\ \text{on } \mathbf{r}_{\phi, \eta}}} f_{i'' j'' k''} \exp(-\Delta \cos \phi \cos \eta \sum_{\substack{(i, j, k)=(n_x, n_y, n_z) \\ (i, j, k)=(i'', j'', k'') \\ \text{on } \mathbf{r}_{\phi, \eta}}} \mu_{i'' j'' k''}) \quad (3.19)$$

Again, the summation is over pixels (voxels) lying on the ray path  $\mathbf{r}_{\phi, \eta}$  and starting from emitting pixel (voxel).

For the projection data set at different rotation angles  $\theta$ , where  $0 \leq \theta \leq 2\pi$ , the attenuation matrix  $A$  is first rotated through angle  $\theta$  and the new attenuation matrix and source matrix obtained using bilinear interpolation. Then the above steps are performed on the rotated matrices to obtain the projection data set at angle  $\theta$ .

### 3.5. Testing the projection data

To test the method of generation of projection data, we reconstruct transmission and emission projection data and compare with the original phantom. In this section, we

discuss some phantoms, their sinogram and reconstructed images. The evaluation presented here tests the simulation scheme for some basic implemented geometry. The projection data have been generated using our technique and the projection data thus generated have been reconstructed using standard algorithms.

### **3.5.1 Reconstruction of Transmission projection Data using FDK algorithm**

Phantom 1 consists of a solid Al cylinder ( $\mu = 0.037\text{mm}^{-1}$ ) of radius 10 mm and height 40mm. It contains a Cu sphere ( $\mu = 0.198 \text{ mm}^{-1}$ ) of radius 2 mm centred at (-3.2, 0, -4.2) and an SS rod ( $\mu = 0.154 \text{ mm}^{-1}$ ) of base radius 2 mm centred at (0, 2.8). This rod is broken (from  $z = -4.2$  to  $z = -12$ ). The linear attenuation coefficient values are at 150 keV energy.

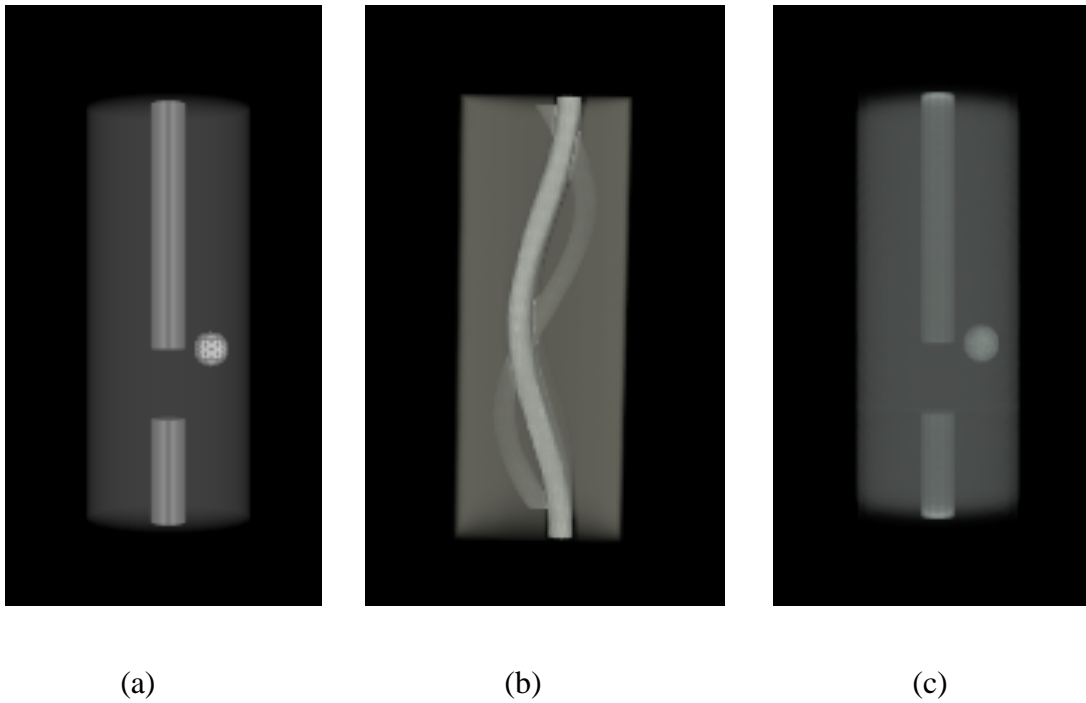


**Fig. 3.7** Phantom 1 (a) original object (b) sinogram (c) reconstructed object

For numerical simulation purpose, Phantom 1 is discretized on a regular grid of 101 X 101 X 241 units. The projections are generated for 300 views/rotations with angular step of 1.2°. The focal distance is taken as 100 mm. The reconstruction is done using FDK algorithm<sup>[104]</sup>.

The reconstructed  $\mu$ -values are found to be in the ratio 1: 0.178: 0.775 (Cu: Al: SS). This is in good agreement with the actual  $\mu$ -value ratio 1: 0.187: 0.777 (Cu: Al: SS).

### 3.5.2 Reconstruction of Emission projection Data using Novikov's inversion formula

Phantom 2 represents a drum of diameter 55 cm and height 87 cm with 2 mm thick lead-lining ( $\mu = 2.4588\text{cm}^{-1}$ ). It (Fig.3.8) consists of a low activity radioactive isotope  $^{239}\text{Pu}$  ( $\mu = 5.6311\text{cm}^{-1}$ ) in the form of small spheres at 15 different locations (refer Table 3.1) in a surrounding matrix ( $\mu = 0.12\text{cm}^{-1}$ ). The attenuation values are at 414 keV.

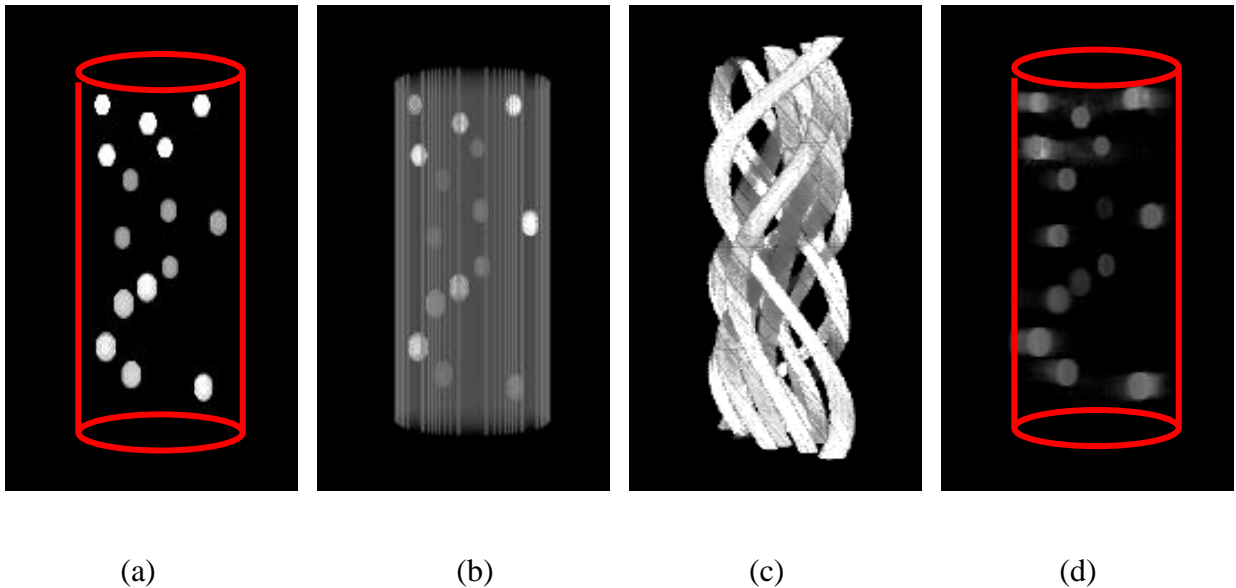


**Fig. 3.8** Phantom 2 (a) Activity (b) Attenuation map (c) sinogram (d) reconstructed activity  
(Note: The boundary of the drum is shown only for illustration purpose)

For numerical simulation purpose, Phantom 2 is discretized on a regular grid of 121 X 121 X 241 units. The projections are generated for 300 views/rotations with angular step of 1.2°. The reconstruction is done using cone-beam SPECT reconstruction algorithm. The focal distance is taken as 100 cm.

**TABLE 3.1** Activity table for drum D-2 (*Note: Central plane is the  $z = 0$  plane*)

<b>Source shape/geometry</b>	<b>Source position/centre (x, y, z) in cm</b>	<b>Source dimension</b>	<b>Activity (emissions/s)</b>
Sphere	(15.6, -15.6, -37.5)	Radius 3.5 cm	$2 \times 10^4$
Sphere	(-11.4, -12.0, -33.7)	Radius 3.5 cm	$2 \times 10^4$
Sphere	(-19.8, 4.2, -25.0)	Radius 3.5 cm	$2 \times 10^4$
Sphere	(-13.8, -1.8, -14.1)	Radius 3.5 cm	$2 \times 10^4$
Sphere	(-5.4, 2.4, -9.8)	Radius 3.5 cm	$2 \times 10^4$
Sphere	(3.0, -15.0, -4.9)	Radius 3.0 cm	$1 \times 10^4$
Sphere	(-15.0, -18.0, 3.3)	Radius 3.0 cm	$1 \times 10^4$
Sphere	(19.2, 12.6, 6.5)	Radius 3.0 cm	$1 \times 10^4$
Sphere	(2.4, -9.0, 10.3)	Radius 3.0 cm	$1 \times 10^4$
Sphere	(-19.8, -19.2, 19.0)	Radius 3.0 cm	$1 \times 10^4$
Sphere	(-18.6, 18.0, 22.8)	Radius 2.5 cm	$3 \times 10^4$
Sphere	(1.2, -11.4, 27.2)	Radius 2.5 cm	$3 \times 10^4$
Sphere	(-4.8, 14.4, 31.0)	Radius 2.5 cm	$3 \times 10^4$
Sphere	(13.2, 19.8, 34.8)	Radius 2.5 cm	$3 \times 10^4$
Sphere	(-21.6, -5.4, 38.1)	Radius 2.5 cm	$3 \times 10^4$

### 3.6 Computation Time

All the calculations were done on a standard PC with 2.4 GHz Pentium 4 processor and 1 GB RAM. For transmission, the CPU time for projection data calculation for a 121x121x241 grid was 4.33 sec per projection. For emission, the CPU time for projection data calculation for a 101x101x241 grid was 4.77 sec per projection.

### 3.7 Image comparison: correlation coefficient

The correlation between the original image  $g(i, j)$  and the reconstructed image  $\hat{g}(i, j)$  provides a classical criterion <sup>[105]</sup> for comparing two images. The correlation coefficient is given by:

$$\text{Correlation}(\rho) = \frac{\sum_{i=1}^N \sum_{j=1}^N g(i, j) \hat{g}(i, j)}{\sqrt{\sum_{i=1}^N \sum_{j=1}^N g(i, j)^2 \sum_{i=1}^N \sum_{j=1}^N \hat{g}(i, j)^2}} \quad (3.20)$$

The correlation is equal to 1 if the images are identical, and less if some differences exist.

#### 3.7.1 Projection data comparison

The main source of error in the projection data using our algorithm can be attributed to the bilinear interpolation and subsequent modification of the matrix values for each ray path. Note that during rebinning the indices  $(i', j'', k''')$  are rounded off to the nearest integer values. This means that the ray path through each voxel is ‘approximated’ to be same, though in reality they differ. This error can be reduced by finer gridding of the data matrix at the cost of computational time.

To compare the quality of the projection data (for transmission case) with the ideal data, we chose a simple object - off-centred sphere within a sphere (Phantom 3 – size: 121 X 121 X 121). The ideal data was calculated geometrically by finding out the chord lengths of the X-ray passing through the object and incorporating attenuation values along its path. Fig.3.9 shows the plot of correlation coefficient (between the projection data as calculated geometrically and the projection data calculated using our algorithm) as a function of the rotation angle. The plot shows dips at rotation angles 90°, 180°, 270° and 360°. This is because the error due to bilinear interpolation will be maximum at rotation angles of 90°, 180° and 270°.

The correlation coefficient between the two images is more than 0.99 which shows that the projection data computed by our algorithm is almost identical to the projection data computed geometrically.

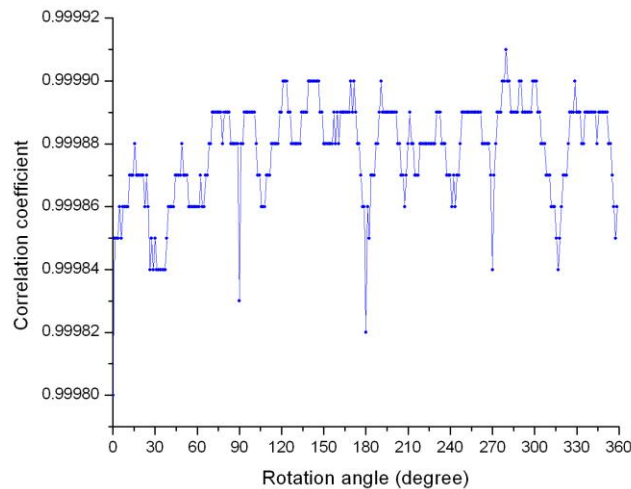


**Fig. 3.9** Plot of correlation coefficient between the projection data (for Phantom 3) computed geometrically and the projection data calculated using the algorithm) as a function of the rotation angle

### 3.7.2 Reconstructed image comparison

The correlation between the reconstructed image and the original phantom has been calculated for testing the quality of the reconstructed image. Fig.3.10 (a) shows the original phantom and Figs.3.10 (b) & 3.10 (c) show the reconstructed images for the projection data computed using the algorithm and the projection data computed geometrically respectively as stated in section 3.5 for Phantom 3. The correlation coefficient between the reconstructed images (Figs. 3.10 (b) & 3.10 (c)) and the original phantom (Fig. 3.10 (a)) for Phantom 3 is plotted as a function of Z-slice no. is shown in Fig.3.10 (d).

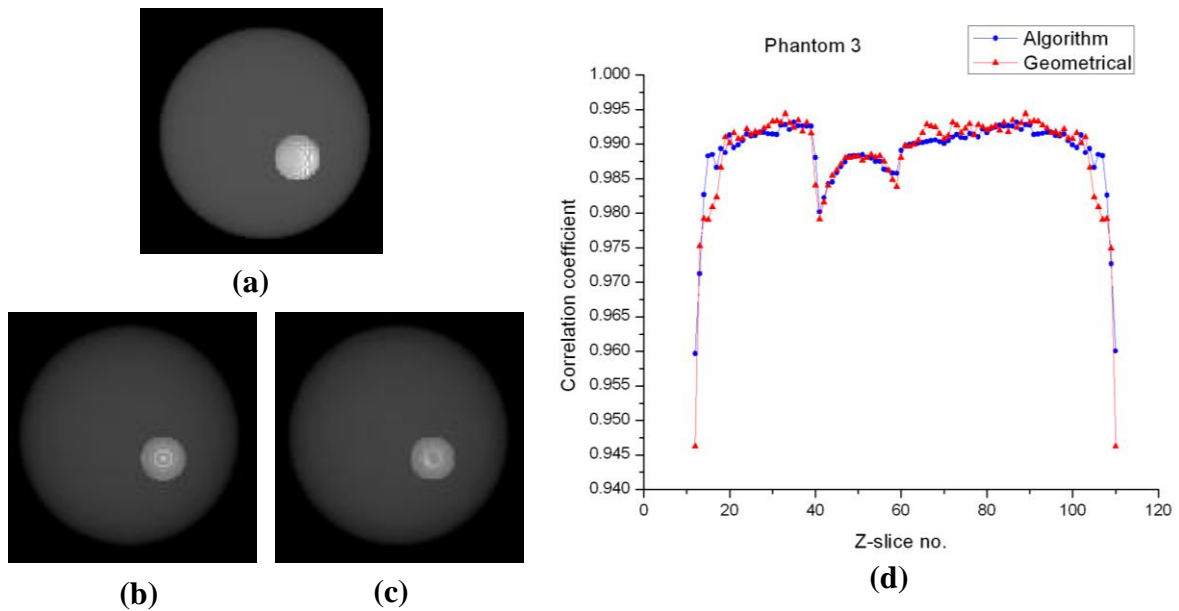


**Fig. 3.10** (a) Phantom 3 (b), (c) Reconstructed images using projection data calculated using the algorithm and the projection data computed geometrically respectively (d) Plot of correlation coefficient as a function of Z-slice no.

The fluctuations in correlation coefficient in Fig.3.10 (d) at Z-slice no. 49 and Z-slice no. 61 correspond to the edges of the smaller sphere. The comparatively lower

correlation coefficient can be accounted to the error introduced in the reconstruction process as they produce high frequency component.

Fig.3.11 shows the plot of correlation coefficient for the Phantom 1 in section 3.5.1. The fluctuations in correlation coefficient around Z-slices 61 and 100 correspond to the broken edges of the stainless steel rod and can be explained as before. This is evident in the sharp fall of correlation coefficient at Z-slice 61. The high frequency component near Z-slice 100 is modified due to the presence of the copper ball and hence the fluctuations in correlation coefficient are less as compared to that at Z-slice 61.

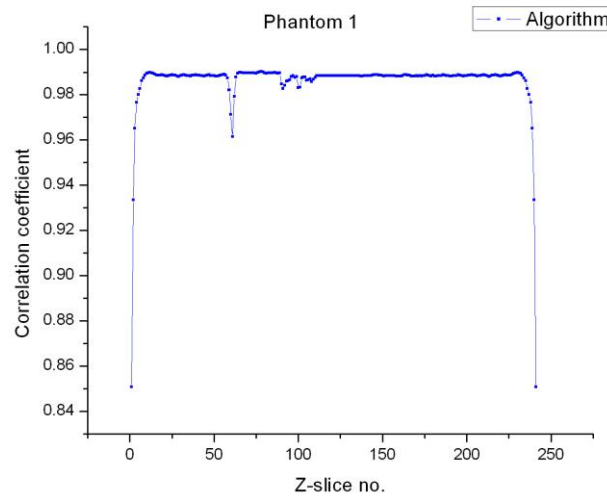


**Fig. 3.11** Plot of correlation coefficient as a function of Z-slice no. for Phantom 1

The correlation coefficient between the reconstructed image and the original phantom is more than 0.97 and 0.98 respectively for Phantom 3 and Phantom 1 for most of the slices. This shows a good correspondence between the original object and the reconstructed volume.

## Section II: Generation of Probability System Matrix

For algebraic and statistical reconstruction techniques (discussed in Chapter 2), the observation model is represented by the set of linear equations given by 3.1

$$g = Af$$

where  $A$  is the probability system matrix. The unknown vector  $f$  can be directly computed by inverting the matrix  $A$ . However, the sparse matrix  $A$  is often ill-posed or singular and cannot be directly inverted. Also the size of the matrix is huge. For example, consider a 64 x 64 object grid with 100 projections and 64 lateral data points in one image dimension. The size of the matrix  $A$  will be 6400 x 4096 which is huge. For such a large matrix, the conventional mathematical models for inversion require huge computational cost. For this reason, Eq.3.1 is solved iteratively.

The accuracy of the techniques used in predicting  $f$  depends on how well the system matrix is modeled. In fact, generation of the probability system matrix is the most important factor in iterative reconstruction techniques.

The system matrix can be estimated from the measurement of spatially variant point spread functions of physical point sources <sup>[106]</sup>, by approximate analytical calculations <sup>[107-116]</sup>, or generated by Monte Carlo simulations <sup>[117]</sup>. We will focus on analytical calculation of the system geometry elements.

### 3.8 The Probability System Matrix

The probability system matrix  $A$  has two components - system geometry factor and system attenuation factor. The system geometry factor is one of the most important

components of the probability system matrix. It is the probability that radioactive decay in the  $j^{th}$  voxel is recorded by the  $i^{th}$  detector unit solely due to the geometrical considerations. The system attenuation factor gives the attenuation suffered by the photons in the object before reaching the detector.

The system matrix can account for various physical effects: attenuation, sensitivity, scatter, collimation, transmission through collimator walls, etc. More the factors modeled, closer will be the resemblance to true experimental conditions. We shall call the elements  $A(i, j)$  of the system matrix as system matrix elements.

### 3.8.1 Structure of system matrix

In order to solve the system of linear equations and find out the activity distribution, only the non-zero elements of  $A$  are used. Let us get an estimate for the number of non-zero matrix elements. If  $n$  is the number of grid elements in one dimension (for the sake of simplicity, let us consider  $n_x = n_y = n_z = n$  and  $n_\theta \cong n, n_l \cong n$ ), the number of matrix elements is  $o(n^4)$  ( $\dim(A) \sim n_x n_y \times n_l n_\theta$ ) for 2D system matrix. Here  $o(\cdot)$  means of the order of the bracketed term. However, the number of non-zero elements is  $o(n^3)$  as on an average only  $o(n)$  grid elements are intersected by the rays from each projection bin (as shown in Fig.3.12). Similarly, for 3D reconstruction, the total number of elements is  $o(n^6)$  ( $\dim(A) \sim n_x n_y n_z \times n_l n_z n_\theta$ ) whereas the number of non zero elements is  $o(n^4)$ . We may thus infer that the matrix becomes much sparse in three dimension in the sense that the number of non zero elements is about two order less than the total number of elements.

The computation time as well as the complexity of iterative methods depends on the number of non-zero elements which increases as the number of grid elements  $n$  increases. The simplest way to increase the sparseness of  $A$  is to increase the collimation so that each collimator now sees a smaller portion of the grid. However, the projection image suffers from a relatively larger statistical variation since the image is now formed from lesser number of photons.

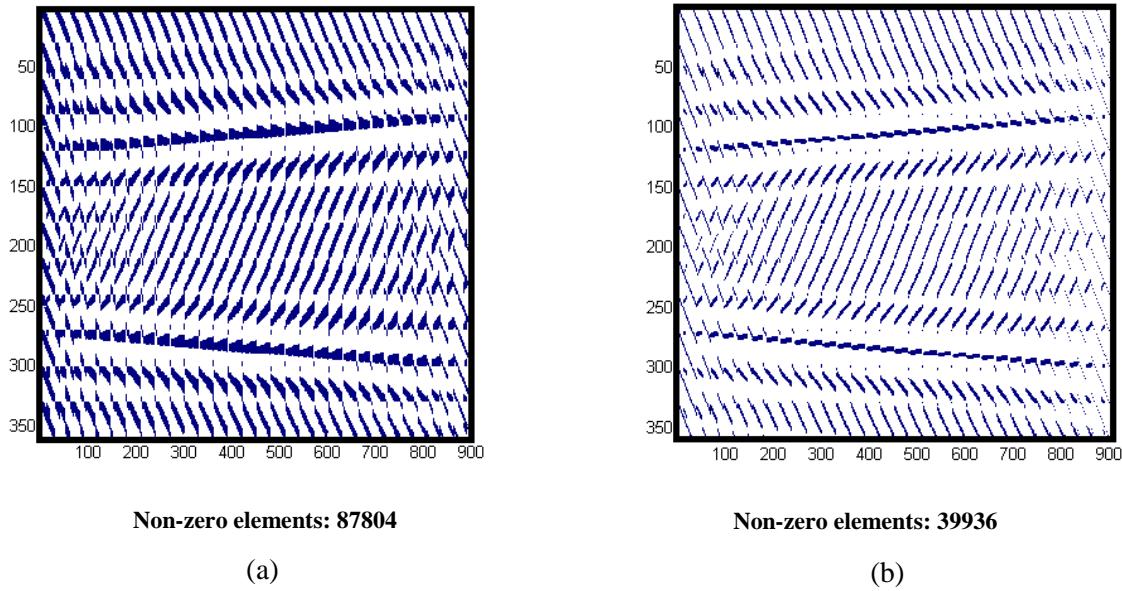


*Fig. 3.12 2D System Matrix for different collimation ratio (a) 5 (b) 20. The rows (y-axis) correspond to measurement/data points whereas the columns (x-axis) correspond to object pixels. The total number of elements in each case is  $3.24 \times 10^5$ . The non-zero elements are marked in blue whereas the zero elements are marked in white.*

### 3.9 2D Reconstruction: Parallel Beam System Model

To a first approximation, each element  $A(i, j)$  can be expressed as:

$$A(i, j) = \frac{Area}{4\pi R_{ij}^2} \exp\left(-\sum_k \mu_k d_{ijk}\right) \quad (3.21)$$

$Area$  is the exposed area of the  $j^{th}$  detector as seen by the  $i^{th}$  pixel

$R_{ij}$  is the distance between the  $i^{th}$  pixel and  $j^{th}$  detector

$\mu_k$  is the attenuation coefficient of the  $k^{th}$  pixel (material) lying on the ray path joining the  $i^{th}$  pixel and  $j^{th}$  detector

$d_{ijk}$  is the path length in  $k^{th}$  pixel traversed by the gamma ray emitted from the  $i^{th}$  pixel and reaching the  $j^{th}$  detector

Eq.3.21 can be split into two components as

$$A(i, j) = A_{geom}(i, j) \cdot A_{att}(i, j) \quad (3.22)$$

where  $A_{geom}(i, j) = \frac{Area}{4\pi R_{ij}^2}$  is the geometrical factor,

and  $A_{att}(i, j) = \exp(-\sum_k \mu_k d_{ijk})$  is the attenuation factor

In terms of matrix notation, we can write

$$A = A_{geom} \odot A_{att} \quad (3.23)$$

where  $\odot$  stands for element-to-element multiplication.

For most analytical calculations, an implicit assumption is that radionuclei are distributed homogenously inside the pixel. For an ideal collimator (line integral model), the ray is assumed to be a “thick” line whose width is equal to the width of the projection bin (or detector). The pixels lying on this path (marked in dark grey in Fig.3.13) contribute to the detector while the pixels lying outside this region do not. However, in practice, the collimator is not ideal and all the pixels lying in the cone of acceptance (marked in light grey and bounded by two bold lines in Fig.3.13) contribute to the intensity in the detector.

To calculate the terms  $d_{ijk}$ , that is, the path length in  $k^{\text{th}}$  pixel traversed by the gamma ray emitted from the  $i^{\text{th}}$  pixel and reaching the  $j^{\text{th}}$  detector, a similar approach is used. For the ideal collimator case,  $d_{ijk}$  is given by the length of intersection of the ray joining  $i^{\text{th}}$  pixel and  $j^{\text{th}}$  detector with the  $k^{\text{th}}$  pixel. Since the ray is always parallel to the detector, a simple way of evaluating this term is to use the approach used in Section I – rotation of the object matrix by angle  $\theta$  followed by bilinear interpolation to find the object matrix in the rotated frame of reference. In this frame of reference, all the  $k$  pixels are parallel to the ray and the  $d_{ijk}$  terms are simply the width (equal) of the pixel in the rotated frame of reference. For the collimator modeled observation, however, the length of intersection of the ray with the voxel is to be evaluated for all the object pixels in the cone of acceptance.

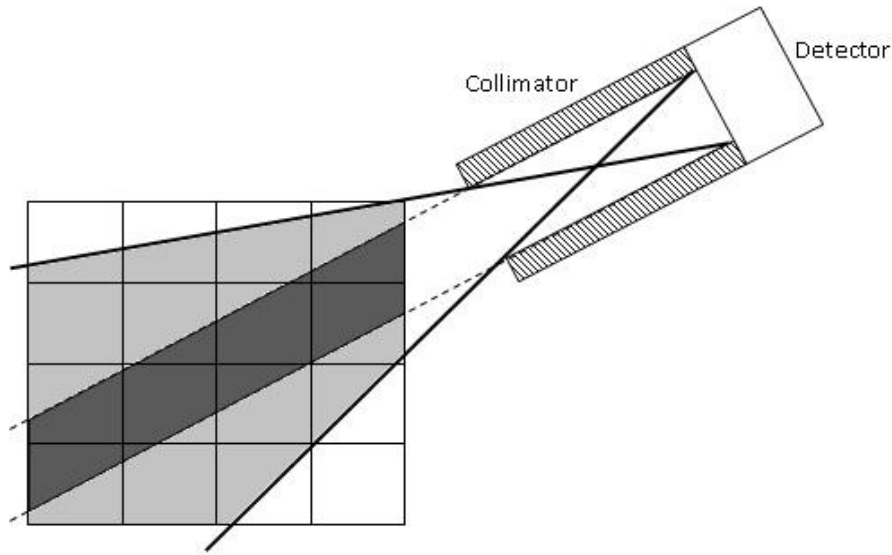


**Fig. 3.13** Pixels contributing to the probability system matrix in the case of ideal collimator (dark grey) and non-ideal collimator (light grey)

The system matrix in Eq.3.23 can be represented in block matrix notation as

$$A = \begin{pmatrix} A_1 \\ A_2 \\ A_3 \\ \cdot \\ \cdot \\ \cdot \\ A_{n_\theta} \end{pmatrix} \quad (3.24)$$

where  $A_1$  is the block matrix for first projection,  $A_2$  is the block matrix for second projection, and so on.  $n_\theta$  is the number of angular projections.

We shall now compute the block matrix for the first projection, that is  $\theta = 0$ , or the zero-angle projection.

### 3.9.1 Geometrical factor

The first term of Eq.3.21 is the geometrical factor which accounts for the solid angle subtended by detector at the pixel. Let us calculate the geometrical factor for the 0<sup>th</sup> angle projection.

The object pixel and the detector are in the same plane. By simple geometrical consideration, the area of the  $j^{\text{th}}$  detector as seen by  $i^{\text{th}}$  pixel is given (from Fig.3.14) as the difference of the projected width of  $w_c$  under angle  $\beta$  and the part of the projected width shadowed by the collimator.

$$Area = (w_c \cos \beta - l_c \sin \beta) h_c \quad (3.25)$$

$w_c$  is the collimator width

$l_c$  is the collimator length

$h_c$  is the collimator height

$\beta$  is the angle subtended by the  $i^{\text{th}}$  pixel at the  $j^{\text{th}}$  detector

From Fig.3.13, we can write  $\cos \beta = \frac{dx}{R_{ij}}$  and  $\sin \beta = \frac{dy}{R_{ij}}$

The calculation of *Area* depends on the shape of the holes in the collimator. For square hole collimator,  $h_c = w_c$ . If collimator is further divided into  $n$  holes per dimension (for multi-hole collimator), the area corresponding to each sub-detector is (neglecting the width of the septa separating the holes)

$$Area = \left( \frac{w_c}{n} \cos \beta - l_c \sin \beta \right) \frac{w_c}{n} \quad (3.26)$$

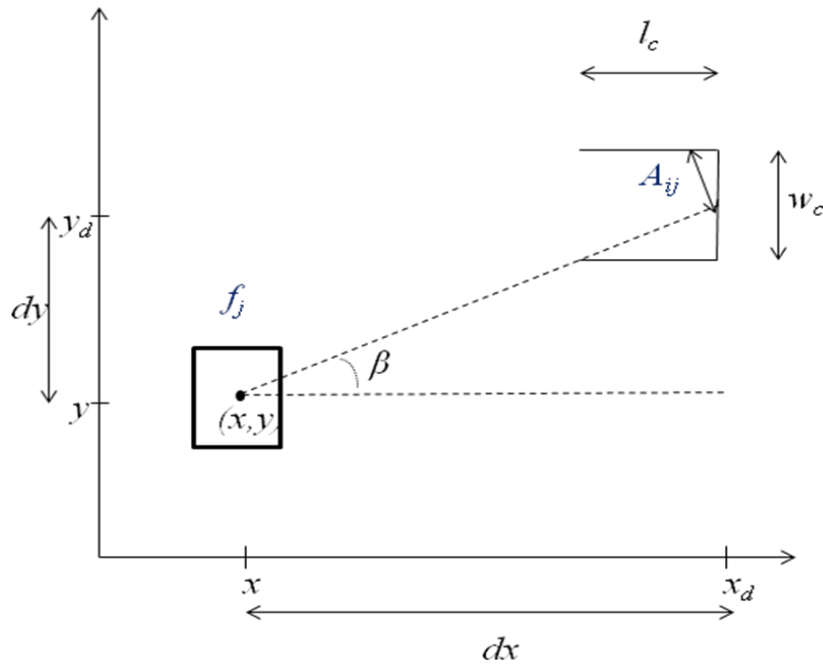


Fig. 3.14 Area of the  $j^{\text{th}}$  detector as seen by  $i^{\text{th}}$  pixel

Since the total number of holes per collimator is  $n^2$ , the total area subtended by the detector will be

$$Area = n^2 \left( \frac{w_c}{n} \cos \beta - l_c \sin \beta \right) \frac{w_c}{n} \quad (3.27)$$

$$Area = (w_c \cos \beta - n l_c \sin \beta) w_c$$

and

$$A_{0,geom}(i, j) = \frac{1}{4\pi R_{ij}^2} (w_c \cos \beta - n l_c \sin \beta) w_c \quad (3.28)$$

where the subscript '0' denotes the 0<sup>th</sup> angle projection.

For  $n=1$ , the width of the hole is equal to the width of the projection bin. Obviously, in the case that  $Area(i, j)$  is less than zero, the pixel does not contribute to projection bin and we have to set  $Area(i, j) = 0$

### 3.9.2 Attenuation factor

The second term in Eq.3.21 is the attenuation factor which accounts for the net attenuation suffered by the gamma photon emitted from the  $i^{th}$  pixel and reaching the  $j^{th}$  detector. For an ideal collimator (infinite collimation), only the pixels lying on the line joining  $i^{th}$  pixel and  $j^{th}$  detector contribute to the attenuation factor. However, for all practical purpose, the collimation is finite and other pixels also contribute to the attenuation factor (see Fig.3.13)

As stated in Eq.3.21, the attenuation factor  $A_{att}(i, j)$  is given by

$$A_{att}(i, j) = \exp\left(-\sum_k \mu_k d_{ijk}\right) \quad (3.29)$$

where  $i = 1, 2, \dots, N_x \cdot N_y$  and  $j = 1, 2, \dots, N_y$ . The summation is done over all  $k$  pixels lying on the ray path joining  $i^{th}$  pixel and  $j^{th}$  detector. This is repeated for all  $i$  and  $j$

We shall briefly discuss the calculation of the factor  $d_{ijk}$ . We consider the ray path as the line joining the centre of  $i^{\text{th}}$  pixel, say  $(x_p, y_p)$  with centre of  $j^{\text{th}}$  detector, say  $(x_d, y_d)$ . Now, the factor  $d_{ijk}$  has to be computed for all  $k$  pixels lying on this ray path. This has been illustrated in Fig 3.15. The ray starting from a source pixel (in red) and reaching a detector bin passes through a number of pixels (in yellow) lying on the path. Now, the intersection length of the ray with the  $k^{\text{th}}$  pixel boundary gives  $d_{ijk}$ .

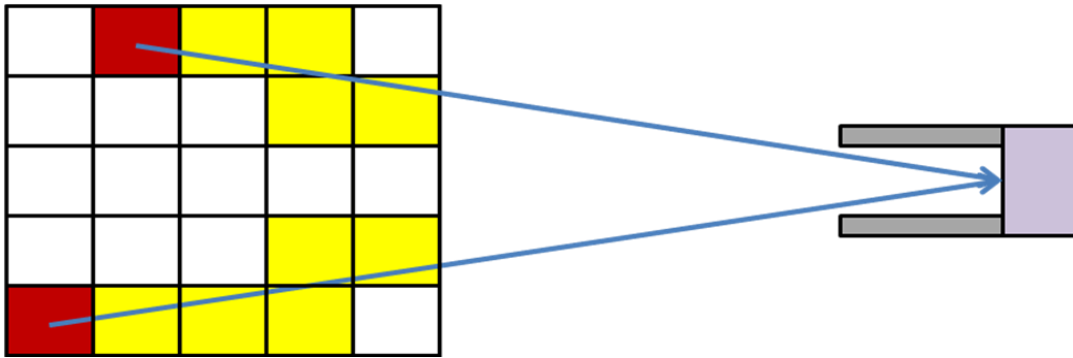


**Fig. 3.15** A ray starting from a (red) pixel passes through (yellow) pixels on its way to the detector bin

Let  $y(x)=0$  denote the line joining  $i^{\text{th}}$  pixel and  $j^{\text{th}}$  detector. Also, let  $x = x_l$ ,  $x = x_{l+1}$ ,  $y = y_m$  and  $y = y_{m+1}$  denote the left, right, bottom and top boundaries of  $k^{\text{th}}$  pixel respectively. The line  $y(x)=0$  can intersect  $k^{\text{th}}$  pixel in 6 ways as shown in Fig.3.16 (ignoring the direction of the ray).

To find out the points of intersection, the following steps are followed:

- Find  $y(x)|_{x=x_l}$  and  $y(x)|_{x=x_{l+1}}$
- If  $y_m \leq y(x)|_{x=x_l} \leq y_{m+1}$ ,  $y1 = y(x)|_{x=x_l}$  and  $x1 = x_l$
- If  $y_m \leq y(x)|_{x=x_{l+1}} \leq y_{m+1}$ ,  $y2 = y(x)|_{x=x_{l+1}}$  and  $x2 = x_{l+1}$

- If  $y1 = null$  and  $y2 \neq null$ 
  - If  $y(x)|_{x=x_i} < y(x)|_{x=x_{i+1}}$ ,  $y1 = y_m$ ,  $x1 = y(x)|_{y=y_m}$
  - If  $y(x)|_{x=x_i} > y(x)|_{x=x_{i+1}}$ ,  $y1 = y_{m+1}$ ,  $x1 = y(x)|_{y=y_{m+1}}$
- If  $y1 \neq null$  and  $y2 = null$ 
  - If  $y(x)|_{x=x_i} < y(x)|_{x=x_{i+1}}$ ,  $y2 = y_{m+1}$ ,  $x2 = y(x)|_{y=y_{m+1}}$
  - If  $y(x)|_{x=x_i} > y(x)|_{x=x_{i+1}}$ ,  $y2 = y_m$ ,  $x2 = y(x)|_{y=y_m}$
- $d_{ijk} = \sqrt{(x1 - x2)^2 + (y1 - y2)^2}$

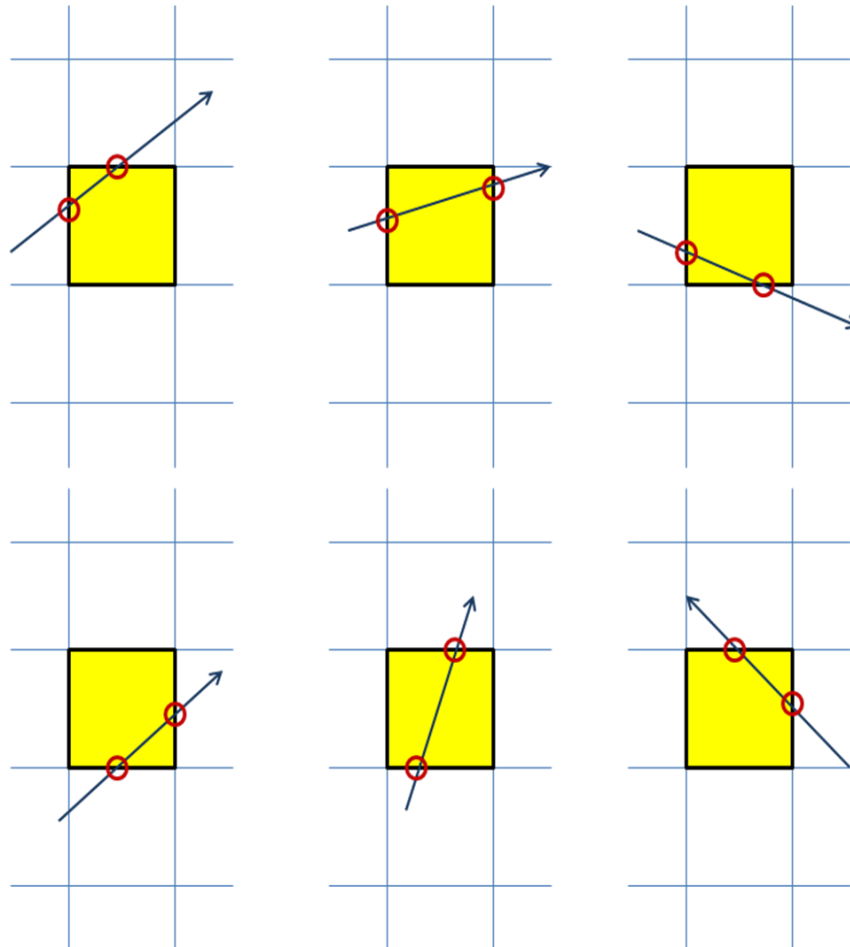


Fig. 3.16 Intersection of a ray with a pixel

In the above steps, the notation  $x_1 = y(x)|_{y=y_m}$  means that  $x_1$  is equal to the value of  $x$  obtained by substituting  $y = y_m$  in the equation  $y(x) = 0$ . If the line  $y(x) = 0$  does not intersect the  $k^{\text{th}}$  pixel,  $d_{ijk}$  is set to zero.

### 3.9.3 Other Projections

To compute the system matrix components for projections at other angles, we follow the method of rotation and bilinear interpolation somewhat similar to the approach followed in Section I. The zero-angle matrix is actually a matrix fixed to the coordinates of the collimator. When the object is rotated by an angle  $\theta$  about the axis of rotation, the observation matrix thus formed can be related to the zero-angle observation matrix as follows.

Let  $f$  be the vector of activity. Under a rotation  $\theta$  and subsequent bilinear interpolation, the rotated activity vector may be written as

$$f_\theta = R_\theta f \quad (3.30)$$

where  $R_\theta$  is the interpolation matrix. Since we have interpolated the image in the original co-ordinates, we can now use the zero-angle observation to form the projection (or observation) at angle  $\theta$  as

$$g_\theta = A_\theta f_\theta = A_0 R_\theta f \quad (3.31)$$

It follows that the system matrix component for angle  $\theta$  can be written as

$$A_\theta = A_0 R_\theta \quad (3.32)$$

From Eq.3.24, we may write in matrix form as

$$A_{geom} = \begin{pmatrix} A_1 \\ A_2 \\ A_3 \\ \cdot \\ \cdot \\ \cdot \\ A_{n_\theta} \end{pmatrix} = \begin{pmatrix} A_0 I \\ A_0 R_2 \\ A_0 R_3 \\ \cdot \\ \cdot \\ \cdot \\ A_0 R_{n_\theta} \end{pmatrix} \quad (3.33)$$

where  $I$  is the identity matrix. The subscript *geom* has been dropped on the right side.

To compute the attenuation factor for other projections, the computation of the distances  $d_{ijk}$  would be computationally heavy task. Thus we use the same kind of method as in forming the geometrical factor. We consider the zero angle projection and compute the distances  $d_{ijk}$  for all  $i, j, k$ . For computing the projections at other angles, we use similar argument as in the previous section and find out the factor  $d_{ijk}$  for the rotated co-ordinates by rebinning. In addition, the attenuation map  $\mu$  is also rotated by angle  $\theta$  and the resulting map  $\mu_\theta$  is used.

The attenuation map vector after rotation and bilinear interpolation may be written as

$$\mu_\theta = R_\theta \mu \quad (3.34)$$

where  $R_\theta$  is the same interpolation matrix as used above. The attenuation factor can now be written as

$$A_{\theta,att}(i, j) = \exp\left(-\sum_k \mu_{\theta,k} d_{ijk}\right) \quad (3.35)$$

The factors  $d_{ijk}$  obtained for the zero-angle projection are used.

Combining the geometrical and attenuation factors, the projection data at angle  $\theta$  is now given by

$$g_\theta = (A_{\theta,geom} \odot A_{\theta,att})f = (A_{\theta,geom} \odot A_{\theta,att})R_\theta f \quad (3.36)$$

Hence, the complete system matrix can now be expressed as

$$A = \begin{pmatrix} (A_{0,geom} \odot A_{0,att})I \\ (A_{0,geom} \odot A_{2,att})R_2 \\ (A_{0,geom} \odot A_{3,att})R_3 \\ \cdot \\ \cdot \\ \cdot \\ (A_{0,geom} \odot A_{n_\theta,att})R_{n_\theta} \end{pmatrix} \quad (3.37)$$

### 3.10 2D Reconstruction: Fan Beam System Model

Parallel beam reconstruction in Active and Passive CT (A&PCT) is widely used due to its rather simple set-up especially for large objects and scanning in three dimensions. A particular example is A&PCT of waste barrels <sup>[69]</sup>. In order to increase the scanning speed and waste drum throughput, multiple detectors (horizontal or vertical or both) in parallel beam configuration may be used and translation of the object or source-detector pair for scanning in-between positions. This yields a linear speedup by a factor approximately equal to the number of detectors used without a compromise in system accuracy. However, using multiple detectors in parallel beam configuration has a limitation in the Active CT step (Fig.3.17(a)) since as many active sources (such as <sup>152</sup>Eu, <sup>166m</sup>Ho, <sup>60</sup>Co) as the number of detectors are required. This is practically not easy due to the increase in cost as well as shielding required for multiple active sources.

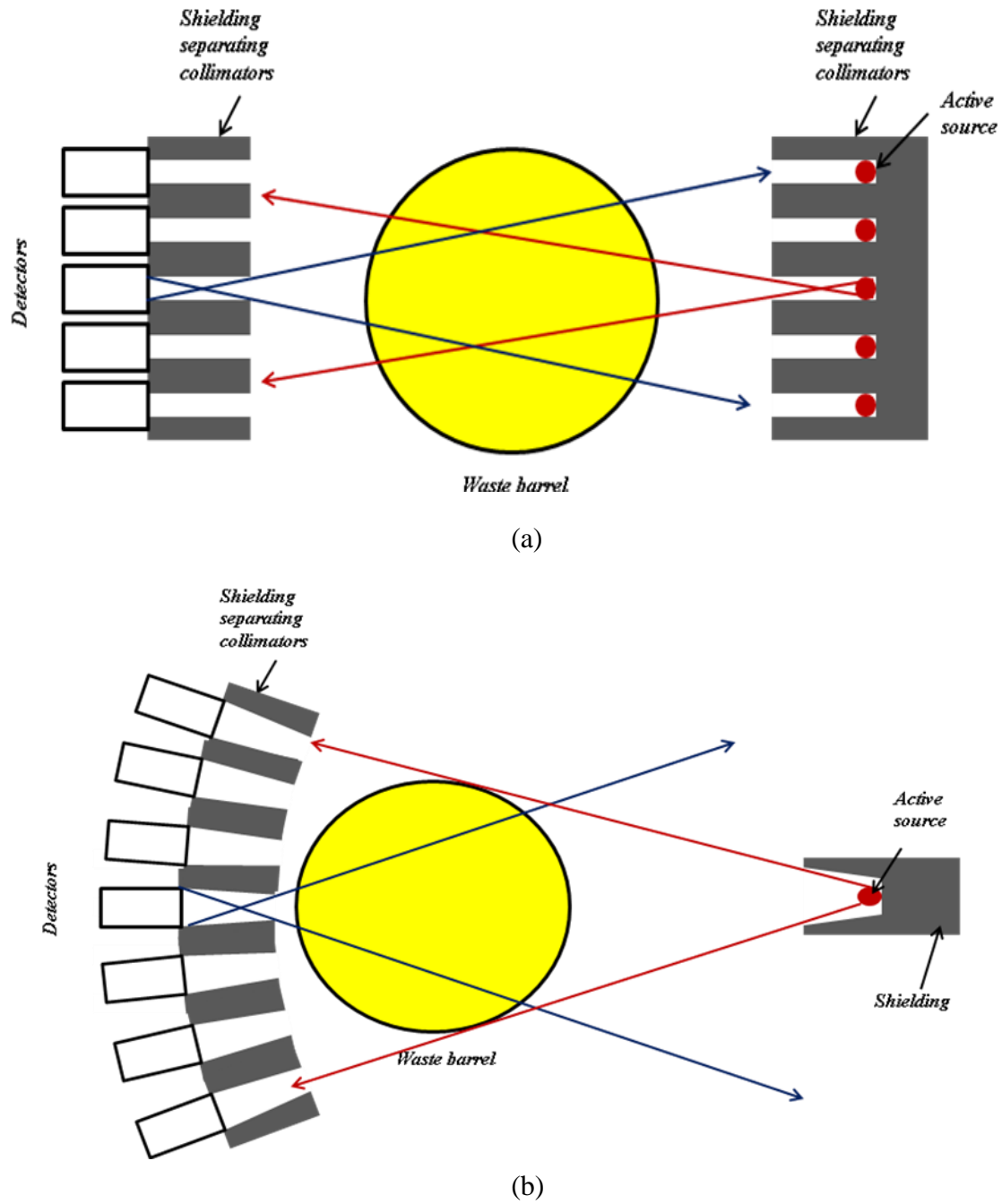


**Fig. 3.17** Schematic arrangement for multiple detector A&PCT scan in (a) Parallel beam and (b) Fan beam configurations showing the requirement of active source(s)

Another limitation is the use of HPGe detectors for waste assay. Since HPGe detectors are bulky and cannot be stacked vertically, it puts a limitation on the number of

detectors that can be used (as the maximum horizontal span of the detectors should be equal to the width of the barrel).

One of the approaches to solve this problem is to devise new scanning geometries. Roberson *et al* <sup>[118]</sup> have discussed some scanning configurations to this effect. One of the scanning methods is a fan-beam geometry with the active source placed at the focal point of the fan (Fig.3.17(b)). In this scenario, there is a possibility of speedup due to the elimination of discrete translation positioning in the active (and/or passive) mode(s). Also, the fan-beam design has only one source and a very simple source collimator compared to the straight in-line case. A disadvantage of fan-beam geometry is that fan-beam detector collimators are somewhat more complicated in construction when compared to the straight in-line collimators.

Fan beam reconstruction has also been used by few other researchers <sup>[82, 83, 119-121]</sup> but has been mainly limited to proof-of-principle experiments or validation of new algorithms <sup>[82, 83]</sup> or intended for small objects for clinical use <sup>[121]</sup>. This section describes a practical implementation of the fan-beam reconstruction model for A&PCT imaging of waste barrels. In the experimental arrangement, the detectors are spaced equally along a straight line with collimators arranged in a fan beam configuration such that the collimator face is perpendicular to the line joining the focal point and detector centre. A simplification introduced is in the use of parallel beam collimators instead of fan beam collimators. For large objects and large focal length, the angular difference of a fan beam collimator and a parallel beam collimator is very small (for example, in the present experiment the angular difference is less than 4°). This makes the implantation of fan beam geometry easy and is a more practical solution.

We shall compute the system matrix for a two dimensional fan beam system matrix with equally spaced detectors. The treatment is similar to that discussed earlier for parallel volume system model.

For 2D reconstruction, the object pixel and the detector are in the same plane. Using the same line of discussion as in Section 3.9.1, the area of the  $j^{th}$  detector as seen by  $i^{th}$  pixel is given (from Fig.3.18) as the difference of the projected width of  $w_c$  under angle  $\beta$  and the part of the projected width shadowed by the collimator.

$$Area = (w_c \cos(\beta - \eta) - l_c \sin(\beta - \eta))h_c \quad (3.38)$$

$w_c$  is the collimator width

$l_c$  is the collimator length

$h_c$  is the collimator height

$\beta$  is the angle subtended by the  $i^{th}$  pixel at the  $j^{th}$  detector

$\eta$  is the fan angle of the  $j^{th}$  detector

From Fig.3.18, if pixel and detector co-ordinates are  $(x_p, y_p)$  and  $(x_d, y_d)$  respectively, we can write

$$\cos \beta = \frac{x_d - x_p}{R_{ij}} ; \sin \beta = \frac{|y_d - y_p|}{R_{ij}} \quad (3.39)$$

$$\cos \eta = \frac{D}{\sqrt{D^2 + y_d^2}} ; \sin \eta = \frac{|y_d|}{\sqrt{D^2 + y_d^2}} \quad (3.40)$$

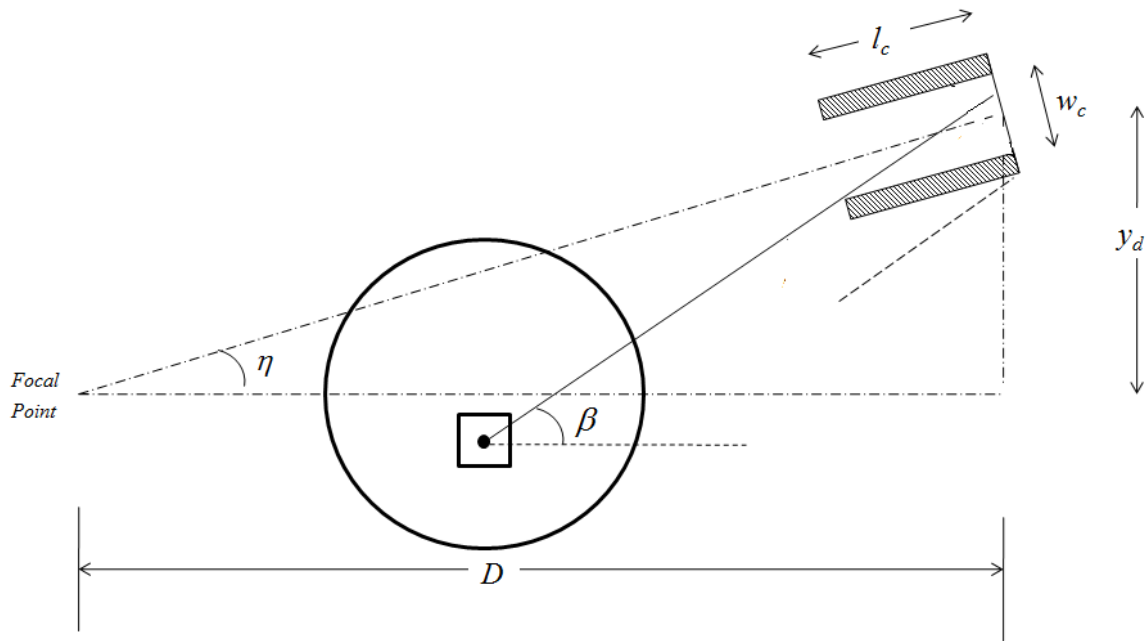


**Fig. 3.18** Computing the geometrical factor of system matrix

The calculation of the geometrical factor depends on the shape of the holes in the collimator. For square hole collimator  $h_c = w_c$ . If collimator is further divided into  $n$  holes per dimension, Eq.3.38 is modified as (by analogy with Eq.3.27)

$$Area = (w_c \cos(\beta - \eta) - n.l_c \sin(\beta - \eta))h_c \quad (3.41)$$

Obviously, if  $Area < 0$ , the pixel does not contribute to the detector bin and we have to set  $Area = 0$ .

For other rotations, the treatment is similar to that discussed earlier for parallel volume system model. The steps for calculating the attenuation factor is same as for parallel beam case and hence is not repeated here.

### 3.11 Fully 3D Reconstruction

For 2D reconstruction, system matrix is constructed for a single slice and the corresponding slice is reconstructed. The geometrical factor has to be computed only once as it remains the same for each slice. The attenuation factor is modified for each slice depending upon the attenuation map for the particular slice. However, the term  $d_{ijk}$  needs to be computed only once. The 3D activity map is then obtained by vertically stacking the respective 2D reconstructed slices.

In 2D reconstruction, it is assumed that all photon counts in a particular row of the planar image are due to photons emitted from the slice at same height. However, the projection data has contribution from other voxels also which are located in other slices. In fact, each detector or projection bin accepts contributions from a cone whose dimensions depend on the shape and size of collimator holes.

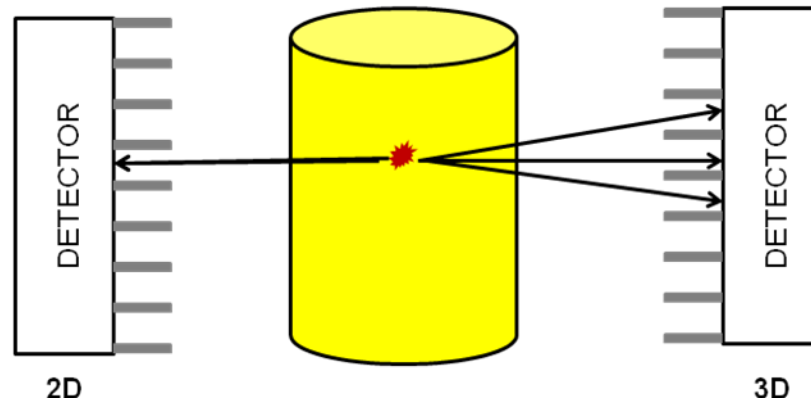


*Fig. 3.19 Schematic representation of 2D (stacked) and fully 3D Reconstruction*

The computation of the system matrix  $A$  in the case of fully 3D reconstruction is computationally heavy. However, it models the collimator more accurately thereby

enabling a reduction of collimator blurring and also better quantitative estimation of activity values.

In order to compute the fully 3D reconstruction we must discretize the whole 3D region where the activity distribution is to be reconstructed. The 3D region is discretized into  $N_x \times N_y \times N_z$  voxels.

The system matrix can be represented in block matrix notation as

$$A = \begin{pmatrix} A_1 \\ A_2 \\ A_3 \\ \cdot \\ \cdot \\ \cdot \\ A_{n_\theta} \end{pmatrix} \quad (3.42)$$

where  $A_1$  is the block matrix for first projection,  $A_2$  is the block matrix for second projection, and so on.  $n_\theta$  is the number of angular projections.

The procedure of forming the matrix  $A$  in 3D case is basically the same as in 2D collimator modeled case. First we form the zero-angle observation matrix  $A_0$  corresponding to the planar image at acquisition angle  $\theta=0$ . Then we can form the matrix  $A$  block by block using rotation and bilinear interpolation.

We now discuss the computation of the geometrical and attenuation factors for the zero angle projection. The factors for other angles follow from the argument for the 2D case.

### 3.11.1 Geometrical factor

For the 3D case, the (source) voxel  $i$  may also be above or below the detector plane. Consider the vector  $\bar{r} \in \mathbb{R}^3$  joining the source voxel to the detector (Fig.3.20). For the sake of simplicity, the co-ordinates have been so chosen that the origin is at the centre of the  $i^{\text{th}}$  voxel and collimator is not shown. In this case, the collimator height  $h_c$  is also modified analogous to the collimator width in Eq.3.25. The modified expression for solid angle becomes

$$A_{0,geom}(i, j) = \frac{1}{4\pi R_{ij}^2} (w_c \cos \beta - nl_c \sin \beta)(h_c \cos \eta - nl_c \sin \eta) \quad (3.43)$$

where  $\beta$  is the angle made by projection (on XY plane) of vector  $\bar{r}$  with the y-axis and  $\eta$  is the angle made by  $\bar{r}$  with the horizontal (XY) plane and  $n$  is the number of holes per dimension of the collimator.

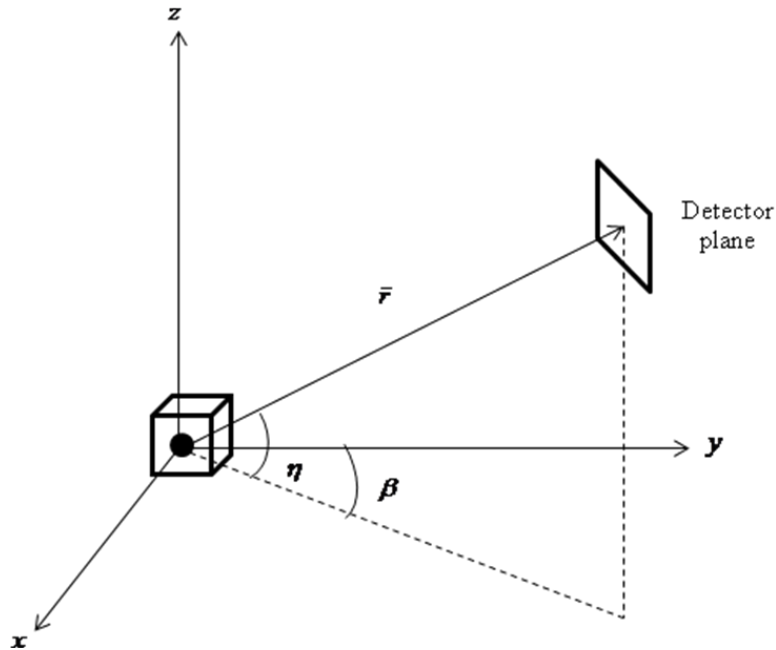


Fig. 3.20 Area of the  $j^{\text{th}}$  detector as seen by  $i^{\text{th}}$  pixel for 3D case

### 3.11.2 Attenuation factor

The attenuation factor is given by Eq.3.28. As the photons from other slices too contribute to any projection bin, the voxel index now takes the range of values  $i = 1, 2, \dots, N_x \cdot N_y \cdot N_z$  and the detector index  $j = 1, 2, \dots, N_y \cdot N_z$ . The path length matrix elements  $d_{ijk}$  may be computed similar to the 2D case (see Section 3.9.2) except that now the voxels other than the reconstruction plane also have to be considered.

Let  $y(x)=0$  denote the line joining  $i^{th}$  pixel and  $j^{th}$  detector. Similar to the discussion in Section 3.9.2, the intersection of the line  $y(x)=0$  with voxel boundaries has to be now considered, instead of pixel boundaries. Since the steps for 3D case simply follow from the steps for 2D case (section 3.10.2), the discussion of the same has been skipped here. If  $(x1, y1, z1)$  and  $(x2, y2, z2)$  are the points of intersection then

$$d_{ijk} = \sqrt{(x1 - x2)^2 + (y1 - y2)^2 + (z1 - z2)^2} \quad (3.44)$$

If the line  $y(x)=0$  does not intersect the  $k^{th}$  voxel,  $d_{ijk}$  is set to zero.

### 3.11.3 Other Projections

Once the zero angle projection has been constructed, the system matrix  $A$  can be obtained block by block as in the 2D case. However, the activity map cannot be rotated by angle  $\theta$  simply by multiplying  $f$  with  $R_\theta$ . This is because the vector  $f$  now represents the activity in three dimensions and the elements  $f_1, \dots, f_{N_x N_y}$  represent the lowermost slice,  $f_{N_x N_y + 1}, \dots, f_{2 N_x N_y}$  the next higher slice and so on. Thus, the blocks of the vector  $f$  for each slice must be multiplied with  $R_\theta$  separately representing the rotation of all the slices at angle  $\theta$ .

From the above argument, the projection at angle  $\theta$  can be written as

$$g_\theta = (A_{\theta,geom}^1 \odot A_{\theta,att}^1) f^1 + \dots + (A_{\theta,geom}^{N_z} \odot A_{\theta,att}^{N_z}) f^{N_z} \quad (3.45)$$

where  $f^1 = (f_1, f_2, \dots, f_{N_x N_y})^T$  and  $f^{N_z} = (f_{N_x N_y (N_z-1)+1}, f_{N_x N_y (N_z-1)+2}, \dots, f_{N_x N_y N_z})^T$

Using the zero angle projection and interpolation matrix, we may write

$$g_\theta = (A_{0,geom}^1 \odot A_{0,att}^1) R_\theta f^1 + \dots + (A_{0,geom}^{N_z} \odot A_{0,att}^{N_z}) R_\theta f^{N_z} \quad (3.46)$$

The system matrix for fully 3D case may now be expressed as

$$A = \begin{pmatrix} (A_{0,geom}^1 \odot A_{0,att}^1)I & (A_{0,geom}^2 \odot A_{0,att}^2)I & \cdot & \cdot & (A_{0,geom}^{N_z} \odot A_{0,att}^{N_z})I \\ (A_{1,geom}^1 \odot A_{1,att}^1)R_1 & (A_{1,geom}^2 \odot A_{1,att}^2)R_1 & \cdot & \cdot & (A_{1,geom}^{N_z} \odot A_{1,att}^{N_z})R_1 \\ \cdot & \cdot & \cdot & \cdot & \cdot \\ \cdot & \cdot & \cdot & \cdot & \cdot \\ (A_{n_\theta,geom}^1 \odot A_{n_\theta,att}^1)R_{n_\theta} & (A_{n_\theta,geom}^2 \odot A_{n_\theta,att}^2)R_{n_\theta} & \cdot & \cdot & (A_{n_\theta,geom}^{N_z} \odot A_{n_\theta,att}^{N_z})R_{n_\theta} \end{pmatrix} \quad (3.47)$$

# Simulation Studies

To test reconstruction algorithms and to measure their performance, simulations are required. They also help to optimize different parameters for experiments, such as, number of iterations required, sensitivity to noise, optimum collimation ratio, etc. Since most of the SPECT reconstruction algorithms are adapted from the medical field, in which experimental conditions do not vary much from one patient to another, they need to be carefully analyzed and suitably modified for applications in nuclear field.

This chapter explores the algorithms extensively using simulated phantoms. We have also tested the 2D and 3D system matrix for both parallel and fan beam geometries as well as fully 3D system matrix.

Section 4.1 describes the various phantoms used for simulations. The phantoms have been used to test reconstruction under different conditions using the following algorithms: FBP (analytical), ART and SART (algebraic) and MLEM and OSEM (statistical). Sections 4.2 and 4.3 present the results for 2D reconstruction in parallel and fan beam geometries respectively. Sections 4.4 and 4.5 discuss the results for 3D reconstruction for line integral model and collimator model respectively. Section 4.6 defines some parameters to assess quality of reconstructed images. Sections 4.7 and 4.8 present the effect of collimator blurring and photon noise on analytical reconstruction.

## 4.1 Phantoms

Different phantoms have been considered to highlight the various cases – point source, distributed source with uniform and non-uniform attenuation, waste drum and PHWR fuel bundle. In order to illustrate the effect of collimator blurring, the observation matrices have been constructed for both line integral model (ideal collimator) and collimator model. The projections using both these approaches have been reconstructed using analytical approach of Novikov. For iterative reconstructions, only collimator modeled projections have been used. Since the collimator modeled projections (forward projection) have been constructed using the probability system matrix (as described in Chapter 2) and the same matrix is also used for solving the linear system of equations  $g = Af$  (backward projection), a direct inversion would lead to an incorrect interpretation. Hence, each data point in the projection data was replaced by a random realization of a Poisson variate with a mean equal to the counts of the corresponding data point. The modified projection data was used to invert the equation  $g = Af$ . For phantoms 1 to 3, the pixel size of the object is 25 mm square. The collimator size is 25 mm x 25 mm which is divided into 4 sections of dimension 10 mm x 10 mm each separated by highly attenuating septa.

Following 2D and 3D phantoms have been chosen for simulation studies.

### 4.1.1 Phantom 1: Point sources (2D)

**Description:** The phantom consists of three point sources (Fig.4.1(a)) (single pixel) of source strength equal to 1 inside a homogeneous circular area with linear attenuation coefficient equal to  $0.05 \text{ cm}^{-1}$  inside the circle and 0 outside Fig.4.1(b)). The phantom is discretized on a 30 x 30 grid.

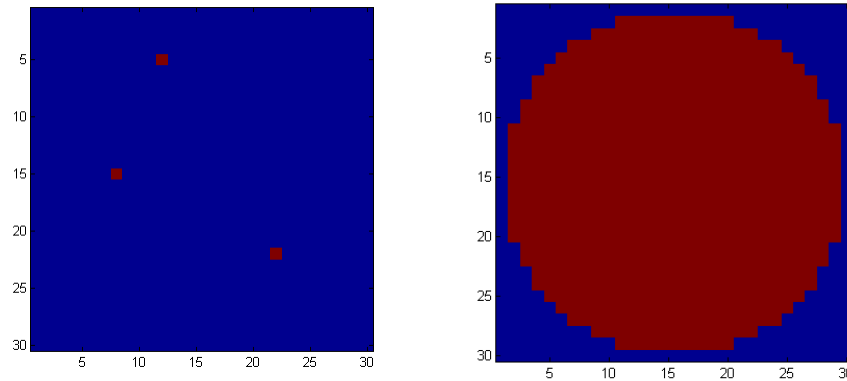


**Fig. 4.1** Phantom 1 (a) Activity map (b) Attenuation map

### 4.1.2 Phantom 2: Distributed sources with uniform attenuation (2D)

**Description:** The phantom consists of two distributed sources: the first (top left) spanning 4 x 4 pixels of source strength equal to 1 per pixel ; the second (bottom right) spanning 3 x 3 pixels of source strength equal to 2 per pixel (Fig.4.2(a)). The surrounding matrix is a homogeneous circular with linear attenuation coefficient equal to  $0.05 \text{ cm}^{-1}$  inside the circle and 0 outside (Fig.4.2(b)). The phantom is discretized on a 30 x 30 grid.

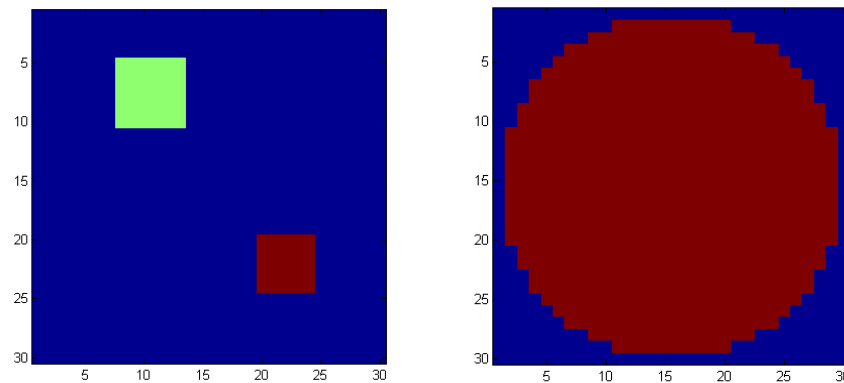


**Fig. 4.2** Phantom 2 (a) Activity map (b) Attenuation map

### 4.1.3 Phantom 3: Distributed sources with non-uniform attenuation (2D)

**Description:** The phantom consists of two distributed sources: the first (top left) spanning 4 x 4 pixels of source strength equal to 1 per pixel; the second (bottom right) spanning 4 x 4 pixels of source strength equal to 1 per pixel;

spanning 3 x 3 pixels of source strength equal to 2 per pixel (Fig.4.3(a)). The surrounding matrix consists of three homogeneous circular area with linear attenuation coefficient inside the respective circle equal to  $0.025 \text{ cm}^{-1}$  (light blue),  $0.05 \text{ cm}^{-1}$  (yellow) and  $0.1 \text{ cm}^{-1}$  (red) (Fig.4.3(b)) and 0 elsewhere. The phantom is discretized on a 30 x 30 grid.

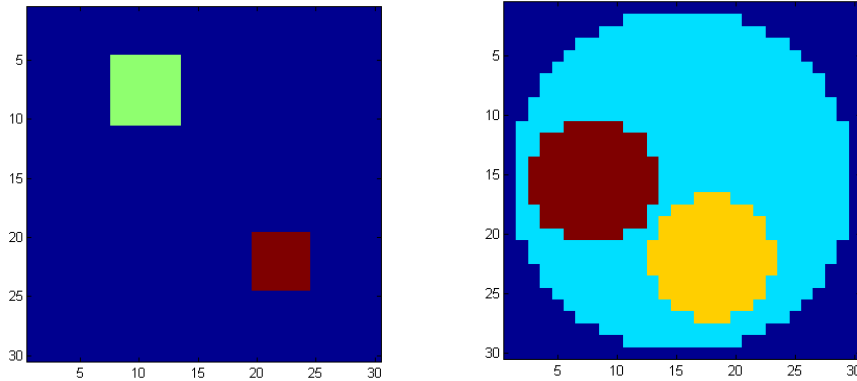


*Fig. 4.3 Phantom 3 (a) Activity map (b) Attenuation map*

#### 4.1.4 Phantom 4: Waste drum with distributed sources and point sources in low attenuating matrix (3D)

**Description:** A stainless steel drum containing radioisotopes has been modeled. The drum has a diameter of 55 cm and a height of 87 cm with 2 mm thick wall. The drum is filled with a homogeneous low attenuating matrix (linear attenuation coefficient:  $0.0185 \text{ cm}^{-1}$  at 414 keV). The phantom (Fig. 4.4) consists of radioactive isotope (linear attenuation coefficient:  $5.6311 \text{ cm}^{-1}$  at 414 keV) in bulk pieces of various shapes and sizes at 5 different locations as well as point sources at 7 different positions with varied activities (refer Table 4.1). The point source is represented by a voxel in 3D space and several such voxels constitute a bulk source such as in the form of a sphere, ellipsoid or cube. The activities of point sources mentioned refer to the activities over each voxel.

The activity of the bulk piece (sphere, ellipsoid or cube) is the sum total of the activities of all such voxels (point sources) within the bulk piece.

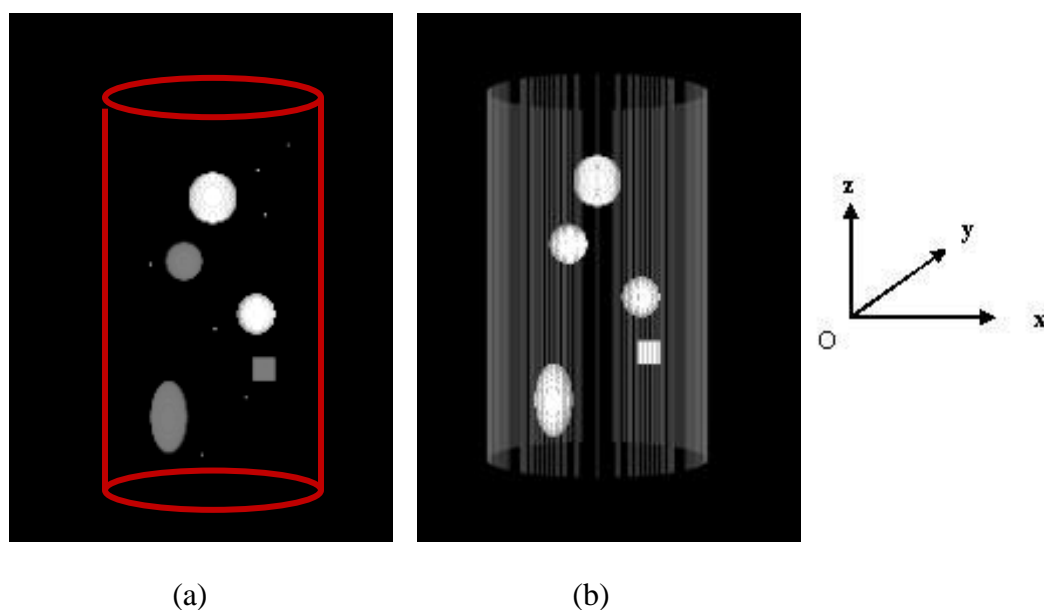


**Fig. 4.4** Phantom 4 (a) Activity map (b) Attenuation map  
(Note: The boundary of the cylinder is shown only for illustration purpose)

**TABLE 4.1** Activity table for Phantom D-1 (Note: Central plane is the  $z = 0$  plane)

Source shape/geometry	Source position/centre (x, y, z)	Source dimension	Activity (emissions/voxel)
Sphere	(11.4, 0, -5.4)	Radius 4.5 cm	$2 \times 10^6$
Sphere	(0, 12.0, 21.2)	Radius 5.5 cm	$2 \times 10^6$
Sphere	(-8.4, 0, 7.1)	Radius 4.5 cm	$1 \times 10^6$
Cube	(13.2, -3.0, -19.0)	5.5 cm x 5.5 cm x 5.5 cm	$1 \times 10^6$
Ellipsoid	(-12.6, 0, -29.9)	Radii: (4.5 cm, 5.5 cm, 8.5 cm)	$1 \times 10^6$
Point	(0, 11.4, -8.7)	-	$2 \times 10^6$
Point	(-18.0, -6.6, 6.5)	-	$2 \times 10^6$
Point	(14.4, -15.0, 19.0)	-	$2 \times 10^6$
Point	(12.0, -6.6, 29.4)	-	$2 \times 10^6$
Point	(-3.6, -15.0, -40.8)	-	$1.5 \times 10^6$
Point	(8.4, 3.6, -25.0)	-	$1.5 \times 10^6$
Point	(21.0, -14.4, 36.4)	-	$1.5 \times 10^6$

### 4.1.5 Phantom 5: Waste drum with distributed sources in high attenuating matrix (3D)

**Description:** An SS drum containing radioisotopes has been modeled. The drum has a diameter of 55 cm and a height of 87 cm with 2 mm thick wall. The drum is filled with a homogeneous high attenuating matrix (linear attenuation coefficient:  $0.12 \text{ cm}^{-1}$  at 414 keV). The phantom (Fig. 4.5) consists of radioactive isotope (linear attenuation coefficient:  $5.63 \text{ cm}^{-1}$  at 414 keV) in the form of small spherical pieces at 15 different locations in a high attenuation surrounding matrix (refer Table 4.2).

**TABLE 4.2** Activity table for Phantom D-2 (Note: Central plane is the  $z = 0$  plane)

Source shape/geometry	Source position/centre (x, y, z)	Source dimension	Activity (emissions/voxel)
Sphere	(15.6, -15.6, -37.5)	Radius 3.5 cm	$2 \times 10^4$
Sphere	(-11.4, -12.0, -33.7)	Radius 3.5 cm	$2 \times 10^4$
Sphere	(-19.8, 4.2, -25.0)	Radius 3.5 cm	$2 \times 10^4$
Sphere	(-13.8, -1.8, -14.1)	Radius 3.5 cm	$2 \times 10^4$
Sphere	(-5.4, 2.4, -9.8)	Radius 3.5 cm	$2 \times 10^4$
Sphere	(3.0, -15.0, -4.9)	Radius 3.0 cm	$1 \times 10^4$
Sphere	(-15.0, -18.0, 3.3)	Radius 3.0 cm	$1 \times 10^4$
Sphere	(19.2, 12.6, 6.5)	Radius 3.0 cm	$1 \times 10^4$
Sphere	(2.4, -9.0, 10.3)	Radius 3.0 cm	$1 \times 10^4$
Sphere	(-19.8, -19.2, 19.0)	Radius 3.0 cm	$1 \times 10^4$
Sphere	(-18.6, 18.0, 22.8)	Radius 2.5 cm	$3 \times 10^4$
Sphere	(1.2, -11.4, 27.2)	Radius 2.5 cm	$3 \times 10^4$
Sphere	(-4.8, 14.4, 31.0)	Radius 2.5 cm	$3 \times 10^4$
Sphere	(13.2, 19.8, 34.8)	Radius 2.5 cm	$3 \times 10^4$
Sphere	(-21.6, -5.4, 38.1)	Radius 2.5 cm	$3 \times 10^4$

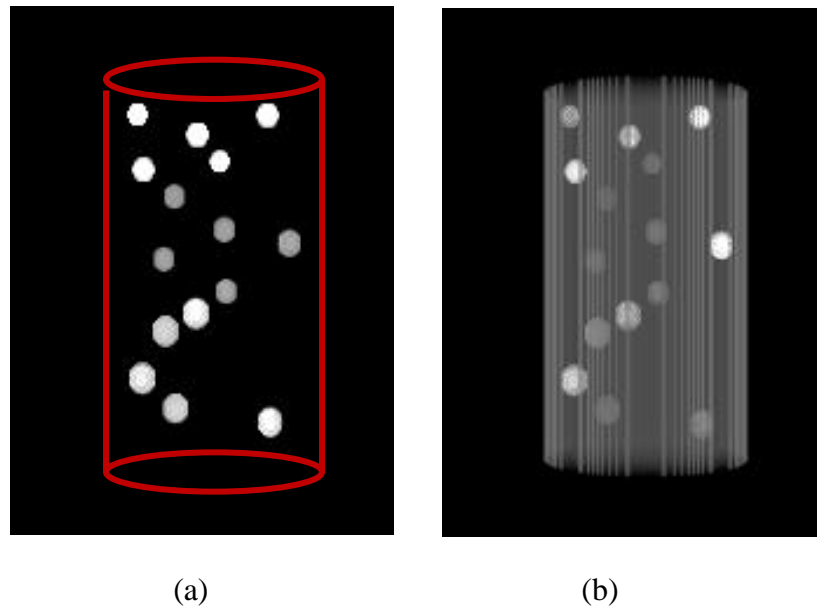


**Fig. 4.5** Phantom 5 (a) Activity map (b) Attenuation map  
(Note: The boundary of the cylinder is shown only for illustration purpose)

#### 4.1.6 Phantom 6: PHWR Fuel Bundle

Fuel pin assembly for PHWR (Pressurized Heavy Water Reactor) has been modeled. It has been assumed that the fuel is continuous throughout the pin instead of being in the pellet form. The details of the pin bundles are given in Table 4.3. The height of the fuel pins in either case has been taken to be 50 cm which is only a representation of the actual fuel pin which is of much greater height.

In the PHWR fuel bundle, one of the rods (as shown in Fig. 4.6 (a) and (b)) has been replaced by a non-active rod. This is to check the sensitivity of the algorithm in case one of the rods is replaced by a non-active rod or a rod with fuel-like material (so that there is minor or no changes in the attenuation matrix).

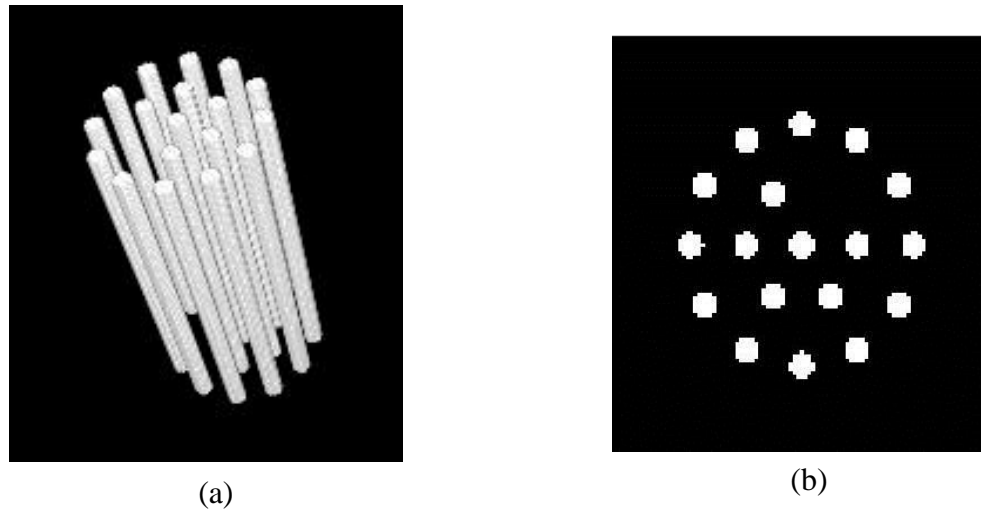


**Fig.4.6** Phantom 6 (a) 3D Activity map (b) Cross-sectional view

**TABLE 4.3** Details of PHWR fuel bundle

Fuel	Natural UO <sub>2</sub>
No. of fuel rods in the bundle	19
Fuel rod diameter	1.52 cm
Length of the fuel rod	50 cm
Clad material	Zircaloy
Clad thickness	0.4 mm

## 4.2 2D Reconstruction (Parallel Beam)

### 4.2.1 Phantom 1: Point Sources

Projections were computed at 100 angles over 360° (0°, 3.6°, 7.2°, ..., 356.4°) for line integral model and 36 angles over 360° (0°, 10°, 20°, ..., 350°) for collimator model with 30 lateral data points per projection. Figure 4.7 (a) and 4.8 (a) present the computed projections in the form of sinogram for line integral and collimator models respectively. The projections of the points are clearly wider in the case of the collimator modeled case.

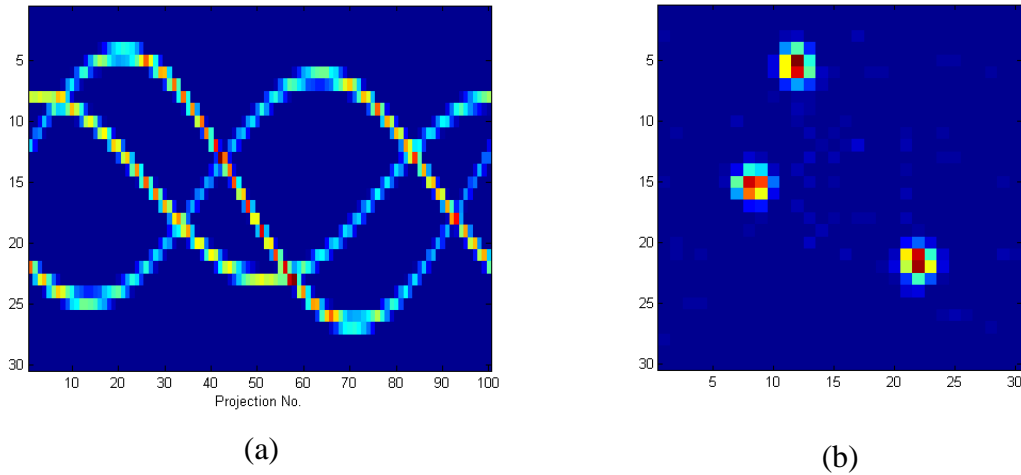


**Fig. 4.7** (a) Sinogram (b) Analytical reconstruction for line integral modeled projection

The spreading of a pixel into several pixels in planar image is due to the collimator blurring effect, as explained earlier in Chapter 3. This is manifested better in Fig. 4.9 which shows the projections at angles  $0^\circ$  and  $90^\circ$  computed using both models. Figures 4.7(b) and 4.8(b) show the analytically reconstructed activity function for line integral and collimator models respectively.

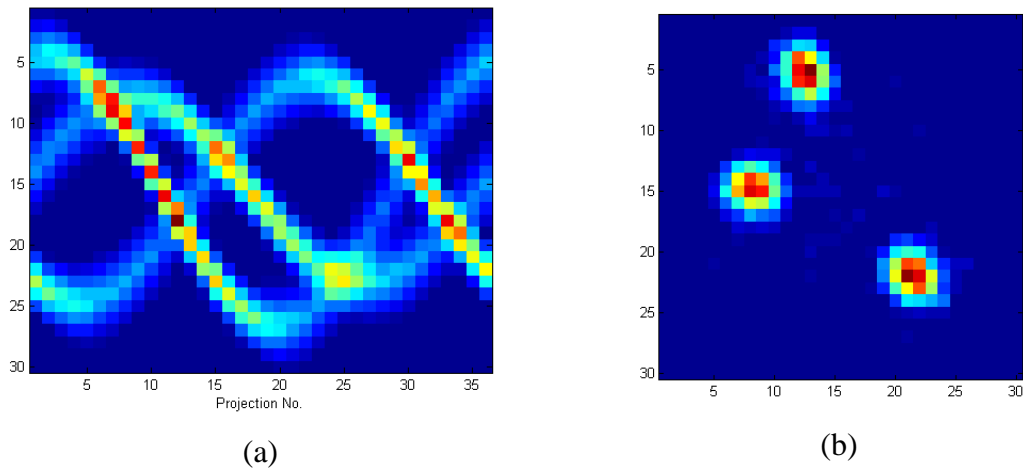


**Fig. 4.8** (a) Sinogram (b) Analytical reconstruction for collimator modeled projection

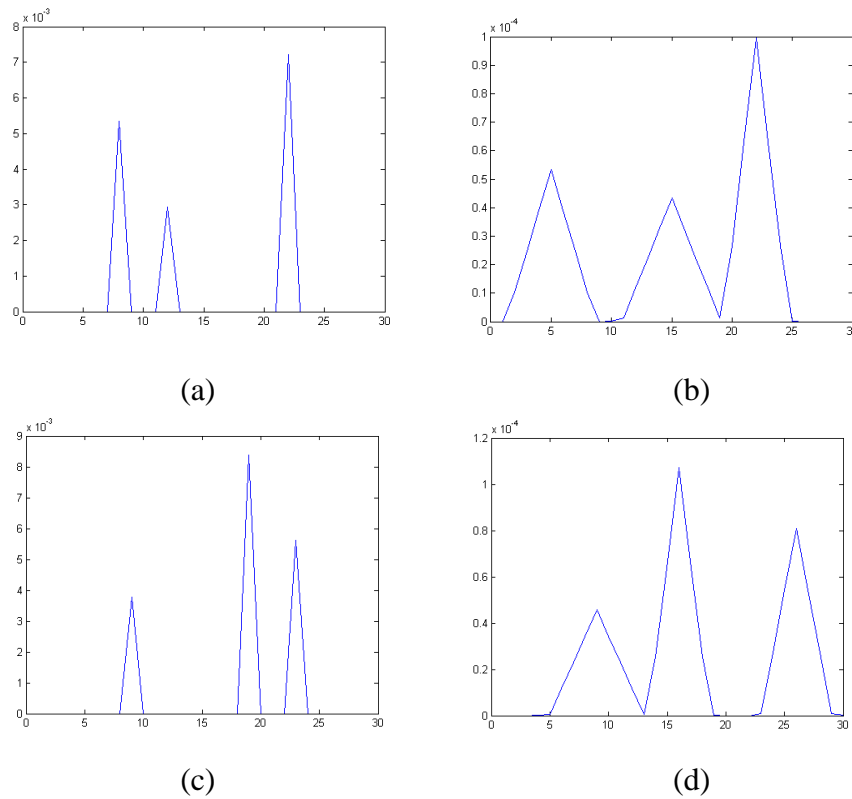


**Fig. 4.9** Line profile at  $0^\circ$  and  $90^\circ$  (a) and (c) Line integral model (b) and (d) Collimator model

To compute the activity function using iterative reconstruction (inverse problem of SPECT), we used the projections added with Poisson noise as data. Figure 4.10 (a) shows the sinogram obtained after adding Poisson noise to the data. Figures 4.10 (b) and 4.10 (c) show the reconstructed activity function using ART and SART algorithms (100 iterations each; relaxation parameter 0.2) whereas Figures 4.10(d) and 4.10(e) show the reconstructed activity function using MLEM (25 iterations) and OSEM (4 subsets, 6 iterations) algorithms.

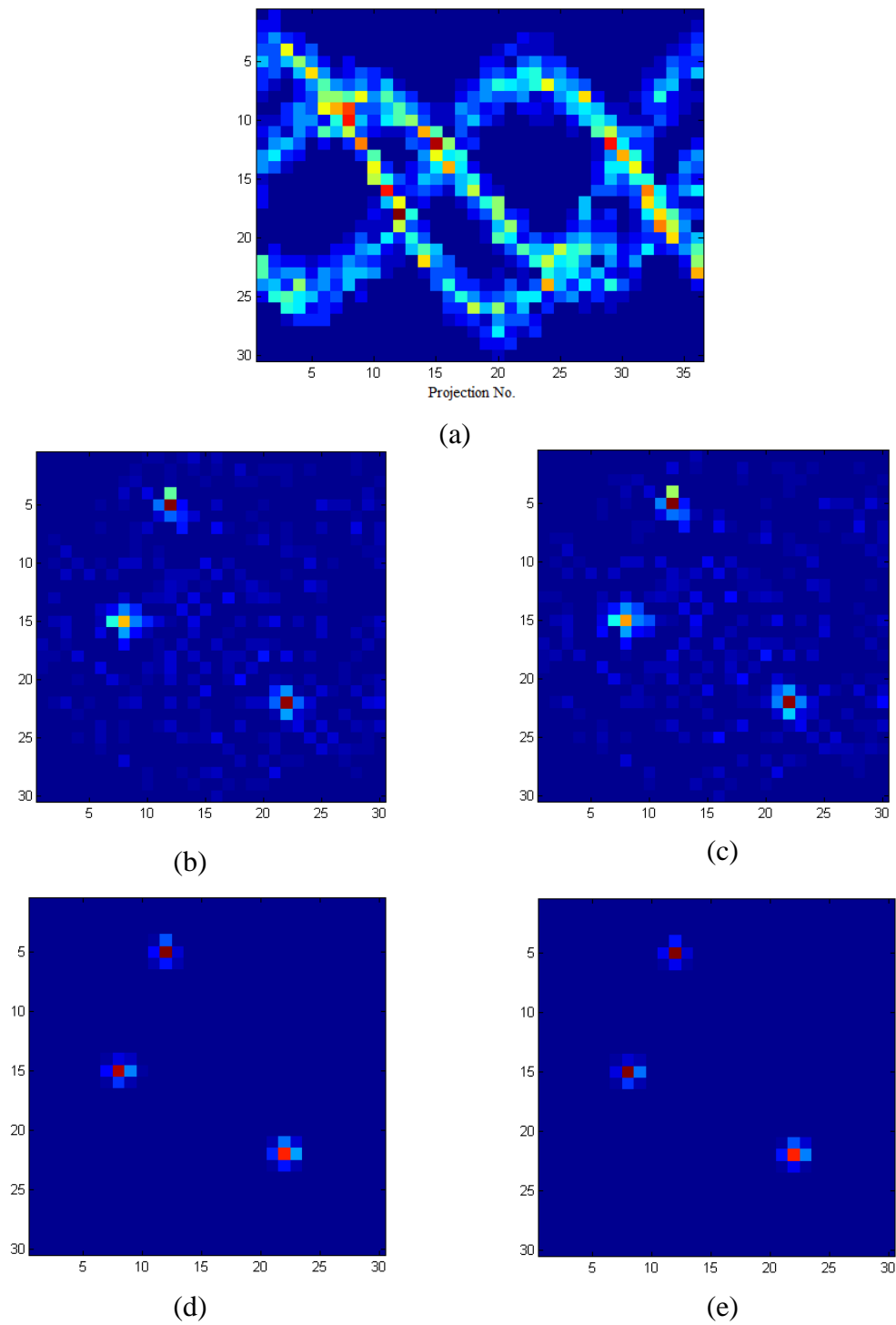


**Fig. 4.10** (a) Sinogram for collimator modeled projection with Poisson noise (b) ART (c) SART (d) MLEM (e) OSEM reconstructions

It can be seen that the background is noisy in the case of ART and SART reconstruction whereas the background is quite low for MLEM and OSEM reconstruction. Another important observation can be made regarding the effect of collimator blurring. The iterative reconstruction reduces the collimator blurring which was evident in the analytically reconstructed activity (Fig. 4.8(b)). Fig. 4.11 shows the line profile across one of the sources for different reconstruction methods. It can be seen that FBP shows the maximum spreading (FWHM) whereas MLEM and OSEM show the least spreading and closely resemble the line profile of the original phantom. For ART and SART reconstructions, although the spreading is less, the image is noisy which can be inferred from the small peaks on either side of the actual peak.

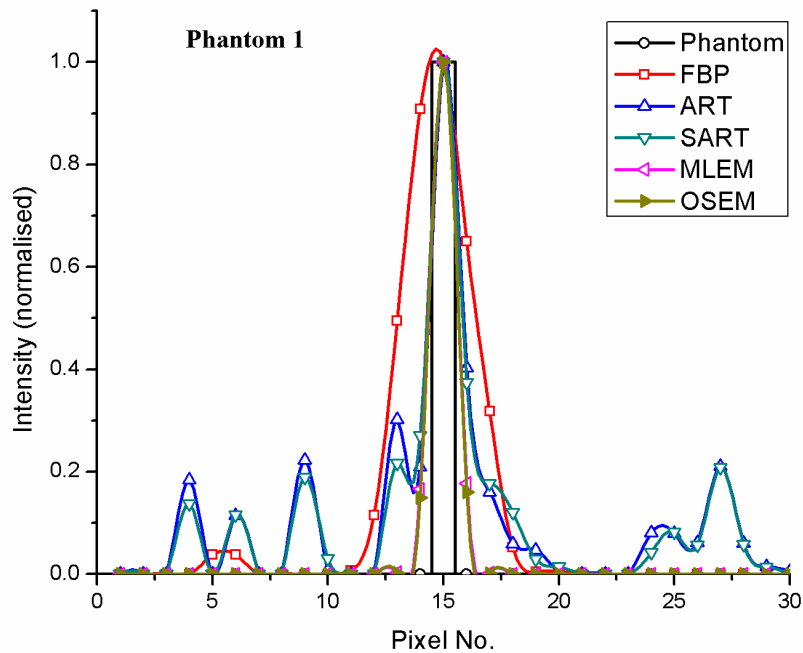


**Fig.4.11** Line profile for reconstructed image using various reconstruction techniques

### 4.2.2 Phantom 2: Distributed sources with uniform attenuation (2D)

Projections were computed at 100 angles over  $360^\circ$  ( $0^\circ, 3.6^\circ, 7.2^\circ, \dots, 356.4^\circ$ ) for line integral model and 36 angles over  $360^\circ$  ( $0^\circ, 10^\circ, 20^\circ, \dots, 350^\circ$ ) for collimator model with 30 lateral data points per projection. Figure 4.12 (a) and 4.13 (a) show the computed projections in the form of sinogram for line integral and collimator models respectively. Figures 4.12 (b) and 4.13 (b) show the analytically reconstructed activity function for line integral and collimator models respectively. It can be seen that the boundary of the square shaped activity region is more pronounced in Fig. 4.12 (b) as compared to Fig. 4.13 (b). This again shows the effect of collimator blurring. Figure 4.15 (a) shows the sinogram obtained after adding Poisson noise to the data which is used for iterative reconstruction.

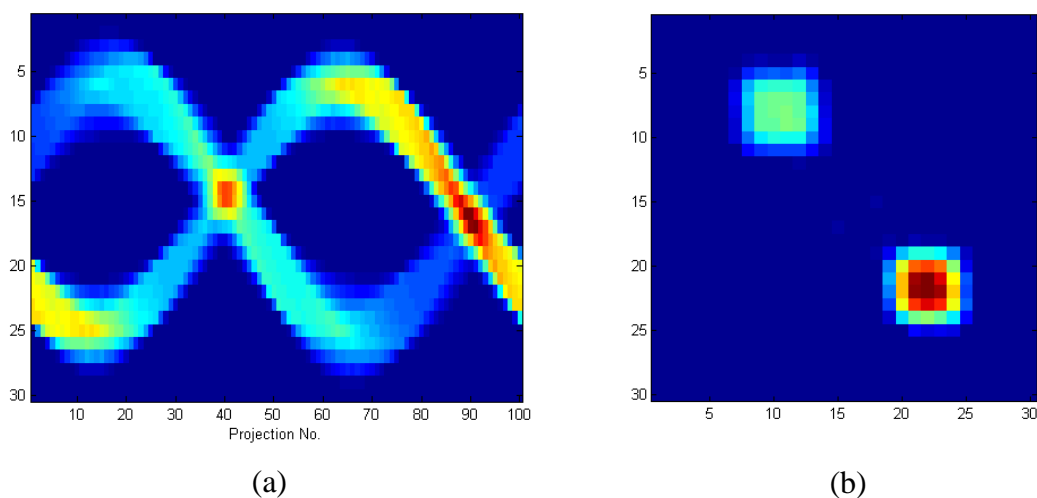


**Fig.4.12** (a) Sinogram (b) Analytical reconstruction for line integral modeled projection

Figures 4.15 (b) and 4.15 (c) show the reconstructed activity function using ART and SART algorithms (100 iterations each; relaxation parameter 0.2) whereas Figures 4.15 (d) and 4.15 (e) show the reconstructed activity function using MLEM (25 iterations) and OSEM (4 subsets, 6 iterations) algorithms. It can be seen that the image is

quite noisy (streaks) in the case of ART and SART reconstruction and the (square) activity region is also not well pronounced though the boundary is almost square.

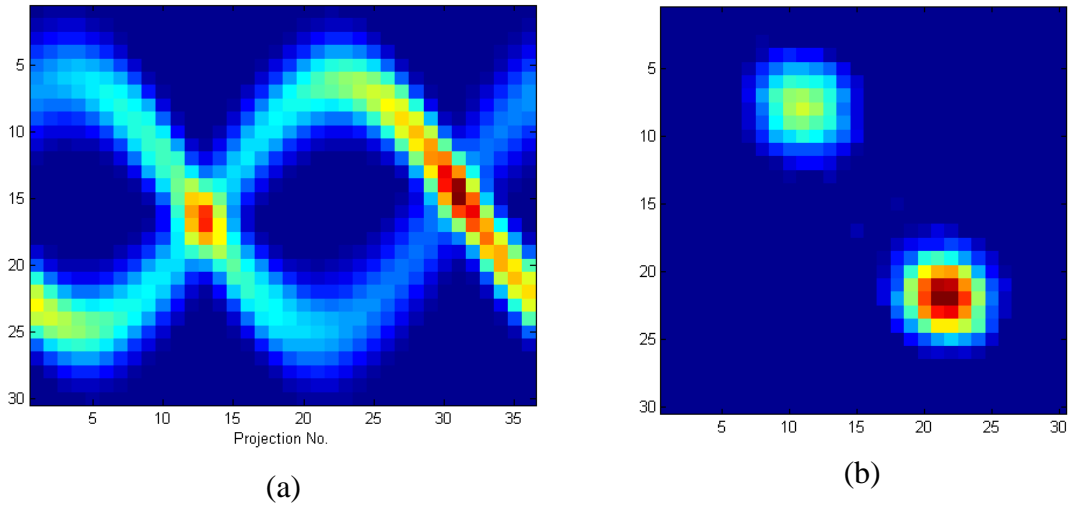


Fig. 4.13 (a) Sinogram (b) Analytical reconstruction for collimator modeled projection

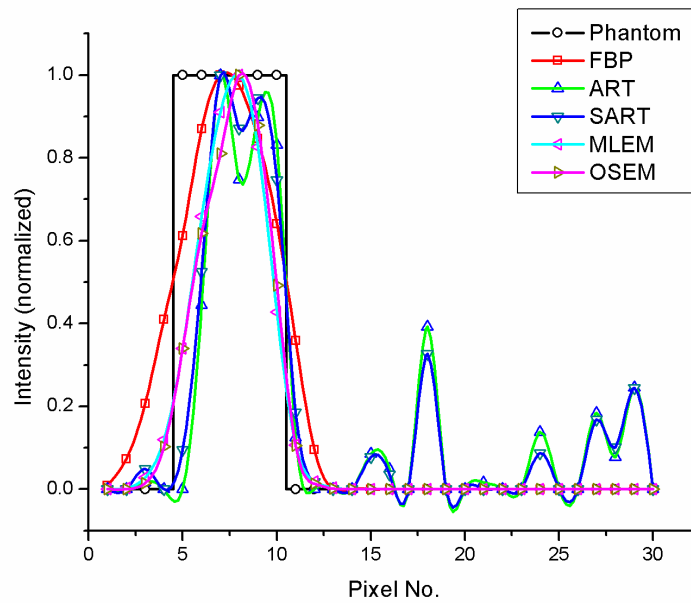
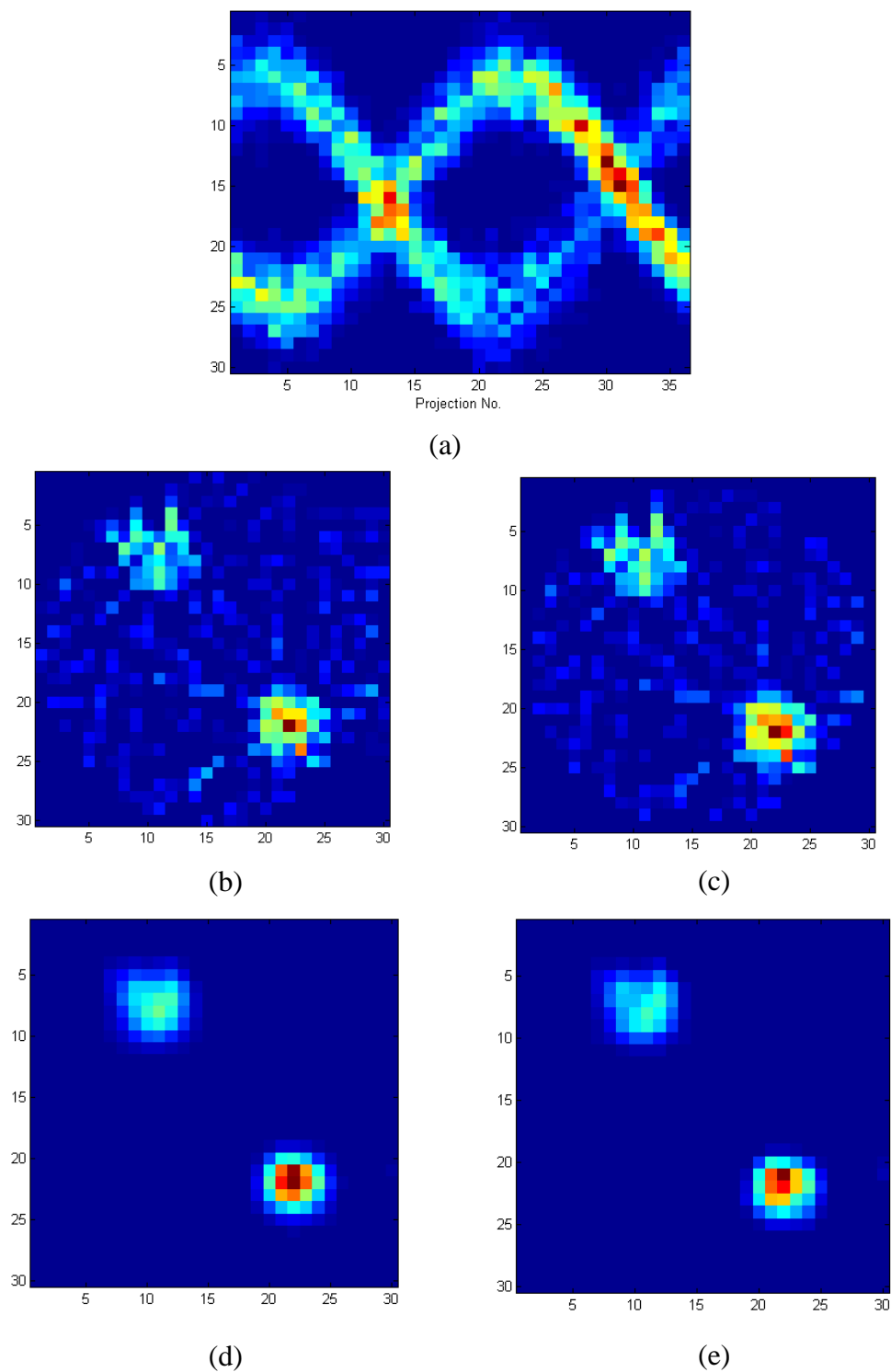


Fig.4.14 Line profile for reconstructed image using various reconstruction techniques



**Fig. 4.15** (a) Sinogram for collimator modeled projection with Poisson noise (b) ART (c) SART (d) MLEM (e) OSEM reconstructions

For MLEM and OSEM reconstruction, the image quality is quite good, almost noise-free and the boundaries of activity regions are very well-defined and square. The above observations are also evident from the line profiles shown in Fig. 4.14. One may, though, note that the reconstructed activity functions are not quite flat-topped even for MLEM and OSEM cases

### 4.2.3 Phantom 3: Distributed sources with non-uniform attenuation (2D)

Projections were computed at 100 angles over  $360^\circ$  ( $0^\circ, 3.6^\circ, 7.2^\circ, \dots, 356.4^\circ$ ) for line integral model and 36 angles over  $360^\circ$  ( $0^\circ, 10^\circ, 20^\circ, \dots, 350^\circ$ ) for collimator model. Figures 4.16 (a) and 4.17 (a) show the sinogram for line integral and collimator model respectively. Figures 4.16 (b) and 4.17 (b) show the analytically reconstructed images for line integral and collimator model respectively.

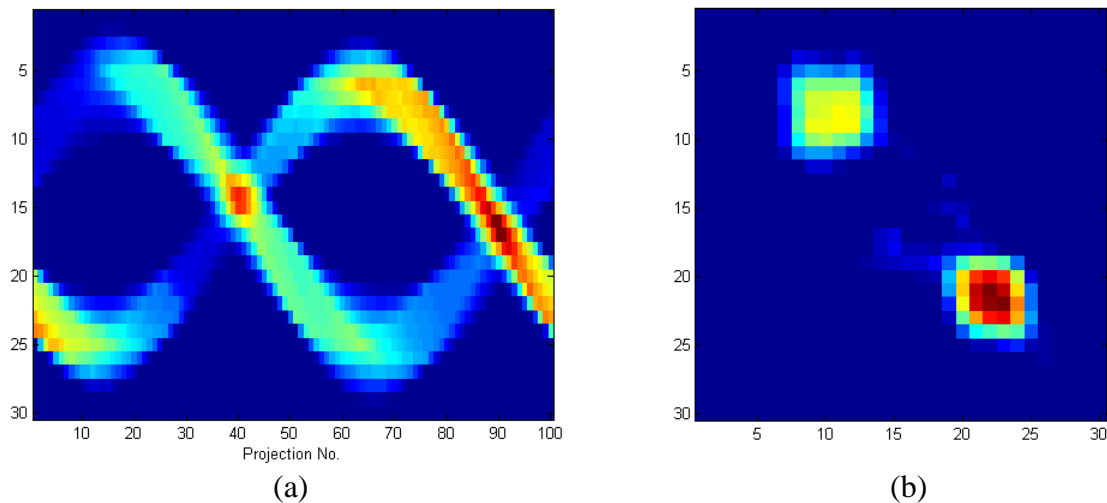


**Fig. 4.16** (a) Sinogram (b) Analytical reconstruction for line integral modelled projection

It is observed that though the boundary of the square shaped activity region is quite pronounced in Fig. 4.16 (b), the shape of the activity region is slightly distorted. This can be attributed to the fact that the attenuation inside the object is non-uniform and certain section of the sinogram show missing data / low intensity data (projections

between 0 to 10, between 30 to 40 and between 90 to 100) caused by high attenuation in certain part of the object (red region in Fig. 4.3 (b)). The missing data is somewhat compensated in the collimator model case (Fig. 4.17 (b)) because of non-zero contributions from neighbouring pixels. Figure 4.18 (a) shows the sinogram obtained after adding Poisson noise to the data which is used for iterative reconstruction. Figures 4.18 (b) and 4.18 (c) show the reconstructed activity function using ART and SART algorithms (100 iterations each; relaxation parameter 0.2) whereas Figures 4.18 (d) and 4.18 (e) show the reconstructed activity function using MLEM (25 iterations) and OSEM (4 subsets, 6 iterations) algorithms. Similar observations, as discussed in the previous sub-section, may be noted here also.

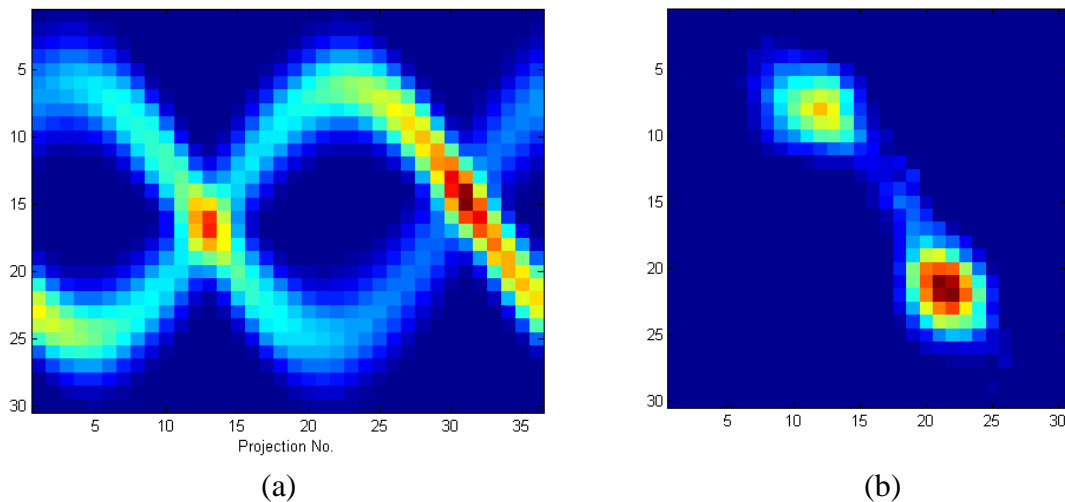


**Fig. 4.17 (a) Sinogram (b) Analytical reconstruction for collimator modelled projection**

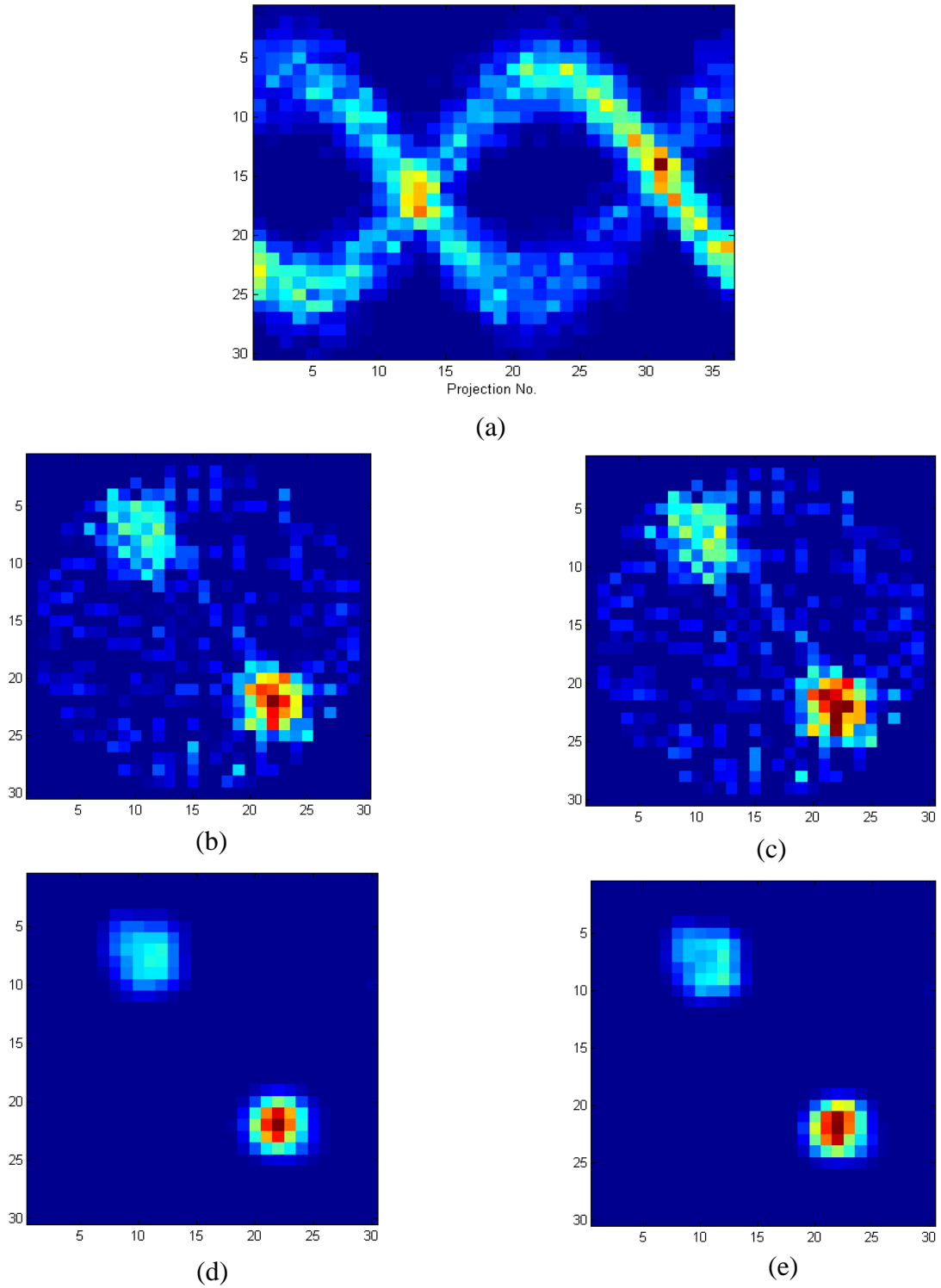


**Fig. 4.18** (a) Sinogram for collimator modeled projection with Poisson noise (b) ART (c) SART (d) MLEM (e) OSEM reconstructions

### 4.3 2D Reconstruction (Fan Beam)

The system matrix has been constructed for collimator modeled projections in fan beam geometry. The focal point of the fan beam is located at 100 cm from the origin (centre of the object). The projections have been reconstructed using analytical approach of Novikov and iterative reconstructions. For iterative reconstruction, the projection data is replaced by Poisson variate whose mean value is equal to the projection data value. The modified projection data is used to invert the equation  $g = Af$ .

#### 4.3.1 Phantom 1: Point sources

Projections were computed at 36 angles over  $360^\circ$  ( $0^\circ, 10^\circ, 20^\circ, \dots, 350^\circ$ ) for collimator model. Figure 4.19 (a) and 4.19 (b) present the sinogram and reconstructed image for analytical reconstruction. Since magnification is inherent in fan beam geometry, the object is reconstructed on a bigger grid (34 X 34; dimension 34 mm X 34 mm). The reconstructed image is later cropped to 30 X 30 image.

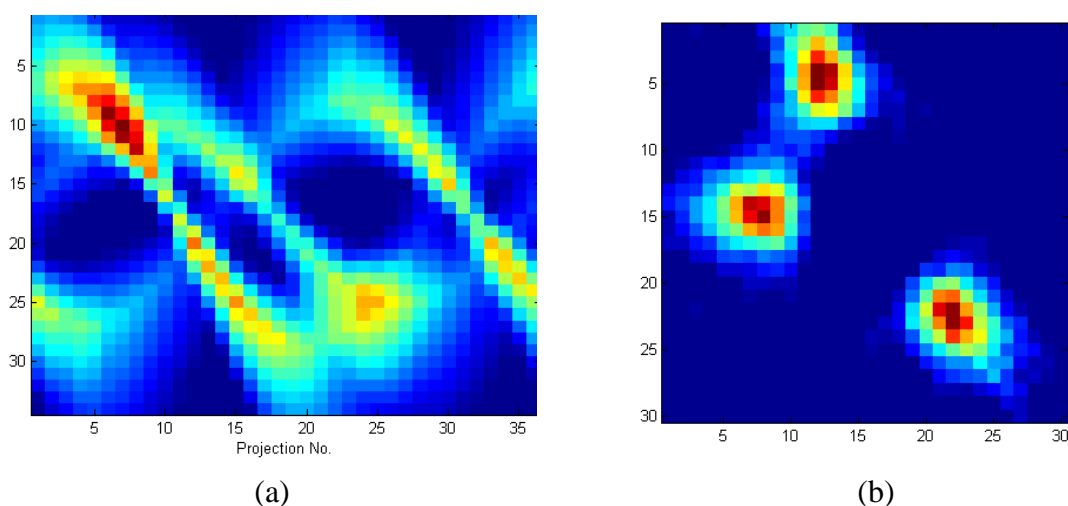


**Fig. 4.19** (a) Sinogram (b) Analytical reconstruction for collimator modelled projection in fan beam geometry

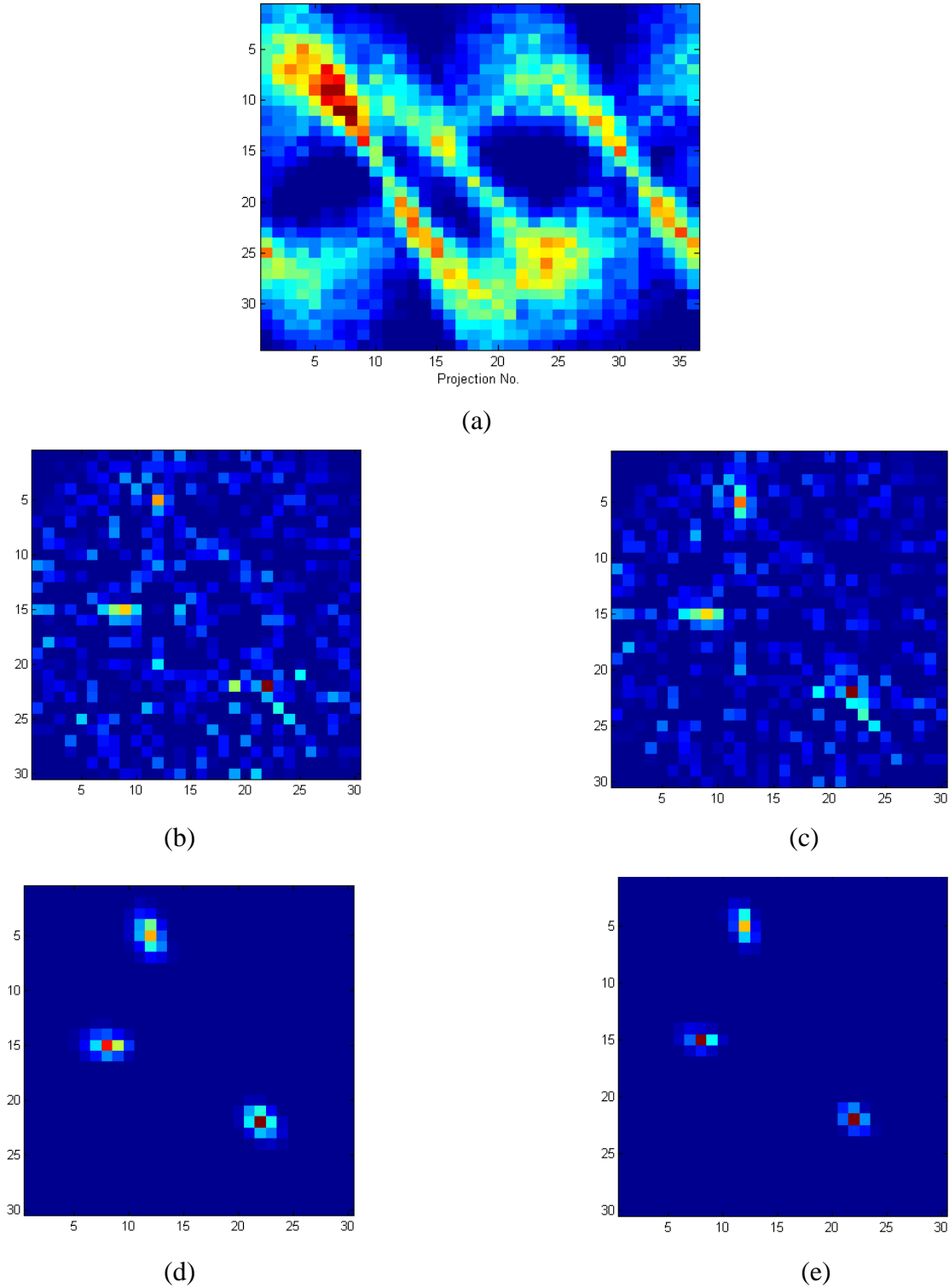


**Fig. 4.20** (a) Sinogram for collimator modeled projection with Poisson noise (b) ART (c) SART (d) MLEM (e) OSEM reconstructions for fan beam geometry

Fig. 4.20 (a) shows the noisy sonogram used for iterative reconstruction. Fig. 20 (b) and Fig. 20 (c) show the reconstructed activity function using ART and SART algorithms (80 iterations each; relaxation parameter 0.2) whereas Figures 4.20 (d) and 4.20 (e) show the reconstructed activity function using MLEM (20 iterations) and OSEM (4 subsets, 6 iterations) algorithms. It can be seen that the background is noisy in the case of ART and SART reconstruction whereas the background is low for MLEM and OSEM reconstruction. It can be observed that the reconstructed source positions match well with the original source positions.

### 4.3.2 Phantom 3: Distributed sources with non-uniform attenuation

Projections were computed at 36 angles over  $360^\circ$  ( $0^\circ, 10^\circ, 20^\circ, \dots, 350^\circ$ ) for collimator model. Figure 4.21 (a) and 4.21 (b) show the sinogram and analytically reconstructed image respectively.

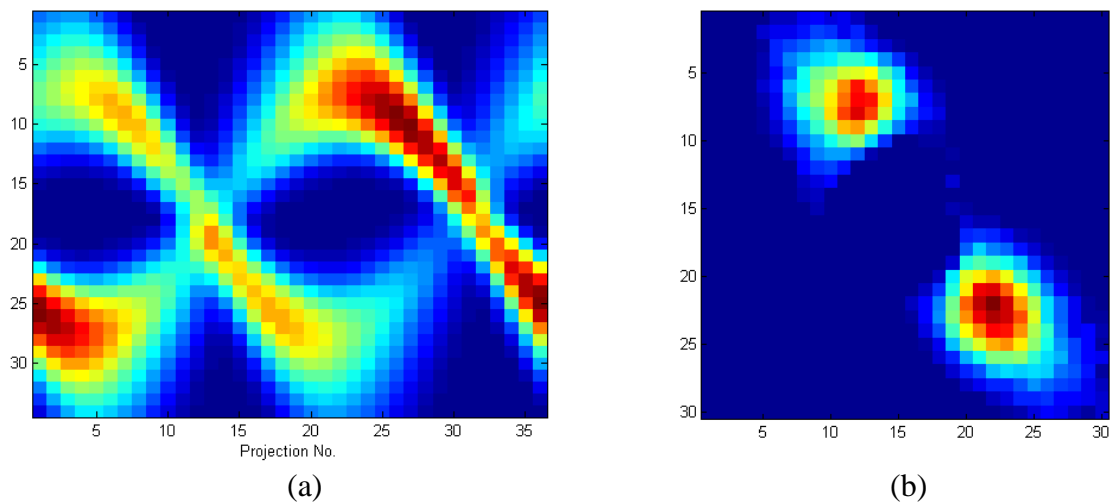


**Fig. 4.21** (a) Sinogram (b) Analytical reconstruction for collimator modeled projection in fan beam geometry

Figure 4.22 (a) shows the sinogram of noisy data which is used for iterative reconstruction. Figures 4.22 (b) and 4.22 (c) show the reconstructed activity function

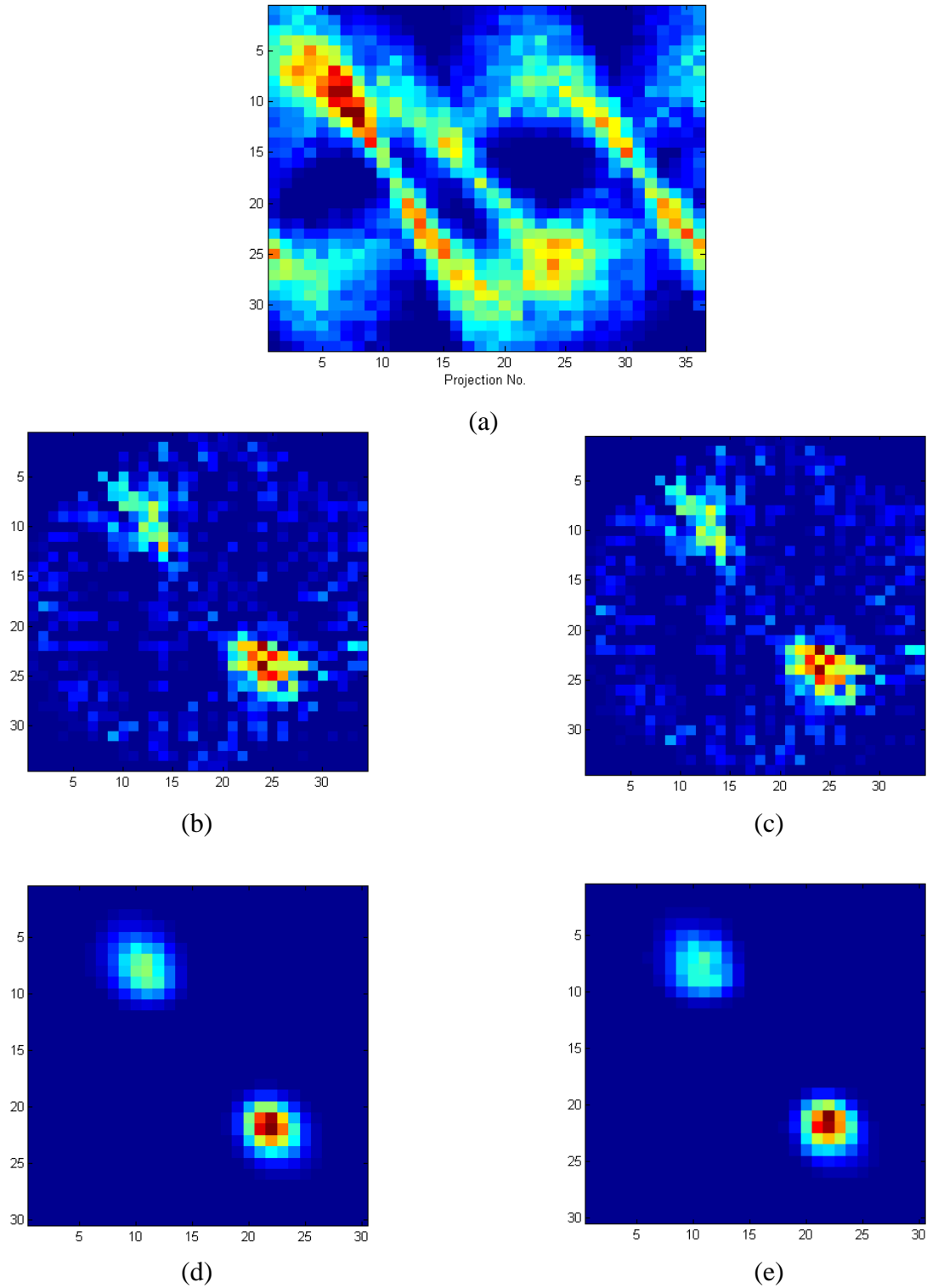


**Fig. 4.22** (a) Sinogram for collimator modeled projection with Poisson noise (b) ART (c) SART (d) MLEM (e) OSEM reconstructions for fan beam geometry

using ART and SART algorithms (80 iterations each; relaxation parameter 0.2) whereas Figures 4.22 (d) and 4.22 (e) show the reconstructed activity function using MLEM (25 iterations) and OSEM (4 subsets, 6 iterations) algorithms. Similar observations, as discussed in the previous sub-section, may be noted here also.

## 4.4 3D Reconstruction – Line Integral Model

Line integral model were used to generate projection data in parallel, fan and cone beam geometries. This was used to test the algorithms.

### 4.4.1 Phantoms 4 and 5: Waste drum

For numerical simulation purpose, phantoms 4 and 5 were discretized on a regular grid of 101 X 101 X 161 units. The physical dimension of each voxel is 5.5mm X 5.5mm X 5.5mm. The noise-free projections were generated for 300 views/rotations with angular step of  $1.2^\circ$  on 101 X 161 equally spaced detector points. The projections have been generated for three different geometries – parallel beam, fan beam and cone beam – using line integral model. For parallel beam geometry, Novikov's inversion formula has been

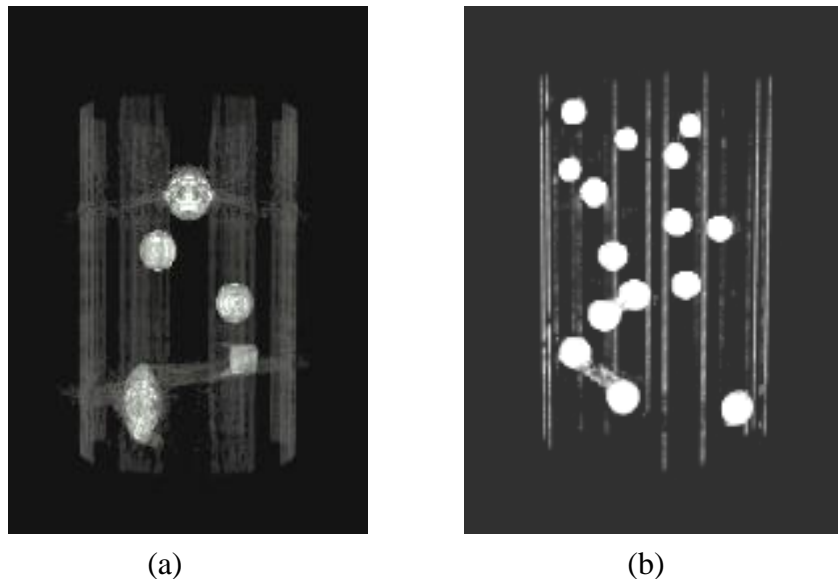


*Fig. 4.23 CT reconstructed image (a) Phantom 4 (b) Phantom 5*

used whereas for fan beam and cone beam geometries modified algorithm by You *et al* (as discussed in Chapter 2) have been used. The final 3D images in the case of parallel beam and fan beam have been obtained by stacking the respective 2D images. For fan-beam and cone-beam reconstructions, the focal length is taken as 100 cm.

Fig.4.24 and Fig.4.25 show the reconstructed activity of phantoms 4 and 5 respectively. For comparison, transmission CT images of phantoms 4 and 5 are shown in Figs.4.23 (a) and (b) respectively.

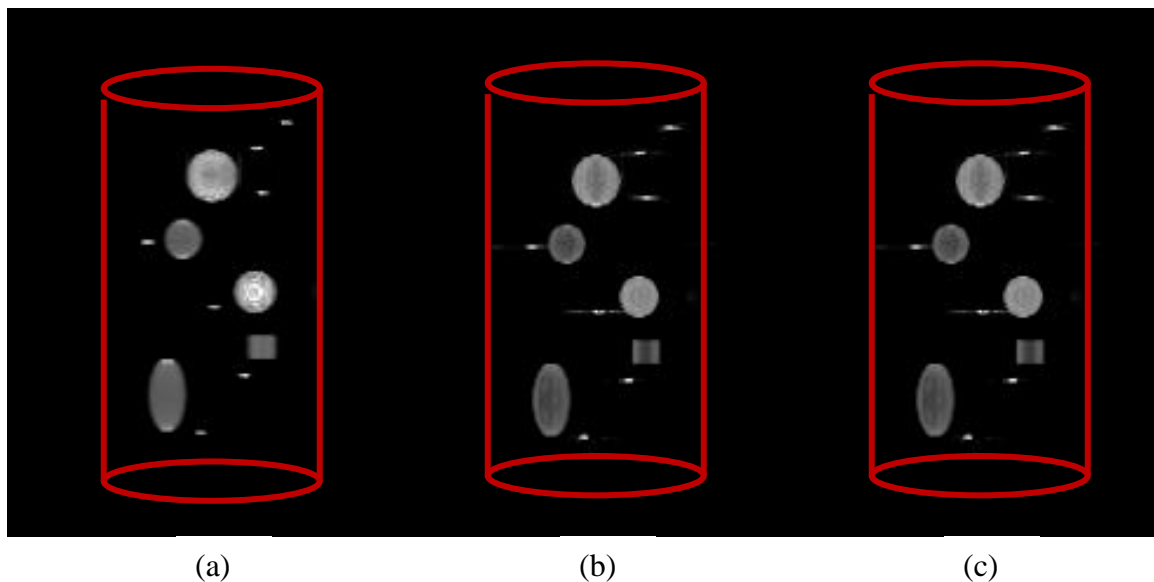


**Fig. 4.24** Reconstructed activity of Phantom 4 (a) Parallel beam (b) Fan beam (c) Cone beam

It can be seen that although the transmission images show the position of the sources and/or identify them, the emission images can distinguish the difference in activities as well. The 3D images were obtained from stacking 2D reconstructed images from different planes for parallel and fan-beam geometry and they are free of any distortion while the reconstruction artifact in cone beam geometry is clearly visible at the edges (Fig. 4.25 (c)). This is because of the fact that the cone beam projection data are

sufficient for exact reconstruction only in the plane of the cone-beam trajectory and approximate in other planes due to Tuy's data sufficiency condition. However the images correctly bring out the spatial location of radioactive elements embedded in the cylinder. As can be seen from Fig.4.25, even the reconstruction result for low activity source in high attenuating matrix is quite reliable and free from reconstruction artifacts. These results indicate the feasibility of getting good quality of reconstruction, provided the statistics is sufficient.

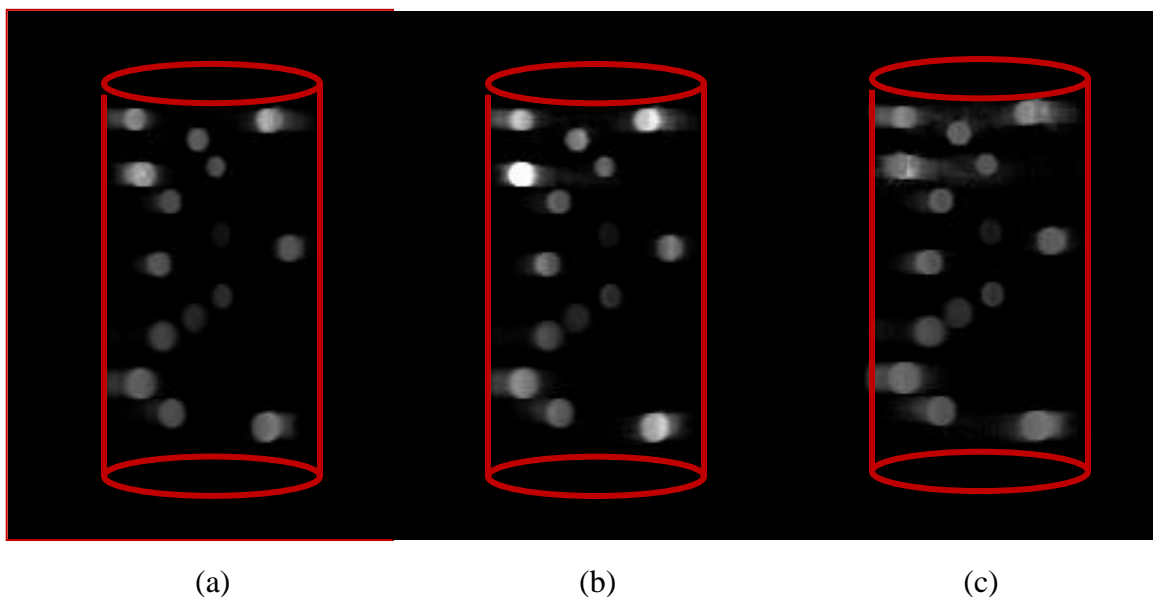


*Fig. 4.25 Reconstructed activity of Phantom 5 (a) Parallel beam (b) Fan beam (c) Cone beam*

#### 4.4.2 Phantom 6: PHWR fuel bundle

Figs. 4.26, 4.27 and 4.28 show the reconstructed activity of PHWR fuel bundle for parallel beam, fan beam and cone beam geometry respectively. These figures indicate the position of non-active rod with correct spatial location. In Fig.4.28 (b), it can be seen that the rods are not properly reconstructed. This is again due to the fact that the cone beam reconstruction is accurate only in the planes close to the cone-beam trajectory plane.

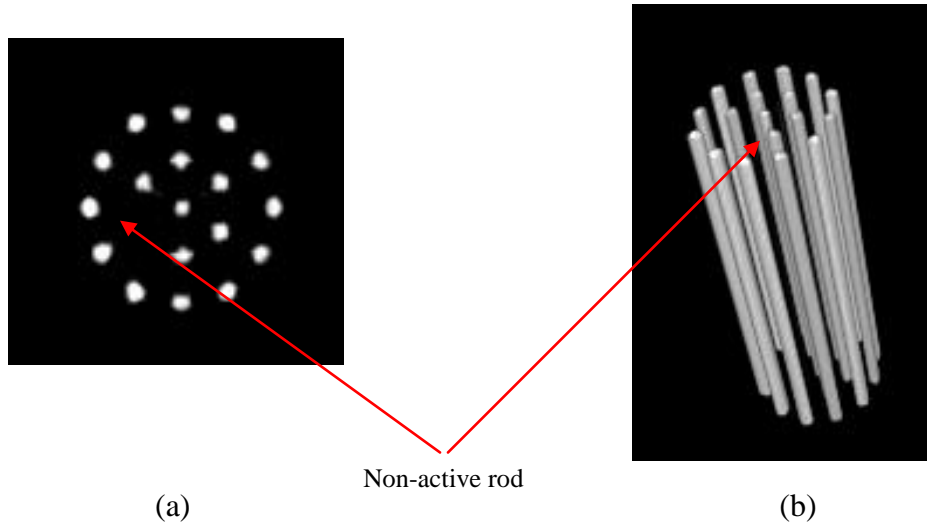


*Fig. 4.26 Parallel beam reconstruction: Reconstructed activity of PHWR fuel bundle (a) cross-sectional view (b) 3D view*

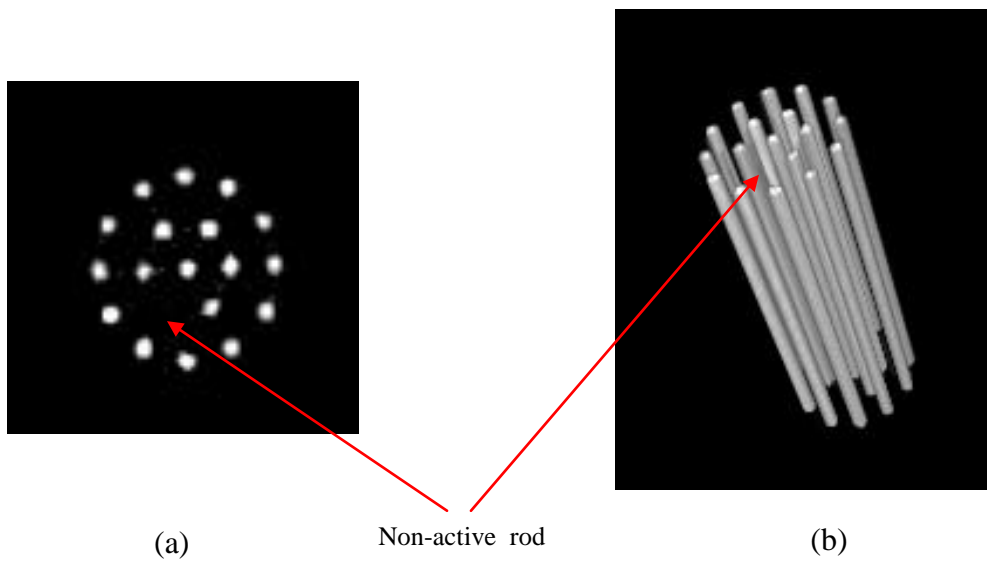


*Fig. 4.27 Fan beam reconstruction: Reconstructed activity of PHWR fuel bundle (a) cross-sectional view (b) 3D view*

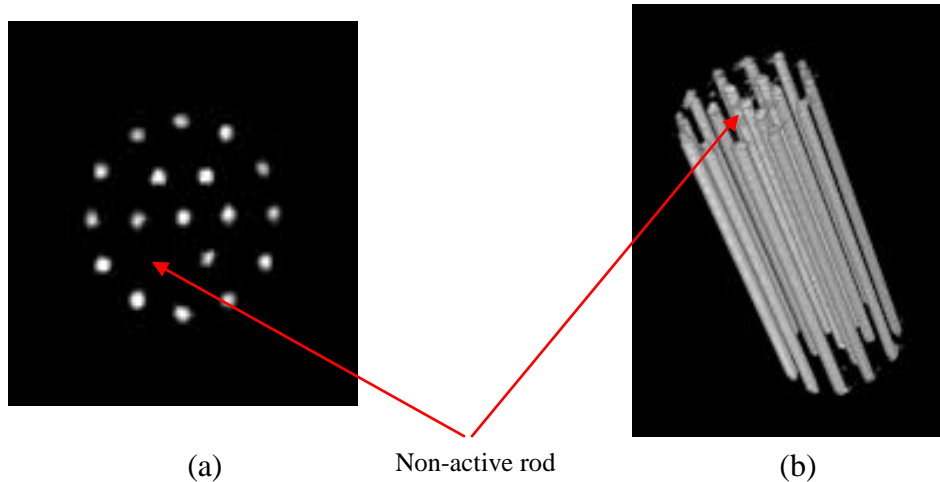


*Fig. 4.28 Cone beam reconstruction: Reconstructed activity of PHWR fuel bundle (a) cross-sectional view (b) 3D view*

## 4.5 3D Reconstruction – 3D Collimator Model

In this section, the projection data for the phantoms have been generated using a 3D collimator model. The data thus generated is then reconstructed in three ways:

- Filtered Back Projection (Novikov)
- 2D (Stacked) MLEM
- Fully 3D MLEM

For FBP reconstruction, the effect of collimator is not taken into account so the effect of collimator blurring should be present in the reconstructed image.

For 2D (stacked) reconstruction, 2D system matrix corresponding to 2D collimator is generated for each z-slice. This 2D system matrix is then used for MLEM reconstruction. This method is computationally less intensive but does not reduce inter-slice blurring.

For fully 3D reconstruction, 3D system matrix corresponding to 3D collimator is generated for the whole object. This 3D system matrix is then used for MLEM

reconstruction. This method requires large storage space for matrices, is computationally quite intensive and much harder to implement. However, fully 3D reconstruction should reduce both intra-slice and inter-slice blurring.

#### 4.5.1 Phantom 1 (3D): Point sources

Phantom 1 is modified such that the three sources are now located in different  $z$ - planes (3, 6 and 9) but their  $(x, y)$  position remains the same. Fig.4.31 shows the three  $z$ -planes of the phantom. All other planes do not have any source.

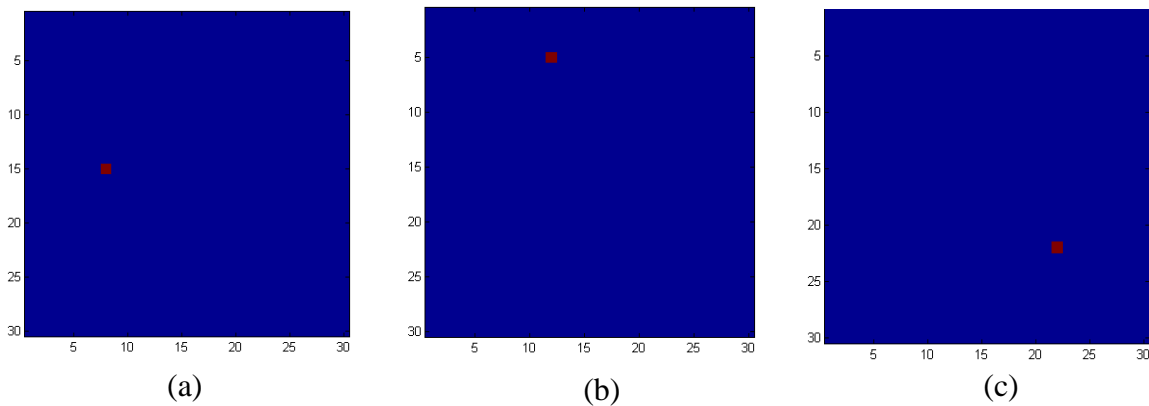


**Fig. 4.29** Phantom 1 (3D) (a) Slice 3 (b) Slice 6 (c) Slice 9

The planar projections are generated at 20 angular positions using 3D collimator model to simulate experimental data. The projections are then used to reconstruct activity distribution using filtered backprojection for each  $z$ -plane. The reconstructed 2D slices are shown in Fig. 4.30. Fig.4.33 (a) shows 3D view obtained by stacking reconstructed slices horizontally. It is observed from these figures that the point sources are blurred in both the horizontal and vertical directions and appears spherical. The streaks observed are due to the fact that only few angular projections are used.

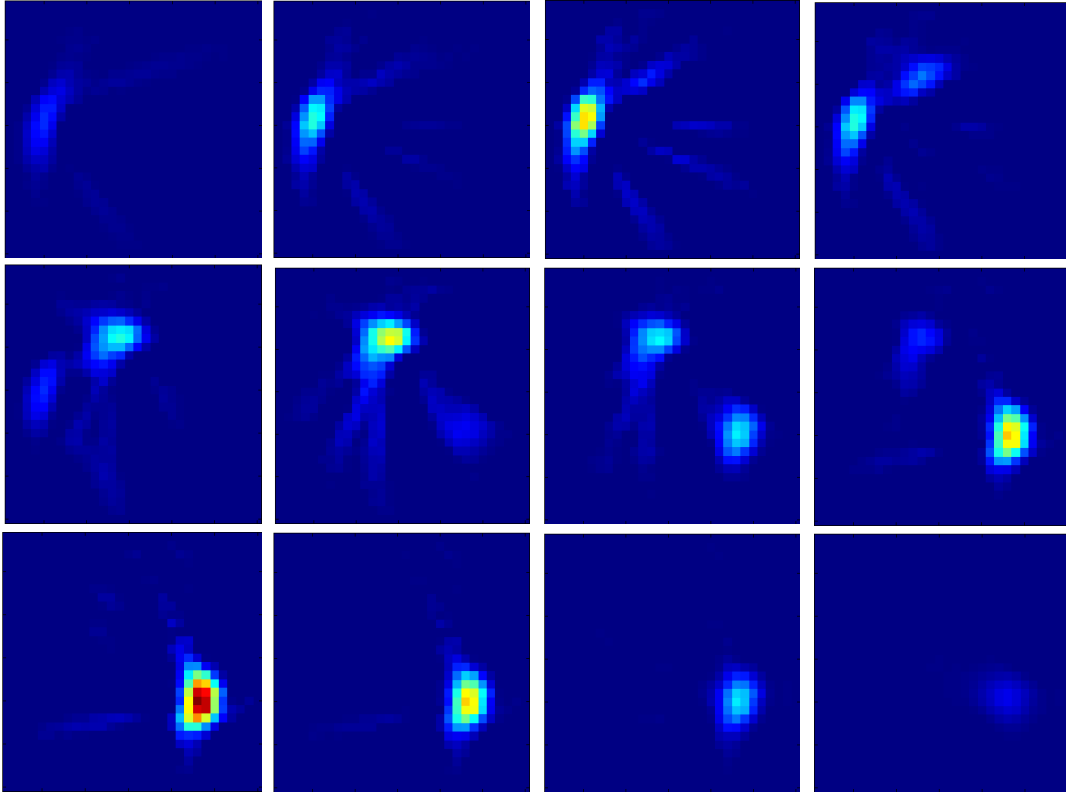


*Fig. 4.30 Reconstructed activity using FBP for different z-slices*

For 2D (stacked) reconstruction, angular projections are used to reconstruct each horizontal plane by MLEM algorithm using 2D system matrix. Figure 4.31 shows reconstructed 2D slices. Again, the 2D reconstructed planes are stacked horizontally to obtain 3D volume (Fig. 4.33 (b)). It can be seen from these figures that blurring within the plane has reduced. However, the intra slice blurring has not reduced significantly. The point source now appears as an ellipsoid.

For fully 3D reconstruction, angular projections were modified by adding Poisson noise. The noisy data is then used to reconstruct activity distribution by MLEM algorithm

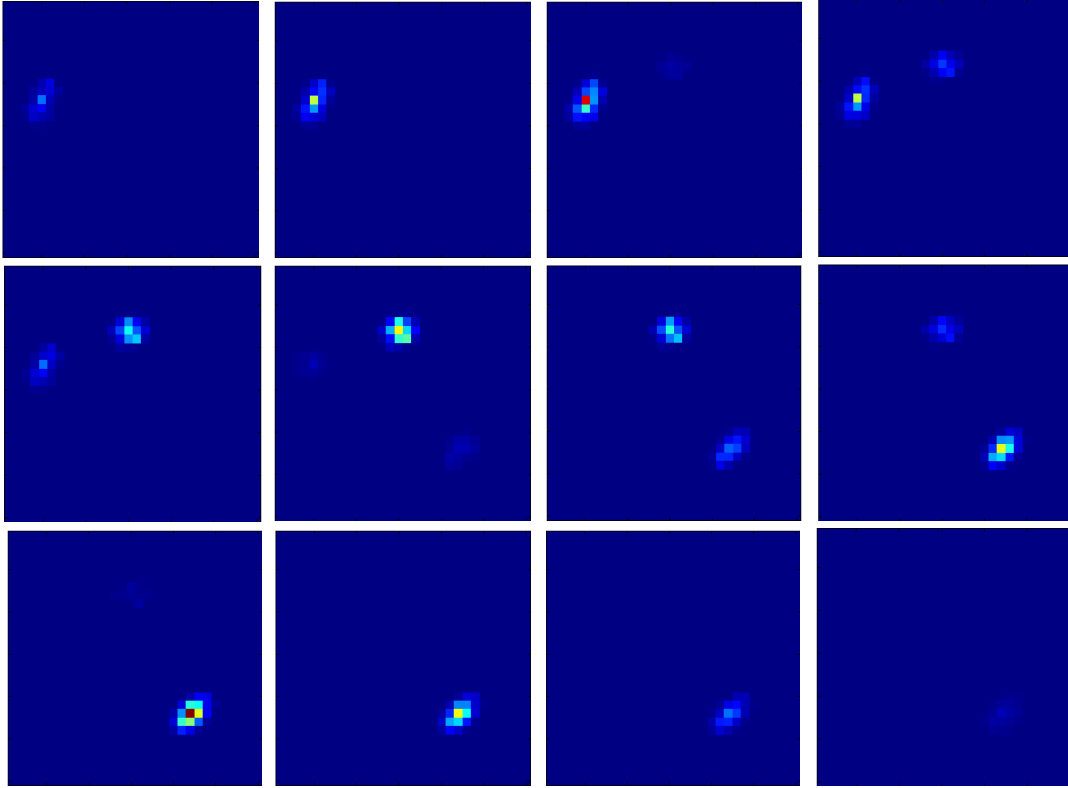


*Fig. 4.31 Reconstructed activity using 3D (stacked) MLEM for different z-slices*

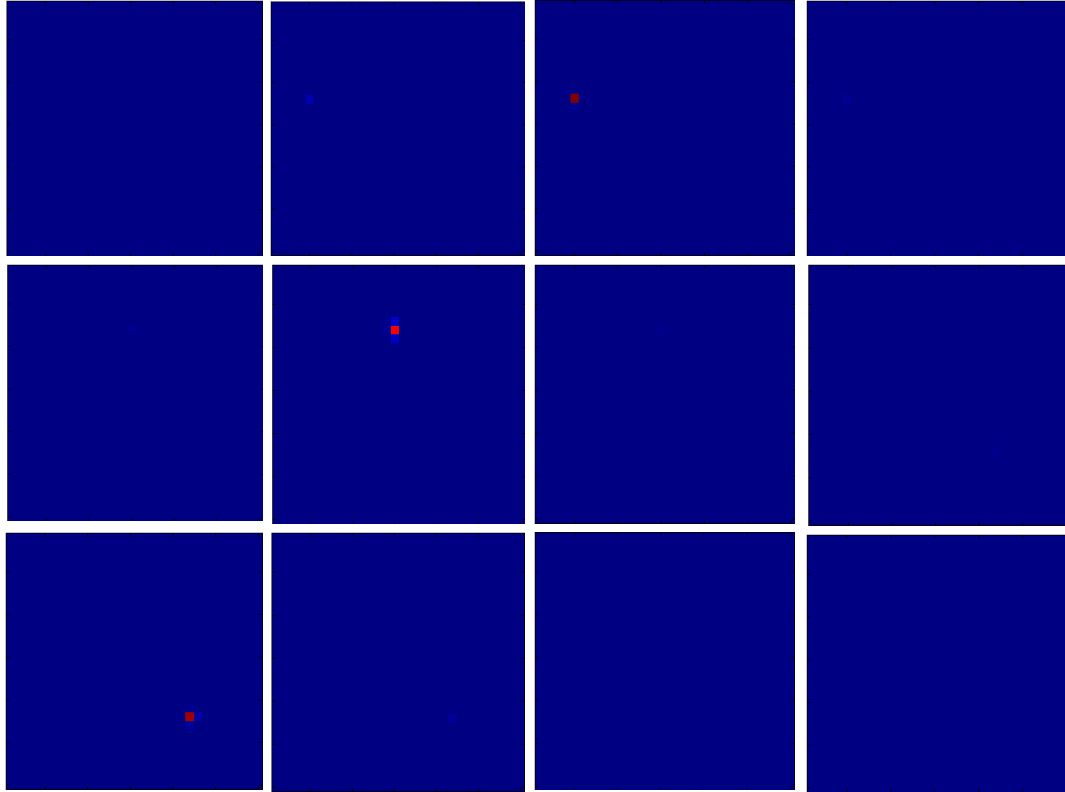


*Fig. 4.32 Reconstructed activity using fully 3D MLEM for different z-slices*

using 3D system matrix. Figure 4.32 shows reconstructed 2D slices and Fig.4.33 (c) shows the 3D volume. Clearly, both inter-slice and intra-slice blurring have been considerably reduced and the sources appear almost as point sources.

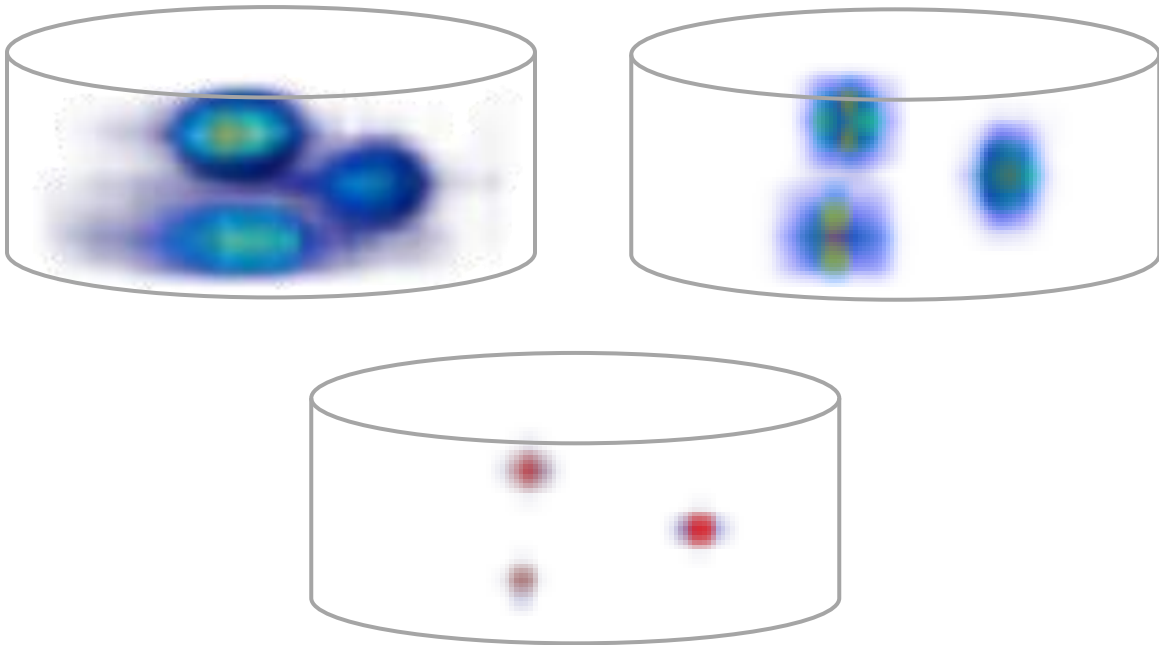


*Fig. 4.33 Reconstructed 3D volume using (a) FBP (b) 2D MLEM (c) Fully 3D MLEM*

## 4.6 Error Estimation of Reconstructed Image

In order to evaluate the quality of reconstructed image, following performance criteria were evaluated:

### a) Mean Squared Error (MSE)

It is defined as the average of the squared pixel difference as

$$MSE = \frac{1}{N} \sum_{i=1}^N (\hat{f}_i - f_i)^2$$

$\hat{f}_i$  and  $f_i$  are the reconstructed and true activity value for  $i^{th}$  pixel respectively and  $N$  is the total number of pixels. MSE is a measure of the average discrepancy of reconstructed image with respect to the original image.

**b) Contrast (C)**

The contrast between activity and background is defined as

$$C = \frac{|S - B|}{S + B}$$

$S$  is the average pixel value in the activity distribution and  $B$  is the average pixel value in the background distribution.

**c) Spatial deviation**

It is measured as the difference between the centre of activity region in true and reconstructed images. The centre of the activity region is found by fitting a Gaussian function for each activity region.

**d) Deviation in reconstructed activity**

The deviation in quantitative value of reconstructed activity is measured as a percentage of the true activity value and is defined as

$$\frac{|\mathbf{True\ activity} - \mathbf{Reconstructed\ activity}|}{\mathbf{True\ activity}} \times 100\%$$

TABLE 4.4 Image assessment parameters for different reconstructed images

Phantom	Recon. Algorithm	MSE ( $\times 10^{-3}$ )	Contrast	Spatial Deviation		Deviation in Recon. Activity (%)
				Recon. Activity centre	Deviation (in pixels)	
Phantom 1 (Parallel)	FBP	3.3	0.95	(5, 13)	1	16.9
				(15, 8)	0	16.4
				(22, 21)	1	14.4
	ART	1.8	0.58	(5, 12)	0	14.3
				(15, 8)	0	20.2
				(22, 22)	0	19.1
	SART	1.8	0.70	(5, 12)	0	7.9
				(15, 8)	0	15.6
				(22, 22)	0	21.0
	MLEM	0.9	1.00	(5, 12)	0	6.4
				(15, 8)	0	0.7
				(22, 22)	0	1.8
	OSEM	0.7	1.00	(5, 12)	0	4.7
				(15, 8)	0	0.2
				(22, 22)	0	0.1
Phantom 1 (Fan)	FBP	3.2	0.86	(4, 12)	1	22.0
				(15, 8)	0	25.2
				(23, 22)	1	1.8
	ART	3.2	0.79	(5, 12)	0	8.3
				(15, 9)	1	20.0
				(22, 22)	0	2.2
	SART	2.6	0.75	(5, 12)	0	8.6
				(15, 9)	1	8.8
				(22, 22)	0	3.5
	MLEM	2.0	1.00	(5, 12)	0	11.8
				(15, 8)	0	11.5
				(22, 22)	0	0.5
	OSEM	1.5	1.00	(5, 12)	0	6.5
				(15, 8)	0	5.9
				(22, 22)	0	1.9
Phantom 1 – 3D	FBP	3.1	0.85	(5, 12, 6)	1	8.5
				(15, 8, 3)	1	9.6
				(22, 22, 9)	0	7.5
	3D (Stacked) MLEM	2.2	0.98	(5, 12, 6)	0	5.4
				(15, 8, 3)	0	2.8
				(22, 22, 9)	0	3.6
	Fully 3D MLEM	0.8	1.00	(5, 12, 6)	0	0.1
				(15, 8, 3)	0	0.5
				(22, 22, 9)	0	0.2

## 4.7 Effect of Collimation

To study the effect of collimator blurring, a point source was simulated inside a homogeneous circular area with linear attenuation coefficient equal to  $0.05 \text{ cm}^{-1}$  inside

the circle and 0 outside. The phantom is discretized on a 30 x 30 grid. 36 projections were acquired uniformly over 360° using collimator model. The collimator width is taken to be 10 mm. The collimator length is varied from 10 mm to 200 mm.

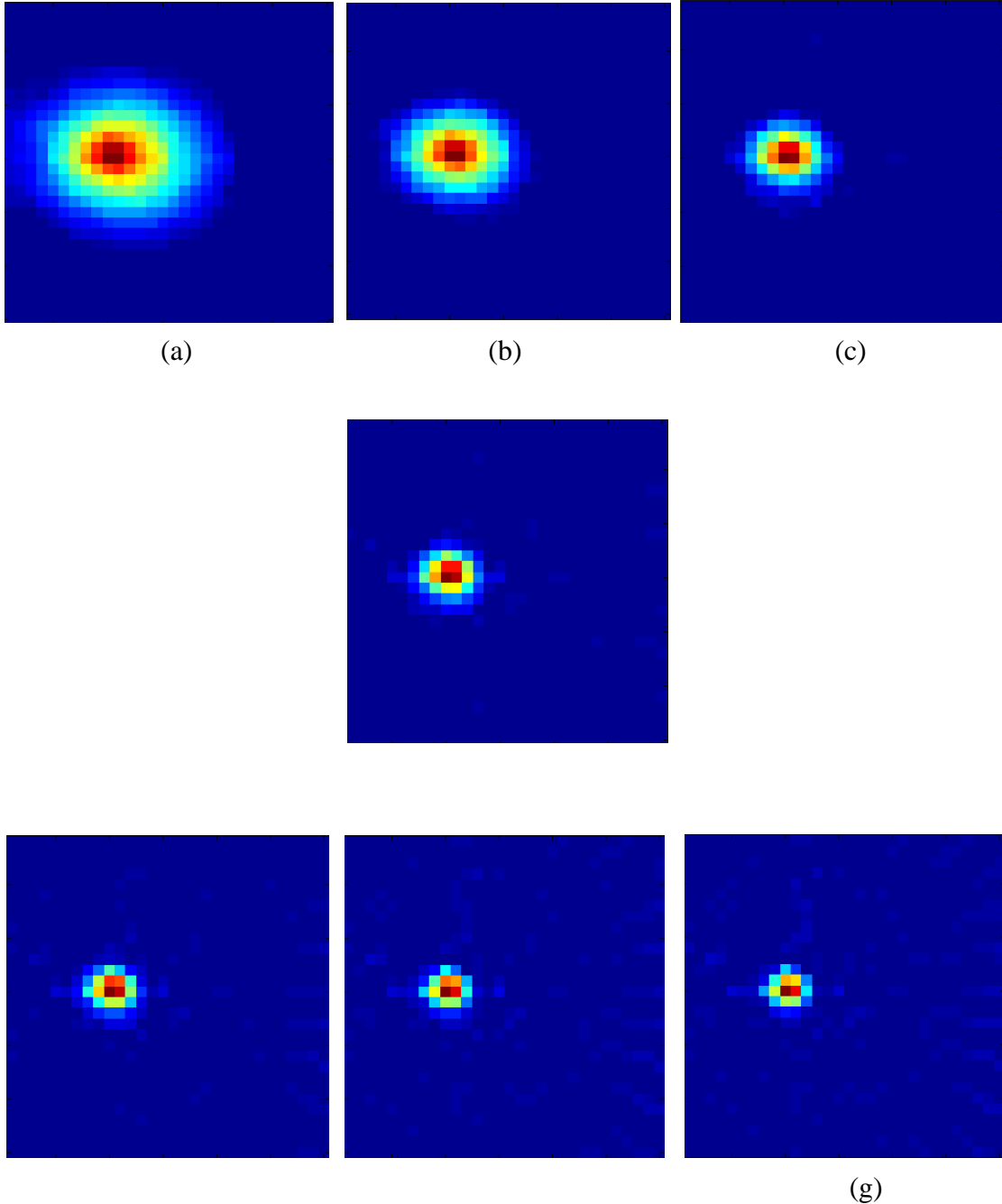


*Fig. 4.34 FBP reconstructed images showing the effect of collimator blurring for collimation ratio of (a) 1 (b) 2.5 (c) 5 (d) 7.5 (e) 10 (f) 15 (g) 20*

The projection data generated is used to reconstruct the image using analytical technique without any correction for collimator blurring. Fig. 4.34 (a) – (g) show the reconstructed image corresponding to effective collimation ratio ( $L/d$ ) of 1, 2.5, 5, 7.5, 10, 15 and 20 respectively. The spread or collimator blurring is easily manifested in the images. It is also observed that the blurring decreases with an increase in  $L/d$  ratio. This can be understood easily. In analytical reconstruction, it is assumed that each detector accepts contribution of photons along straight parallel ray paths (infinite collimation). When the collimator is finite, the detectors record contribution from other pixels which do not lie on the ray path as well. During backprojection, these contributions are attributed to pixels which lay on the original ray path which thus results in blurring. Fig. 4.35 shows the variation of FWHM as a function of collimation ratio. The FWHM is computed by fitting a Gaussian curve to the spatial line profile for images in Fig.4.34.

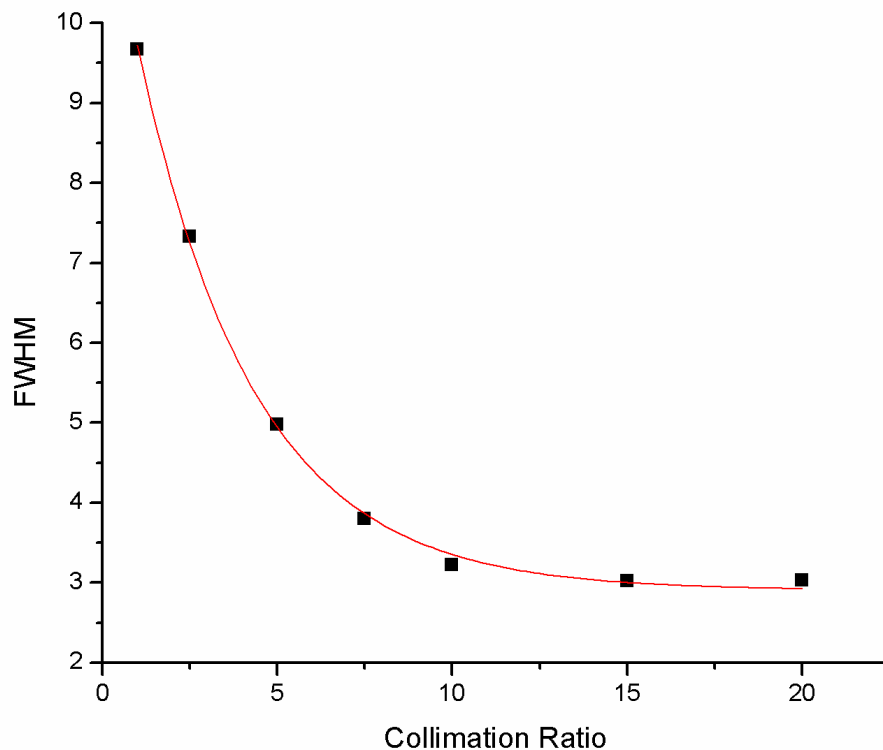


*Fig. 4.35 FWHM as a function of collimation ratio*

## **4.9 Discussion**

In this chapter, different algorithms have been tested for simulated phantoms. Analytical reconstruction technique has been used for both line integral and collimator modelled projections. The reconstruction in the latter case leads to collimator blurring. The collimator modelled projections were also reconstructed using algebraic techniques (ART and SART) and statistical techniques (MLEM and OSEM). It is observed that the collimator blurring is reduced in all these techniques. However, ART and SART images are generally noisy and also require larger number of iterations to converge. MLEM and OSEM images are much less noisy and also require lesser number of iterations to converge.

Simulations were also carried out to test fully 3D system matrix. Analytical reconstruction for 3D objects show blurring both within the slice and above and below the reconstruction lane also. Using 2D system matrix helps in reducing intra-slice blurring only. However, a fully 3D matrix reduces both intra-slice as well as inter-slice blurring.

It may be noted here that the method of generating projection data using collimator model for iterative reconstruction technique is not ideal as the same model is also used for reconstruction. Although some Poisson noise has been added to test the reconstruction technique, a better way is to use an independent model (say, using Monte Carlo methods) to create the projection data. Another way of overcoming this problem is to test the reconstruction techniques using experimental data. This shall be explored in the next chapter.

# **Experimental Studies**

In this chapter, we have described the experimental techniques and a variety of test samples with varying degree of complexity which has been analyzed to optimize different experimental parameters. For 2D reconstruction, sources in air (no attenuation) and sources in solid perspex disc have been considered. Both analytical and iterative techniques have been used for reconstruction. For 3D objects, both 2D and fully 3D reconstruction have been performed. Mock waste drums with non-homogeneous matrix have been used. Both parallel and fan beam data acquisition geometries have been explored.

The results have been divided into two sections. Section I discusses the experimental results using  $^{137}\text{Cs}$  passive sources. Section II deals with the application of Active & Passive CT for nuclear waste assay. Experimental results with  $^{239}\text{Pu}$  in mock waste drums shall be discussed.

## **5.1 Experimental set-up**

The experimental set-up consists of the following:

- Sample Stage
- Sample / object matrix with source
- Detector and associated electronics
- Collimator
- Data Acquisition system

- (External) Active source (for transmission measurement)

These shall be briefly discussed below.

### 5.1.1 Sample Stage

The object (waste drum) is placed on a 3-axis sample manipulator. During the scanning, the drum is rotated and translated whereas the source-detector pair is elevated for vertical scanning. It can scan an object of diameter 600 mm (maximum) and 1000 mm height and can handle object / drum weighing upto 500 kg.

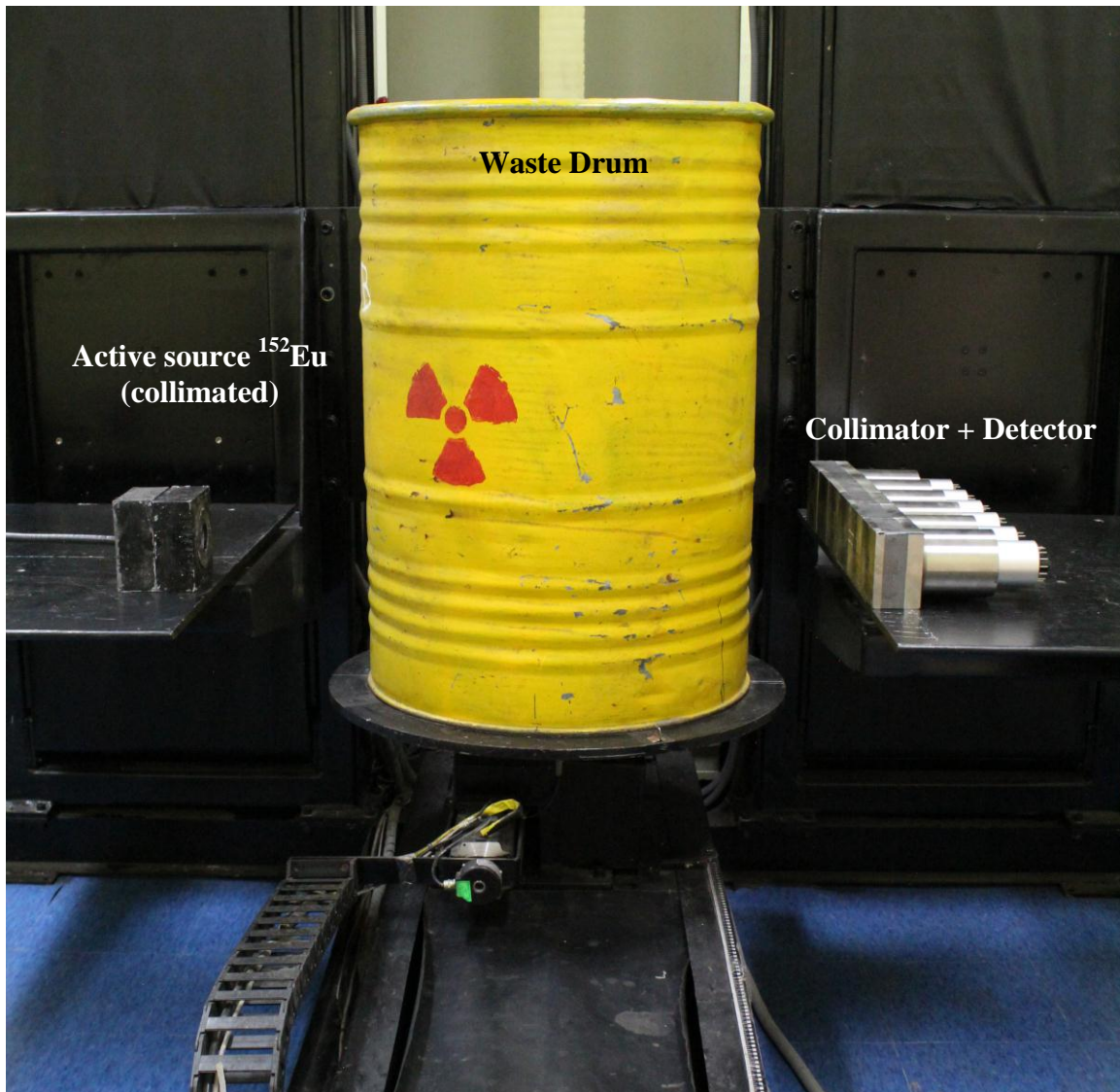


*Fig. 5.1 Experimental set-up for 3D imaging*

### 5.1.2 Sample (Matrix)

#### A. Sample: Hollow SS rods

18 Hollow SS rods of diameter 10 mm and height 50mm are arranged on a thin Perspex plate at indexed positions arranged in two concentric circles of radii 60 mm and 120 mm respectively as shown in Fig.5.2 (a). A schematic arrangement is shown in Fig.5.2 (b).

The sources are placed inside the SS rods at different indexed locations.

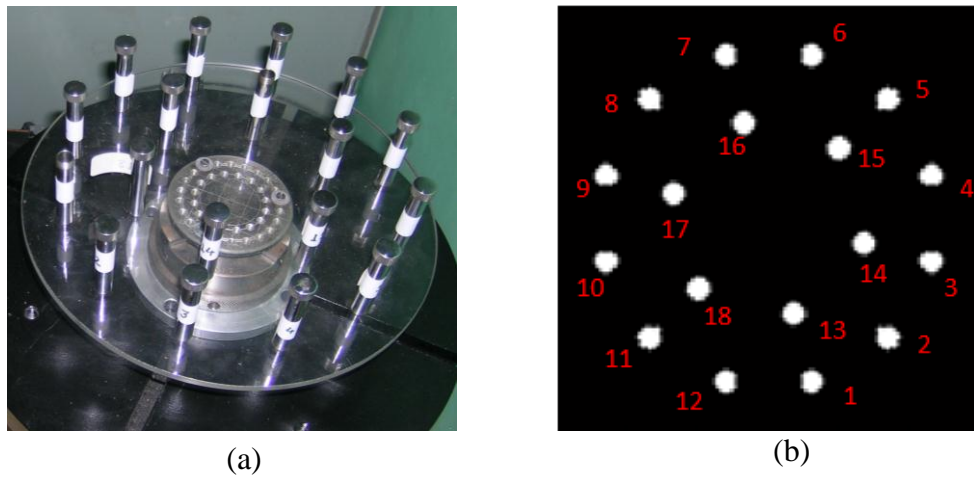


*Fig. 5.2 Hollow SS rods (a) Photograph (b) Cross-section (schematic)*

#### B. Sample: Solid Perspex disc with indexed holes

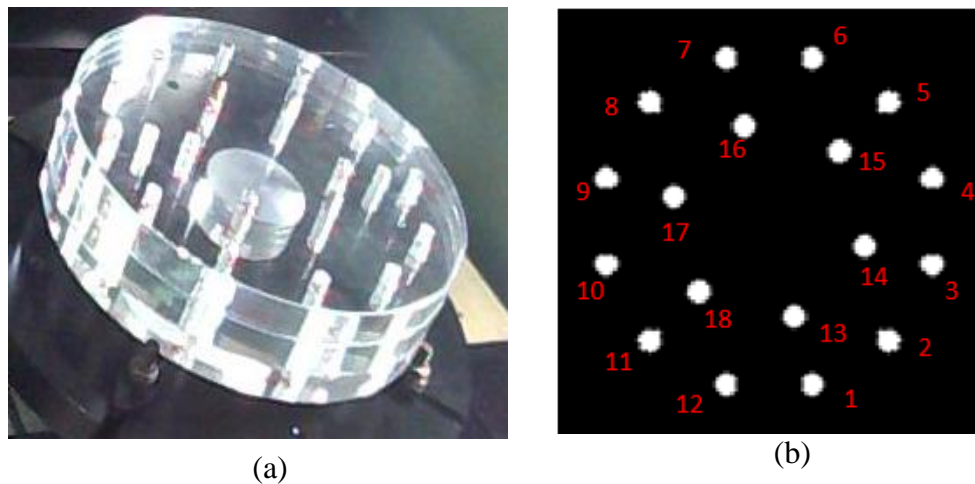


*Fig. 5.3 Solid perspex discs with indexed holes (a) Photograph (b) Cross-section (schematic)*

Solid Perspex disc of diameter 300mm and thickness 25mm with 18 indexed holes arranged in two concentric circles of radii 60mm and 120mm respectively is used as shown in Fig.5.3 (a). A schematic arrangement is shown in Fig.5.3 (b). The sources are placed inside the holes at different indexed locations. Multiple discs stacked vertically have been used for 3D imaging.

**C. Sample: Aluminum drum**

An aluminum drum (Fig. 5.4) of diameter 300mm and height 600mm (wall thickness 2mm) filled with different materials is used for 3D imaging. The sources are placed inside the drum at various locations.

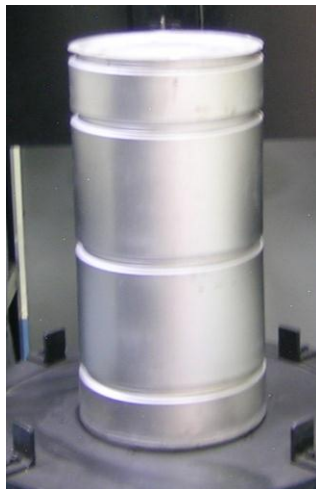


*Fig. 5.4 Aluminum drum*



*Fig. 5.5 SS waste barrel*

**D. Sample: SS waste barrel**

SS waste barrel (Fig. 5.5) of diameter 580 mm and height 850 mm (wall thickness 5mm) filled with different materials is used for 3D imaging. The sources are placed inside the drum at various locations.

### 5.1.3 Source (Passive)

Three  $^{137}\text{Cs}$  sources (Emission energy: 662 keV; Branching ratio (for 662 keV): 0.85) are used for the experiments. The sources are kept at different positions inside the sample for different configurations. Table 5.1 lists the details of the sources used. Fig.5.6 shows the decay scheme of  $^{137}\text{Cs}$

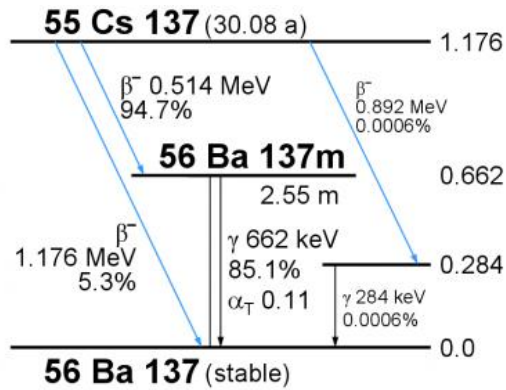


Fig. 5.6 Decay scheme of  $^{137}\text{Cs}$

TABLE 5.1 Details of passive  $^{137}\text{Cs}$  sources used

Source	Activity (MBq)
A	26.7
B	21.0
C	37.8

### 5.1.4 Active Source

An external (collimated) gamma source  $^{152}\text{Eu}$  (33mCi) is used for ACT. The source is housed in a portable industrial gamma radiography exposure device (ROLI-3) <sup>[122]</sup> which

is remotely operated. The collimation of the source reduces scatter and helps direct radiation towards the detector.

### 5.1.5 Detector

#### A. NaI(Tl)

NaI(Tl) detectors (cylindrical) of dimension 3'' (diameter) X 1'' (thickness) (Amcrs) are used. Fig. 5.7 shows the energy resolution of these detectors as a function of energy in the range 100-1500 keV. The energy resolution at 662 keV is 8.8 %

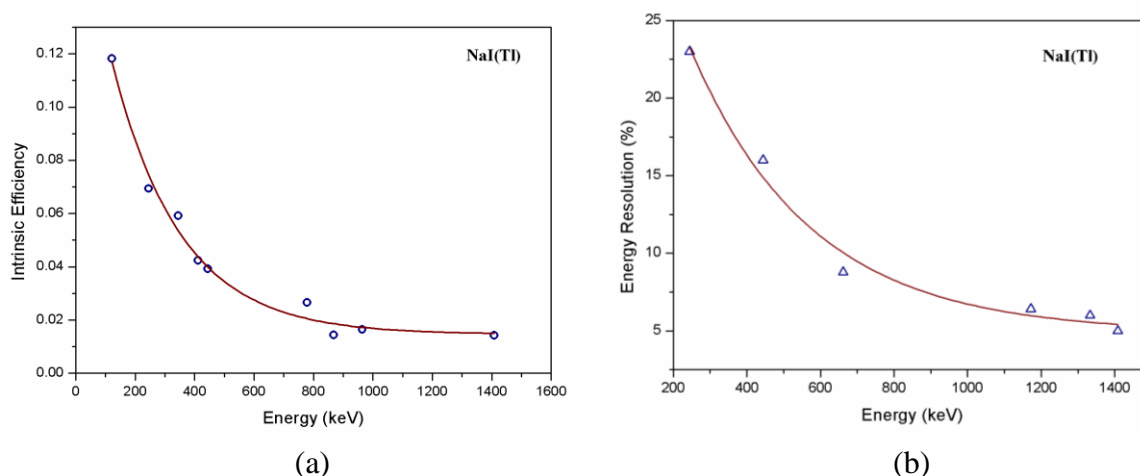


*Fig. 5.7 (a) Intrinsic photopeak efficiency and (b) Energy resolution of 3'' X 1'' NaI(Tl) as a function of energy*

#### B. LaBr<sub>3</sub>(Ce)

A novel feature of the thesis is the use of LaBr<sub>3</sub>:Ce detectors for SPECT imaging. LaBr<sub>3</sub>(Ce) detectors (cylindrical) of dimension 1'' (diameter) X 1'' (thickness) (BrilLanCe 380 : Saint-Gobain) are used. Fig.5.8 shows intrinsic photopeak efficiency of these detectors as a function of energy. Fig. 5.9 presents the variation of energy resolution of these detectors with energy. The energy resolution at 662 keV is 3.4 %.

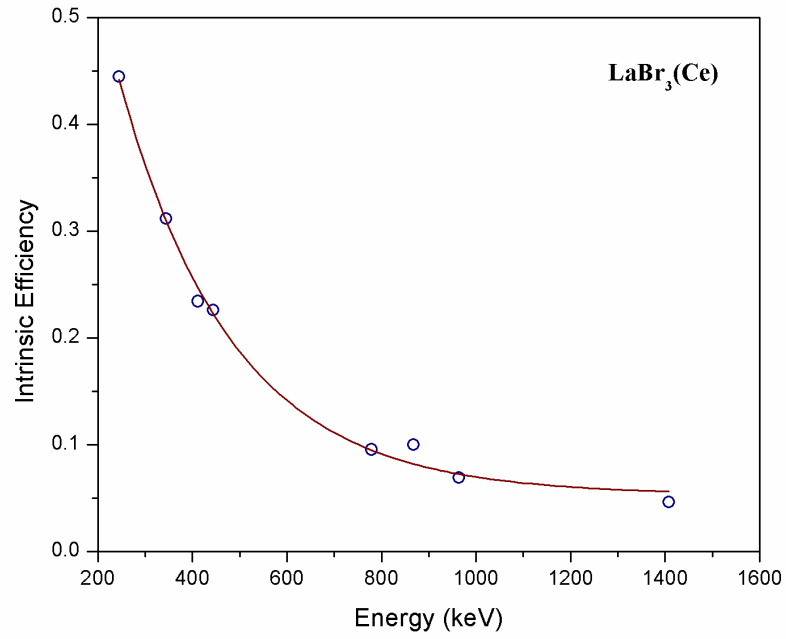


Fig. 5.8 Intrinsic photopeak efficiency of 1" X 1" LaBr<sub>3</sub>(Ce) as a function of energy

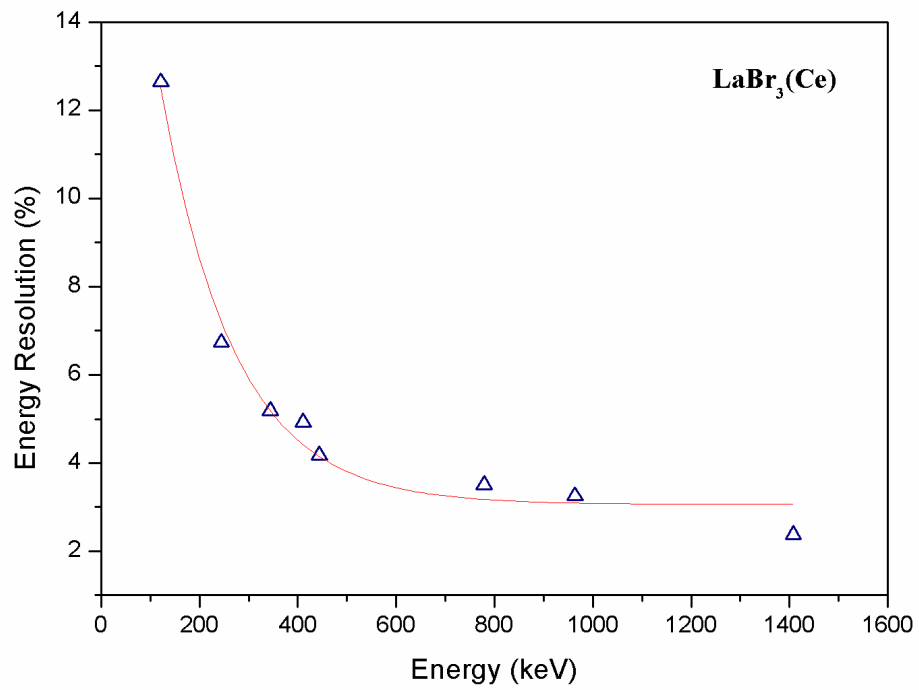
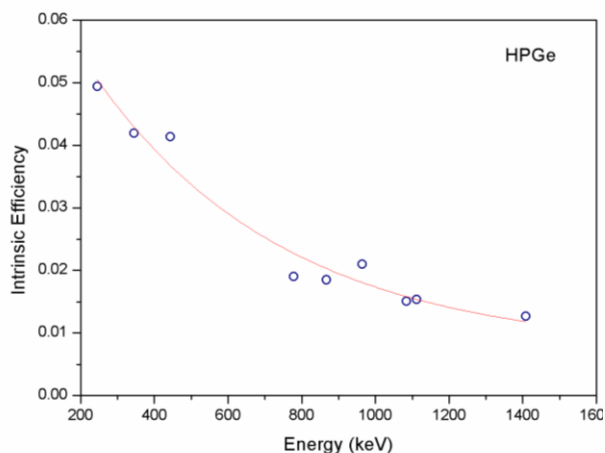


Fig. 5.9 Energy resolution of LaBr<sub>3</sub>(Ce) as a function of energy

### C. High Purity Ge (HPGe)

A P-type HPGe detector (L-shaped configuration) is used for SPECT imaging. The relative efficiency of the detector is 30% (with respect to 3" X 3" NaI(Tl)). Fig.5.10 (a) shows intrinsic photopeak efficiency of this detector as a function of energy. Fig. 5.10 (b) presents the variation of its energy resolution with energy. Fig. 5.11 shows gamma spectrum recorded with NaI(Tl), LaBr<sub>3</sub>(Ce) and HPGe detectors.



**Fig. 5.10(a)** Intrinsic photopeak efficiency of HPGe as a function of energy

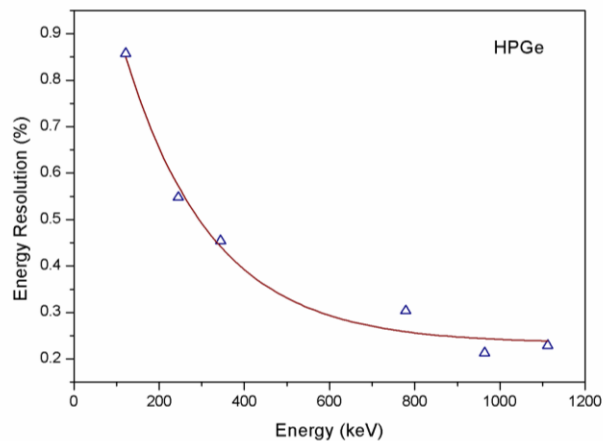


**Fig. 5.10(b)** Energy resolution of HPGe as a function of energy

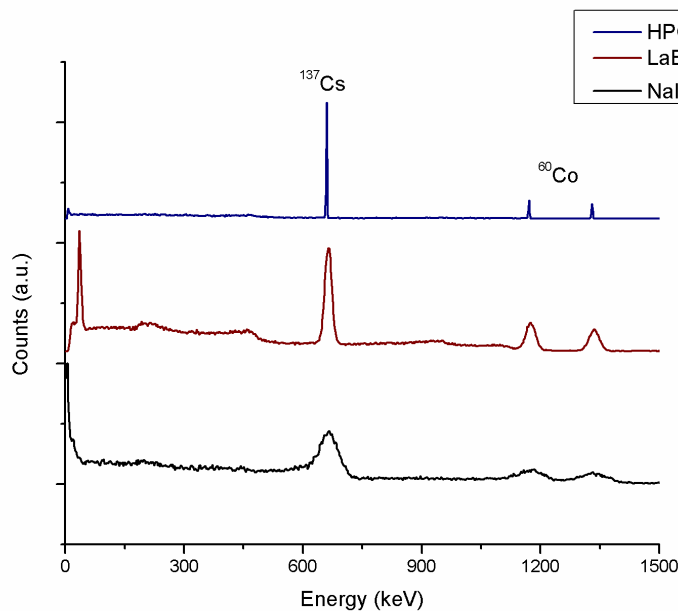


**Fig. 5.11** Gamma spectrum recorded with NaI(Tl), LaBr<sub>3</sub>(Ce) and HPGe detectors

### 5.1.6 Collimator

A specially designed square collimator (Fig.5.12 (b)) made of SS-Pb-SS with thickness 10 mm, 30 mm and 10 mm respectively has been used. A four segment tungsten septa of thickness 1.6 mm is used to increase the L/d ratio. Septa are highly attenuating, dividing-plates that run the length of the collimator which can be used to reduce the collimator length yet retain the effective L/d. These plates help collimate the gamma-ray beam, providing an effective aspect ratio that is better than that provided by the aperture size alone. The collimator has a square aperture of 25mm x 25mm is divided into four equal segments using high attenuating tungsten septa of thickness 1.6mm. The length of each collimator is 50mm which gives an effective aspect ratio (collimator length divided by collimator width) of 5:1 (with septa) or 2:1 (without septa). For higher collimation, a series of such collimators is used.

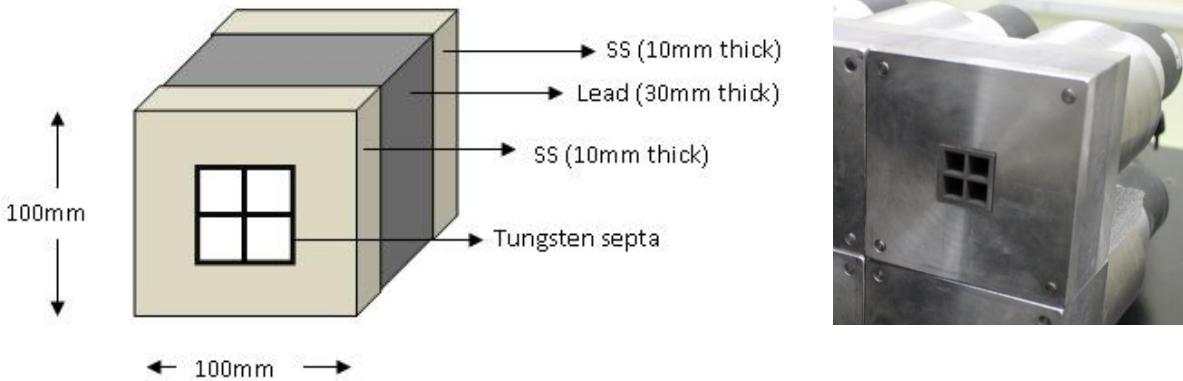


**Fig. 5.12** Collimator with tungsten septa (a) Schematic (b) Photograph

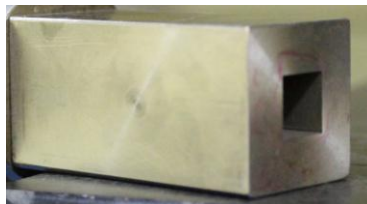


**Fig. 5.13** Collimator (10 mm X 10mm)

For smaller collimator opening, another square SS collimator of dimension 25 mm X 25 mm with a square aperture of dimension 10 mm X 10 mm has been used (Fig. 5.13). This collimator can be inserted in the above mentioned 25 mm x 25 mm collimator.

### **5.1.7 Data Acquisition System**

Data acquisition system has been developed for collection and storage of data. The detector is coupled to a Photomultiplier tube. Portable USB based plug-on MCA (ScintiSPEC and ScintiSPEC-L respectively) are used with NaI(Tl) and LaBr<sub>3</sub>(Ce) detectors. The data acquisition system includes interfacing of the sample manipulator controls and the MCA such that the sample is rotated and a projection data is recorded by the MCA and saved in a pre-determined format as specified by the user. The steps are subsequently repeated till the whole scan is complete. Depending upon the energies of interest for the radioisotope under study, the total net counts (gross counts - background) for the particular peak(s) from the MCA spectrum are calculated and saved. The whole data acquisition system is automated and computer controlled.

## **Section I: SPECT Reconstruction with <sup>137</sup>Cs sources**

In this section, we discuss experimental results for <sup>137</sup>Cs source distribution in matrix with different acquisition geometries and for 2D and 3D configuration. Before presenting the results, we shall discuss some aspects involved in qualitative and/or quantitative analysis.

- ***Reconstructed spatial position***

The reconstructed spatial position is obtained by finding out the centroid about each intensity maxima in the image.

- **Reconstructed activity**

The activity (in disintegrations per second) for each voxel is given by

$$A = \frac{C}{t\beta_{\gamma}\varepsilon} \quad (5.1)$$

where  $C$  is the reconstructed function value (counts) in the voxel,  $t$  is the acquisition time,  $\beta_{\gamma}$  is the branching ratio of the emitted gamma for the particular isotope and  $\varepsilon$  is the detector intrinsic efficiency. The total activity for each distinct source is calculated by summing all the voxels in the neighbourhood. The reconstructed activity values are quoted with  $1\sigma$  error values (only stochastic error is taken into account).

- **Efficiency Calibration for Multiple detectors**

Since multiple NaI(Tl) or LaBr<sub>3</sub>(Ce) detectors have been used, the efficiency  $\varepsilon$  (in Eq. 5.1) has to be properly accounted for as it would vary from detector to detector. It is particularly essential to perform a relative detector efficiency calibration when using more than one detector in a measurement.

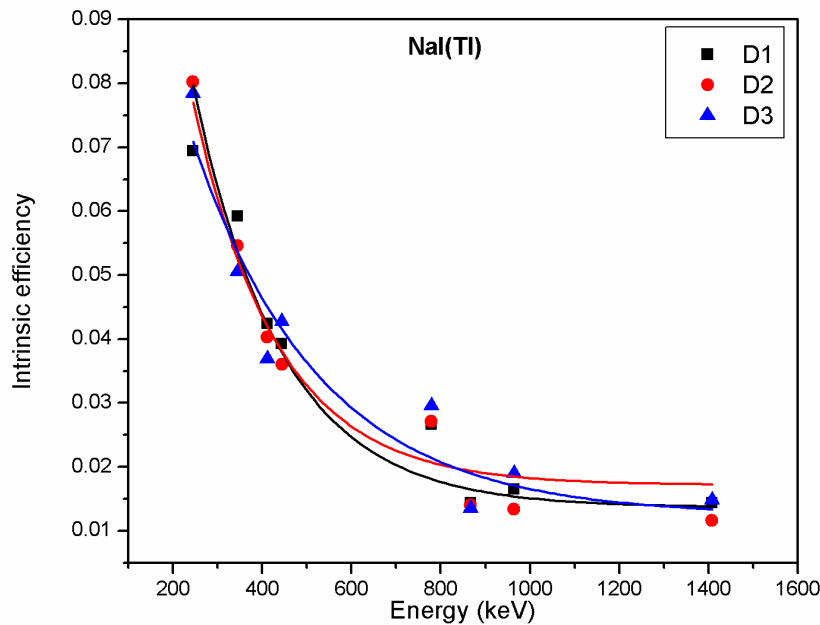


**Fig. 5.14** Intrinsic photopeak efficiency of three NaI(Tl) detectors used in experiments

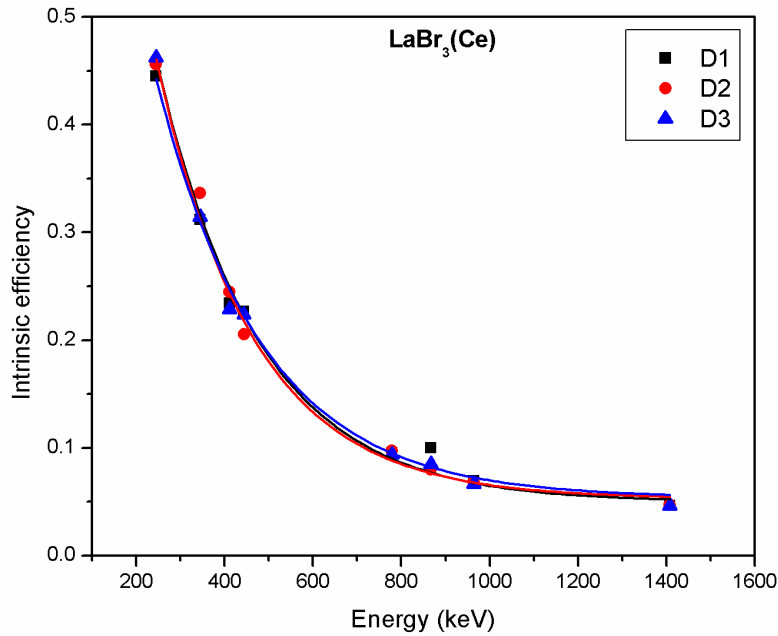


**Fig. 5.15** Intrinsic photopeak efficiency of three  $\text{LaBr}_3(\text{Ce})$  detectors used in experiments

Figs. 5.14 and 5.15 show the detector efficiency for  $\text{NaI}(\text{Tl})$  and  $\text{LaBr}_3(\text{Ce})$  detectors respectively used in the experiments. The counts recorded by individual detectors are corrected for efficiency variation relative to one of the detectors whose absolute efficiency value is used for further analysis.

- **Convergence criterion**

To investigate the convergence properties of the implemented iterative algorithms, following convergence criterion has been examined. The progress of the reconstruction is monitored by observing the root mean residual squares error (RMSE) at each iteration. RMSE is defined as follows:

$$RMSE = \sqrt{\frac{1}{N} \sum_{i=1}^N (\hat{f}_i - f_i)^2} \quad (5.2)$$

$\hat{f}_i$  and  $f_i$  are the reconstructed and true activity value for  $i^{th}$  pixel respectively and  $N$  is the total number of pixels. It is interpreted as how well the forward projection of the image matches with the measured data. Therefore it will be expected to decrease with increasing the iteration number, and approach to a plateau.

For implementation, both the reconstructed and true activity images are normalized.

- **FBP calibration**

In FBP reconstruction, the filtering step does not preserve the norm and the reconstructed value do not produce the true quantitative value, though the relative ratio of intensity is maintained. This calls for calibration procedures to obtain absolute activity values. For calibration, SPECT image of a point source in air is reconstructed using FBP and correction factor  $f$  is evaluated as follows:

$$f = \frac{\text{Reconstructed activity}}{\text{True activity}} \quad (5.3)$$

This correction factor is used for experimental FBP reconstruction to obtain true quantitative value.

## 5.2 2D SPECT Reconstruction: Parallel beam geometry

We shall first discuss results for 2D reconstruction in parallel beam geometry.

### 5.2.1 Sample: Hollow SS Rods

Two  $^{137}\text{Cs}$  sources (B and C) are placed at indexed locations 17 and 1 respectively (see Fig. 5.2 (b)). The indexed locations correspond to spatial locations (in terms of pixel) (4, 6) and (7, 11) respectively.

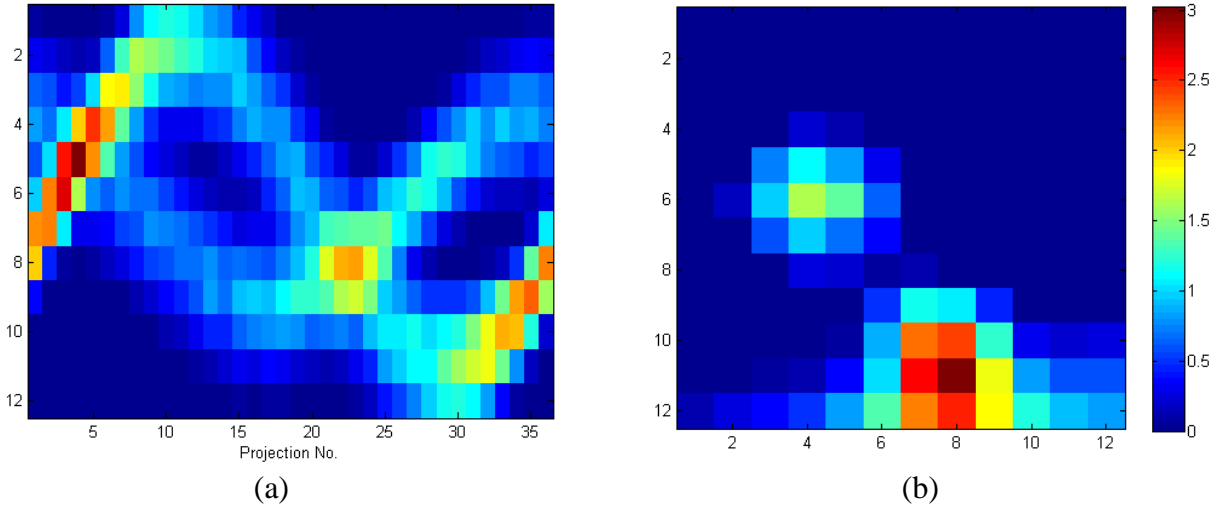


Fig. 5.16 (a) Sinogram (b) FBP reconstruction

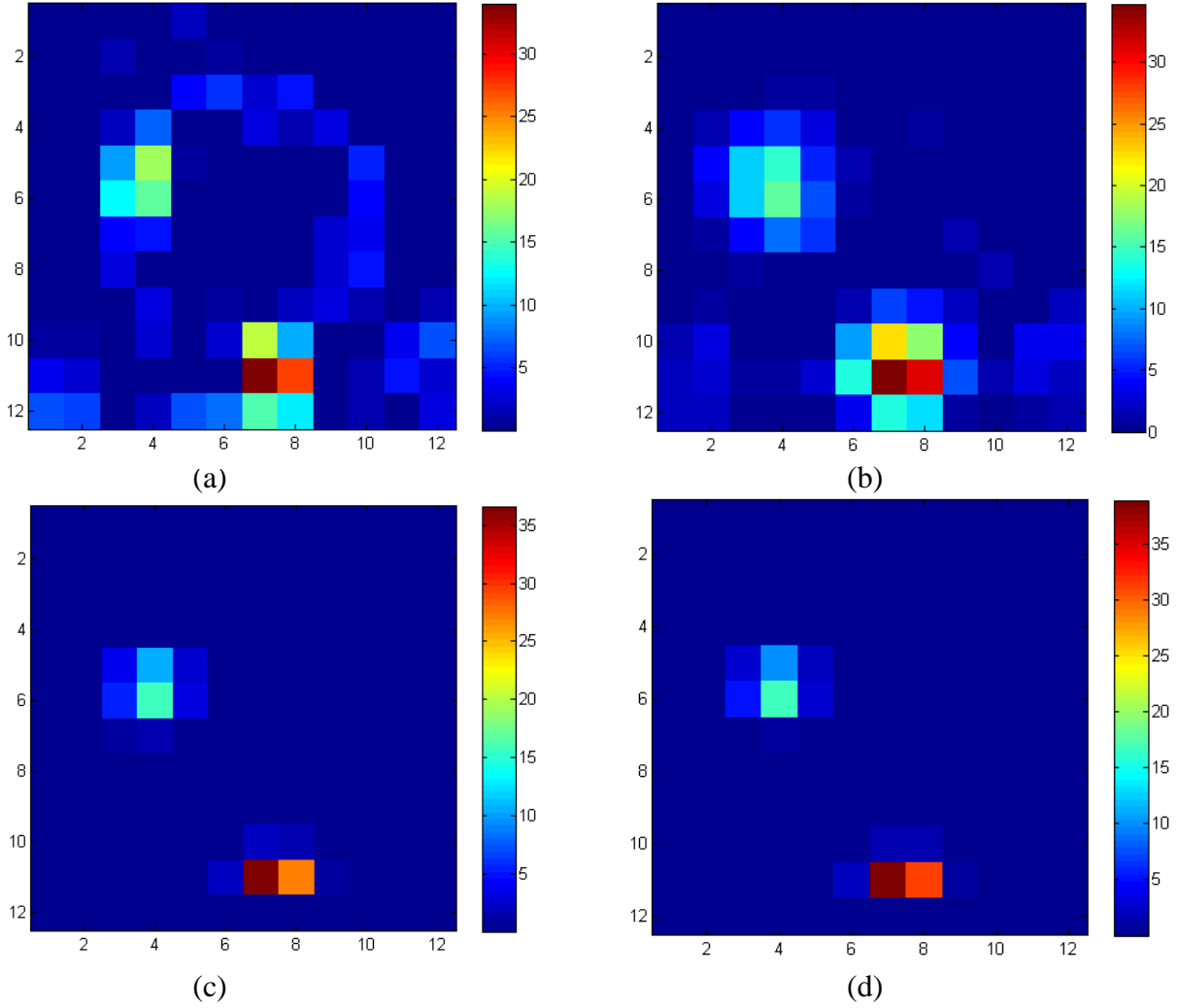


Fig. 5.17 Reconstructed image using (a) ART (b) SART (c) MLEM (d) OSEM

The planar images are acquired with three NaI(Tl) detectors at 36 angular positions with 12 lateral data points per projection. The acquisition time for each data point is 20s. The total assay time (including sample manipulator motion) is approximately 1.2 hr. The collimator opening is 25 mm (without septa) and collimator length is 150 mm (collimation ratio: 6). The distance from the centre of object to collimator opening is 310 mm. Fig.5.16 (a) shows the sinogram for 36 projections.

**TABLE 5.2** Comparison of reconstructed and true source activity and spatial location

Reconstructed Algorithm	Reconstructed Spatial Location (Pixel)	Deviation in Spatial Location (Pixel)	Reconstructed Activity (MBq)	Deviation in Reconstructed Activity (%)
<b>FBP</b>	(4, 6)	0	$16.2 \pm 1.8$	22.8
	(8, 11)	1	$28.8 \pm 2.6$	23.8
<b>ART</b>	(4, 5)	1	$17.7 \pm 1.6$	15.7
	(7, 11)	0	$34.0 \pm 2.5$	10.1
<b>SART</b>	(4, 6)	0	$18.1 \pm 1.6$	13.8
	(7, 11)	0	$34.7 \pm 2.8$	8.2
<b>MLEM</b>	(4, 6)	0	$19.8 \pm 1.8$	5.7
	(7, 11)	0	$36.6 \pm 2.6$	3.2
<b>OSEM</b>	(4, 6)	0	$19.9 \pm 1.7$	5.2
	(7, 11)	0	$38.9 \pm 2.9$	5.2

The projection data is used to reconstruct the activity distribution using filtered backprojection technique based on Novikov's formula and iterative reconstruction. The FBP reconstructed activity image is shown in Fig. 5.16 (b). For ART and SART

reconstruction, 40 iterations are required with relaxation parameter of 0.1 for both the cases. Figures 5.17 (a) and (b) present the activity functions generated using ART and SART respectively. For MLEM, 35 iterations are used whereas for OSEM, 4 subsets and 18 iterations are used. Figures 5.17 (c) and (d) present the activity functions generated using MLEM and OSEM respectively. Table 5.2 presents the reconstructed spatial position and activity of sources for different algorithms used.

It is observed that for MLEM and OSEM algorithms, there is no spatial deviation and the deviation in reconstructed activity is minimum (less than 6%) as compared to other algorithms and should be the preferred choice. FBP algorithm shows the maximum deviation in reconstructed activity (nearly 20%) owing to the collimator blurring and is not acceptable.

### 5.2.2 Sample: Solid Perspex disc

Three  $^{137}\text{Cs}$  sources (A, B and C) are placed at indexed locations 7, 1 and 4 respectively (see Fig.5.3 (b)). The indexed locations correspond to spatial locations (in terms of pixel) (10, 4), (26, 23) and (27, 11) respectively.

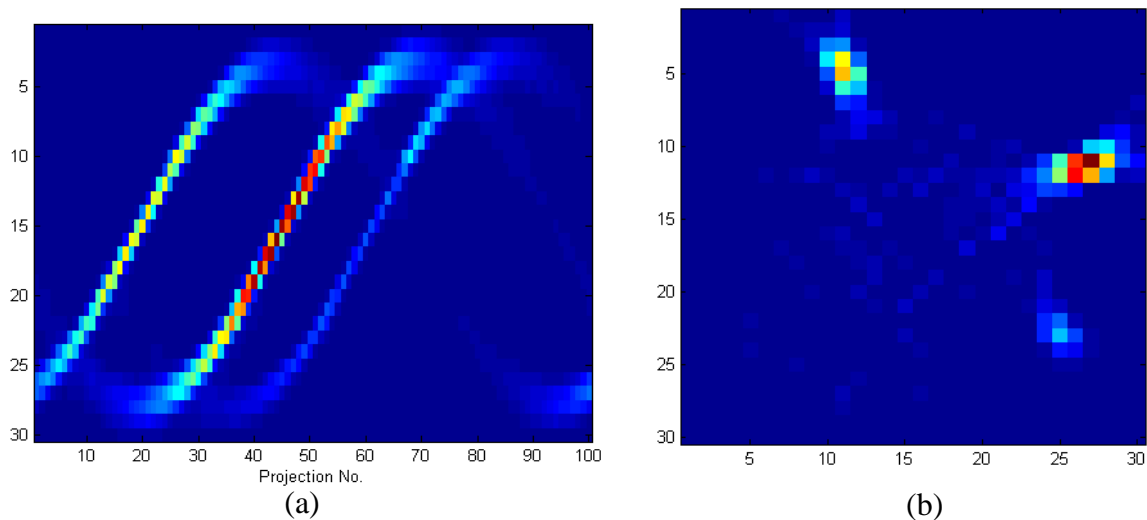


**Fig. 5.18 (a) Sinogram (b) FBP reconstruction**

The planar images are acquired with three LaBr<sub>3</sub>(Ce) detectors at 100 angular positions with total of 30 lateral data points (10 data points per detector) per projection. The acquisition time for each data point is 15s. The total assay time (including sample manipulator motion) is approximately 5.5 hrs. The collimator opening is 10 mm (without septa) and collimator length is 150 mm (collimation ratio: 15). The distance from the centre of object to collimator opening is 180 mm.

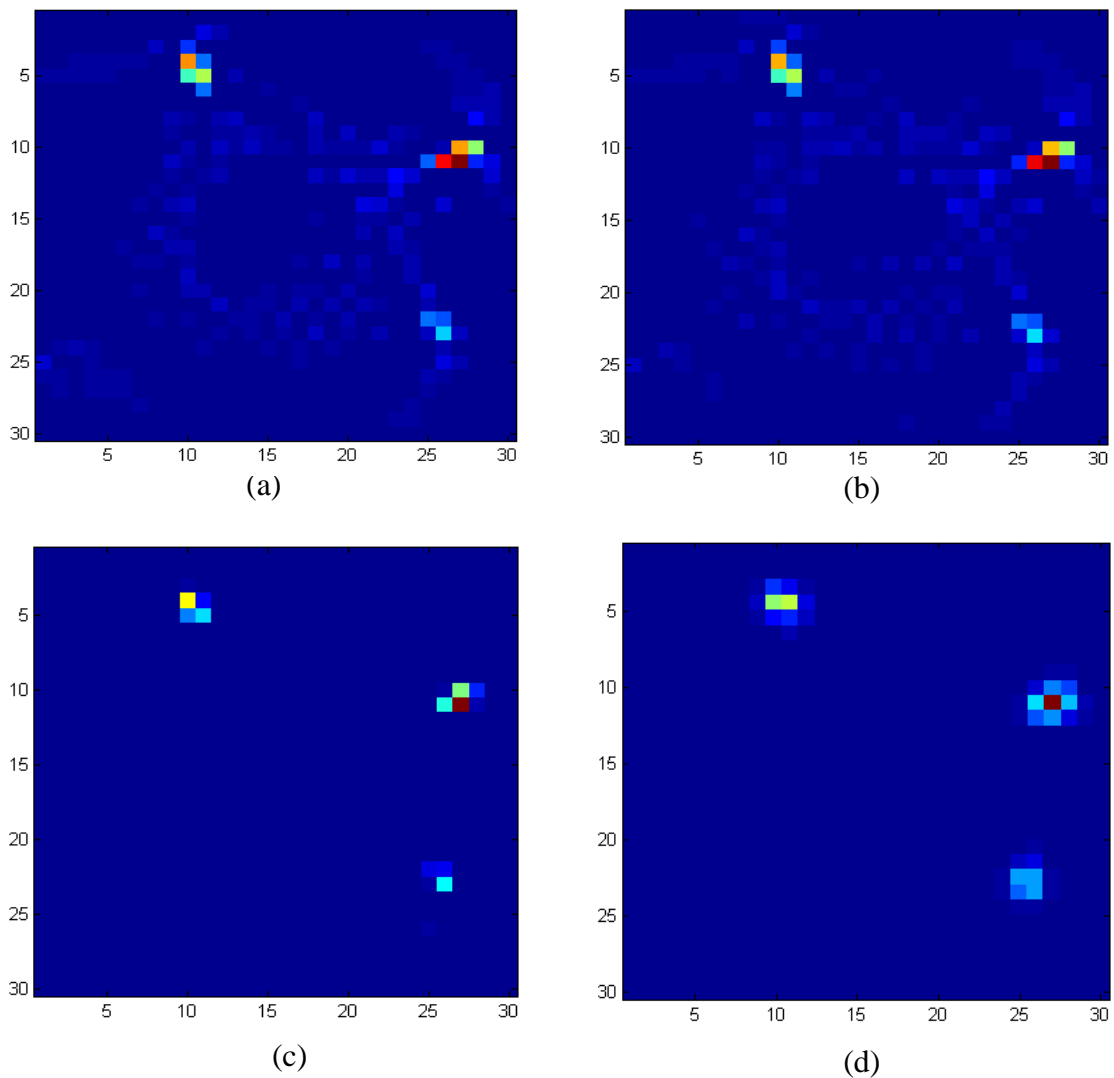


**Fig. 5.19** Reconstructed image using (a) ART (b) SART (c) MLEM (d) OSEM

**TABLE 5.3** Comparison of reconstructed and true source activity and spatial location

Reconstructed Algorithm	Reconstructed Spatial Location (Pixel)	Deviation in Spatial Location (Pixel)	Reconstructed Activity (MBq)	Deviation in Reconstructed Activity (%)
<b>FBP</b>	(11, 5)	1	20.2 ± 2.2	24.3
	(25, 23)	1	17.6 ± 1.8	16.2
	(27, 11)	0	34.3 ± 2.9	9.3
<b>ART</b>	(10, 4)	0	28.9 ± 2.4	8.2
	(26, 23)	0	18.7 ± 1.6	10.9
	(27, 11)	0	41.5 ± 2.8	9.8
<b>SART</b>	(10, 4)	0	29.8 ± 2.6	11.6
	(26, 23)	0	18.3 ± 1.7	12.8
	(27, 11)	0	41.4 ± 2.9	9.5
<b>MLEM</b>	(10, 4)	0	25.7 ± 2.2	3.7
	(26, 23)	0	19.4 ± 1.6	7.6
	(27, 11)	0	39.4 ± 2.6	4.2
<b>OSEM</b>	(11, 5)	1	24.4 ± 2.3	8.6
	(26, 23)	0	19.0 ± 1.6	9.5
	(27, 11)	0	37.0 ± 2.4	2.1

Fig.5.18 (a) shows the sinogram for 100 projections. The projection data is used to reconstruct the activity distribution using filtered backprojection technique based on Novikov’s formula and iterative reconstructions. The FBP reconstructed activity image is shown in Fig. 5.18 (b). For ART reconstruction, 10 iterations are required with relaxation

parameter of 0.2. For SART reconstruction, 16 iterations are required with relaxation parameter of 0.2. Figures 5.19 (a) and (b) present the activity functions generated using ART and SART respectively. For MLEM, 40 iterations are required whereas for OSEM, 5 subsets and 20 iterations are required. Figures 5.19 (c) and (d) present the activity functions generated using MLEM and OSEM respectively. The reconstructed spatial position and activity values for different algorithms are listed in Table 5.3.

It is observed that for MLEM algorithm, there is no spatial deviation and the deviation in reconstructed activity is minimum for MLEM and OSEM (less than 10%) as compared to other algorithms and should be the preferred choice. Once again, FBP algorithm shows the maximum deviation in reconstructed activity (nearly 10-25%) and is not acceptable.

### **5.3 3D SPECT Reconstruction: Parallel beam**

In this section, we shall discuss SPECT reconstruction in parallel beam geometry for 3D volume. The analytical reconstructions have been performed for each horizontal plane independently of other planes. Similarly for iterative reconstruction, 2D system matrix has been used for each horizontal plane. The independently reconstructed 2D slices have been stacked vertically to form a (pseudo) 3D volume or stacked 3D volume. Essentially, the reconstruction procedure is still 2D but the object is 3D and a pseudo 3D volume is rendered.

Furthermore, in order to take into account the intra-slice blurring, fully 3D system matrix has also been used for iterative reconstruction. For the experiments described below, the projection data are reconstructed with analytical technique, 2D system matrix and fully 3D system matrix.

### **5.3.1 Sample: Al Drum**

An aluminum drum (described in Section 5.1.2 C) filled with cotton gloves, nylon gloves and cotton fibre is used as object matrix. Three  $^{137}\text{Cs}$  sources are placed inside the drum at different locations. The exact locations of the samples are not known beforehand. Projections are acquired with three  $\text{LaBr}_3(\text{Ce})$  detectors at 36 angular locations with total of 12 lateral data points (4 data points per detector) per projection for each z-position. In the vertical direction, 24 z-positions are scanned. Thus each slice thickness is 25mm. Each data point is acquired for duration of 10s. The collimator opening is 25 mm (with septa) and collimator length is 100 mm (collimation ratio: 10). The distance from the centre of object to collimator opening is 450 mm.

In the experiments described so far, the attenuation coefficient of the object matrix is uniform. For attenuation compensation during reconstruction, an average (measured) value of linear attenuation coefficient is considered. However, in this case, the attenuation map of the matrix object is non-homogeneous. Hence, attenuation map of the object is obtained from transmission tomography of the object.

Transmission computed tomography (TCT) of the drum is carried out using external  $^{152}\text{Eu}$  source. The TCT data are acquired for different energies (244 keV, 344 keV, 444 keV, 778 keV and 867 keV). The attenuation map is reconstructed for each energy using Filtered Back Projection algorithm. The absolute attenuation values have been obtained by calibrating with standard objects with known attenuation values. Fig. 5.20 shows the reconstructed TCT data for three slices at different energies. Fig. 5.21 shows the plot of attenuation coefficient as a function of energy. The attenuation map for

662 keV (emission energy in SPECT) is interpolated from these data pixel by pixel. This attenuation map is then used for attenuation compensation.

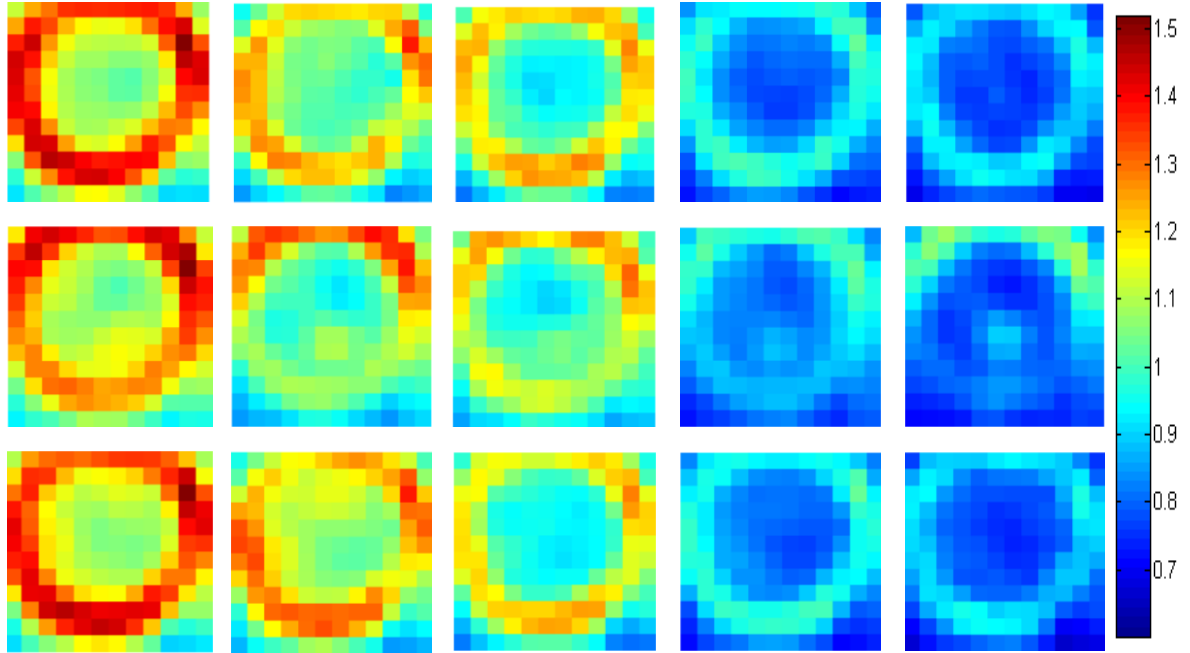


**Fig. 5.20** TCT data for three different slices (top to bottom) at different energies (from left to right) – 244 keV, 344 keV, 444 keV, 778 keV and 867 keV; Colour bar is shown on the right (in unit of  $\text{cm}^{-1}$ )

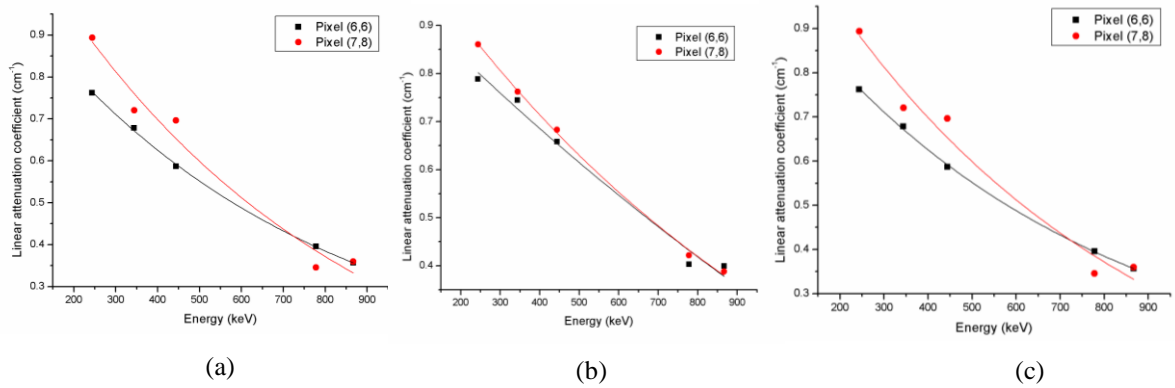


**Fig. 5.21** Plot of linear attenuation coefficient as a function of energy for (a) Top row (b) Middle row (c) Bottom row of TCT data in fig.5.20

### A. Analytical Reconstruction

The passive CT data is reconstructed using Filtered Backprojection scheme with attenuation compensation based on Novikov’s Inversion Formula. The reconstructed volume is discretized on a 12 X 12 X 24 grid. Fig. 5.22 shows sinogram corresponding to three XY slices corresponding to the slices containing the passive sources (as inferred from reconstructed images). Reconstructed XY slices at different Z-positions are shown in Fig. 5.23.

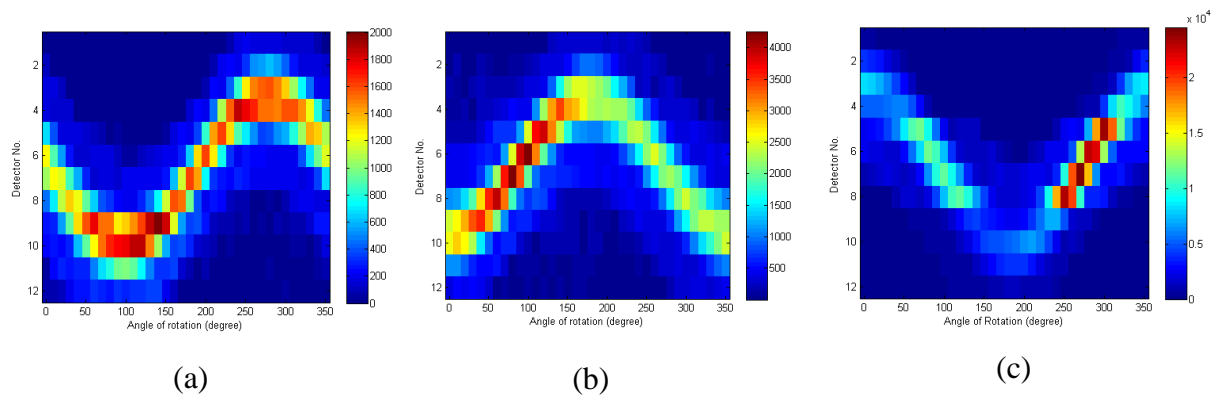


**Fig. 5.22** Sinogram of SPECT data for (a) Slice 5 (b) Slice 13 (c) Slice 18

The reconstructed 3D volume is shown in Fig. 5.24 (a). For 3D volume visualization, the data is also interpolated on finer grid (30 X 30 X 60) as shown in Fig. 5.24 (b). It can be seen that spatial position of the radioisotopes can be easily located. The reconstructed activity distribution in the images matches well with the true source activity in the original object (see Table 5.4).

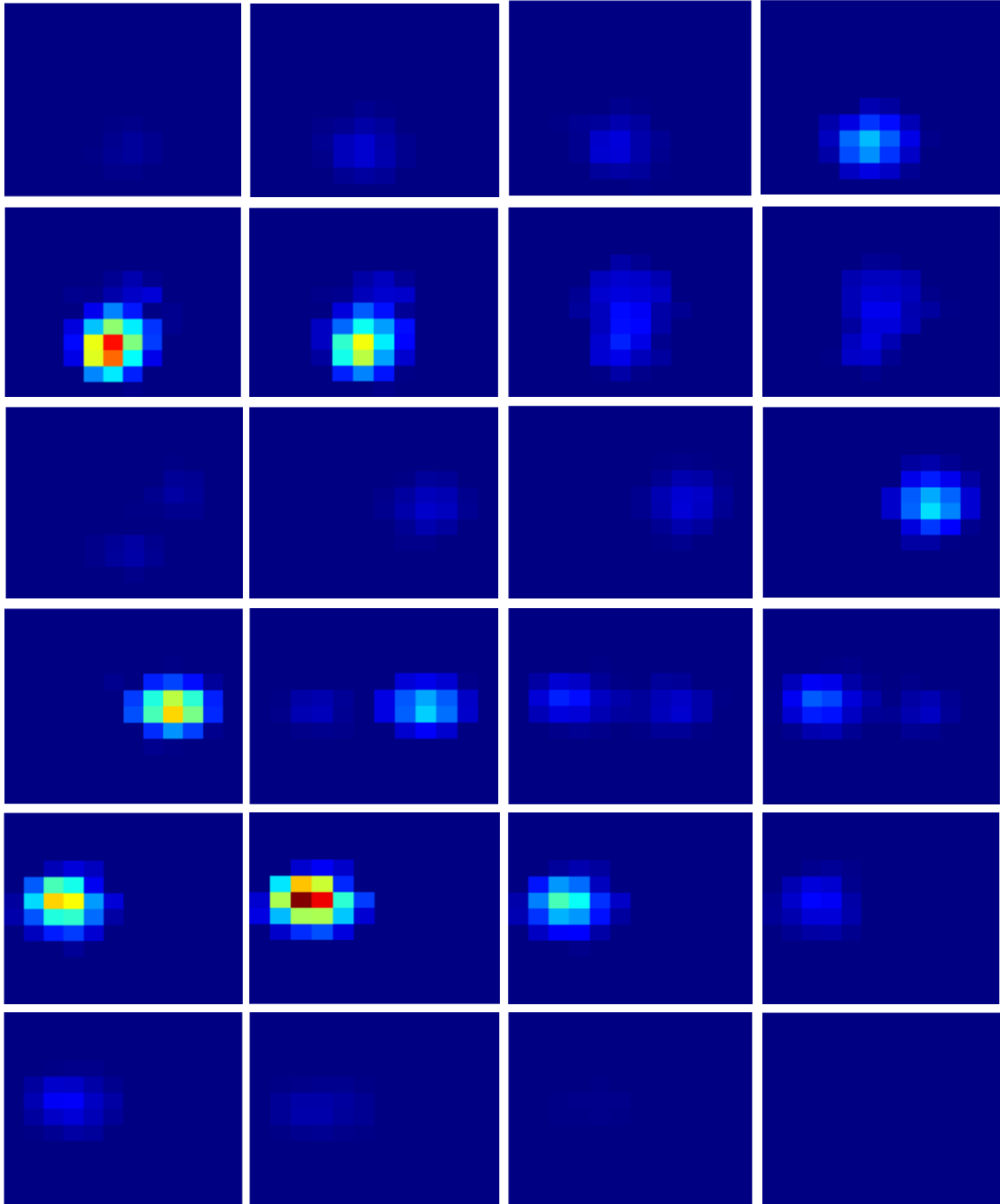


*Fig. 5.23 Analytical reconstructed slice images showing  $^{137}\text{Cs}$  activity in a drum. The images show XY Slices at different Z-positions starting from bottom to top (ordered row-wise left to right)*

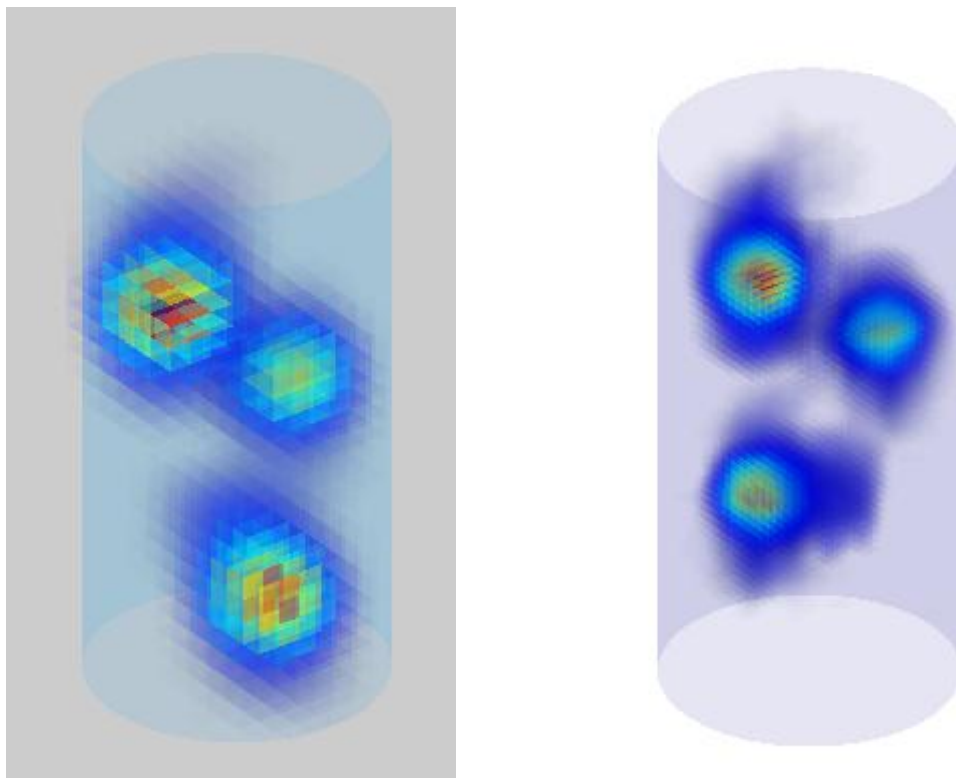


**Fig. 5.24** (a) Reconstructed 3D volume showing  $^{137}\text{Cs}$  activity in the drum (b) 3D volume interpolated on a finer grid. Note that the drum outline is shown for illustration.

Fig. 5.25 shows the line profiles along x-axis, y-axis and z-axis respectively for the sources. The spread in the line profiles is mainly due to the collimator blurring (and scattering) which is one of the important factor of image degradation in SPECT. Deconvolution methods may be applied on the obtained images to reduce the blurring effect. However, it can be seen from these results that even without any correction for collimator blurring, it is possible to locate the radioisotopes with reasonable accuracy.

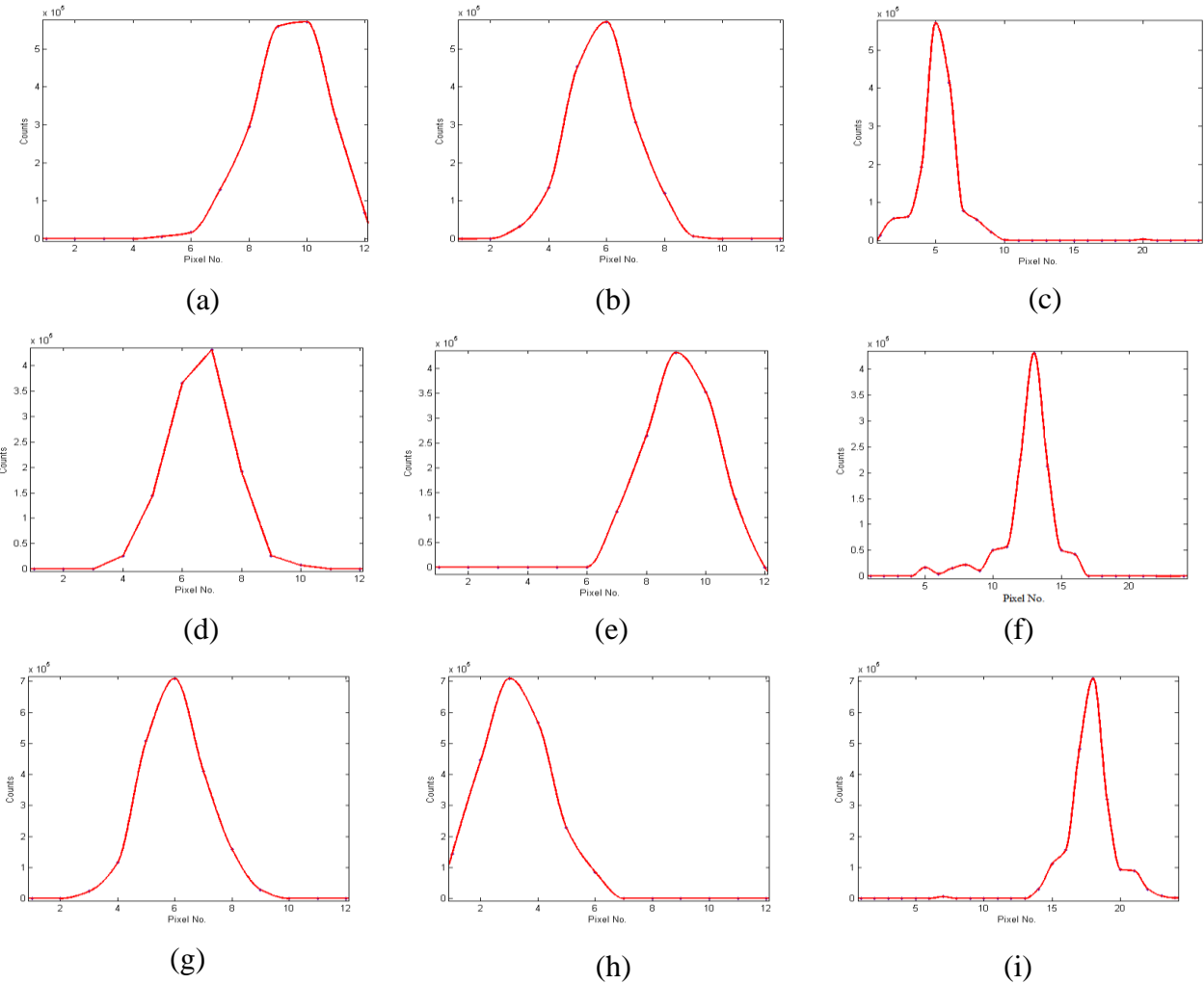


**Fig. 5.25** Intensity profile along x-axis, y-axis and z-axis respectively for Source A (a-c), Source B (d-f) and Source C (g-i)

## B. 2D (Stacked) MLEM Reconstruction

The passive CT data is reconstructed using MLEM for a 2D system matrix. Each slice is reconstructed independently and the reconstructed slices are stacked to form a 3D volume. The number of iterations required is 50. Fig. 5.26 shows the reconstructed slice images for 2D MLEM reconstruction.

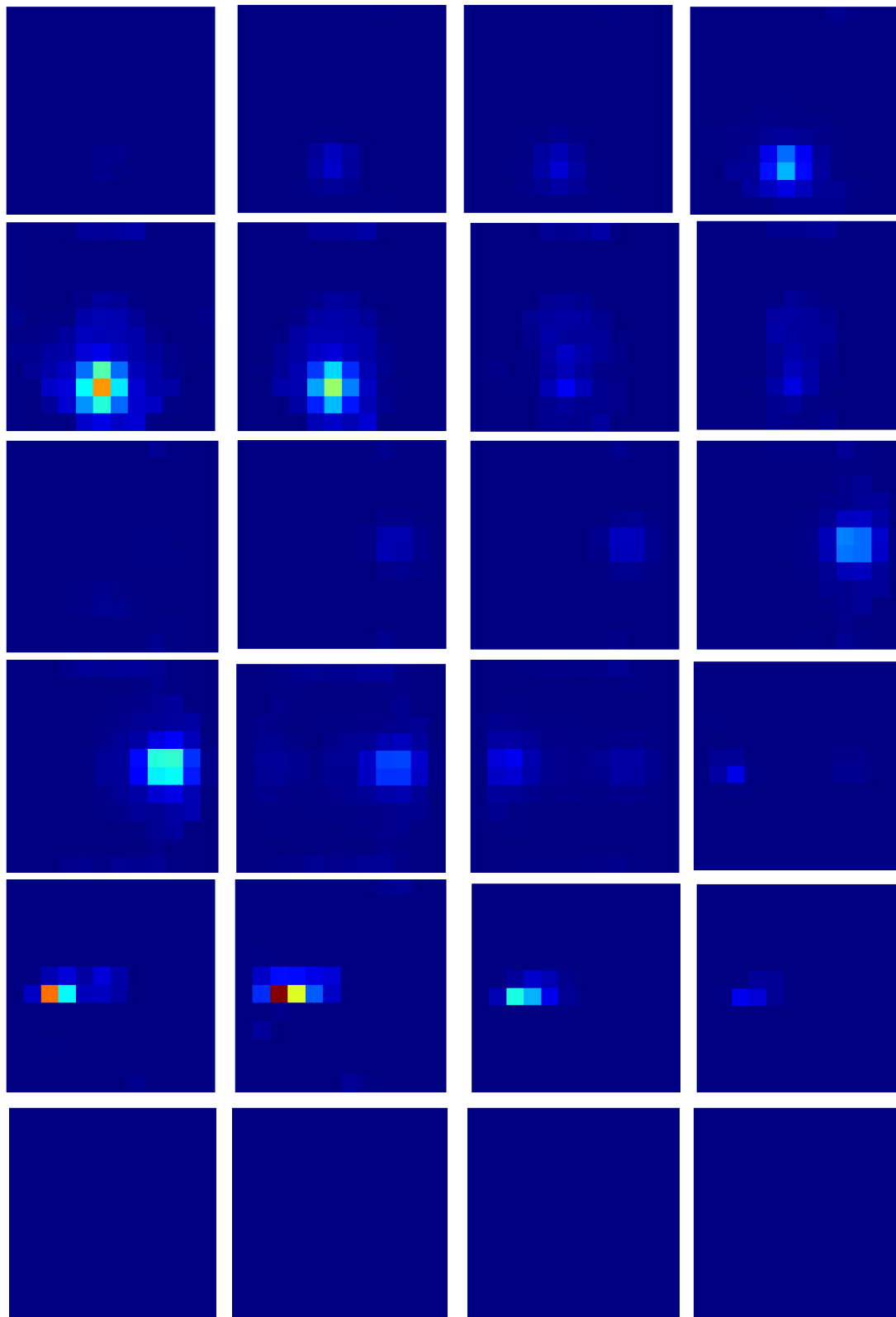
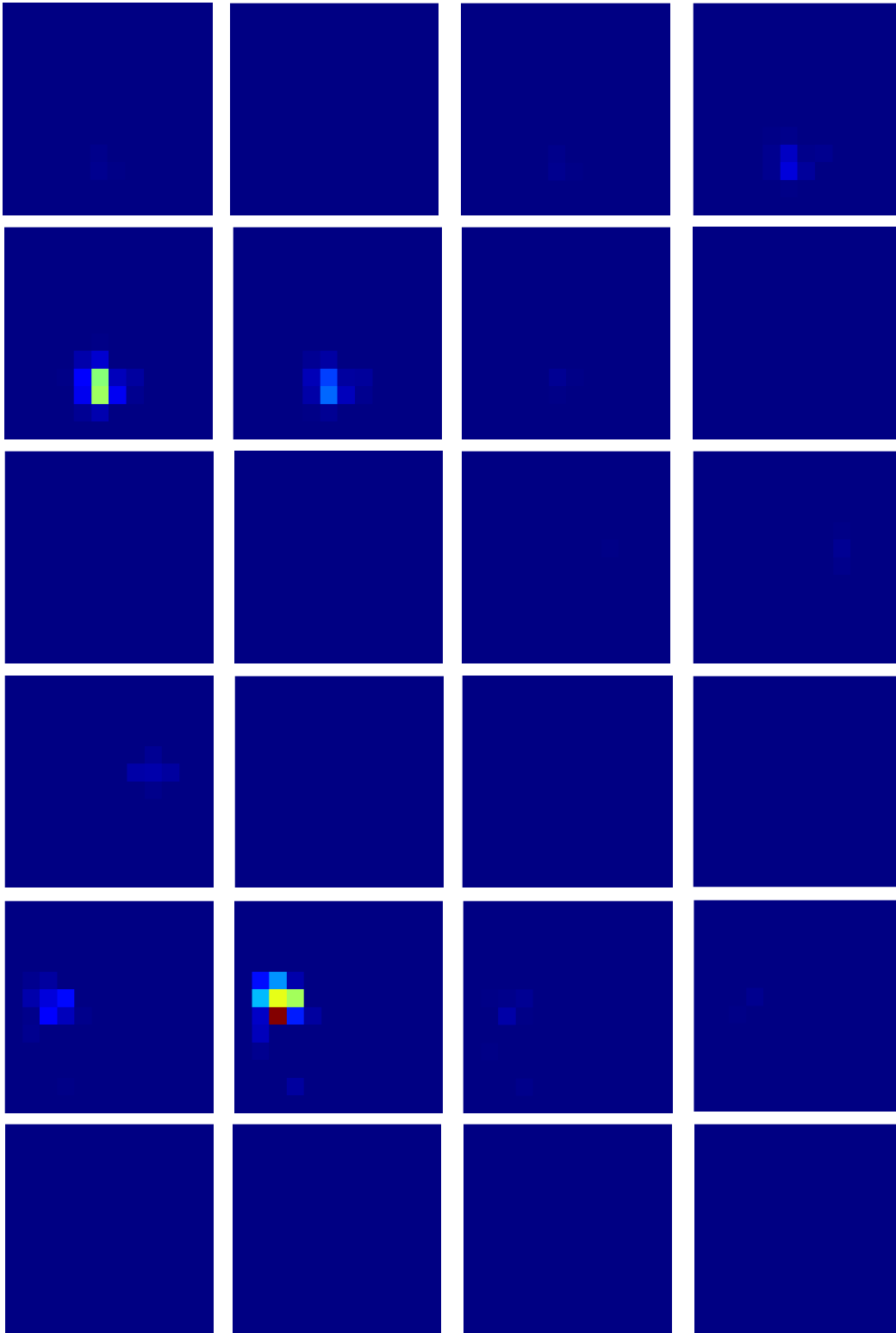


Fig. 5.26 2D MLEM reconstructed slice images showing  $^{137}\text{Cs}$  activity in a drum. The images show XY Slices at different Z-positions starting from bottom to top (ordered row-wise left to right)

### C. Fully 3D MLEM Reconstruction



**Fig. 5.27** Fully 3D MLEM reconstructed slice images showing  $^{137}\text{Cs}$  activity. The images show XY slices at different Z-positions starting from bottom to top (ordered row-wise left to right)

The passive CT data is reconstructed using MLEM for fully 3D system matrix. The number of iterations required is 30. Fig. 5.27 shows the reconstructed slice images for fully 3D MLEM reconstruction.

Fig. 5.28 (a), (b) and (c) show the 3D view of  $^{137}\text{Cs}$  activity distribution using analytical, 2D MLEM and fully 3D MLEM reconstruction respectively for the Al drum sample. The effect of collimator blurring is clearly evident from these images. For analytical reconstruction (Fig. 5.28(a)), both inter- and intra-slice blurring are observed and a point source appears spherical. For 2D MLEM reconstruction (Fig. 5.28(b)), the intra-slice blurring is reduced but inter-slice blurring remains. For fully 3D MLEM reconstruction (Fig. 5.28(c)), both inter- and intra-slice blurring are reduced considerably and the point source appears point-like.

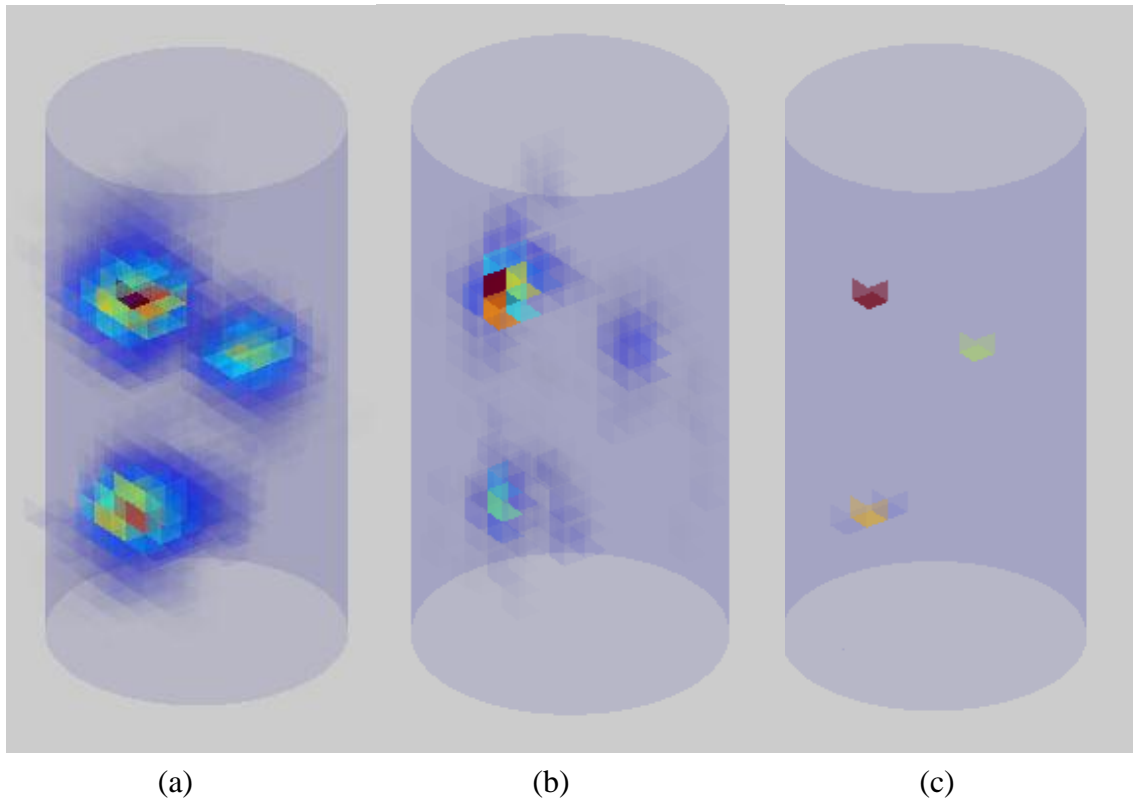


**Fig. 5.28** Reconstructed activity for Al drum sample (a) FBP (b) 2D (Stacked) MLEM  
(c) Fully 3D MLEM

The reconstructed spatial position and activity values for different algorithms are listed in Table 5.4.

**TABLE 5.4** Comparison of reconstructed and true source activity

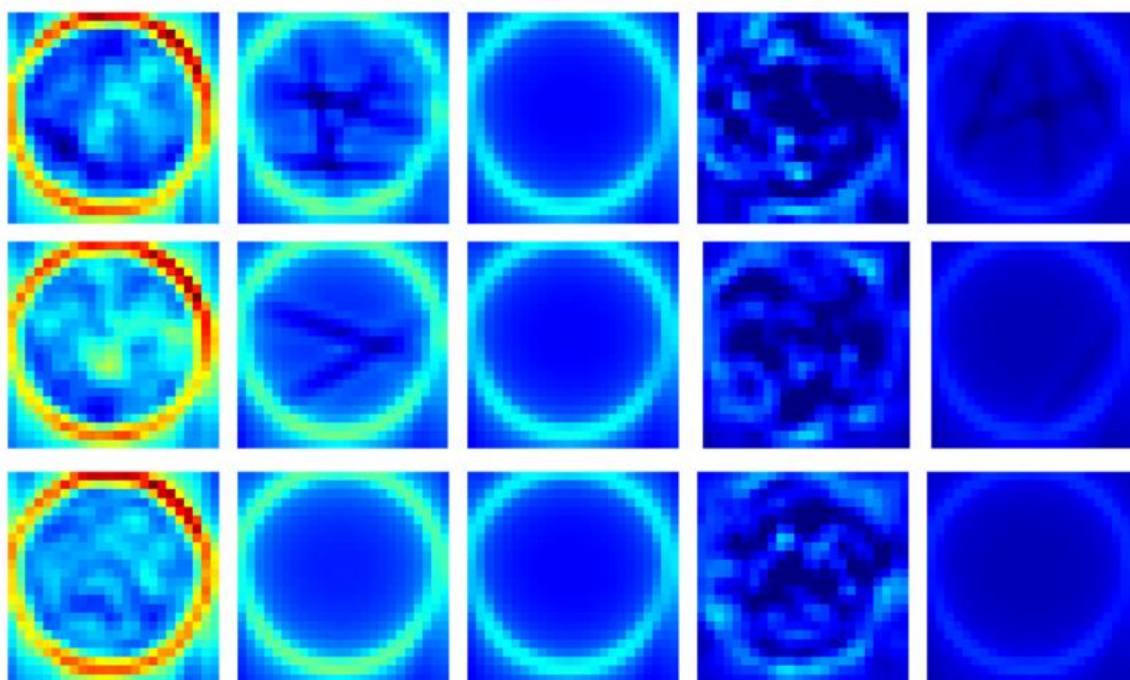
Reconstruction Technique	Source	Reconstructed Source Position (pixel) (x, y, z)	Reconstructed activity (MBq)	Deviation in Reconstructed Activity (%)
<b>FBP</b>	<b>A</b>	(10, 6, 5)	$27.9 \pm 2.5$	4.5
	<b>B</b>	(7, 9, 13)	$19.5 \pm 2.0$	7.1
	<b>C</b>	(6, 3, 18)	$34.7 \pm 2.9$	8.2
<b>2D MLEM</b>	<b>A</b>	(10, 6, 5)	$27.0 \pm 2.3$	1.1
	<b>B</b>	(7, 9, 13)	$20.1 \pm 1.9$	4.3
	<b>C</b>	(6, 3, 18)	$38.2 \pm 2.3$	1.1
<b>Fully 3D MLEM</b>	<b>A</b>	(10, 6, 5)	$27.2 \pm 2.3$	1.9
	<b>B</b>	(6, 9, 13)	$18.7 \pm 2.1$	10.9
	<b>C</b>	(6, 3, 18)	$37.0 \pm 2.1$	2.1

### 5.3.2 SS Drum

A mock SS waste drum (described in Section 5.1.2 D) filled with cotton gloves, nylon gloves and cotton fibre is used as object matrix. Three  $^{137}\text{Cs}$  sources are placed inside the drum at different locations. Exact locations of the sources are not known beforehand. Projections are acquired with  $\text{LaBr}_3(\text{Ce})$  detectors at 36 angular locations and 24 lateral positions for each z-position. In the vertical direction, 34 z-positions are scanned. Thus each slice thickness is 25 mm. Each image data point is acquired for duration of 10s. The

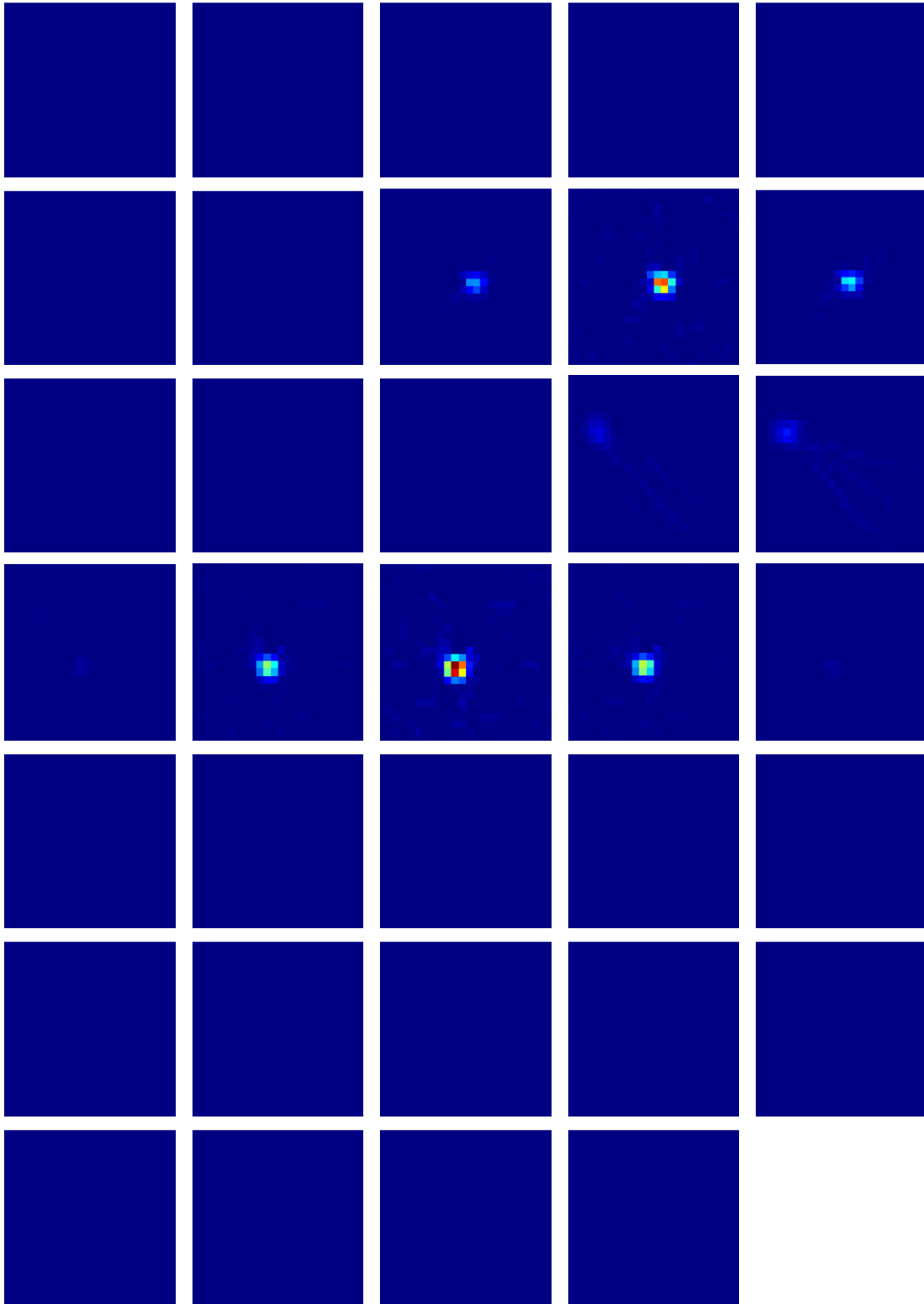
collimator opening is 25 mm (with septa) and collimator length is 150 mm (collimation ratio: 15). The distance from the centre of object to collimator opening is 450 mm.

Transmission computed tomography (TCT) of the drum is carried out using external  $^{152}\text{Eu}$  source. The TCT data are acquired for different energies (121 keV, 244 keV, 344 keV, 444 keV, 778 keV and 867 keV). The attenuation map is reconstructed for each energy using FDK algorithm. Fig. 5.29 shows the reconstructed TCT data for three slices at different energies. The attenuation map for 662 keV (emission energy in SPECT) is interpolated from these data. This attenuation map is then used for attenuation compensation.



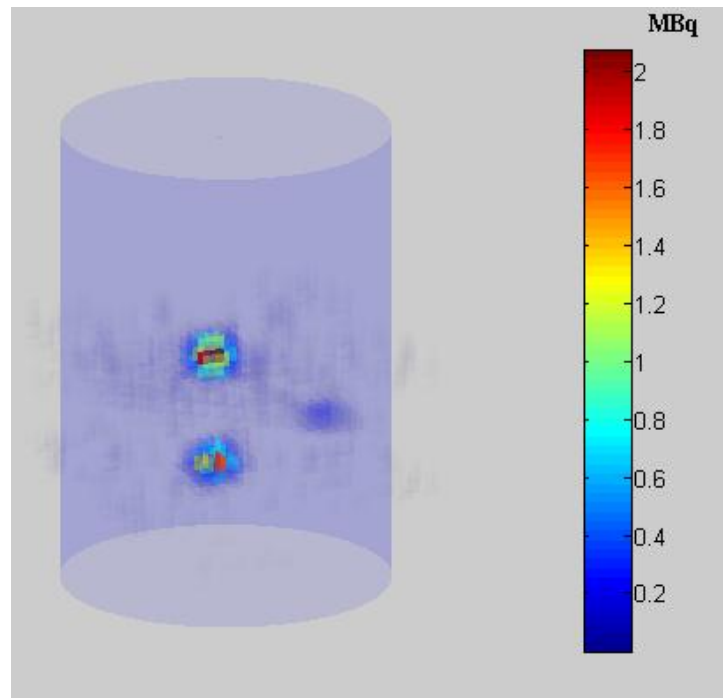
*Fig. 5.29 TCT data for three different slices (top to bottom) at different energies (from left to right) – 121 keV, 244 keV, 344 keV, 444 keV, 778 keV*

**A. Analytical Reconstruction**



*Fig. 5.30 Analytical reconstructed slice images showing  $^{137}\text{Cs}$  activity. The images show XY Slices at different Z-positions starting from bottom to top (ordered row-wise left to right)*

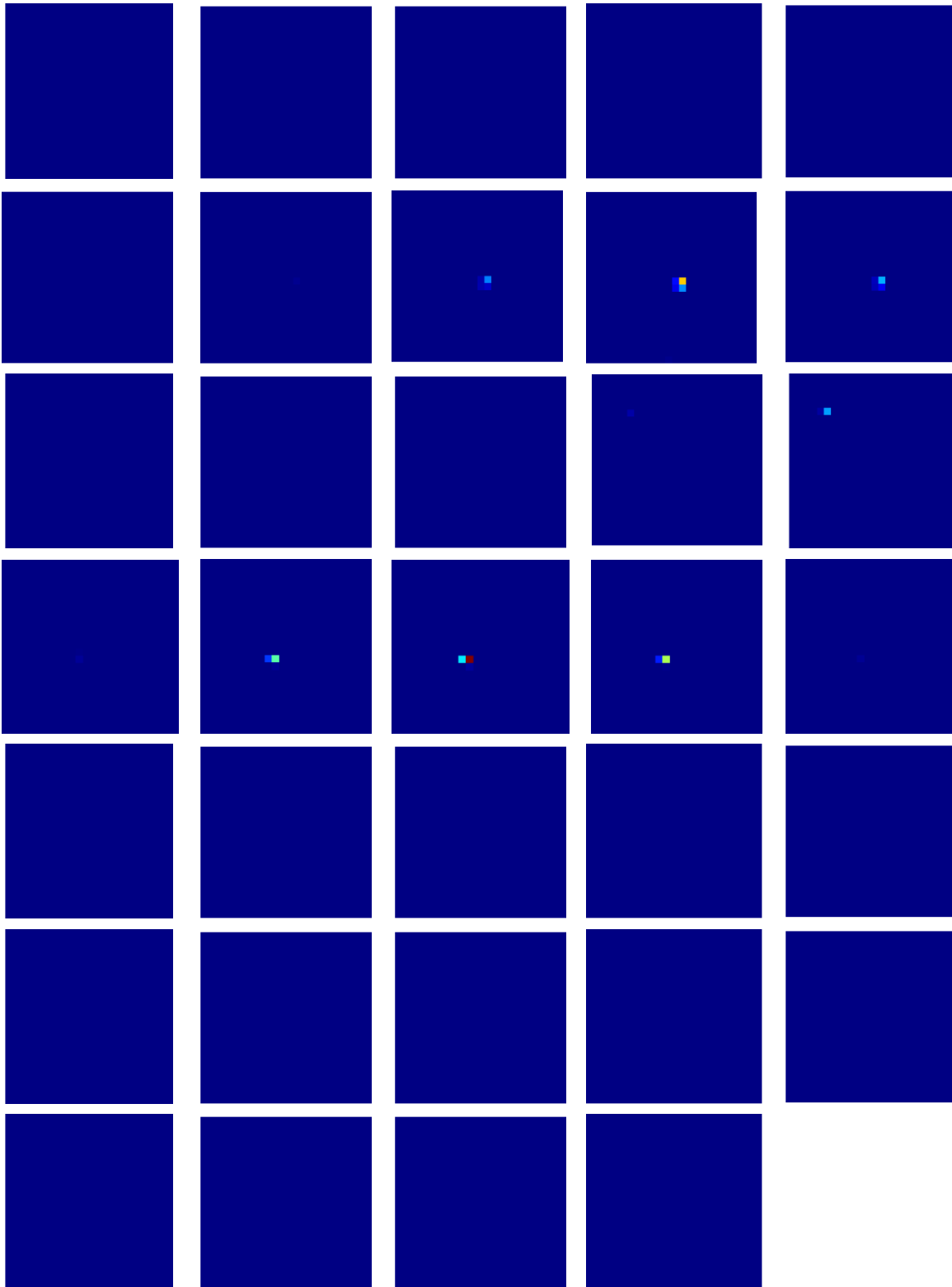
Reconstruction is done using Filtered Backprojection scheme with attenuation compensation based on Novikov's Inversion Formula. The reconstructed volume is discretized on a 24 X 24 X 34 grid. Reconstructed XY slices at different Z-positions are shown in Fig. 5.30. The reconstructed 3D volume is shown in Fig. 5.31.



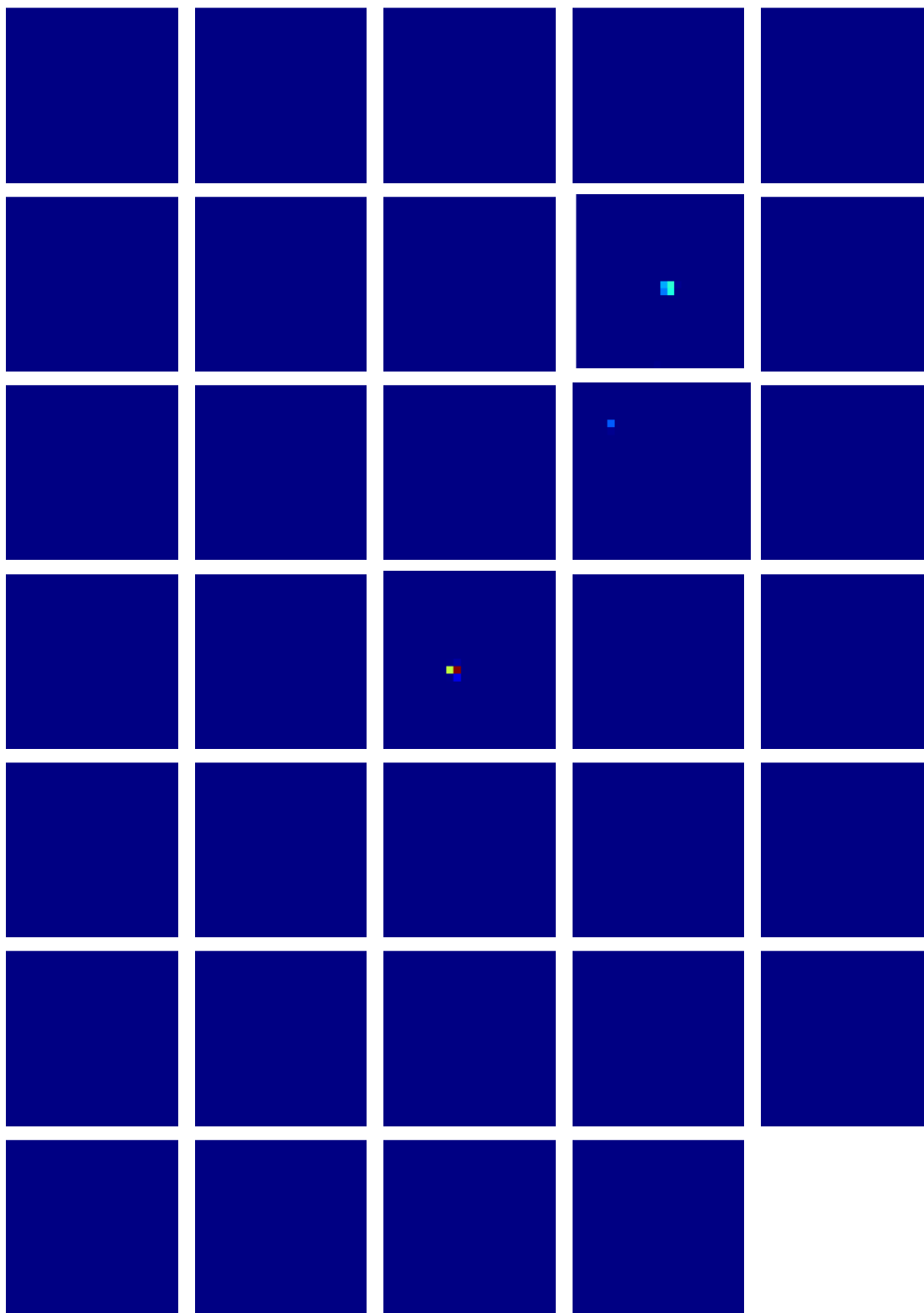
*Fig. 5.31 3D view of <sup>137</sup>Cs activity*

### **B. 2D (Stacked) MLEM Reconstruction**

The passive CT data is reconstructed using MLEM for a 2D system matrix. Each slice is reconstructed independently and the reconstructed slices are stacked to form a 3D volume. The number of iterations required is 36. Fig. 5.32 shows the reconstructed slice images for 2D MLEM reconstruction.



*Fig. 5.32 2D MLEM reconstructed slice images showing  $^{137}\text{Cs}$  activity. The images show XY Slices at different Z-positions starting from bottom to top (ordered row-wise left to right)*

**C. Fully 3D MLEM Reconstruction**

**Fig. 5.33** Fully 3D MLEM reconstructed slice images showing  $^{137}\text{Cs}$  activity. The images show XY Slices at different Z-positions starting from bottom to top (ordered row-wise left to right)

The passive CT data is reconstructed using MLEM for fully 3D system matrix. The number of iterations required is 25. Fig. 5.33 shows the reconstructed slice images for fully 3D MLEM reconstruction.

Fig. 5.34 (a), (b) and (c) show the 3D view of  $^{137}\text{Cs}$  activity distribution using analytical, 2D MLEM and fully 3D MLEM reconstruction for the SS waste drum sample.

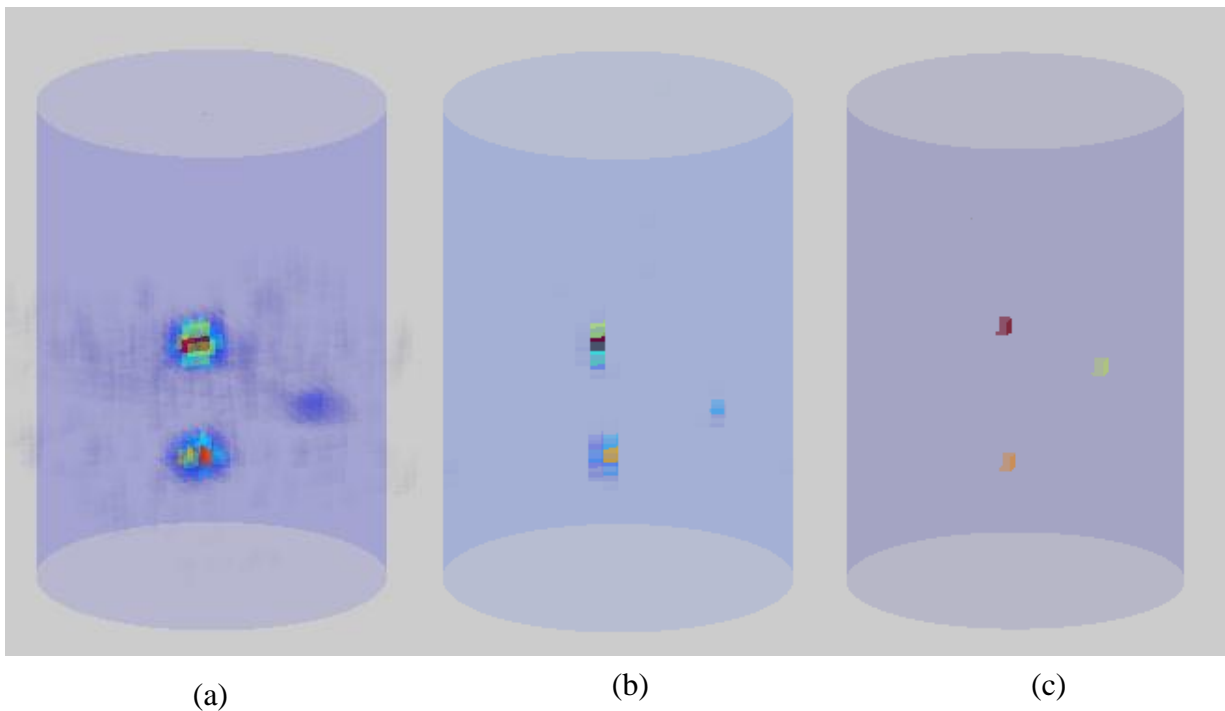


**Fig. 5.34** Reconstructed activity for SS drum sample (a) FBP (b) 2D (Stacked) MLEM (c) Fully 3D

It is observed that analytical reconstruction results in collimator blurring both within the reconstruction plane and between different planes. This results in a point source being spread over a volume as a sphere. The use of 2D system matrix reduces blurring within the reconstruction plane only and the point source now resembles an elongated sphere. When fully 3D system matrix is used, both inter-slice and intra-slice blurring are reduced and the point source appears to be point-like.

The reconstructed spatial position and activity values for different algorithms are listed in Table 5.5.

*TABLE 5.5 Comparison of reconstructed and true source activity and location*

<b>Reconstruction Technique</b>	<b>Source</b>	<b>Reconstructed Spatial Position (in pixel) (x, y, z)</b>	<b>Reconstructed activity (MBq)</b>	<b>Deviation in Reconstructed Activity (%)</b>
<b>FBP</b>	<b>A</b>	(11, 11, 9)	$27.4 \pm 2.1$	2.6
	<b>B</b>	(3, 7, 14)	$21.1 \pm 2.0$	0.5
	<b>C</b>	(9, 12, 18)	$36.4 \pm 2.8$	3.7
<b>2D MLEM</b>	<b>A</b>	(11, 11, 9)	$28.0 \pm 2.0$	4.9
	<b>B</b>	(3, 7, 14)	$20.2 \pm 1.8$	3.8
	<b>C</b>	(9, 12, 18)	$38.5 \pm 3.0$	1.9
<b>Fully 3D MLEM</b>	<b>A</b>	(11, 11, 9)	$27.1 \pm 1.8$	1.5
	<b>B</b>	(3, 7, 14)	$21.3 \pm 2.1$	1.4
	<b>C</b>	(9, 12, 18)	$37.4 \pm 2.6$	1.1

## **5.4 3D SPECT Reconstruction: Fan Beam**

A mock waste barrel (580 mm diameter and 850 mm height) is filled with cotton waste / gloves / tissues / cellulose matrix. Three  $^{137}\text{Cs}$  sources have been placed at different locations inside the barrel. For the Active CT measurement, a single external gamma source ( $^{152}\text{Eu}$ ; 33mCi) and three  $\text{LaBr}_3(\text{Ce})$  detectors in fan beam configuration are used. Data has been acquired at 33 lateral positions and 15 angular positions over  $180^\circ$  for each z-position. In the vertical direction, 34 z-positions are scanned. Each slice thickness is

25mm. The acquisition time for each scan is 5 sec. The peak area corresponding to 121 keV, 244 keV, 344 keV, 444 keV, 778 keV and 964 keV are used for reconstructing the active data set. The attenuation coefficient at emission energy of 662 keV is obtained by interpolating the values pixel by pixel from the above data set.

For passive CT, the detectors are used in the same configuration. Data is acquired at 33 lateral positions and 24 angular positions over 360° for each z-position. In the vertical direction, 34 z-positions are scanned. The collimator opening is 25 mm (with septa) and collimator length is 150 mm (collimation ratio: 15). The focal length (distance of the focal point from the detector surface) is 1540 mm. The acquisition time for each data point is 10 sec.

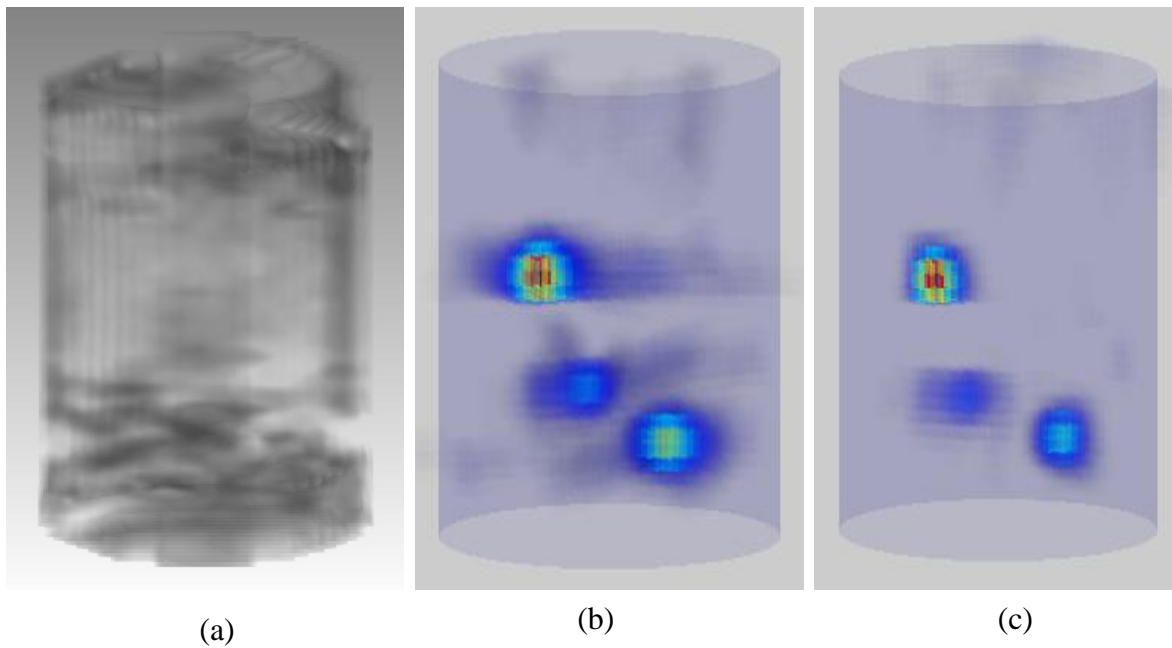


**Fig. 5.35** (a) Reconstructed attenuation map (b) & (c) Analytical and 2D MLEM reconstructed volume showing  $^{137}\text{Cs}$  activity respectively

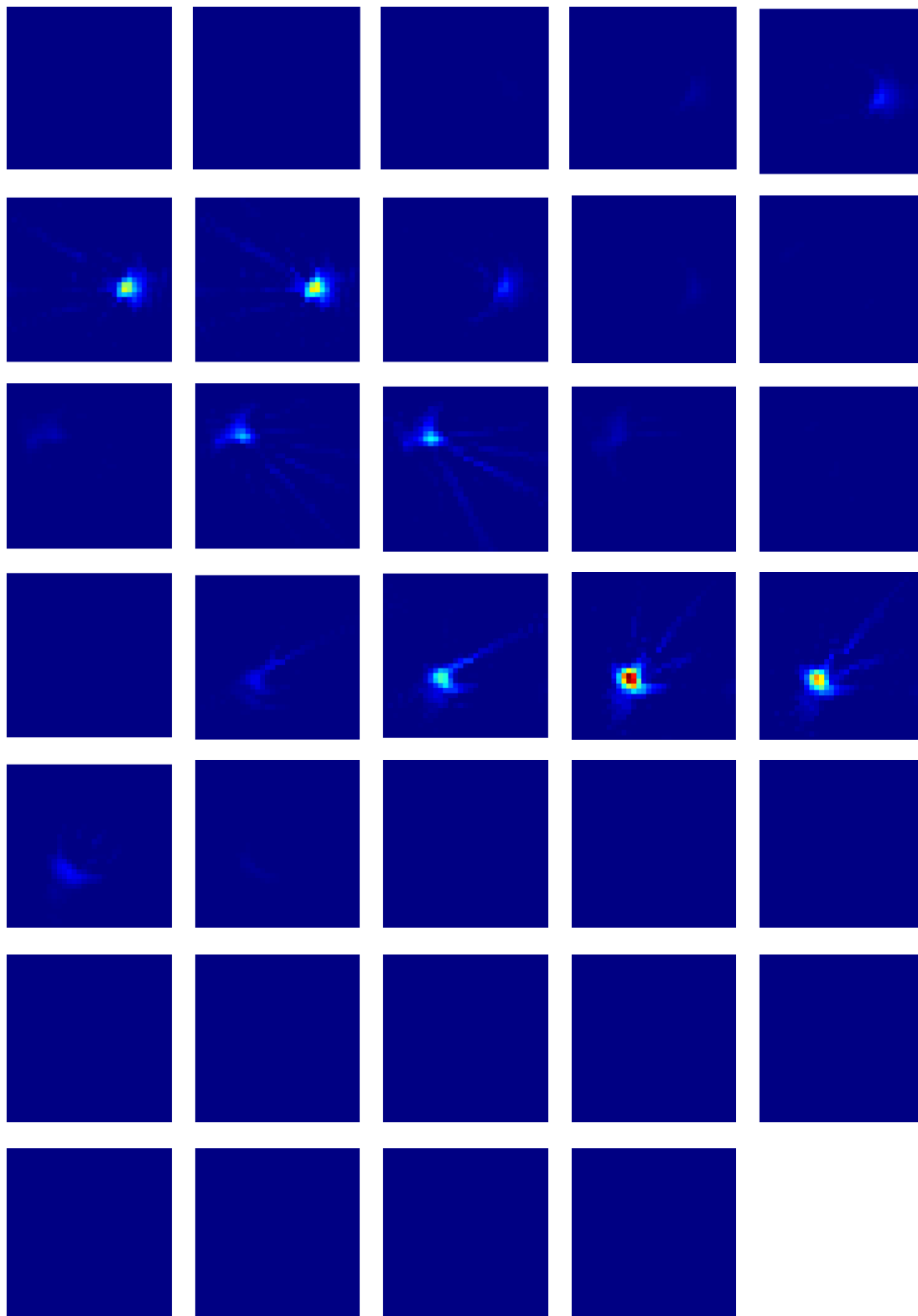


**Fig. 5.36** Reconstructed (Analytical) slice images showing  $^{137}\text{Cs}$  activity. The images show XY Slices at different Z-positions starting from bottom to top (ordered row-wise left to right)

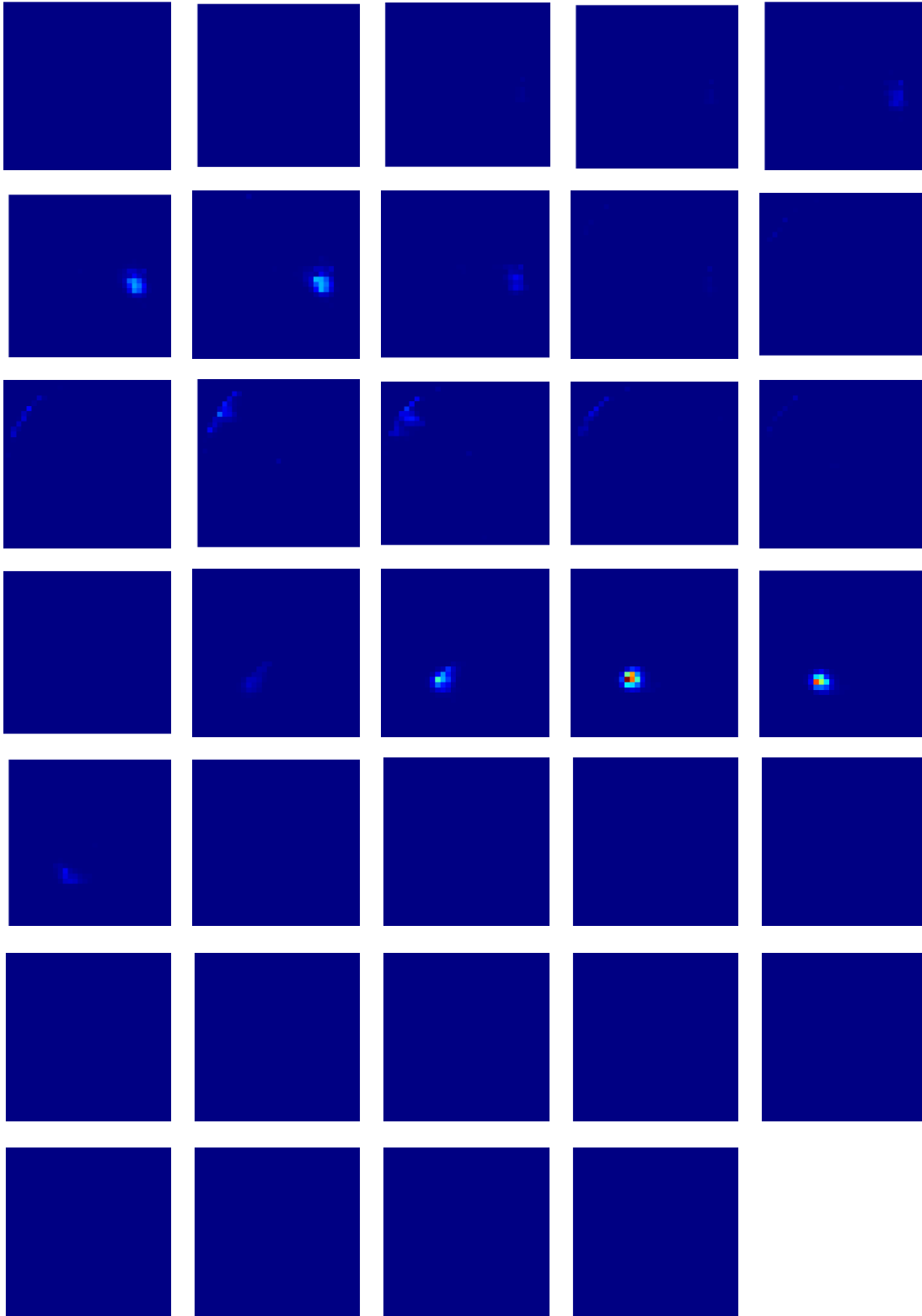


**Fig. 5.37** Reconstructed (2D MLEM) slice images showing  $^{137}\text{Cs}$  activity. The images show XY Slices at different Z-positions starting from bottom to top (ordered row-wise left to right)

Fig. 5.35 (a) shows the attenuation map at 662 keV obtained from the Active CT data. The attenuation map shows high density materials (densely packed rubber gloves) in the bottom one-third of the drum, nearly homogeneous attenuation in the middle one-third of the drum (nearly uniformly distributed cellulose matrix). Fig.5.35 (b) shows the analytical reconstruction for  $^{137}\text{Cs}$  activity in the waste barrel. Fig.5.35 (c) shows the MLEM reconstruction using 2D system model. The number of iterations required for MLEM technique is 50.

Fig. 5.36 shows the slice images for analytical reconstruction. Fig. 5.37 shows the slice images for 2D MLEM reconstruction. Table 5.6 shows the reconstructed activity for the three sources.

*TABLE 5.6 Comparison of reconstructed and true source activity*

<b>Reconstruction Technique</b>	<b>Source (Slice-wise location)</b>	<b>Reconstructed activity (MBq)</b>	<b>Deviation in Reconstructed activity (%)</b>
<b>FBP</b>	<b>A (Bottom)</b>	$24.9 \pm 1.8$	6.7
	<b>B (Middle)</b>	$18.7 \pm 1.5$	10.9
	<b>C (Top)</b>	$35.1 \pm 1.9$	7.1
<b>2D MLEM</b>	<b>A (Bottom)</b>	$26.6 \pm 1.6$	3.6
	<b>B (Middle)</b>	$19.9 \pm 1.4$	5.2
	<b>C (Top)</b>	$36.9 \pm 1.8$	2.4

Fig. 5.38 shows the  $^{137}\text{Cs}$  activity using analytical reconstruction (no collimator modelling) (top row) and MLEM reconstruction (bottom row) using the fan beam system model. The activity map for three consecutive z-slices is shown. It can be seen that the

collimator blurring is reduced in the MLEM reconstruction as the collimator modeling has been implemented in the system matrix.

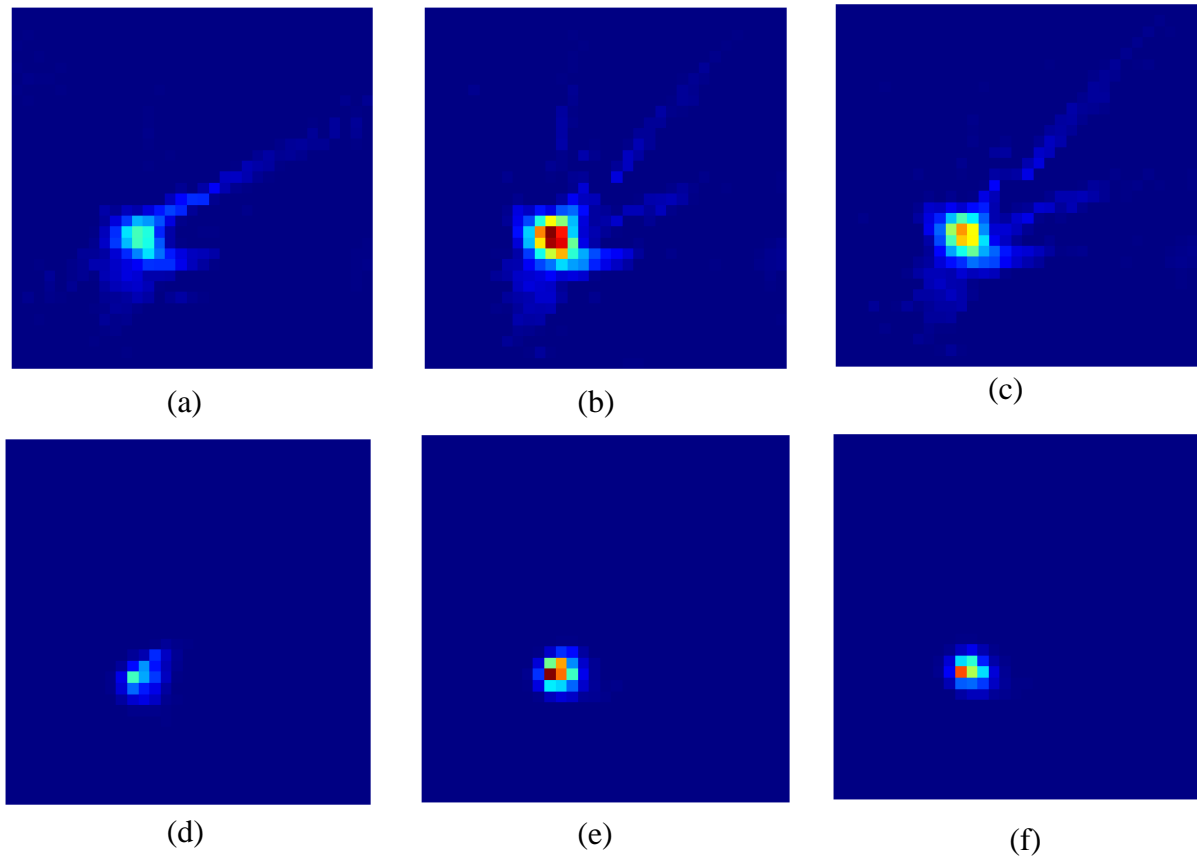


*Fig. 5.38*  $^{137}\text{Cs}$  activity for Slice 18, Slice 19 and Slice 20 (left to right) using analytical (a -c) and MLEM (d -f) reconstruction

## 5.5 Effect of Collimation

Increasing the collimation reduces the blurring due to collimator effects. To study this effect, experiments have been carried out at different collimation ratios using a single  $\text{LaBr}_3(\text{Ce})$  detector. Two  $^{137}\text{Cs}$  source (C and B) are placed inside a perspex disc of diameter 300mm (Section 5.1.2 Sample B) at indexed locations 18 and 15 respectively. The distance from the centre of the object to collimator is 200 mm which is fixed for all the experiments. The collimator opening (d) of 10 mm is also fixed whereas the

collimator length ( $L$ ) is varied from 50 mm to 200 mm. The projection data has been acquired for 100 angular positions. The acquisition time for each data point is 10 sec.

Since intra-slice blurring is studied, only 2D analysis has been performed. The projection data are reconstructed using Novikov's Inversion formula. The reconstructed images are shown in Fig.5.39.

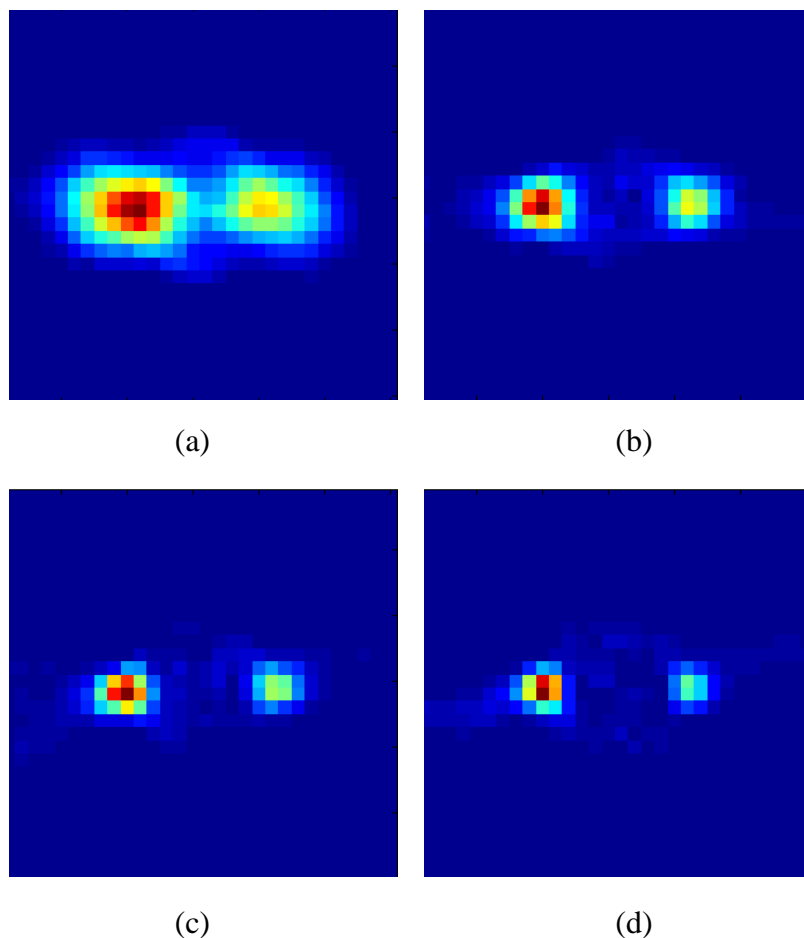


**Fig. 5.39** Effect of collimation ratio on analytically reconstructed image for different collimation ratio (a) 5 (b) 10 (c) 15 (d) 20

For each intensity peak, a Gaussian profile was fitted and correspondingly FWHM is calculated. It can be seen that FWHM reduces with an increase in  $L/d$ , as expected. As is evident from Fig.5.40 and Fig. 5.41, the FWHM reduces slowly above

L/d of 10. This can also be observed from the reconstructed images that increasing the L/d above a certain value improves the image marginally and a trade-off between FWHM and L/d can be reached while choosing an optimum value of L/d. For most of the present experiments, a value of L/d equal to 10 has been chosen.

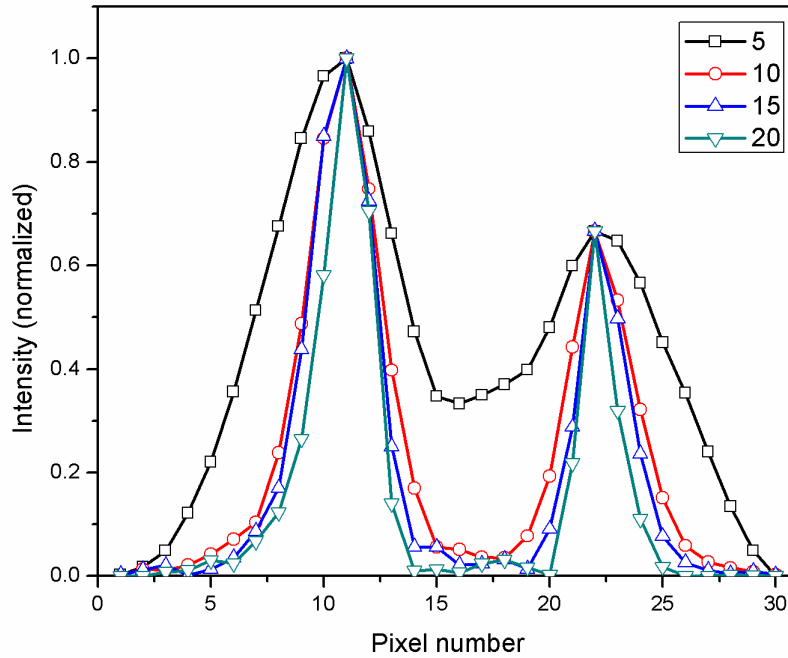


Fig. 5.40 Plot of normalized intensity as a function of pixel number for different collimation ratio (a) 5 (b) 10 (c) 15 (d) 20

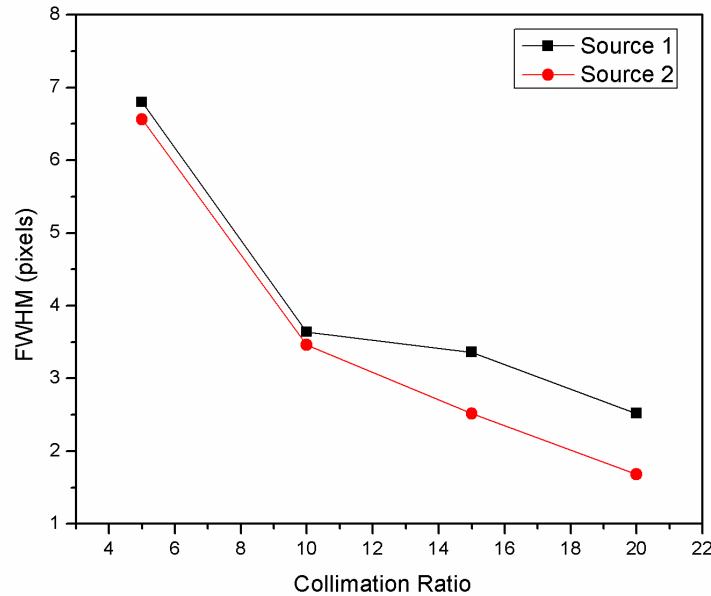


Fig. 5.41 Variation of FWHM for spatial profile of intensity as function of collimation ratio

## **5.6 Discussion**

Experiments on 2D and 3D SPECT imaging using  $^{137}\text{Cs}$  sources have been discussed in Section I. For 2D reconstruction in parallel beam geometry, both analytical and iterative reconstructions have been used. For fully 3D reconstruction, analytical and MLEM techniques have been used. The fully 3D technique clearly brings out the role of collimator modeling as is evident from images reconstructed using analytical, 2D MLEM and fully 3D MLEM techniques. Experiments have also been presented for reconstruction of waste drum in fan beam geometry.

Analytical reconstruction does not take into account the role of collimator and results in blurring which has been evident in the experiments. The iterative techniques reduce the collimator blurring by modelling the collimator. It is observed that ART and SART tend to be noisy and also require larger number of iterations to converge. MLEM and OSEM images are much less noisy and also require lesser number of iterations to converge. The 3D collimator modelling used in fully 3D system matrix reduces the intra slice blurring also. Thus, fully 3D MLEM / OSEM provides a better spatial resolution and lesser noise over the other algorithms used. For experiments discussed in the next section, fully 3D MLEM reconstruction has been adopted as the most suitable reconstruction technique.

## **SECTION II: Active and Passive CT for Nuclear Waste Assay**

Assay of nuclear waste drums is required for disposition decisions, safe transportation, permanent storage as well as nuclear material accounting, especially  $^{239}\text{Pu}$ . Traditionally, the drums are inspected by conventional transmission radiography or tomography.

However, these techniques do not yield information about the radioisotopes inside the drum, but just on the material density. Gamma spectroscopy in open geometry or segmented gamma scanning can be performed to this aim.

Commonly employed gamma ray based non-destructive techniques <sup>[1-3]</sup> or conventional gamma ray spectroscopy methods rely on the assumption that the sample matrix and the activity are in a uniform configuration. In fact, waste drums are often heterogeneous in matrix and radionuclide material distribution, and span a wide range of composition and matrix type. These errors can be reduced by imaging techniques that better measure the spatial locations of sources and matrix attenuations.

One of the most commonly applied non-destructive techniques for assaying radioactive materials in waste drums is the segmented gamma-ray spectrometry (SGS) <sup>[5]</sup> technique. The SGS technique measures spatially averaged gamma-ray intensities in few segments, i.e., horizontal disk-shaped slices of the drum. The average matrix attenuation value for each slice is measured by the transmission of an external source by measuring the attenuated intensity for few ray paths only. These attenuation values are used to correct average passive gamma-ray emitted intensity for each section.

To improve accuracy and provide information about the spatial distribution of the radioisotopes, an active and passive computed tomography (A&PCT) technique is best suited. The A&PCT technique is a more refined technique that improves the imaging from few segments to few thousand volume elements or voxels.

In this chapter, we have explored LaBr<sub>3</sub>(Ce) detectors for A&PCT of <sup>239</sup>Pu in waste assay. This is one of the highlights of this thesis. For comparison, the experiments have also been performed with high energy resolution HPGe detectors.

## **5.7 Active and Passive CT**

Active and Passive Computed Tomography (A&PCT) is one of the most efficient techniques for characterization and localization of radioisotopes in nuclear waste assay. The A&PCT method consists of two steps to perform an assay: active CT and passive CT. This has earlier been discussed in Chapter 1 (Section 1.5).

## **5.8 Experimental set-up**

The experimental set-up discussed in Section 5.2 has been used for the present experiments. An addition to the set-up is the use of filter(s).

A typical problem in plutonium spectroscopic measurement is the relatively high count rate from the 59.54-keV  $^{241}\text{Am}$  gamma ray which dominates the unfiltered spectrum. If the detector is unfiltered, the americium peak will cause unnecessary deadtime. For this purpose, the detector is covered with 3 mm cadmium (followed by 0.250 mm copper) to filter the 59.54-keV gamma ray.

## **5.9 A&PCT of Plutonium with $\text{LaBr}_3(\text{Ce})$**

Most plutonium samples contain the isotopes  $^{238}\text{Pu}$ ,  $^{239}\text{Pu}$ ,  $^{240}\text{Pu}$ ,  $^{241}\text{Pu}$ , and  $^{242}\text{Pu}$ .  $^{241}\text{Am}$  and  $^{237}\text{U}$  are always present as decay products of  $^{241}\text{Pu}$ . Table 5.7 lists some of the gamma energies of these important isotopes.

Traditionally, high purity germanium detectors have been used for gamma spectroscopy of transuranic isotopes especially plutonium. The complex energy spectrum coupled with many closely spaced gamma energies makes it imperative to use a semiconductor detector which has an excellent energy resolution as compared to inorganic scintillators ( $\text{NaI}(\text{Tl})$ ,  $\text{CsI}(\text{Tl})$ ,  $\text{BGO}$ , etc.). Recently, development of cerium

activated lanthanum bromide (LaBr<sub>3</sub>(Ce)) scintillators which have a better energy resolution than their other inorganic counterparts have prompted the need to explore its use for spectroscopy of complex energy spectra. In this section, we explore the use of LaBr<sub>3</sub>(Ce) detectors for SPECT imaging of <sup>239</sup>Pu in nuclear waste assay.

**TABLE 5.7** Main gamma rays in plutonium spectrum

<sup>238</sup> Pu		<sup>239</sup> Pu		<sup>240</sup> Pu		<sup>241</sup> Pu		<sup>241</sup> Am	
keV	γ/s-g								
43.48	2.49 X 10 <sup>8</sup>	51.63	6.19 X 10 <sup>5</sup>	45.23	3.80 X 10 <sup>6</sup>	103.68	3.86 X 10 <sup>6</sup>	59.54	4.54 X 10 <sup>10</sup>
99.86	4.59 X 10 <sup>7</sup>	98.78	2.80 X 10 <sup>4</sup>	104.24	5.86 X 10 <sup>5</sup>	148.57	7.15 X 10 <sup>6</sup>	98.95	2.57 X 10 <sup>7</sup>
152.68	6.05 X 10 <sup>6</sup>	129.29	1.44 X 10 <sup>5</sup>	160.28	3.88 X 10 <sup>4</sup>	164.58	1.73 X 10 <sup>6</sup>	102.97	2.47 X 10 <sup>7</sup>
766.41	1.39 X 10 <sup>5</sup>	203.54	1.28 X 10 <sup>4</sup>	642.48	1.05 X 10 <sup>3</sup>	208.00	2.04 X 10 <sup>7</sup>	125.29	5.16 X 10 <sup>6</sup>
		345.01	1.28 X 10 <sup>4</sup>			332.35	1.14 X 10 <sup>6</sup>	335.40	6.28 X 10 <sup>5</sup>
		375.04	3.60 X 10 <sup>4</sup>			370.93	1.04 X 10 <sup>5</sup>	662.42	4.61 X 10 <sup>5</sup>
		413.71	3.42 X 10 <sup>4</sup>					721.99	2.48 X 10 <sup>5</sup>
		645.97	3.42 X 10 <sup>2</sup>						
		717.72	6.29 X 10 <sup>1</sup>						

### 5.9.1 Experimental Results

A mock waste drum (580mm diameter and 850mm height) is filled with cotton waste / gloves / tissues. A total of 1g plutonium (0.04% <sup>238</sup>Pu, 93.0 % <sup>239</sup>Pu, 6.72% <sup>240</sup>Pu, 0.24% <sup>241</sup>Pu) sealed in 20 aluminum cylinders (approximately 25mm diameter and 25mm height) containing 50 mg each are distributed at three different locations inside the drum. 11 cylinders (0.512g <sup>239</sup>Pu) lumped together are located at region #1 (approx. height 275 mm), 5 cylinders (0.232g <sup>239</sup>Pu) lumped together are located at region #2 (approx. height 700 mm) and 4 cylinders (0.186g <sup>239</sup>Pu) lumped together are located at region #3

(approx. height 475 mm). The data are acquired with LaBr<sub>3</sub>(Ce) detectors. Fig. 5.42 (a) and (b) show the gamma spectrum by LaBr<sub>3</sub>(Ce) detector for Active CT (using <sup>152</sup>Eu source) and Passive CT respectively.

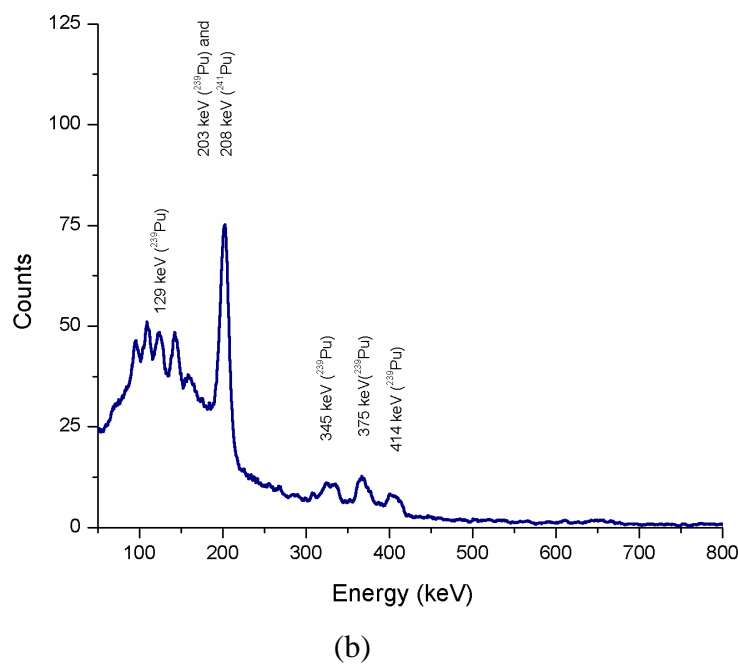
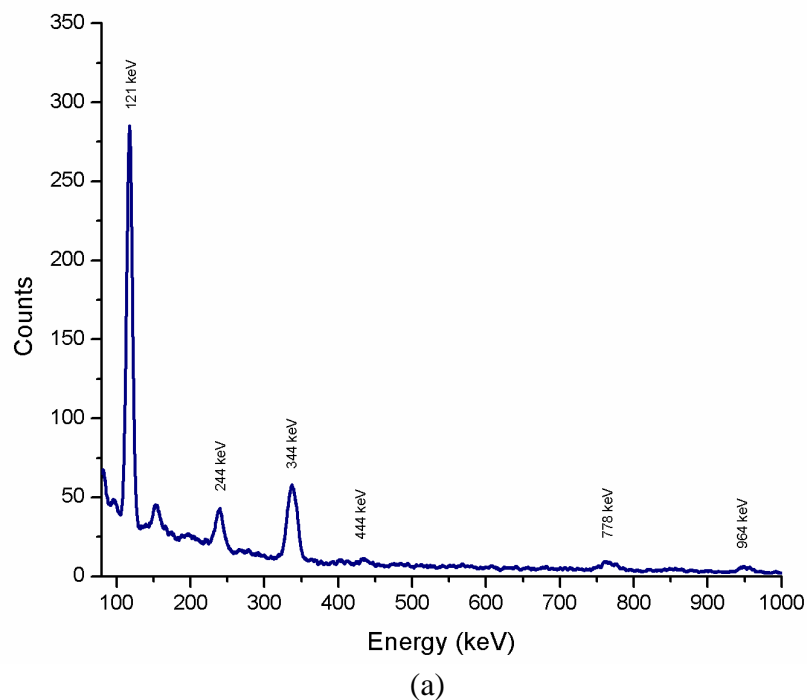


**Fig. 5.42** Gamma spectrum recorded by LaBr<sub>3</sub>(Ce) detector (a) <sup>152</sup>Eu (for Active CT) (b) 93% <sup>239</sup>Pu (for Passive CT). The major <sup>152</sup>Eu and <sup>239</sup>Pu peaks have been labeled

### 5.9.1.1 Active CT

For the ACT measurement, the external gamma source and a single LaBr<sub>3</sub>(Ce) detector are used. Data is acquired at 24 lateral positions and 18 angular positions over 180° for each z-position. In the vertical direction, 33 z-positions are scanned. Each slice thickness is 25 mm. The acquisition time for each data point is 10 sec. The peak area corresponding to 244 keV, 444 keV, 778 keV, 964 keV and 1407 keV are used for reconstructing the active data set. The 344 keV peak is avoided as it interferes with the 345 keV peak from <sup>239</sup>Pu. The attenuation coefficient at emission energy (414 keV peak is analyzed for assessing the <sup>239</sup>Pu distribution in the consecutive PCT measurement) is obtained by interpolating the values from the above data set. The reconstructed attenuation map is shown in Fig. 5.43 (a) and Fig. 5.43 (b).

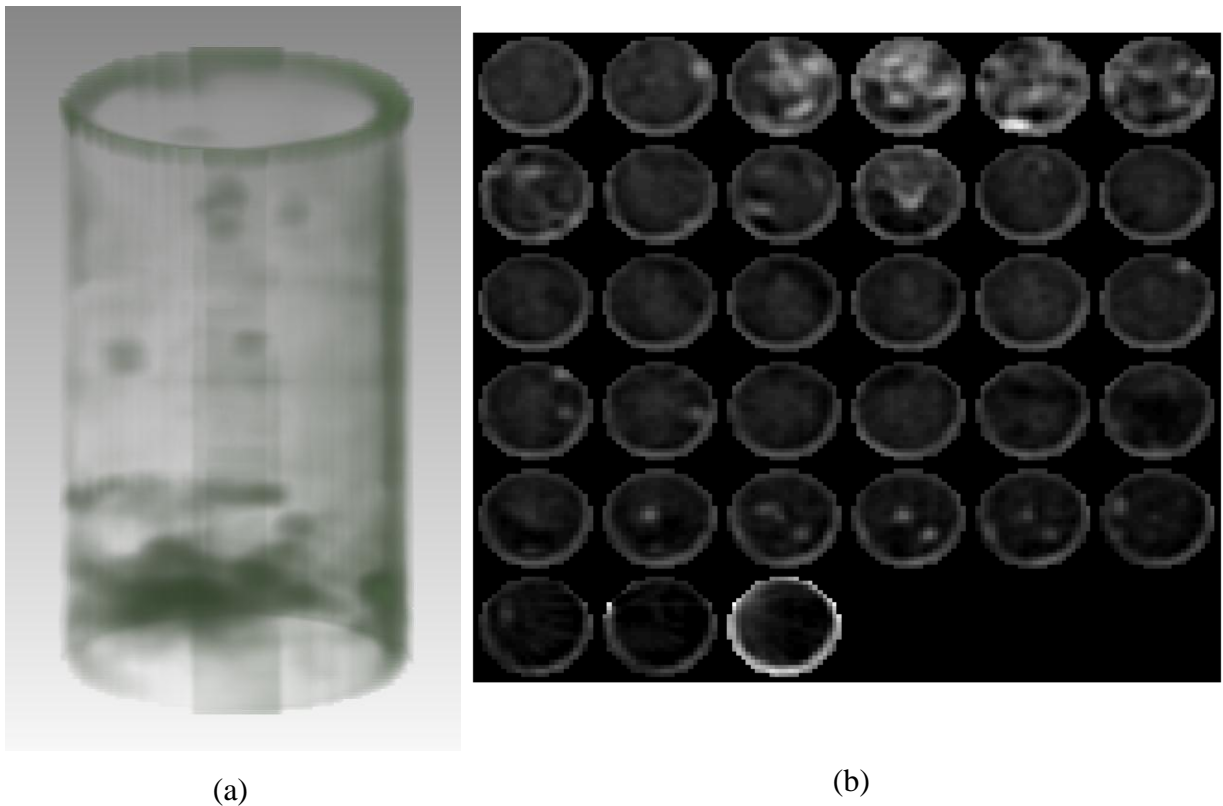


**Fig. 5.43** (a) Reconstructed 3D attenuation map at 414 keV (b) Reconstructed Active CT slice images at different elevations

### 5.9.1.2 Passive CT

For the PCT measurement, the external source is removed and gamma rays emitted from within the drum are recorded by three collimated LaBr<sub>3</sub>(Ce) detectors. For each z-position, data are acquired at 12 angular positions over 360° with 24 lateral data points per projection. In the vertical direction, 33 z-positions are scanned. Each slice thickness is 25 mm. The collimator opening is 25 mm (with septa) and collimator length is 100 mm (collimation ratio: 10). The distance from the centre of object to collimator opening is 450 mm. The acquisition time for each data point is 20 sec.

The passive data set is reconstructed using fully 3D MLEM technique. The reconstructed volume is discretized on a 24 X 24 X 33 grid. The 414 keV peak from <sup>239</sup>Pu is used for PCT measurement. The reconstructed 3D volume is shown in Fig. 5.44. Reconstructed XY slices at different Z-positions are shown in Fig. 5.45. It can be seen that spatial position of the radioisotopes can be easily located.

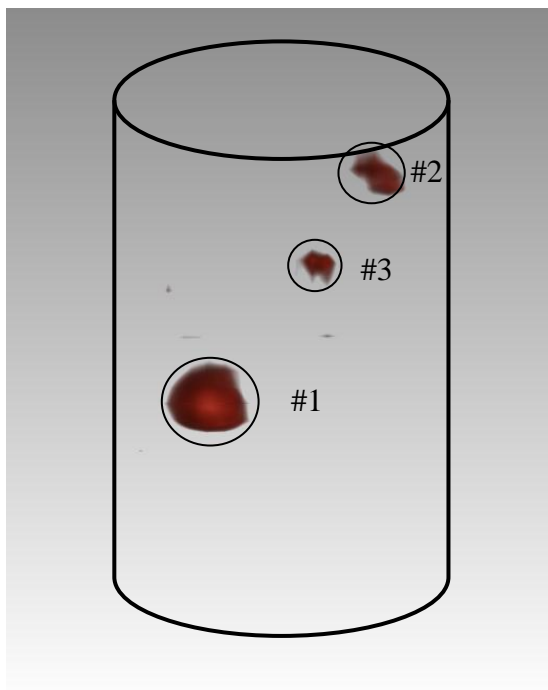


*Fig. 5.44 Reconstructed 3D volume showing activity distribution of <sup>239</sup>Pu. The drum outline is shown for illustration*

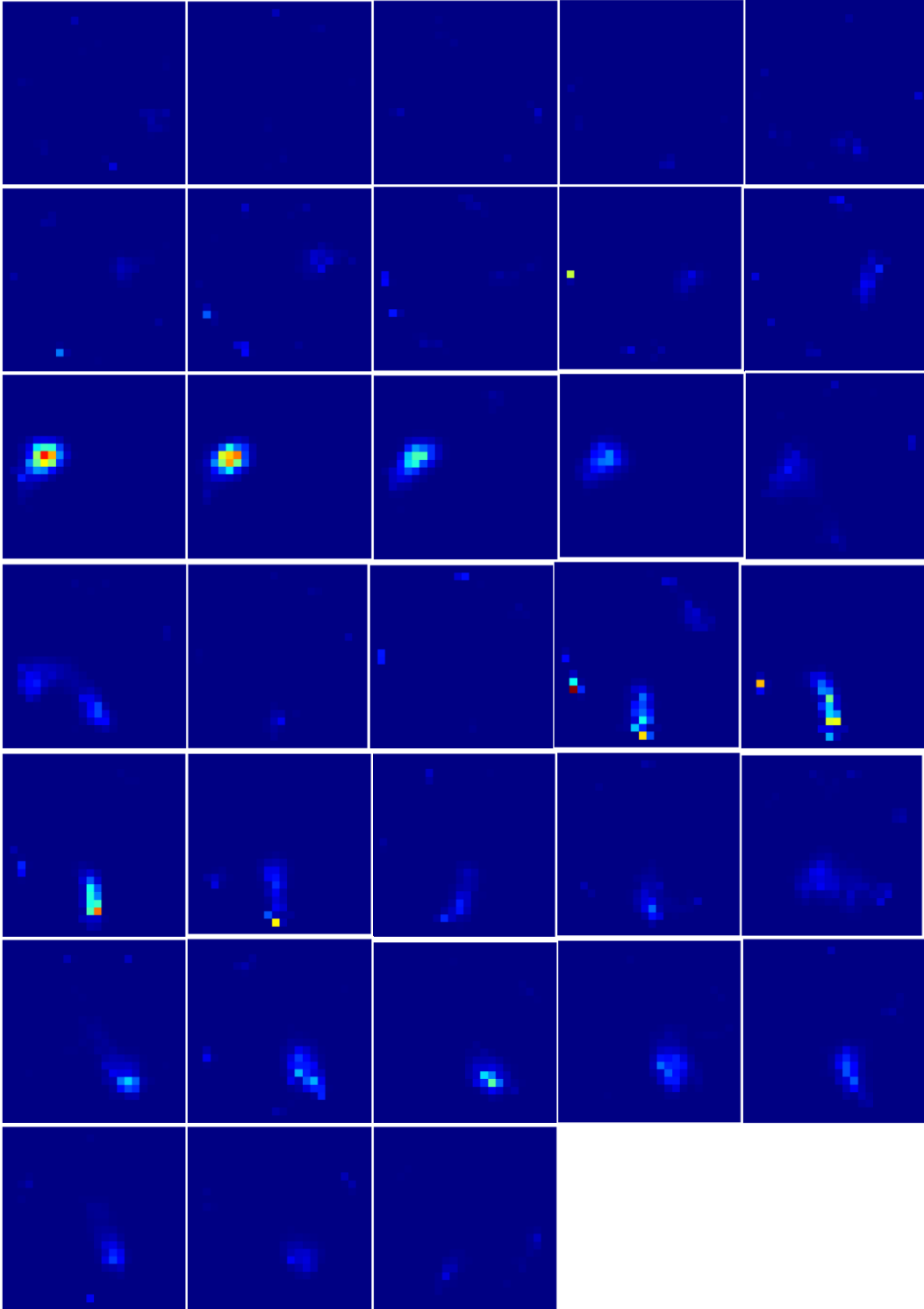


*Fig. 5.45 Fully 3D MLEM reconstructed Passive CT slice images at different elevations*

The total activity for each distinct source is calculated by summing all the voxels in a given region. The measured activity can be converted to its mass (in gram) using the following relation:

$$m = \frac{A}{A_{sp}} \quad (5.4)$$

where  $A_{sp}$  is the specific activity of the radioisotope. The specific activity of  $^{239}\text{Pu}$  is 0.063 Ci/g (or  $2.33 \times 10^3$  MBq/g).

The reconstructed activity distribution in the images matches well with the true source activity (see Table 5.8).

**TABLE 5.8: Reconstructed  $^{239}\text{Pu}$  mass**

	<b>True <math>^{239}\text{Pu}</math> mass</b>	<b>Reconstructed <math>^{239}\text{Pu}</math> mass</b>
	<b>(g)</b>	<b>(g)</b>
# 1	0.512	$0.519 \pm 0.023$
# 2	0.232	$0.233 \pm 0.015$
# 3	0.186	$0.168 \pm 0.013$
<b>Total</b>	<b>0.930</b>	<b><math>0.920 \pm 0.030</math></b>

## 5.10 A&PCT of Plutonium with HPGe

High resolution gamma spectroscopy is used to determine isotopic composition of plutonium. In the previous sections, we have discussed the SPECT imaging of  $^{239}\text{Pu}$  with  $\text{LaBr}_3(\text{Ce})$  detectors. It can be combined with high resolution spectroscopy to increase sensitivity.

### 5.10.1 Spectral Features of Plutonium

In this sub-section, we shall analyze the spectral features which are essential in measurement of isotopic composition of plutonium. The same sample of plutonium used for A&PCT measurements is used for spectral measurements.

#### A. Energy Range: 0 – 160 keV

Table 5.8 shows that the lower energy gamma rays are more intense than those at higher energies. The lower energy gamma rays should be used whenever possible. However, it is often impossible to use them. This is because if too much  $^{241}\text{Am}$  is present, the 59.54 keV gamma ray overwhelms all other peaks in the region. Usually, the region below 60 keV is useful for 15 to 30 days after a separation of americium and uranium.

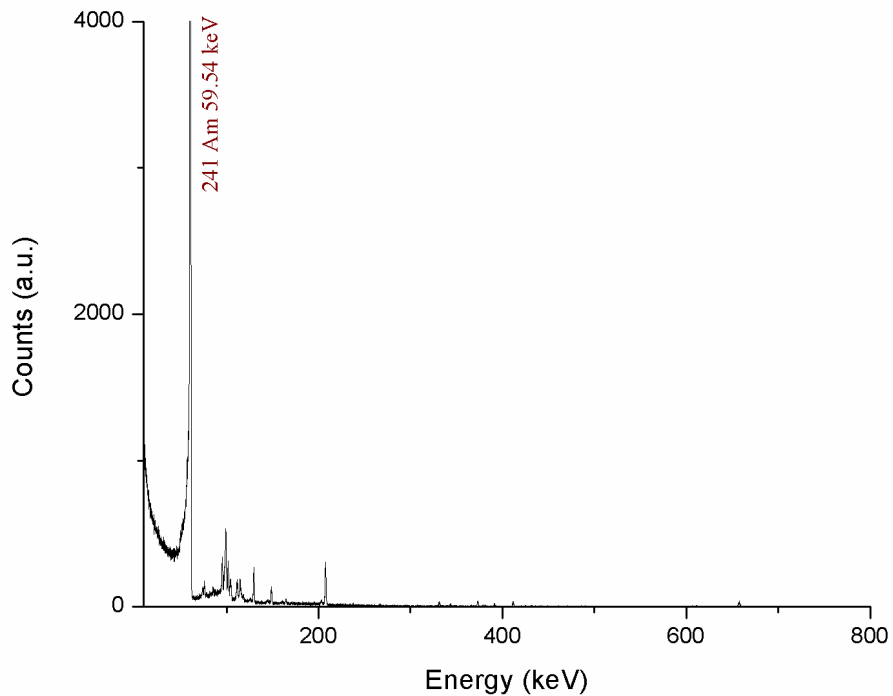


*Fig. 5.46 Gamma spectrum of Plutonium (without Cd filter)*

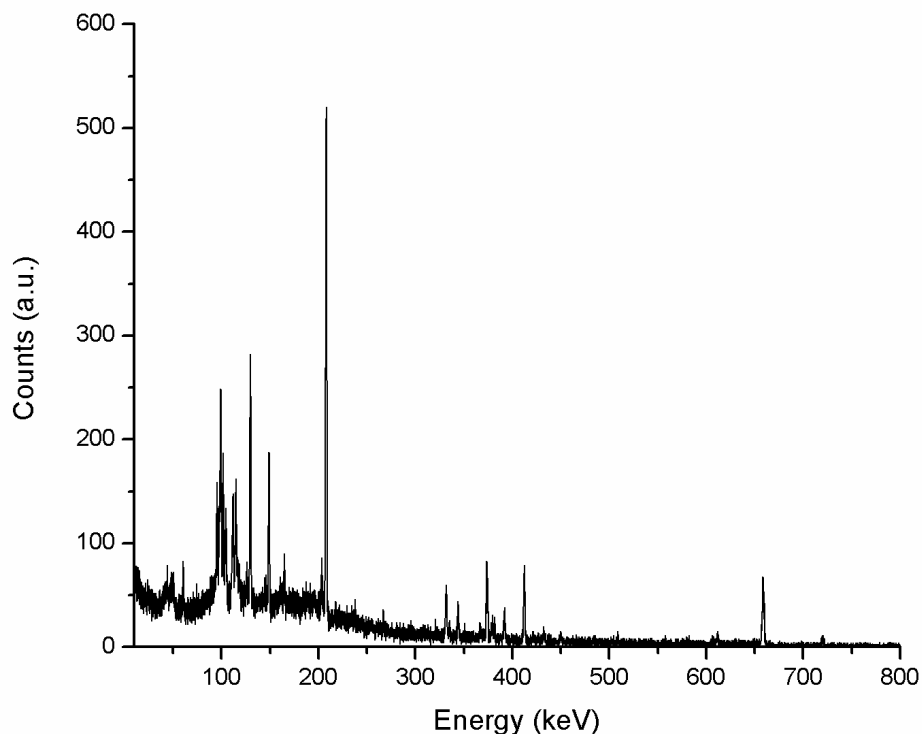


*Fig. 5.47 Gamma spectrum of Plutonium (with Cd filter)*

To minimize the spectral interference of the 59.54 keV  $^{241}\text{Am}$  gamma ray, the detector is covered with 3 mm cadmium (followed by 0.250 mm copper) to selectively absorb the 59.54-keV gamma ray. Fig. 5.46 and 5.47 show the unfiltered and filtered gamma spectrum respectively.

Fig. 5.48 shows the gamma spectrum for energies less than 160 keV. The region 90-120 keV is a complex region consisting of X-rays and gamma rays. The uranium X-rays arise from plutonium decay and can be used to measure the plutonium isotopes. The neptunium X-rays arise from the decay of  $^{241}\text{Am}$  and  $^{237}\text{U}$  whereas the plutonium X-rays appear from gamma-ray and alpha particle induced X-ray fluorescence. This is the only region in which gamma rays from all isotopes are present.

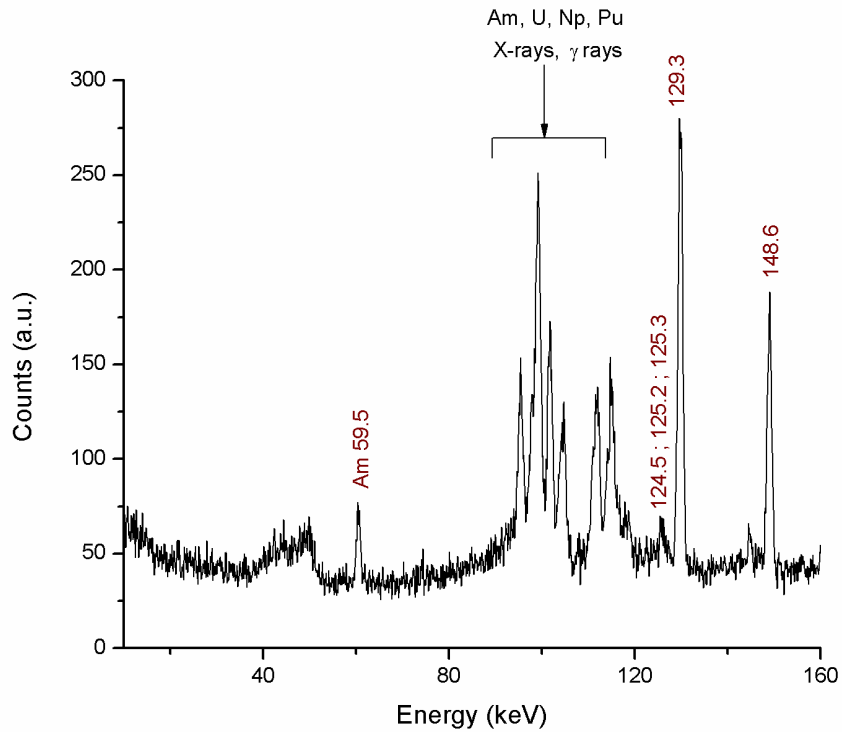


*Fig. 5.48 Gamma spectrum of plutonium (239 - 93 %) in the energy range less than 160 keV*

$^{241}\text{Am}$  and  $^{239}\text{Pu}$  can be measured from gamma rays at 125.29 and 129.29 keV. There are strong interferences to the 125.29-keV  $^{241}\text{Am}$  gamma ray from  $^{239}\text{Pu}$  lines at 125.21 and 124.51 keV. The use of filters also affects the count rate in this region.

The 148.57-keV  $^{241}\text{Pu}$  peak is the only useful gamma ray outside of the complex 100-keV region that comes directly from  $^{241}\text{Pu}$ . The 152.68 keV peak from  $^{238}\text{Pu}$ , although weak, is often the only useful gamma ray from  $^{238}\text{Pu}$  above 100 keV.

### **B. Energy Range: 160 – 320 keV**

Fig. 5.49 shows the gamma spectrum for energies in the range 160 – 320 keV. The strong  $^{241}\text{Pu}$ - $^{237}\text{U}$  peak at 208.00 keV dominates this region. Usually it is the most intense peak in the spectrum. Because this gamma-ray comes from  $^{237}\text{U}$  it can be used only for aged samples.

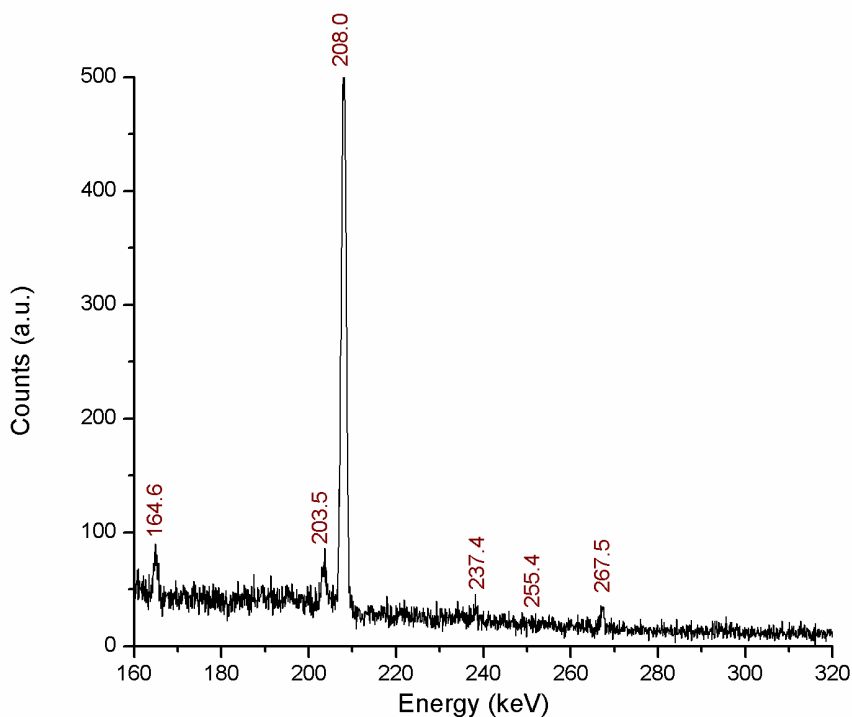


**Fig. 5.49** Gamma spectrum of plutonium (239 - 93 %) in the energy range 160 – 320 keV

The 203.54 keV  $^{239}\text{Pu}$  line is another important peak in this region. The  $^{239}\text{Pu}/^{241}\text{Pu}$  ratio formed with the 203.54/208.00 line pair gives best results for low burnup material. For high burnup material, the precision of the 203.54-keV  $^{239}\text{Pu}$  peak becomes worse because of the Compton background and the long tail from the very strong 208.00 keV  $^{237}\text{U}$  peak.

### C. Energy Range: 320 – 460 keV

Fig. 5.50 shows the gamma spectrum for energies in the range 320 – 460 keV. The ratio of the 345 keV  $^{239}\text{Pu}$  peak to the 332.35 keV  $^{241}\text{Pu}$ - $^{237}\text{U}$  peak is useful for measuring the  $^{239}\text{Pu}/^{241}\text{Pu}$  ratio. Both the 332.35- and 335.40-keV peaks from  $^{241}\text{Pu}$ - $^{237}\text{U}$  contain very close interferences from  $^{239}\text{Pu}$  peaks.

The 375 keV region also has components from  $^{241}\text{Pu}$ - $^{237}\text{U}$ ,  $^{241}\text{Am}$ , and  $^{239}\text{Pu}$ . For all isotopes except  $^{239}\text{Pu}$  the branching ratios are lower than in the 332-keV region, so the isotopic information will be less precise.

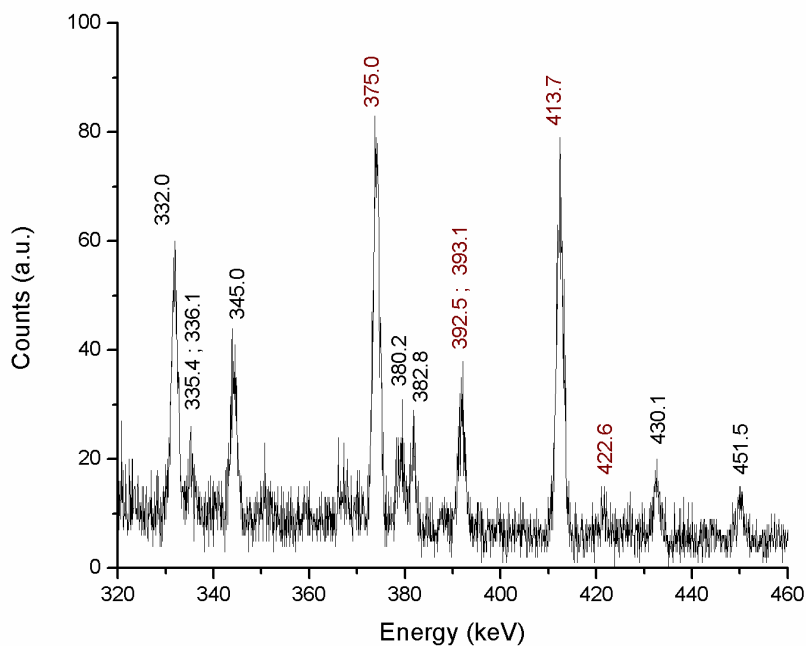


*Fig. 5.50 Gamma spectrum of plutonium (239 - 93 %) in the energy range 320 – 460 keV*

The 413.7 keV peak from  $^{239}\text{Pu}$  is the only peak which is free from interference from other Pu peaks and is often used for absolute measurement of  $^{239}\text{Pu}$  mass in the sample. This is the energy peak which has been used for Passive CT experiments in this thesis

#### **D. Energy Range: 460 –800 keV**

Fig. 5.51 shows the gamma spectrum for energies in the range 460 – 800 keV. This is the only region above 160 keV that can be used for measuring  $^{240}\text{Pu}$ . The region is useful only for large samples because of the low intensity of the 642.48-keV  $^{240}\text{Pu}$  gamma ray.

Nearby peaks from  $^{239}\text{Pu}$  and  $^{241}\text{Am}$  complicate the region. The 645.97 keV and 662.42 keV peaks are useful for measuring  $^{239}\text{Pu}$  and  $^{241}\text{Am}$ .

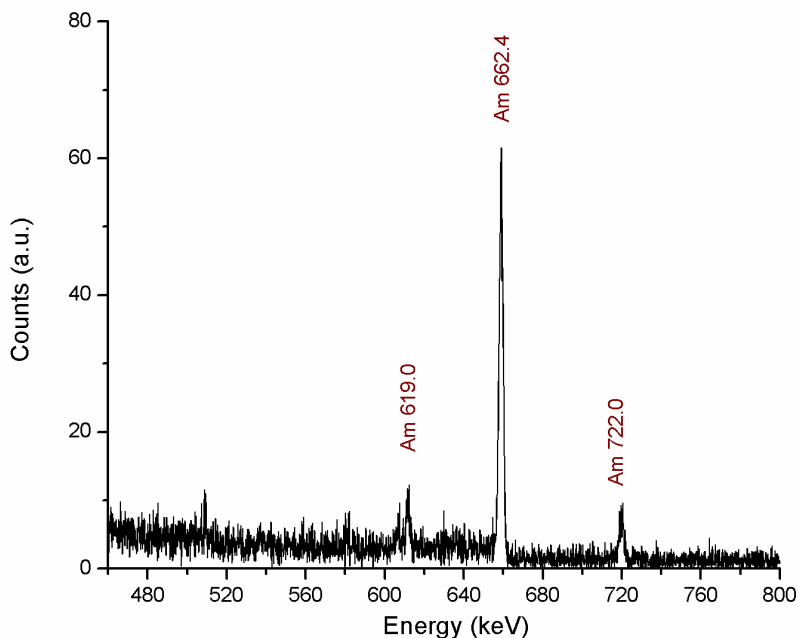


*Fig. 5.51 Gamma spectrum of plutonium (239 - 93 %) in the energy range 460 – 800 keV*

### 5.10.2 Active CT

For the ACT measurement, the external gamma source and single HPGe detector are used. Data is acquired at 18 angular positions with 24 lateral data points per projection over  $180^\circ$  for each z-position. In the vertical direction, 33 z-positions are scanned. Each slice thickness is 25mm. The acquisition time for each data point is 10 sec. The peak area corresponding to 244 keV, 444 keV, 778 keV, 867 keV, 964 keV and 1407 keV are used for reconstructing the active data set. The reconstructed attenuation map is shown in Fig. 5.52 (a).

### 5.10.3 Passive CT

For the PCT measurement, the external source is removed and gamma rays emitted from within the drum are recorded by single collimated HPGe detector. Data are acquired at 12 angular positions with 24 lateral data points per projection over  $360^\circ$  for each z-position. In the vertical direction, 33 z-positions are scanned. Each slice thickness is 25mm. The collimator opening is 25 mm (with septa) and collimator length is 100 mm (collimation ratio: 10). The distance from the centre of object to collimator opening is 450 mm. The acquisition time for each data point is 50 sec.

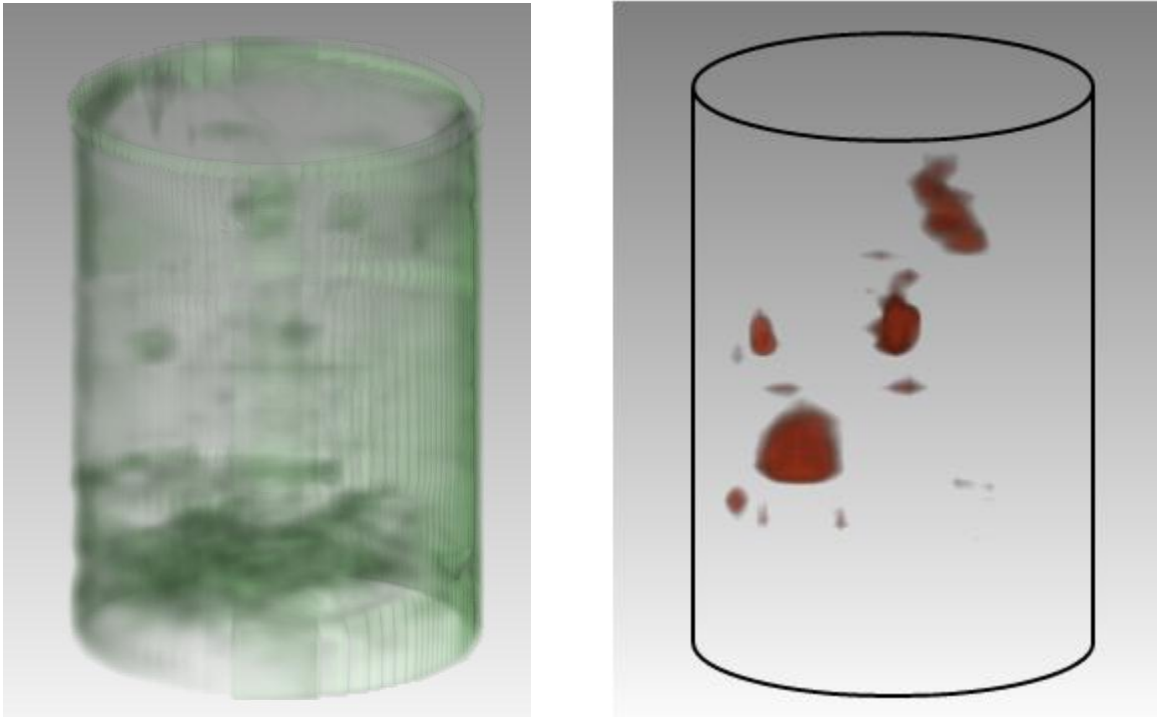


*Fig. 5.52 3D view (a) Attenuation map (b)  $^{239}\text{Pu}$  activity distribution*

The passive data set is reconstructed using fully 3D MLEM technique. The reconstructed volume is discretized on a  $24 \times 24 \times 34$  grid. The 414 keV peak from  $^{239}\text{Pu}$  is used for PCT. The reconstructed 3D volume is shown in Fig. 5.52 (b). It can be seen

that spatial position of the radioisotopes can be easily located. Fig. 5.53 shows the 3D volume of the drum which both the active and passive data overlapped.



*Fig. 5.53 3D (perspective) view with superimposed active and passive data set*

The reconstructed activity distribution in the images matches well with the true source activity (see Table 5.9).

*TABLE 5.9: Reconstructed  $^{239}\text{Pu}$  mass*

	True $^{239}\text{Pu}$ mass (g)	Reconstructed $^{239}\text{Pu}$ mass (g)
# 1	0.512	$0.528 \pm 0.025$
# 2	0.232	$0.225 \pm 0.016$
# 3	0.186	$0.166 \pm 0.010$
<b>Total</b>	<b>0.930</b>	<b><math>0.919 \pm 0.030</math></b>

## 5.11 Discussion

An Active and Passive CT facility has been developed for detection and imaging of  $^{239}\text{Pu}$  in waste drum. The results show that the three dimensional distribution of  $^{239}\text{Pu}$  as well as the mass/quantity assayed matches well with the true distribution. A novel feature of the work is the use of  $\text{LaBr}_3(\text{Ce})$  for imaging of  $^{239}\text{Pu}$  which, to the best of our knowledge, is being reported for the first time.  $\text{LaBr}_3(\text{Ce})$  detectors may be used for SPECT of radioactive waste (including transuranic waste) especially for multi-detector systems. An HPGe detector, owing to its better energy resolution, can be used for SPECT imaging of other plutonium isotopes also. The experiments have been repeated with an HPGe detector and it is observed that so far as the imaging of  $^{239}\text{Pu}$  is concerned, the results obtained with  $\text{LaBr}_3(\text{Ce})$  and HPGe match reasonably well.

## **Concluding Remarks**

The thesis describes emission tomography studies on nuclear materials, with specific focus on waste barrels. The work covered in this thesis includes development of simulation codes for producing virtual parallel-, fan- and cone-beam data, development of tomographic reconstruction codes and software based on analytical and iterative algorithms, implementing hardware for tomographic data collection and evaluation of these reconstruction methods on experimental data collected using an advanced measurement setup combining Active and Passive CT.

For the simulation part, dedicated codes have been developed for simulating projection data, especially for fan- and cone-beam configurations. Similarly, dedicated codes have been developed for both analytical and iterative reconstruction techniques.

Analytical reconstruction techniques based on filtered backprojection are fast and easy to implement but result in significant blurring due to the physical size of the collimator. The effect of collimator blurring can be reduced by using iterative reconstruction. This necessitates the use of iterative techniques.

For iterative techniques, a key factor is the precise modeling of the forward projection, that is, the construction of the system matrix. The construction of the system matrix is not often discussed in literature although it plays a fundamental role in iterative reconstruction. Generally, 3D reconstructions are performed using a 2D system matrix where each horizontal plane is reconstructed independently of the other planes and a

pseudo 3D volume is obtained by stacking different reconstructed 2D planes. This method of 3D imaging reduces intra-slice blurring but results in inter-slice blurring due to cross-talk between different planes.

For a truly 3D reconstruction, a fully 3D system matrix is required. A novelty of this work is the implementation and testing of a fully 3D iterative method, where the inter-slice contributions to the detector signals are taken into account, enabling the reduction of inter-slice blurring in the resulting images.

Amongst the iterative reconstruction techniques explored, the algebraic techniques ART and SART tend to produce noisy image and also require a larger number of iterations, in general, to converge. The statistical techniques, MLEM and OSEM, in comparison, produce a less noisy image and converge faster. Hence, the MLEM technique is used to reconstruct most of the images in experimental section. Instances where qualitative information or fast reconstruction is required, analytical reconstruction has been used.

In addition to parallel beam SPECT geometries discussed so far, a practical fan-beam Active and Passive CT technique for waste assay has also been developed. The scanning geometry uses a fan beam with the active source placed at the focal point of the fan. This results in speedup due to the elimination of discrete translation positioning in the active (and/or passive) mode(s). Also, the fan-beam design has only one source and a very simple source collimator compared to the straight in-line case. This scanning geometry has been experimentally demonstrated. For reconstruction, an expression for 2D fan beam system matrix has been analytically determined and implemented.

For the experimental part, an advanced setup for combining (active) transmission tomography and (passive) emission tomography has been set-up for three dimensional imaging of waste drums. A novel feature of this thesis is the application of relatively novel detector  $\text{LaBr}_3(\text{Ce})$  for SPECT imaging of  $^{239}\text{Pu}$  samples in low level waste. Although high resolution HPGe detectors are conventionally used for spectral analysis of plutonium, we have explored medium-high energy resolution  $\text{LaBr}_3(\text{Ce})$  detectors for SPECT imaging of  $^{239}\text{Pu}$ . The results have been compared with high energy resolution reconstruction with HPGe detectors and it has been observed that both match reasonably well. Although  $\text{LaBr}_3(\text{Ce})$  cannot determine isotopic ratios, it can be used for absolute measurement of  $^{239}\text{Pu}$ .

The highlights of the work done under this thesis may be summarized as follows:

- (i) Implementation of analytical and iterative reconstruction techniques
- (ii) Novel method for generation of fan and cone beam data for simulated objects
- (iii) Development and implementation of fully 3D SPECT reconstruction
- (iv) Development and implementation of a practical fan-beam Active and Passive CT technique for waste assay
- (v) Developing a three dimensional SPECT imaging facility for scanning of waste drums using  $\text{LaBr}_3(\text{Ce})$  detectors
- (vi) Active and Passive CT for  $^{239}\text{Pu}$  assay in waste drums

Future work will involve implementation of the developed technique for quantitative SPECT imaging of real waste drums. Another application where this technique will be used is in burnup determination of PHWR fuel pin / fuel assemblies.

# References

- [1] E. R. Martin, D.F. Jones, J.L. Parker, “Gamma-ray measurements with the segmented gamma scanner”, LA-7059-M, Los Alamos Scientific Laboratory (1977).
- [2] J.T. Caldwell, R.D. Hastings, G.C. Herrera, W.E. Kounz, E.R. Shrunck, “The Los Alamos second generation system for passive and active neutron assays of drum size containers”, LA-10774-MS, Los Alamos Scientific Laboratory (1986).
- [3] M.E. McIlwain, G.K. Becker, “Nondestructive waste assay capability evaluation program”, Proceedings of the Sixth Nondestructive Assay and Nondestructive Examination Waste Characterization Conference, Salt Lake City, Utah, CONF-981105, 171–190 (1998).
- [4] F. Tzika, A. Savidou, I. E. Stamatelatos, “Nondestructive characterization of radioactive waste drums by gamma spectrometry: a Monte Carlo technique for efficiency calibration”, *Health Phys.* **93**, 174-179 (2007).
- [5] J.K.Sprinkle, Jr. and S.T.Hsue, “Recent advances in SGS Analysis”, Proceedings, Third International Conference on Facility Operations - Safeguards Interface, San Diego, California, 188 (1987)
- [6] G.P. Roberson, H.E. Martz, D.J. Decman, J.A. Jackson, R.T. Bernardi, D.C. Camp, “Nondestructive assay using active and passive computed tomography”, Presented at the INMM 39th Annual Meeting, Naples, FL (1998).
- [7] G.P. Roberson, H.E. Martz, D. Nisius, “Active and passive computed tomography for nondestructive assay”, Proceedings for the American Nuclear Society 1999, Winter Meeting and Embedded Topical Meetings, Long Beach, CA, **81**, 229–231 (1999).

- 
- [8] [http://eeweb.poly.edu/~yao/EL5823/NuclearImaging\\_ch8\\_9.pdf](http://eeweb.poly.edu/~yao/EL5823/NuclearImaging_ch8_9.pdf)
- [9] Todd E. Peterson and Lars R. Furenlid, “SPECT detectors: the Anger Camera and beyond”, *Phys Med Biol.* **56** (17) (2011)
- [10] H. Anger, “A new instrument for mapping gamma-ray emitters”, *Biology and Medicine Quarterly Report*, UCRL 3653: 38, University of California Radiation Laboratory, Berkeley (1957)
- [11] H. O. Anger, “Scintillation camera with multichannel collimators”, *J Nucl Med*, **65** 515-531, (1964)
- [12] H. O. Anger, D. J. Rosenthal, “Scintillation camera and positron camera”, *Medical Radioisotope Scanning*, Vienna: International Atomic Energy Agency, 59–75 (1959)
- [13] H. O. Anger, “Scintillation camera”, *Rev. Sci. Instrum.* **29** 27–33 (1958)
- [14] D. E. Kuhl, R. Q. Edwards, “Image separation radioisotope scanning”, *Radiology* **80**:653–662 (1963)
- [15] D. E. Kuhl, R. Q. Edwards, “Cylindrical and section radioisotope scanning of the liver and brain” *Radiology* **83**:926–936 (1964)
- [16] D. E. Kuhl, “A clinical radioisotope scanner for cylindrical and section scanning”, *Medical Radioisotope Scanning*, **Vol. 1**, Vienna: International Atomic Energy Agency, 273–289 (1964)
- [17] D. E. Kuhl, R. Q. Edwards, “Cylindrical and section radioisotope scanning of the liver and brain”, *Radiology* **83** 926–935, (1964)
- [18] D. E. Kuhl, R. Q. Edwards, “The Mark III scanner: a compact device for multiple-view and section scanning of the brain”, *Radiology* **96**:563–570 (1970)

## References

---

- [19] D. E. Kuhl, R. Q. Edwards and A. R. Ricci, "Transverse section scanner at the University of Pennsylvania" *Tomographic Imaging in Nuclear Medicine* (eds.) G S Freedman (New York: Society of Nuclear Medicine) 19–27 (1974)
- [20] D. E. Kuhl, R. Q. Edwards, A. R. Ricci, R. J. Yacob, T. J. Mich and A. Alavi, "The Mark IV system for radionuclide computed tomography of the brain", *Radiology* **121** 405–413, (1976)
- [21] D. E. Kuhl, J. Hale and W. L. Eaton, "Transmission scanning: a useful adjunct to conventional emission scanning for accurately keying isotope deposition to radiographic anatomy", *Radiology* **87** 278–284, (1966)
- [22] G. Muehllehner, "A tomographic scintillation camera", *Phy Med Biol*, **16**:87–96. (1971)
- [23] J. W. Keyes, N. Oleandea, W. J. Heetderks, P. F. Leonard, W. L. Rogers, "The humongotron: A scintillation camera transaxial tomography", *J Nucl Med*, **18**:381–387. (1977)
- [24] R. J. Jaszczak, D. Huard, P. Murphy, J. Burdine, "Radionuclide emission tomography with a scintillation camera", *J Nucl Med*, **17**:551 (1976)
- [25] [http://www-pub.iaea.org/MTCD/publications/PDF/te\\_1597\\_web.pdf](http://www-pub.iaea.org/MTCD/publications/PDF/te_1597_web.pdf), "Clinical Applications of SPECT/CT: New Hybrid Nuclear Medicine Imaging System", IAEA-TECDOC-1597
- [26] A.C. Kak and M. Slaney, "Principles of computerized tomographic imaging", IEEE Press (1987)
- [27] G. T. Herman, "Image reconstruction from projections: The fundamentals of computerized tomography", Academic Press (1980)
- [28] J. Radon, "On the determination of functions from their integrals along certain manifolds" [in German], *Math Phys Klass*, **69**:262–277, (1917)

- 
- [29] M. Wernick and J. Aarsvold, "Emission Tomography: The fundamentals of PET and SPECT", Elsevier Academic Press (2004)
- [30] F. Natterer, "The Mathematics of Computerized Tomography", (New York: Wiley) (1986)
- [31] J. M. Ollinger and J. A. Fessler, "Positron-emission Tomography", *IEEE Signal Processing Magazine*, **14(1)**, 43-55 (1997)
- [32] G. L. Brownell and S. Cochavi, "Transverse section imaging with carbon-11 labeled carbon monoxide," *I. Comput. Assist. Tomog.*, **2**, 533-538 ( 1978).
- [33] H. Cho, M. B. Cohen, M. Singh, L. Eriksson, J. Chan, N. MacDonald and L. Spolter, "Performance and evaluation of the circular ring transverse axial positron camera," *IEEE Trans. Nucl. Sci.*, **NS-24**, 532-543 (1977)
- [34] G. F. Knoll, "Single-photon emission computed tomography", *Proc IEEE*, **71**, 320-329 (1983).
- [35] Aku O. Seppanen, "Correction of Collimator Blurring and Attenuation in Single Photon Emission Computed Tomography", M.Sc Thesis, University of Kuopio (2000)
- [36] S. Bellini, M. Piacentini, C. Cafforio and F. Rocca, "Compensation of tissue absorption in emission tomography", *IEEE Trans. Acoust. Speech Signal Process.* **27** 213–218 (1979)
- [37] O. J. Tretiak and C. Metz, "The exponential Radon transform", *SIAM. J. Appl. Math.* **39** 341–354, (1980)
- [38] W. G. Hawkins, P. K. Leichner and N. C. Yang, "The circular harmonic transform for SPECT reconstruction and boundary conditions on the Fourier transform of the sinogram", *IEEE Trans. Med. Imaging* **7**:135–148 (1988)

## References

---

- [39] T. Inouye, K. Kose and A. Hasegawa, “Image reconstruction algorithm for single-photon-emission computed tomography with uniform attenuation” *Phys. Med. Biol.* **34** 299–304 (1989)
- [40] I. Shneiberg, “The exponential Radon transform”, *Dokl. Akad. Nauk* **320** 567–571 (in Russian) (1991) (Engl. transl. *Sov. Math.–Dokl.* **44** 512–516 (1992))
- [41] I. Shneiberg, I. Ponomarev, V. Dmitrichenko and S. Kalashnikov, “On a new reconstruction algorithm in emission tomography” *Applied Problems of Radon Transform* ed S Gindikin (*AMS Transl. Ser. 2* **162** 247–255) (1994)
- [42] C. E. Metz and X. Pan, “A unified analysis of exact methods of inverting the 2D exponential Radon transform, with implications for noise control in SPECT”, *IEEE Trans. Med. Imaging* **14** 643–658 (1995)
- [43] P. Kuchment and I. Shneiberg, “Some inversion formulas in the single photon emission tomography” *Appl. Anal.* **53** 221–231 (1994)
- [44] P. Kuchment, “On inversion and range characterization of one transform arising in emission tomography”, *Proc. Conf. on 75 Years of the Radon Transform* (Hong Kong: International) 240–248 (1994)
- [45] E. V. Arbuzov, A. L. Bukhgeim and S. G. Kazantsev, “Two-dimensional tomography problems and the theory of  $A$ -analytic functions”, *Siberian Adv. Math.* **8** 1–20 (1998)
- [46] R. Novikov, “An inversion formula for the attenuated X-ray transformation”, *Ark. Mat.*, **40**: 145–167 (2000)
- [47] F. Natterer, “Inversion of the attenuated Radon transform”, *Inverse Problems* **17** 113–119 (2001)

- 
- [48] L. A. Shepp, Y. Vardi, “Maximum likelihood reconstruction for emission tomography”, *IEEE Trans Med Imaging*; MI-1:113–122, (1982)
- [49] H. M. Hudson, R. S. Larkin, “Accelerated image reconstruction using ordered subsets of projection data”, *J Nucl Med*, **13**:601–609, (1994)
- [50] G. F. Knoll, “Radiation Detection and Measurement”, 3rd ed. (Wiley, New York, 2000)
- [51] R. Hofstadter, “Alkali Halide Scintillation Counters”, *Phys. Rev.* 74, 100 (1948)
- [52] S. Koicki, A. Koicki and V. Ajdacic, “The investigation of the 0.15 s phosphorescent component of NaI(Tl) and its application in scintillation counting”, *Nucl. Instrum. Meth.* **108**, 297 (1973)
- [53] A. Iltis, M. R. Mayhugh, P. Menge, C. M. Rosza, O. Selles and V. Solovyev, “Lanthanum halide scintillators: Properties and applications”, *Nucl. Instr. Meth. A* **Vol. 63**, 359-363 (2006)
- [54] M. A. Saizu, G. Cata-Danil, “Lanthanum Bromide scintillation detector for gamma spectrometry applied in internal radioactive contamination measurements”, *U.P.B. Sci. Bull., Series A* **Vol. 73**, Iss. 4, 2011
- [55] A. Favalli, H. C. Mehner and F. Simonelli, “Wide energy range efficiency calibration for a lanthanum bromide scintillator detector”, *Radiation Measurements* **Vol. 43**, 506-509 (2008)
- [56] [www.detectors.saint-gobain.com/uploadedFiles/SGdetectors/Documents/Technical Information Notes/BrilLanCe-Scintillators-Performance-Summary.pdf](http://www.detectors.saint-gobain.com/uploadedFiles/SGdetectors/Documents/Technical%20Information%20Notes/BrilLanCe-Scintillators-Performance-Summary.pdf)
- [57] G. Dearnaley and D. C. Northrop, “Semiconductor Counters for Nuclear Radiations”, 2nd ed., Wiley, New York (1966).
- [58] G. Bertolini and A. Coche (eds.), “Semiconductor Detectors”, Elsevier-North Holland, Amsterdam (1968).

## References

---

- [59] S. J. Glick, B. C. Penney, M. A. King, and C. L. Byrne, "Non iterative compensation for the distance dependent detector response and photon attenuation in SPECT imaging", *IEEE Trans Med Imaging*, **13**:363-374, (1994).
- [60] D. R. Gilland, R. J. Jaszczak, H. Wang, T. G. Turkington, K. L. Greer, and R. E. Coleman, "A 3D model of non-uniform attenuation and detector response for efficient iterative reconstruction in SPECT", *Phys Med Biol*, **39**:547-561 (1994).
- [61] Z. Liang, T. G. Turkington, D. R. Gilland, R. J. Jaszczak, and R. E. Coleman, "Simultaneous compensation for attenuation, scatter and detector response for SPECT reconstruction in three dimensions", *Phys Med Biol*, **37**:587-603 (1992).
- [62] S. H. Manglos, F. D. Thomas, and R. B. Capone, "Attenuation compensation of cone beam SPECT images using maximum likelihood reconstruction", *IEEE Trans Med Imaging*, **10**:66-73 (1991).
- [63] V. Dicken, "Simultaneous activity and attenuation reconstruction in single photon emission computed tomography, a nonlinear ill-posed problem", PhD thesis, University at Potsdam (1998).
- [64] J. Nuyts, P. Dupont, S. Stroobants, R. Benninck, L. Mortelmans, and P. Suetens, "Simultaneous maximum a posteriori reconstruction of attenuation and activity distributions from emission sinograms", *IEEE Trans Med Imaging*, **18**:393-403 (1999)
- [65] X. Wang and K. F. Koral, "A regularized deconvolution fitting method for Compton-scatter correction in SPECT", *IEEE Trans Med Imaging*, **11**:351-360 (1992).
- [66] F. J. Beekman and M. A. Viergever, "Fast SPECT simulation including object shape dependent scatter" *IEEE Trans Med Imaging*, **14**:271-282 (1995).

- 
- [67] D. J. Kadrmas, E. C. Frey, S. S. Karimi, and B. M. W. Tsui, “Fast implementations of reconstruction based scatter compensation in fully 3D SPECT image reconstruction”, *Phys Med Biol*, **43**:857-873 (1998).
- [68] D. C. Camp, H. E. Martz, G. P. Roberson, D. J. Decman, R. T. Bernardi, “Nondestructive waste-drum assay for transuranic content by gamma-ray active and passive computed tomography”, *Nucl. Inst. Meth. - A* **495**: 69–83 (2002)
- [69] G. P. Roberson, H. E. Martz, D. J. Decman, J. A. Jackson, D. Clark, R. T. Bernardi, D. C. Camp, “Active and passive computed tomography for nondestructive assay”, Sixth Nondestructive Assay and Nondestructive Examination Waste Characterization Conference, Salt Lake City, Utah, 359 (1998).
- [70] Waste Inspection Tomography (WIT), Innovative Technology Summary Report, DOE/EM-0579 (2001)
- [71] R. T. Bernardi et al, Rapid Commercialization Initiative Final Report for the Waste Inspection Tomography, 96-RCI-09, DOE FETC (1998).
- [72] S. Jacobsson, “A tomographic measurement technique for irradiated nuclear fuel assemblies”, *Phd thesis*, Uppsala University
- [73] S. Holcombe, K. Eitheim, S. Jacobsson Svärd, L. Hallstadius, C. Willman, “Feasibility of Performing Pool-Side Fission Gas Release Measurements on Fuel Rods with Short Decay Time”, Proceedings of 2011 Water Reactor Fuel Performance Meeting / LWR/Top Fuel, Chengdu, China (2011).
- [74] Scott Holcombe, Staffan Jacobsson Svärd, Knut Eitheim, Lars Hallstadius, Christofer Willman, “Method for Analyzing Fission Gas Release in Fuel Rods Based on Gamma-Ray

## References

---

- Measurements of Short-Lived Fission Products”, *Journal of Nuclear Technology*, **184**, 1, 96-106 (2013)
- [75] S. Jacobsson, A. Håkansson, A. Bäcklin, P. Jansson, O. Osifo, C. Willman, “Tomography for partial-defect verification – experiences from measurements using different devices”, *ESARDA Bulletin* No.33
- [76] S. Jacobsson, A. Håkansson, P. Jansson, A. Bäcklin, “A Tomographic Method for Verification of the Integrity of Spent Nuclear Fuel Assemblies – I: Simulation Studies”; *Nuclear Technology*, Vol. 135, No 2; ISSN: 0029-5450 (2001)
- [77] S. Jacobsson, A. Håkansson, P. Jansson, A. Bäcklin, “A Tomographic Method for Verification of the Integrity of Spent Nuclear Fuel Assemblies – II: Experimental Investigation”, *Nuclear Technology*, Vol. 135, No 2; ISSN: 0029-5450 (2001)
- [78] H. Zaidi, “Quantitative Analysis in Nuclear Medicine Imaging”, *Springer*, New York (2006)
- [79] S. Vandenberghe, Y. D’Asseler, R. Van de Walle, et al “Iterative reconstruction algorithms in nuclear medicine”, *Comput Med Imaging Graph.* **25**:105–111 (2001)
- [80] C. Jacobsson, “Fourier Methods in 3D-Reconstruction from cone-beam data”, *PhD Thesis*, Linköping University (1996)
- [81] G. L. Zeng, “Image reconstruction - a tutorial”, *Computerized Medical Imaging and Graphics* **25**: 97-103, (2001)
- [82] Q. Huang, G. L. Zeng, J. You and G. T. Gullberg, “An FDK-like cone-beam SPECT reconstruction algorithm for non-uniform attenuated projections acquired using a circular trajectory”, *Phys. Med. Biol.* **50**: 2329–2339 (2005)
- [83] J. You, G. L. Zeng and Z. Liang “FBP algorithms for attenuated fan-beam projections”, *Inverse Problems* **21**: 1179–1192 (2005)

- 
- [84] H. Guan and R. Gordon, "Computed tomography using algebraic reconstruction techniques (ART) with different projection access schemes: a comparison study under practical situations", *Phys. Med. Biol.*, **41**:1727-1743 (1996)
- [85] K. Mueller, "Fast and accurate three-dimensional reconstruction from cone-beam projection data using algebraic methods", *PhD thesis*, The Ohio State University (1998)
- [86] R. Rangayyan, A. Prakash, and R. Gordon, "Algorithms for limited view computed tomography: an annotated bibliography and challenge", *Applied Optics*, **24 (23)**: 4000-4012 (1985)
- [87] A. H. Anderson, "Algebraic reconstruction in CT from limited view", *IEEE Transactions on Medical Imaging*, **8(1)**: 50-55 (1989)
- [88] H. Gilbert, "Iterative methods for the three-dimensional reconstruction of an object from projections", *Journal of Theoretical Biology*, **36**, 105-117 (1972).
- [89] A. B. Wolbarst, *Physics of Radiology*. Madison, Wisconsin: Medical Physics Publishing, 2000.
- [90] J. A. Fessler, "Statistical Methods for Image Reconstruction," *2004 NSS-MIC Short Course*, <http://www.eecs.umich.edu/~fessler/papers/talk.html> (2004).
- [91] K. Lange and R. Carson, "EM reconstruction algorithms for emission and transmission tomography", *J Comput Assist Tomogr*, **8**:306-316, (1984)
- [92] P. P. Bruyant, "Analytic and Iterative Reconstruction Algorithms in SPECT," *J. Nucl. Med.*, **43**, 1343-58, 2002.
- [93] H. M. Hudson and R. S. Larkin, "Accelerated image reconstruction using ordered subsets of projection data" *IEEE Trans. Med. Img.*, **39**, 1-38 (1977)

## References

---

- [94] A. Krol, D. H. Feiglin, W. Lee, V. R. Kunniyur, R. B. Salgado, I. L. Coman, et al., "Application of Ordered-Subsets Expectation- Maximization (OSEM) algorithm to cone-beam SPECT for accelerated 3D reconstruction," *IEEE Nuclear Science Symp. and Medical Imaging Conf.*, **6**, 3971-73 (2004).
- [95] S. Ahn, J. A. Fessler, D. Blatt, and A. O. Hero, "Convergent incremental optimization transfer algorithms: application to tomography," *IEEE Trans. Med. Imaging*, **25**, 283-296 (2006).
- [96] P. J. Green, "Bayesian reconstructions from emission tomography data using a modified EM algorithm," *IEEE Trans. Med. Imaging*, **9**, 84-93 (1990).
- [97] D. S. Lalush and B. M. W. Tsui, "Simulation evaluation of Gibbs prior distributions for use in maximum a posteriori SPECT reconstructions," *IEEE Trans. Med. Imaging*, **11**, 267-275 (1992).
- [98] G. K. Loudos, K. S. Nikita, N. K. Uzunoglu, N. D. Giokaris, C. N. Papanicolas, S.C. Archimandritis, et al., "Improving spatial resolution in SPECT with the combination of PSPMT based detector and iterative reconstruction algorithms," *Comput. Med. Imaging Graph.*, **27**, 307-313 (2003).
- [99] F. A. Mettler and M. J. Guiberteau, *Essentials of Nuclear Medicine Imaging*, 5<sup>th</sup> ed. Philadelphia, Pennsylvania: Elsevier (2006).
- [100] NDT: <http://www.ndt-ed.org/EducationResources/CommunityCollege/Radiography/Physics/radmatinteraction.htm> (2007).
- [101] M. Rafecas, B. Mosler, M. Dietz, M. Pogl, A. Stamatakis, D. P. McElroy, et al., "Use of a monte carlo-based probability matrix for 3-D iterative reconstruction of MADPET-II data," *IEEE Trans. Nucl. Sci.*, **51**, 2597-605 (2004).

- 
- [102] S. Moehrs, A. Del Guerra, D. J. Herbert and M. A. Mandelkern, "A detector head design for small-animal PET with silicon photomultipliers (SiPM)," *Phys. Med. Biol.*, **51**, 1113-27 (2006).
- [103] J. J. Scheins, F. Boschen, and H. Herzog, "Analytical calculation of volumes-of-intersection for iterative, fully 3-D PET reconstruction," *IEEE Trans. Med. Imaging*, **25**, 1363-9 (2006).
- [104] L. A. Feldkamp, L. C. Davis and J. W. Kress, "Practical cone-beam algorithm," *J. Opt. Soc. Amer.*, **1**, 612-619 (1984).
- [105] J. L. Starck, F. Murtagh and A. Bijaoui, *Image processing and data analysis* (Cambridge University Press, Cambridge) 287 (1998)
- [106] V. Y. Panin, F. Kehren, C. Michel, and M. Casey, "Fully 3-D PET reconstruction with system matrix derived from point source measurements," *IEEE Trans. Med. Imaging*, **25** (2006) 907-921.
- [107] C. A. Johnson, Y. Yuchen, R. E. Carson, R. L. Martino, and M. E. Daube-Witherspoon, "A system for the 3D reconstruction of retracted-septa PET data using the EM algorithm," *IEEE Trans. Nucl. Sci.*, **42**, 1223-1227 (1995).
- [108] S. C. B. Lo, "Strip and line path integrals with a square pixel matrix: A unified theory for computational CT projections," *IEEE Trans. Med. Imaging*, **7**, 355-363 (1988).
- [109] T. M. Peters, "Algorithms for fast back- and re-projection in computed tomography," *IEEE Trans. Nucl. Sci.*, **28**, 3641-3647 (1981).
- [110] R. B. Schwinger, S. L. Cool and M. A. King, "Area weighted convolutional interpolation for data reprojection in single photon emission computed tomography," *Med. Phys.*, **13**, 350-353 (1986).

## References

---

- [111] J. Gregor, T. Benson, S. Gleason, M. Paulus, S. Figueroa, T. Hoffman, et al., "Approximate volumetric system models for MicroSPECT," *IEEE Trans. Nucl. Sci.*, **53**, 2646-2652 (2006).
- [112] J. Gregor, S. Gleason, S. Kennel, M. Paulus, T. Benson, and J. Wall, "Approximate volumetric system models for microSPECT," *2004 IEEE Nuclear Science Symposium Conference Record*, **4**, 2475-2478 (2004).
- [113] J. J. Scheins, F. Boschen, and H. Herzog, "Analytical calculation of volumes-of-intersection for iterative, fully 3-D PET reconstruction," *IEEE Trans. Med. Imaging*, **25**, 1363-1369 (2006).
- [114] G. L. Zeng, G. T. Gullberg, B. M. W. Tsui, and J. A. Terry, "Three-dimensional iterative reconstruction algorithms with attenuation and geometric point response correction," *IEEE Trans. Nucl. Sci.*, **38**, 693-702 (1991).
- [115] R. L. Siddon, "Fast calculation of the exact radiological path for a three-dimensional CT array," *Med. Phys.*, **12**, 252-255 (1985).
- [116] George K. Loudos, "An efficient analytical calculation of probability matrix in 2D SPECT", *Computerized Medical Imaging and Graphics* **32**, 83-94 (2008).
- [117] M. Rafecas, B. Mosler, M. Dietz, M. Pogl, A. Stamatakis, D. P. McElroy, et al., "Use of a Monte Carlo based probability matrix for 3-D iterative reconstruction of MADPET-II data," *IEEE Trans. Nucl. Sci.*, **51**, 2597-2605 (2004).
- [118] G. P. Roberson, H. E. Martz, D. C. Camp, D. J. Decman, E. M. Johansson, "Preliminary A&PCT Multiple Detector Design", UCRL-ID-128052, Lawrence Livermore National Laboratory (1997)

- [119] Hongwei Ye, “Development and implementation of fully 3D iterative reconstruction approaches in SPECT with parallel-, fan- and cone-beam collimators”, *Ph.d Thesis*, Syracuse University
- [120] Q. Tang, G. L. Zeng and G. T. Gullberg, “Analytical fan-beam and cone-beam reconstruction algorithms with uniform attenuation correction for SPECT”, *Phys. Med. Biol.*, **50**, 3153–3170 (2005).
- [121] M. V. Narayanan, M. A. King, and C. L. Byrne, “Combined Fan/Parallel Beam Reconstruction in Cardiac SPECT Imaging”, *Conf. Record IEEE NSS* (1999).
- [122] [www.ndt.net/article/nde-india2009/pdf/4-C-5.pdf](http://www.ndt.net/article/nde-india2009/pdf/4-C-5.pdf)
- [123] Tuy H K: An inversion formula for cone-beam reconstruction *SIAM J. Appl. Math.* **43** 546–52 (1983)